6-1-2018

Synthesis of polysulfone/polyamide thin film nanocomposite membranes for forward osmosis applications

Ahmed Omaia Abdelfattah Mohamed Rashed

THE AMERICAN UNIVERSITY IN CAIRO
الجامعة الأمريكية بالقاهرة

School of Sciences and Engineering

Chemistry Department

Synthesis of Polysulfone/Polyamide Thin Film Nanocomposite Membranes for Forward Osmosis Applications

A Thesis in Chemistry

By

Ahmed Omaia Abdelfattah Mohamed Rashed

BSc, Chemistry, Cairo University, 2007

Under the supervision of

Prof. Adham Ramadan, Department of Chemistry

Prof. Amal Esawi, Department of Mechanical Engineering

Submitted to the School of Sciences and Engineering, Department of Chemistry, The American University in Cairo

In Partial Fulfillment of the Requirements for the Degree of Master of Science in Chemistry

Spring 2018

ACKNOWLEDGMENTS

First and foremost, I would like to express my sincere gratitude to my advisors, Prof. Adham Ramadan and Prof. Amal Esawi for their continuous support throughout my master studies. They taught me a lot inside and outside the lab, and I really had great opportunities and experiences by working under their supervision. I am so grateful to Prof. Adham Ramadan, who supported and encouraged me from the first day I joined AUC as a staff member. He taught me how to organize my lab work and how to write my thesis efficiently. I always consider you as my role model. Thank you Prof. Adham for guiding and encouraging me.

I would like to thank Prof. Amal Esawi, who taught and guided me during my studies. I never forget her simple explanation and clear analysis to solve any research challenges. She has responded to me whenever I need her help, and she called for regular meetings to discuss my work progress. Thank you Prof. Amal for your encouragement, effort and kindness.

I would like to thank The American University in Cairo for funding my studies as a staff member. I am really happy to work and study in this great university. AUC is a well-developed research place that give all the possible opportunities to achieve promising research projects.

I would like to thank all my professors in Chemistry Department for their continuous help during my studies, and I would to express my intense appreciation to Prof. Pakinam Askalani for the course of structural determination methods that helped me. I would like to thank Dr. Nahed Yacoub for helping and supporting me. Thank you Dr. Nahed for everything.

I would like to thank Dr. Mohamed El-Morsi in Mechanical Engineering Department for his help with setting up the test cell. I really appreciate his great efforts. I also wish to thank Dr. Hatem Elayat for the design of experiments course that helped in the statistical analysis.

I would like to thank all my colleagues and friends for their support and encouragement during my Master program. I am so grateful to Ayat Ashour, Ahmed Nour, Hoda Saad, Madina Ashour, Nouran Ashraf, Osama Elsayed, Samir Nabhan and Sherine Saad for their extensive inspiration.

The pursuit of my thesis project could not be done without the support of my family. I would like to thank my parents for loving and pushing me to finalize the Master program. I would like to thank my lovely brother and sister, Abdel Fattah Omaia and Eman Omaia for inspiring me.

LIST OF ABBREVITIONS

Abbreviation	Meaning
AFM	Atomic Force Microscopy
ANOVA	Analysis Of Variance
BET	Brunauer Emmett-Teller
CA	Cellulose Acetate
CAB	Cellulose acetate butyrate
CAP	Cellulose acetate propionate
DI	Deionized
DMAc	Dimethyl acetamide
DMF	Dimethyl formamide
DOE	Design of Experiments
ED	Electrodialysis
EG	Ethylene gylcol
F-MWCNTs	Functionalized Multi-walled Carbon nanotubes
FO	Forward Osmosis
FTIR	Fourier-Transform Infrared Spectrophotometer
ICP	Internal Concentration Polarization
IP	Interfacial Polymerization
MED	Multi-Effect Distillation
MPD	m-phenylenediamine
MSF	Multi-Stage Flashing
NF	Nano-Filtration
NMP	N-methyl pyrrolidone
PA	Polyamide
PBI	polybenzimidazole
PEG	Polyethylene glycol
PES	Polyethersulfone
ppm	part per million
PRO	Pressure Retarded Osmosis
PSF	Polysulfone
PVA	Polyvinyl alcohol
PVDF	Polyvinylidene fluoride
PVP	Polyvinylpyrrolidone

Ra	Surface Roughness
rGO	Reduced Graphene Oxide
RO	Reverse Osmosis
SDS	Sodium dodecyl sulfate
SEM	Scanning Electron Microscopy
SPEK	Sulfonated poly(ether ketone)
sPPSU	Sulfonated polyphenyl sulfone
TDS	Total Dissolved Solids
TFC	Thin Film Composite
TFNC	Thin Film Nano-Composite
TMC	1,3,5-trimesoyl chloride
UNFAO	United Nations Food and Agriculture Organization
VCD	Vapor Compression Distillation
WHO	World Health Organization
Wt.%	Weight percent
Wt/vol%	Weight per volume percent

ABSTRACT

Forward osmosis (FO) has attracted significant interest as a promising alternative to reverse osmosis (RO) in membrane-based water desalination applications. FO water flux, salt rejection and reverse solute flux are three critical parameters affecting membrane performance. Thin film composite (TFC) membranes have been widely used in FO processes. A typical TFC membrane consists of a rejection polyamide (PA) layer on top of a highly porous support layer. In the current study, carboxyl functionalized multi-walled carbon nanotubes (F-MWCNTs) were used as nano-fillers in the membrane rejection layer to enhance the FO membrane performance. Polyamide (PA) thin film nano-composite (TFNC) membranes were synthesized on top of polysulfone (PSF) porous support layers by interfacial polymerization (IP) using m-phenylenediamine (MPD) in water and trimesoyl chloride (TMC) in hexane. The PSF support layer was synthesized by phase inversion in a water bath of a casting solution of PSF and polvinylpyrrolidone (PVP) (pore forming agent) dissolved in anhydrous dimethyl formamide (DMF). Multi-walled carbon nanotubes were functionalized by oxidation in strong acidic solutions, and then incorporated in the MPD aqueous solution during IP. For the support layer, PSF and PVP concentrations were varied while monomers (MPD, TMC) concentrations, contact time and curing temperature were varied for the rejection layer. Experimental designs for both the support and the rejection layers were carried out using Design-Expert software including statistical analysis to identify the most significant factors affecting the membrane performance. The support layer of 18 wt% PSF and 2 wt% PVP was selected as the membrane support with the highest possible FO water flux and minimum reverse solute flux while the PA rejection layer of 4 wt/vol% MPD and 0.2 wt/vol% TMC was selected as the membrane rejection layer with a salt rejection of 88.30±0.11%. Finally, the amount of F-MWCNTs was varied from 0.01 to 0.2 wt/vol% to study their effect on the membrane morphology and performance. The synthesized membranes were characterized using Scanning Electron Microscopy (SEM), Atomic Force Microscopy (AFM), Fourier Transform Infrared Spectrophotometry (FTIR) and Brunauer-Emmett-Teller gas adsoprtion analysis (BET). FO performance was investigated using deionized water as the feed solution and 2 M NaCl as the draw solution. It was found that F-MWCNTs enhanced the membrane hydrophilicity and surface roughness that led to increased FO water flux. Most importantly, the salt rejection was also increased at low concentrations of F-MWCNTs (< 0.05 wt/vol%). The membrane with 0.01 wt/vol% F-MWCNTs showed the highest

salt rejection (90.05±0.25%) with a FO water flux of 50.23±0.93 L/m^2 h and a reverse solute flux of 2.76±0.21 g/m^2h, thus outperforming thin film composite FO membranes reported in literature.

Table of Contents

List of Figures

List of Tables

1. Chapter 1: Introduction

1.1. Global water challenges

Water is the basic source of life, and people need to have access to safe and readily available water resources. Water is essential for public health because it is used for drinking and food. In addition, it can be used in energy production. However, the amount of fresh water on earth is limited, and the quality of fresh water is challenging because of the presence of water pollutants and toxic chemicals. Although about 72% of earth's surface is covered by water, 97% of water is in oceans and seas and fresh water represents only 3%. Moreover, 77.6% of fresh water is frozen polar ice, 21.8% is groundwater, and less than 1% is available in lakes and rivers. Only 0.3% of fresh water is accessible for direct human usage [1].

In 2013, World Economic Forum in Davos approved water scarcity as the second most vital challenge facing humanity in the future, and according to the United Nations Food and Agriculture Organization (UNFAO), 1.9 billion people will suffer from absolute water scarcity and two thirds of the world population will be under water stress conditions by 2025 [2][3]. Therefore, water desalination has become an essential solution to face the global water crisis.

Water scarcity has become a challenging issue in Egypt since the availability of fresh water per capita rate is one of the lowest in the world. The average available fresh water per capita has declined from 1000 m^3/capita/year in the nineties to 670 m^3/capita/year in 2017 and it is expected to reach 500 m^3/capita/year by 2025. In addition, the total population of Egypt has increased from around 56 million in nineties to around 92 million in 2017, and it is expected to exceed 100 million by 2025. On the other hand, the Nile River, which is the main source of water in Egypt has been affected by the climate changes and precipitation changes due to the global warming and the low rainfall while the ground water is too deep, non-renewable, and it needs high cost to exploit it [4][5][6].

Therefore, desalination deserves to have a high priority as a water resource to exploit the extremely large areas of Red and Mediterranean Seas. However, the challenge is to find an efficient desalination technology with the minimal cost.

1.2. Desalination technology

Desalination is the process of removing dissolved salts and minerals from saline water to produce fresh water. Saline water sources are varied, including seawater, brackish water and wastewater. The salinities of the different saline water sources are expressed in terms of the total dissolved solids (TDS). The average TDS for seawater is 35,000 ppm and brackish water has 1,000 to 35,000 ppm TDS and those are the main feed sources for desalination processes. According to World Health Organization (WHO), fresh water contains less than 1,000 ppm and drinking water should not have more than 500 ppm TDS. Desalination requires energy. For example, the production of 1000 cubic meters of water per day requires about 10000 tons of fossil fuel per year. Therefore, it is crucial to minimize the energy required for desalination on the one hand, and to shift to renewable energy sources for desalination, on the other [7].

Desalination has developed significantly since 1960. In 1952, there were only about 225 desalination facilities all over the world with a total capacity of about 100,000 m^3/day. Recently, there are more than 15,000 desalination facilities with a total global capacity of 65 million m^3/day [3].

Desalination techniques can be categorized according to the principle of operation to include thermal-based and membrane-based techniques. Thermal-based techniques include multi-stage flashing (MSF), multi-effect distillation (MED) and vapor compression distillation (VCD) while membrane-based techniques include electrodialysis (ED), reverse osmosis (RO) and forward osmosis (FO). In addition, there are other new techniques that are still under investigation. In the next sections, the different desalination techniques will be discussed [8].

1.2.1 Multi-stage flashing (MSF)

MSF is based on the principles of flash evaporation and condensation. MSF consists of multiple flash chambers (18 to 25 stages) of decreasing pressure. In MSF, the saline feed water is preheated by a brine heater, and passed over a series of closed pipes. Then, the hot saline water is directed to a series of flash chambers of progressively decreasing pressure. The reduction in pressure in each chamber leads to flashing (boiling) of the saline water. Then, the fresh water is evaporated, and the vapor is collected and condensed by a heat exchange process between the vapor and the cooler saline feed water. The distillate is collected and directed to the fresh water containers and the remaining saline feed water (brine) is discharged or recirculated into the flash

chambers to get more fresh water. The typical TDS of the produced fresh water is 2 to 10 ppm. MSF systems usually operate at temperatures of 90 to 120 °C, and heating at higher temperatures could increase the system efficiency. However, the system metal surface would suffer from an accelerated corrosion. The main advantages of MSF is the simple operation and management. In addition, MSF can desalinate highly concentrated saline water up to 70,000 mg/L. The major disadvantage of MSF is the high energy consumption as it requires 3 to 5 KWh/m^3 electricity and 233 to 258 MJ/m^3 heat [7][9][10].

1.2.2 Multi-effect distillation (MED)

The multi-effect distillation (MED) technique is the oldest desalination method. The MED is similar to the MSF because it is based on the principles of evaporation and condensation at progressively reduced pressures in consecutive evaporator vessels. However, the setup is different from MSF. Each MED unit consists of an evaporator and a condenser. The evaporator is constituted by heat exchanger, a vapor zone, and a brine accumulation zone at the bottom of the evaporator. The condenser is a heat exchanger that is used to preheat the saline feed water and to condense the produced vapor. In MED, the saline feed water is heated until boiling to induce evaporation, and the steam inside the evaporator condensates due to heat exchange while the remaining saline feed water is pumped to the following effect at lower pressure and temperature. Hence, the process of evaporation and condensation continues inside different consecutive effects until the required production capacity. Then, the fresh water vapor is condensed and collected at the final stage while the brine concentrated saline water is discharged. One of the main advantages of MED is the reduced capital cost because 8 to 16 effects are used in MED, which is lower than the number of stages used in MSF. Also, the electrical energy consumption is only 1.5 KWh/m^3, which is lower than the consumption of MSF. However, fouling and scaling of the evaporators tubes are considered the main disadvantages of the MED technique [3][7][9][11].

1.2.3 Vapor compression distillation (VCD)

Vapor compression is a thermal distillation method that is used for desalination. This method also uses the principle of reducing the boiling point of the saline feed water by reducing the pressure to evaporate the water. However, the saline feed water is preheated using compressed vapor instead of the direct exchange of heat from the steam produced in a boiler. In VC process, compressed vapor is used to evaporate the saline feed water. Then, the produced vapor is withdrawn by the compressor and the compressed vapor is then condensed in the tube side of the evaporator by cooling using a plate heat exchanger. Fresh water is produced at the end of the cycle while the remaining saline water is discharged. The use of high capacity compressor allows operation at low temperatures below 70°C, which reduces the required heat and the potential for scale formation and corrosion. VC desalination is usually used for small-scale desalination units to produce about 3000 m^3/day. Therefore, VCD units are often used in resorts and drilling sites where fresh water is not readily available [9][12][13].

1.2.4 Electrodialysis (ED)

ED is a membrane-based desalination technique that has been used for many years. It is an electrochemical process that separates the ions from the feed solution using charged membranes and the effect of an electrical potential difference. As shown in Figure 1.1, a typical electrodialysis cell consists of a series of anion and cation exchange membranes arranged alternatively between an anode and a cathode to form individual cells. The ionic solution used in these cells is the salt solution. When an electrical potential is applied, the positively charged cations migrate towards the cathode and the negatively charged anions migrate towards the anode. The cations pass through the negatively charged cation exchange membrane and they are retained by the positively charged anion exchange membrane. On the other hand, the negatively charged anions pass through the anion exchange membrane, and they are retained by the cation exchange membrane. As a result, the ion concentration increases in alternate compartments while it decreases simultaneously in other compartments. The low ion concentration solution is the desalinated water (diluate) while the concentrated solution is the brine (concentrate). ED ion exchange membranes are composed of fine polymer particles incorporated with ion exchange groups. The ideal properties of ED ion exchange membrane include high selectivity, low electrical resistance, high chemical and thermal stability and high and good mechanical stability. ED can separate salts from water without any phase change. As a result, ED energy consumption

is relatively low. In addition, the ED process is not affected by the osmotic pressure. The main disadvantage of ED is the fouling resulting from the accumulation of the organic materials and colloids on the ED membranes because ED system can remove only the ions [14][15][16].

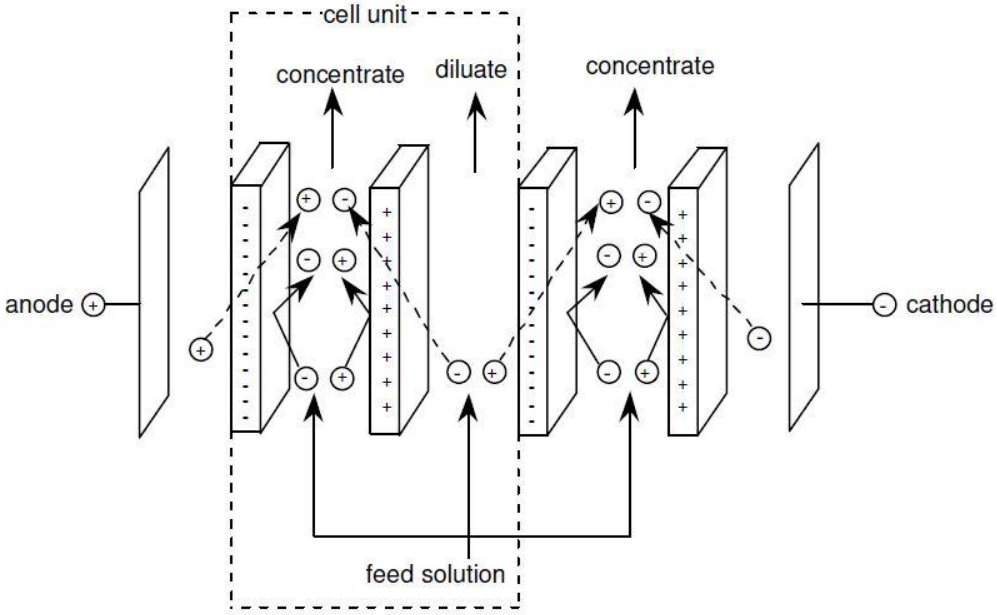

Figure 1.1: ED system schematic diagram [14]

1.2.5 Reverse Osmosis (RO)

Reverse osmosis (RO) is a membrane technology widely used in water desalination for the production of fresh water. In RO technology, a semi-permeable membrane is placed between a saline feed solution and a fresh water permeate solution. An external pressure is applied to force the water flow from the feed to the permeate solutions with the rejection of salts. In an osmosis process, the natural water flow is from the low salt concentration solution to the high salt concentration solution. Therefore, external pressure is needed in RO to overcome the osmotic pressure of the saline feed solution as shown in Figure 1.2. In seawater desalination, the required pressure ranges from 50 to 80 bar. The major advantage of RO over the thermal desalination methods is that heating and phase separation processes are not required for the desalination process [9][17].

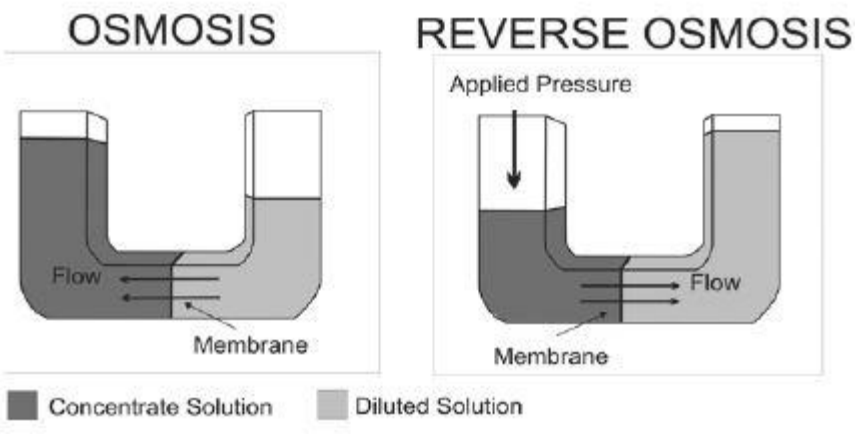

Figure 1.2: Osmosis versus Reverse Osmosis [18]

The efficiency of RO depends on the permeability and the selectivity of the semi-permeable membranes. RO membranes have a nominal pore size of 0.0001 micron to remove most of the dissolved compounds from water. A typical RO membrane consists of a very thin non-porous rejection layer and a porous support layer for mechanical stability. This combination of two layers is a characteristic of asymmetric membranes. Cellulose acetate (CA) asymmetric membranes were the first commercially available RO membranes since 1970. CA membranes were prepared by phase inversion. Although CA membranes are still used in RO, they showed apparent drawbacks such as low resistance to bacterial deterioration, ability to hydrolysis and stability in short pH range (4-5) for the feed solution. As a result, thin film composite membranes (TFC) were developed to overcome the drawbacks of the CA membranes. Most of TFC membranes are made of a porous support layer and a rejection polyamide layer. The rejection layer can be controlled since it is synthesized separately on top of the support layer. TFC membranes are chemically and physically more stable than CA membranes. They showed a strong resistance to bacterial deterioration. In addition, they do not hydrolyze and they are stable in a wider range of pH (3–11) [17][18].

The major disadvantage of RO is membrane fouling. Fouling is a process where solute particles in the feed water deposit on the membrane surface that leads to a water flux decline and affects the quality of the produced water. Therefore, membrane fouling leads to higher operating pressure requirements, frequent membrane cleaning, shorter membrane life, and consequently higher required energy and cost.

There are four main types of fouling on RO membranes:

1. Inorganic fouling which is caused by salt precipitations, such as metal hydroxides and carbonates.
2. Organic fouling which is caused by natural organic compounds, such as humic acid.
3. Colloidal fouling that results from suspended particles, such as silica.
4. Biological fouling that aroused from bacteria and fungi.

There are various fouling control strategies that include membrane pretreatment, membrane cleaning and surface modification. Generally, membranes with smooth, hydrophilic surfaces showed lower fouling tendency than those with rough, hydrophobic surfaces [19][20].

1.2.6 Forward Osmosis (FO)

The physical phenomenon of forward osmosis (FO) is a spontaneous process that entails the movement of water molecules across a semipermeable membrane from a low osmotic pressure side to a high osmotic pressure side. Basically, the difference in osmotic pressure is the driving force across the membrane. In FO, only water molecules can pass through the semipermeable membrane while the salt molecules move in the opposite direction, and they are rejected. FO does not need external pressure, a fact that makes it attractive in different applications that include pharmaceutical industry, fruit juices concentration, power generation, wastewater treatment and seawater desalination [21].

The efficiency of FO depends on the draw solution and the membrane. The draw solution is the source of the osmotic pressure while the membrane is used to reject salt molecules. In FO water desalination, saline water is used as the feed solution while a highly concentrated draw solution is used to generate high osmotic pressure. Under the effect of osmosis, the draw solution will be diluted as a result of drawing pure water from the feed solution, and the solutes of the draw solution are separated from these solutions either thermally or mechanically as shown in Figure 1.3. In another approach, saline water can be used as the draw solution while fresh water or lower concentration salt solution can be used as the feed solution, and this serves as a pretreatment step to dilute the saline water, and consequently reduce the energy required to desalinate the saline water [8].

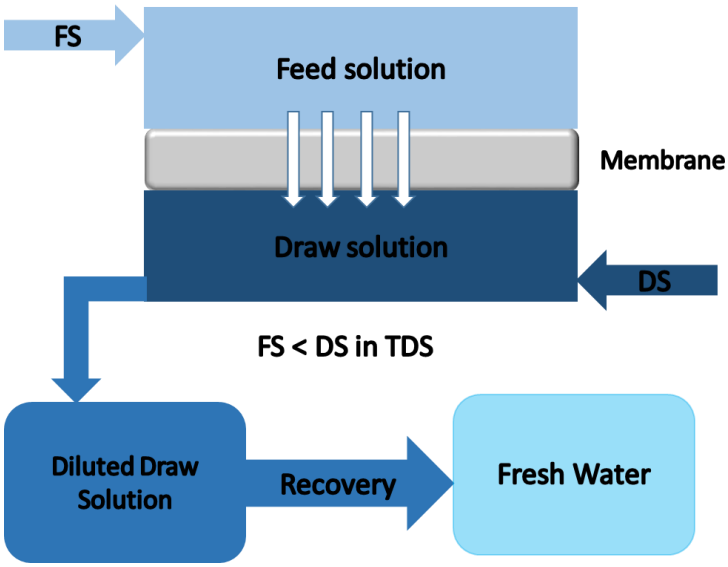

Figure 1.3: Forward osmosis water desalination process [8]

There are various membrane types that can be used in FO. An ideal FO membrane should be designed with a porous support layer and a high density, thin active layer. The highly porous, less tortuous support layer with hydrophilic properties is required to minimize the internal concentration polarization (ICP) and increase the water flux while the high density active layer is required to achieve high salt rejection and to minimize the reverse solute flux from the draw solution. FO membranes can be oriented in two orientations that include FO mode and pressure retarded osmosis (PRO) mode. In FO mode, the membrane rejection layer faces the feed solution, and the main application of this process is seawater desalination while in PRO mode, the membrane rejection layer faces the draw solution, and this orientation is commonly used for brackish water desalination and power generation by converting the osmotic pressure difference between the feed and the draw solutions into a hydrostatic pressure that can be utilized to generate electricity [22].

Research has shown that ICP is the major disadvantage of FO. Concentrative ICP is the result of water and solute permeation through the porous support layer that causes accumulation of solute molecules in the porous support and formation of a polarized layer on the active layer of the membrane. This takes place when the active layer of the membrane faces the draw solution. In consequence, the effective osmotic pressure will be reduced leading to a lower water flux. On the other hand, dilutive ICP occurs when the active layer of the membrane faces the feed solution, and water flows from the feed side to the draw side leading to draw solution dilution within the

porous support layer of the membrane. This also leads to a decrease in water flux [23]. In addition, the performance of FO membranes is affected by membrane fouling due to the accumulation of organic, inorganic, colloidal and microbial compounds on the membrane surface leading to a decline in the water flux. Another disadvantage of FO process is the reverse solute flux from the draw solutions that can affect the FO process negatively by reducing the FO performance and the membrane selectivity [24][25].

Therefore, thin film composite (TFC) membranes have been developed to overcome the latter disadvantages. A highly porous support layer with hydrophilic properties is prepared to enhance the water flux while a rejection polyamide layer is developed on top of the support to be responsible for the salt rejection and to minimize the reverse solute flux [26].

2. Chapter 2: Literature Review

This chapter will present a comprehensive review on the progress of FO membranes highlighting the main types of the FO membranes and the factors affecting their efficiency for water desalination. In addition, the main challenges for FO desalination will be identified based on different studies. Finally, the main factors affecting both the support layer and the rejection layer of the membrane will be reviewed.

2.1. Historical background

The osmosis phenomenon was observed by Nollet in 1748 [27]. However, there was not any progress on membrane development until the 1960's when Loeb and Sourirajan [28] managed to synthesize an asymmetric cellulose acetate RO membrane with high flux and high salt rejection. In 1965, Batchelder [29] was the first scientist to prepare an FO membrane using natural cellulose. Then, Frank used cellulose acetate (CA) RO membrane in water desalination in 1972 [30]. Votta et al. in 1974 [31] and Anderson in 1977 [32] analyzed various, commercial CA RO membranes for dilute wastewater treatment by FO using seawater as the draw solution. In 1975, Kravath and Davis [33] used CA flat sheet RO membranes from Eastman and hollow fiber membranes from Dow for seawater desalination by FO using glucose as the draw solution. In 1978, Goosens and Van-Haute [34] utilized CA RO membranes supported with mineral fillers to evaluate whether membrane performance under RO conditions could be estimated through FO testing. In 1979, Mehta and Loeb [35] investigated the FO performance of flat sheet and hollow fiber RO membranes synthesized from an aromatic polyamide polymer. FO membranes were not available in 1970's. Therefore, RO membranes were used in all studies on the FO process, and the observed water fluxes were of lower values than theoretical values predicted from the classical solution diffusion theory. The low water flux was attributed to the large thickness of the support layer of RO membranes that caused internal concentration polarization (ICP) [22].

In the 1990s, Hydration Technologies Inc. (HTI, Albany, OR) developed and marketed commercial FO membranes for the first time. These membranes consisted of cellulose triacetate with a woven fabric mesh that carried the porous support layer. The membranes showed a salt rejection above 95%, FO water flux in the range of 0.1 to 0.5 L/m^2h and reverse solute flux in the range of 0.6 to 11 g/m^2h. Therefore, these membranes have been used in FO desalination. However, the need for new fabrication techniques and advanced FO membranes that show

reduced ICP and reverse solute flux, with high FO water flux and good salt rejection is still valid [23].

Recently developed FO membranes can be classified into three main categories according to the method of fabrication. These categories include phase inversion fabricated membranes and thin film composite membranes.

2.2. Types of forward osmosis (FO) membranes

2.2.1 Phase inversion fabricated membranes

A. Hollow fiber membranes

In 2007, Wang et al. [36] used the phase inversion process to synthesize polybenzimidazole (PBI) nano-filtration (NF) hollow fiber membranes for use in FO desalination. The membranes were tested with deionized water as the feed, and different draw solutions of 2 M concentrations were used, such as NaCl, $MgSO_4$, $MgCl_2$, and Na_2SO_4. The membranes exhibited a water flux of 5.65 L/m^2h with 99.99% salt rejection when using $MgCl_2$ draw solution. However, the salt rejections were low for NaCl, $MgSO_4$, and Na_2SO_4 draw solutions. In addition, the recovery of pure water was too difficult and required high energy.

In 2009, Yang et al. [37] carried out some modifications to the PBI NF hollow fiber membrane by synthesizing a dual layer polybenzimidazole–polyethersulfone (PBI–PES) NF hollow fiber membrane by adding polyethersulfone (PES) and polyvinylpyrrolidone (PVP) in the casting solution. The membrane showed high water flux and good salt rejection (87%) using deionized water as the feed solution and 5 M $MgCl_2$ as the draw solution. However, NaCl salt rejection was not high (40%). In addition, the high cost and mechanical instability of PBI forced the researchers to find an alternative material for FO membranes.

B. Flat sheet cellulose acetate (CA) membranes

Cellulose acetate (CA) has been widely used to synthesize FO membranes by phase inversion followed by annealing in hot water. In 2011, Sui Zhang et al. [38] studied the formation mechanism of cellulose ester membranes on different casting substrates (glass, teflon, mica, TiO_2) in order to determine the optimum preparation conditions for forward osmosis (FO) membranes. The membrane was prepared by phase inversion by dissolving different cellulose acetate esters in different solvents that include N-methyl pyrrolidone (NMP), acetone,

formamide and water followed by phase inversion. Moreover, the selective layer formation during phase inversion was studied, and the dense selective layer was formed at the bottom interface between the polymer and the glass substrate. It was found that the casting substrate, cellulose hydrophilicity and solvent composition affected the structure and performance of the cellulose esters (FO) membranes. The membrane cast from hydrophobic cellulose acetate propionate (CAP) on a glass plate had a porous structure at the interface between the polymer solution and the glass plate while the membrane cast from hydrophilic cellulose acetate (CA) on a TiO_2 plate had the densest interface layer. Therefore, the CA membrane on a TiO_2 showed the highest salt rejection of 51.7% while the CA membrane on mica showed a lower salt rejection of 41.3%. The CA membrane on teflon was fully porous, resulting in 0% salt rejection. The four CA polymers had different numbers of hydroxyl groups, propionate, and butyrate groups. Hydroxyl groups increased the hydrophilicity of the membranes while propionate and butyrate groups increased the hydrophobicity of the membranes. Therefore, the membrane with hydrophilic CA showed the highest water flux (9.4 L/m^2h) while the membrane with hydrophobic CA showed a lower water flux (7.4 L/m^2h). In addition, it was found that NMP was the best solvent for CA due to the high porosity of the resulting membrane with finger-like macrovoids while acetone and formamide resulted in lower porosity for the corresponding membrane. The membrane cast from cellulose acetate (CA) using a 30 µm casting knife showed low internal concentration polarization (ICP) with high water flux (10 to 15 L/m^2h) when sea water was used as the feed, and the membrane showed a salt rejection value that reached 62%. Practically, this membrane was promising for FO water desalination.

In 2011, M. Sairam et al. [39] used phase inversion to prepare flat sheet composite membranes for FO applications using $MgSO_4$ draw solution. CA membranes were cast on a nylon fabric. The casting solution contained different pore formers: lactic acid, maleic acid and zinc chloride. Furthermore, the produced membranes were annealed at different temperatures. It was found that water flux and salt rejection depended on the pore forming agent. The performance of the CA membranes can be improved by adding organic acids or inorganic salts to the polymer solution in order to obtain high water flux membranes. In this investigation, lower flux (0.9 L/m^2h) and high salt rejection (99%) were observed using maleic acid as a pore forming agent. The water flux slightly increased to 1.3 L/m^2h when lactic acid was used during the membrane preparation with a salt rejection of 98%. CA membranes with zinc chloride as a pore forming agent showed a

higher water flux of 6.5 L/m^{2}h with 88% salt rejection. It was explained that $ZnCl_2$ could form stable complexes with hydroxyl groups of CA. Therefore, it can be completely incorporated into CA membrane. Then, the incorporated $ZnCl_2$ would be hydrated during the phase inversion in water, producing swollen CA membranes with high water flux.

In 2013, Ong et al. [40] investigated the effect of different functional groups of CA on the performance of FO membranes. It was found that hydrophilic CA membranes with high content of hydroxyl groups showed high water flux and low salt rejection while hydrophobic CA membranes with high content of propionyl and butyryl groups exhibited a lower water flux with a higher salt rejection. However, a much higher content of hydrophobic groups led to enlarged free volume sizes due to steric hindrance, resulting in a decrease in the salt rejection. Therefore, the investigation recommended using CA membranes with moderate content of hydrophilic hydroxyl groups and hydrophobic (propionyl and butyryl) groups.

The research emphasis on the synthesis of flat sheet CA FO membranes using phase inversion is supported by the inherent advantages of CA, such as low fouling susceptibility, mechanical strength, high resistance to chlorine, market accessibility, low cost, and high hydrophilicity that leads to high water flux. However, CA membranes are not chemically stable at highly acidic or basic conditions or at high temperatures (above 40 °C), as they undergo hydrolysis. Thus, these drawbacks must be taken into consideration when considering the use of CA FO membranes [23].

2.2.2 Thin film composite (TFC) membranes

Thin film composite (TFC) polyamide membranes have been synthesized on top of flat sheet or nanofiber substrates for FO applications. In general, these membranes have been prepared by the fabrication of a porous support layer by either phase inversion or by electrospinning, followed by the synthesis of a top rejection polyamide layer by interfacial polymerization (IP).

A. Flat sheet thin film composite membranes

Flat sheet TFC FO membranes were first fabricated by Yip et al. [41]. They used polysulfone (PSF) to prepare the support layer by phase inversion while the rejection layer was synthesized by IP between m-phenylenediamine (MPD) and 1,3,5-trimesoyl chloride (TMC). The membrane exhibited high salt rejection (97%) with FO water flux that exceeded 18 L/m^{2}h using deionized water as the feed solution and 1.5 M NaCl as the draw solution. The membrane was also tested

using 1.5 M ammonium bicarbonate draw solution to examine the chemical stability of the membranes under high pH, and the membrane showed good chemical stability with a water flux of 16.28 L/m^{2}h.

In 2011, Widjojo et al. [42] fabricated flat sheet TFC membranes with a sulfonated copolymer of polyether sulfone and sulfonated polyphenyl sulfone (PES-co-sPPSU) blended with PES as the support layer to increase the hydrophilicity of the membrane. The amount of the sulfonated copolymer was varied to study the effect of sulfonation on the structure and the performance of the membrane. It was found that the TFC-FO membrane with 50 wt.% sulfonated copolymer exhibited a fully sponge-like structure and high FO water flux of 21 L/m^{2}h using deionized water as the feed solution and 2 M NaCl as the draw solution.

In 2013, Widjojo et al. [26] used sulfonated polyphenyl sulfone (sPPSU) with different contents of sulfonated groups as a polymer for the support layer. The casting solution of the support layer contained 13 wt.% of the sulfonated polymer, 16 wt.% of ethylene glycol (EG) as an additive and 71 wt.% NMP as a solvent, and the support layer was developed by phase inversion in water. A rejection polyamide layer was synthesized on top of the support layer by IP between 2 wt.% MPD aqueous solution and 0.05 wt.% TMC in n-heptane solution. It was found that the increase of the sulfonated groups in the membrane led to an increase in the membrane porosity, and consequently a lower structural parameter and a reduced internal concentration polarization (ICP) because the diffusion of solutes across the highly porous, thin membrane became easier, thus leading to enhanced FO performance. The structural parameter is an indicator of the membrane porosity since it is a ratio of the membrane thickness and tortuosity to porosity [43]. Therefore, a highly porous, thin membrane resulted in a lower structural parameter. The investigators managed to prepare sulfonated membranes with a fully sponge-like structure. Consequently, the sulfonated membranes had a much higher water flux up to 78 L/m^{2}h under pressure retarded (PRO) mode with an applied pressure of 2.5 bar where the rejection layer was facing the draw solution and 62 L/m^{2}h under FO mode using 2 M NaCl as the draw solution. Water fluxes of the sulfonated membranes increased linearly with increasing the draw solution concentration as shown in Figure 2.1. However, salt rejection results did not exceed 84 % for the sulfonated membrane and 82 % for the non-sulfonated membrane.

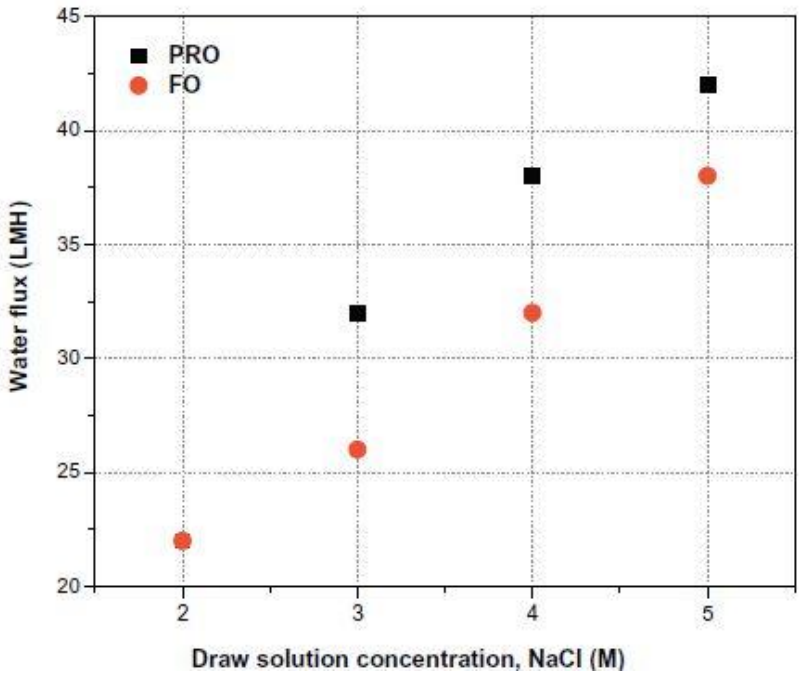

Figure 2.1: The water flux in FO and PRO modes of sulfonated TFC FO membrane using different draw solutions concentrations and 3.5 % NaCl solution as a feed [26]

In 2012, Han et al. [44] blended sulfonated poly(ether ketone) (SPEK) into a polysulfone support layer to increase the hydrophilicity of the thin film composite TFC for FO desalination with reduced ICP that increased the FO water flux of the synthesized membrane. A rejection polyamide layer was synthesized on top of the SPEK polysulfone support layer by IP reaction between 2 wt.% MPD in water and 0.2 wt.% TMC in hexane. Then, the membrane was heated under hot water at 95 °C. In this work, different amounts of SPEK (0, 25,50 wt.%) were added to the casting solution of polysulfone in NMP. The highest FO water flux was achieved by the membrane with 50 wt.% SPEK. The maximum values of FO water flux was 35 and 50 L/m^{2}h under FO and PRO modes respectively, using deionized water as the feed solution and 2M NaCl as the draw solution. On the other hand, the highest salt rejection (91%) was achieved by the membrane with 0 wt.% SPEK while the 50 wt.% SPEK membrane exhibited 89.5 %, and these results showed that the effect of SPEK content on the salt rejection was not as high as its effect on the FO water flux.

Another approach to synthesize TFC was suggested in 2014 by Sun et al. [45] who used a mixture of PSF and PES in NMP solution with a fixed amount of polyethylene glycol (PEG), and

investigated the effect of PSF/PES ratio on the porous support layer structure of the thin film composite (TFC) FO membrane. Three different sections were observed in the cross-section of the resulting support layer, using SEM imaging. A dense, skin layer was formed on top the support layer, a porous layer was formed in the middle of the support layer, and macrovoids were observed in the bottom of the substrate as shown in Figure 2.2. IP was conducted on top of the support layer using 2% of MPD aqueous solution and 0.1% of TMC in hexane solution to produce a polyamide thin layer. This was then cured at 95 $^{\circ}$C for three minutes. It was found that membranes with a PSF/PES ratio of 2/3 exhibited the highest water flux value of 27.6 L/m^{2}h, using deionized water feed solution and 2M NaCl draw solution. Furthermore, the water flux was 10.6 L/m^{2}h under FO mode and 12.7 L/m^{2}h under (PRO) mode using 3.5 wt.% of NaCl solution in the feed tank. This high water flux was attributed to the presence of cone shaped protrusions on the surface of the membrane and open sections on the bottom of the membrane. These protrusions were formed due to immediate precipitation of the polymer in water. Then, the protrusions were amplified during IP due to the repelling nature between aqueous and organic solutions. Therefore, the higher points of the hydrophilic MPD surface had more contact with the hydrophobic TMC hexane solution, leading to formation of bigger protrusions with high surface roughness. The high surface roughness increased the contact area with water which, together with macrovoids, led to high water flux membranes. In addition, the observed rejection layer was dense and homogeneous without leakage. This led to the formation of excellent salt rejection membranes. An interesting outcome from this investigation was the absence of ICP for the synthesized membranes: the water flux and reverse solute flux were almost fixed over a time period of 60 minutes when the membrane was tested with an FO cell using deionized water as the feed and 2 M NaCl as the draw solution as presented in Figure 2.3.

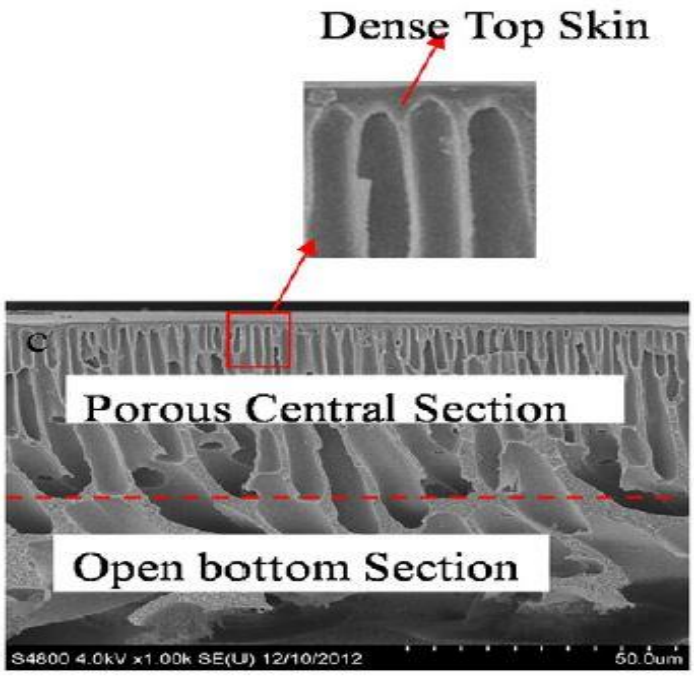

Figure 2.2: The cross-section of the membrane made from PSF/PES [45]

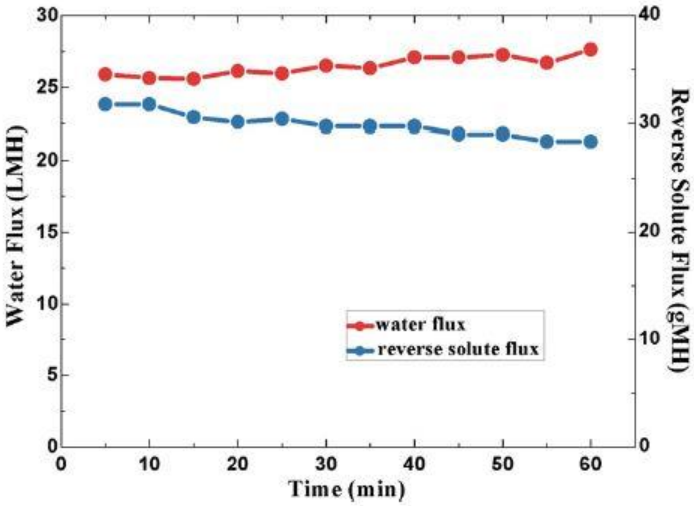

Figure 2.3: The water flux and reverse solute flux of 2/3 PSF/PES membrane using a 2 M NaCl solution as draw solution and deionized water as feed solution [45]

In 2015, Ong et al. [46] managed to prepare a novel thin film composite FO membrane using hydrophilic cellulose acetate propionate (CAP) and cellulose acetate butyrate (CAB) for the support. The aim of their work was to increase the hydrophilicity of the membrane support layer to improve the FO performance of the membrane. The support layer was prepared by phase

inversion using a casting solution consisting of 10 wt.% cellulose ester,42 wt.% N-methyl-2-pyrrolidone (NMP) as solvent, 42 wt.%PEG400 as a pore forming agent and 6 wt.% deionized (DI) water as a non-solvent. The rejection layer was synthesized on top of the support layer by IP between 2 wt.% aqueous MPD and 0.05 wt.% TMC in hexane. This was followed by immersion in sodium dodecyl sulfate (SDS)/glycerol solution to induce the IP. Then, the membrane was heated at 60 $^{\circ}$C to tighten the membrane pores and increase the salt rejection. Cellulose acetate ester thin film composite showed high water flux that reached 34 L/m^{2}h using 2 M NaCl draw solution, and it reached 90 L/m^{2}h when the rejection layer was oriented toward the draw solution in the (PRO) mode.

B. Nanofiber thin film composite membranes

On the other hand, in 2013, Tian et al. [47] explored the feasibility of using nanofibers to synthesize the support layer of FO membranes. They used electrospinning to fabricate nanofibrous mats of polyvinylidene fluoride (PVDF) to be used as a support layer. IP was then used to form a polyamide rejection layer. To this end, PVDF nanofber mats were soaked in an aqueous solution of m-phenylendiamine (MPD). Then, trimesoyl chloride (TMC) was poured onto the substrate surface in order to form the selective polyamide (PA) layer. The concentrations of MPD and TMC were varied to optimize the preparation conditions of the polyamide layer. In the first series, the aqueous solutions contained MPD with a concentration ranging from 1 to 10 wt.%, while the organic solutions had a fixed TMC concentration of 0.15 wt.% in n-hexane. In the second series, the MPD concentration was kept constant at 5.0 wt.%, while the TMC concentration was varied from 0.1 to 0.5 wt.%. The results showed that increasing MPD concentration from 1 to 5 wt.% at fixed TMC concentrations resulted in a slight decrease in the water flux from 2.7 L/m^2 h to 1.34 L/m^2 h while the salt rejection increased from 52.3% to 92.1%. On the other hand, increasing TMC concentration from 0.15 to 0.5 wt.% at a fixed MPD concentration resulted in a slight decrease in the salt rejection while the water flux increased. Therefore, it was concluded from this investigation that the separation properties of the ultrathin polyamide layer synthesized by IP were significantly influenced by the monomers concentrations and the reactants ratio. When the MPD/TMC ratio increased, the cross-linking degree increased resulting in a denser polyamide layer with smaller pore sizes that enhanced the salt rejection on the expense of the water flux of the membrane.

Another type of nanofiber FO membrane was prepared by John Marc C. Puguan et al. [2] in 2014. They synthesized a nanofiber thin film composite membrane from crosslinked electrospun polyvinyl alcohol (PVA) that exhibited higher FO performance than the Hydration Technology Innovations (HTI) commercial membranes. The synthesized membrane showed an FO water flux that was 8 times higher than the commercial membranes due to the high porosity and hydrophilicity of PVA nanofibers. In addition, a rejection layer of PA was developed on top the PVA nanofiber support layer by IP between 3 wt.% MPD, 2 wt.% TEA in water and 0.15 wt.% TMC in hexane. Then, the membrane was cured at 90 $^{\circ}$C in an oven to increase the crosslinking degree of the rejection PA layer. Thus, the obtained membranes showed an excellent salt rejection (97%), which outperformed the salt rejection of the HTI commercial membranes (92%). It was found that the crosslinking modification increased the hydrophilicity of the support layer that helped to reduce the ICP. In addition, FO water flux was increased from 6 L/m^{2}h using HTI membranes to 27 L/m^{2}h using PVA membrane.

Although most TFC membranes have been synthesized with a polyamide rejection layer, polyamide membranes are highly vulnerable to fouling due to their inherent surface physicochemical characteristics, such as surface charge and surface roughness that can attract organic foulants. Therefore, nanoparticles have been added to the rejection layer or to the support layer to overcome the fouling problem and to enhance the FO performance of the fabricated membranes [48].

C. Effect of different nanoparticles on thin film nanocomposite (TFNC) membranes

In order to overcome fouling, in 2012, Tiraferri et al. [48] synthesized thin film nanocomposite (TFNC) polyamide membranes for FO applications, with optimized surface properties using tailored silica nanoparticles functionalized with ligands containing quaternary ammonium groups. The super hydrophilic silica nanoparticles exhibited low intermolecular adhesion forces with organic foulants. The support layer was synthesized by dissolving 9 wt.% PSF in anhydrous DMF, followed by phase inversion in water while the rejection layer was synthesized by IP between MPD and TMC dissolved in Isopar-G. The membrane was then immersed in a suspension of functionalized silica nanoparticles in deionized water for 16 hours with only the rejection layer side being in contact with the suspension to obtain a nanocomposite membrane. It was found that incorporation of super hydrophilic silica nanoparticles into the membrane

enhanced the membrane performance by decreasing the fouling because the hydrophilic surface of the membrane had a better resistance to the organic foulants.

In 2014, silica nanoparticles were also incorporated in the polyamide active layer in another study by Neksefat et al. [49]. The silica nanoparticles were sonicated for 1 hour in MPD aqueous solution. Then, the membrane support layer was immersed in this solution. This was followed by the immersion of the membrane in TMC hexane solution. The study reported that the TFNC membranes showed higher water flux and better salt rejection in the range of 0.01 to 0.1 wt/v% silica loading in comparison with the conventional TFC membrane because the water flux of TFNC membranes increased from 10.3 to 22.5 L/m^{2}h in FO mode while it reached 36 L/m^{2}h in PRO mode. In addition, the salt rejection of TFNC membranes increased from 72% to 90% for 0.05 wt/v% silica loading due to pore blocking by the silica nanoparticles. However, a slight decrease in salt rejection to78% was observed at the highest silica loading of 0.1 wt/v% because of the agglomeration of the silica nanoparticles in certain locations which limited the IP, leading to a weak rejection layer.

In addition to the silica nanoparticles, incorporation of NaY zeolite nanoparticles into the polyamide rejection layer was presented as an efficient way to enhance water flux due to the porous nature of zeolite. In 2012, Ma et al. [50] prepared thin film nanocomposite (TFC) membranes with incorporated zeolite nanoparticles in the polyamide rejection layer on top of polysulfone (PSF) support layer. The support layer was prepared by dissolving 15.5 wt.% PSF, 0.5 wt.% PVP and 3 wt.% LiCl in NMP solution followed by phase inversion while the polyamide layer was synthesized on top of the support layer by IP between 1 wt.% MPD in water and 0.05 wt.% in n-hexane. In addition, zeolite nanoparticles were added to TMC solution in hexane followed by ultrasonication to disperse them effectively. TFNC membranes were prepared by immersing the support layer in MPD aqueous solution. Then, the TMC hexane solution with dispersed zeolite nanoparticles was poured on the membrane surface to form the polyamide rejection layer. It was found that the incorporation of zeolite nanoparticles into the polyamide layer increased the FO water flux from 11 L/m^{2}h for TFC without zeolite nanoparticles to 14.6 L/m^{2}h and 17 L/m^{2}h for TFNC with zeolite nanoparticle loadings of 0.05 and 0.1 weight/hexane volume% respectively. However, further increase in zeolite loading led to a reduction in water flux to 14 L/m^{2}h for 0.4 weight/hexane volume%. This was attributed to the

formation of a thicker polyamide layer. On the other hand, the results of salt rejection were not promising because zeolite loadings in the range of 0-0.2 weight/ hexane volume% resulted in lower salt rejection. Salt rejection decreased from 95.6% for TFC without zeolite nanoparticles to 75.1% for TFNC with 0.2 % zeolite nanoparticles. Surprisingly, it was found that further increasing the amount of zeolite nanoparticles led to an increase in the salt rejection to reach 90.5% using TFNC with 0.4% zeolite nanoparticles. This was explained by the development of a thicker polyamide layer.

In 2013, Ma et al. [51] incorporated NaY zeolite into the support layer of polysulfone (PSF). They demonstrated the use of porous particles and nanocomposite membranes for controlling internal concentration polarization (ICP). TFNC membranes were prepared using the same composition in their previous investigation summarized above, except that they incorporated zeolite nanoparticles within the support layer of polysulfone (PSF) by mixing the zeolite nanoparticles with PSF, PVP and LiCl (pore forming agents) in NMP solvent. Their work aimed to overcome the problem of internal concentration polarization (ICP) of solutes in the porous support layer, which would improve FO water flux. It was found that zeolite nanoparticles improved the surface porosity and hydrophilicity of the membrane that led to a higher water flux. For example, TFNC membrane with 0.5 wt.% loading showed 40 L/m^2h water flux in FO mode and 80 L/m^2h in PRO mode, and this water flux was more than double that of the conventional TFC without zeolite nanoparticles using 0 to 0.01 M NaCl as feed solutions and 2 M NaCl as a draw solution. It was explained that zeolite nanoparticles enhanced the membrane porosity and water flux due to creation of additional water pathways through the porous particles. However, salt rejection was only 86 % in case of TFNC with 0.05% zeolite loading while it was more than 90 % in case of TFC using NaCl solutions. Moreover, higher zeolite nanoparticles loading led to formation of a weak polyamide rejection layer on the support layer because zeolite nanoparticles could agglomerate in the reaction sites of IP. Hence, the zeolite loading required optimization.

In 2014, Emadzadeh et al. [52] incorporated titanium dioxide (TiO_2) nanoparticles with different amounts (from 0 to 1 wt.%) into a polysulfone support layer. It was found that the addition of TiO_2 nanoparticles increased porosity and hydrophilicity of the resulting nanocomposite membranes. In addition, the membrane cross-section in Figure 2.4 showed long finger-like macrovoids that increased with increasing the amount of TiO_2 nanoparticles. These long finger-

like macrovoids led to an enhancement in the water flux of the membrane. In order to use the membrane in FO applications, a rejection polyamide layer was synthesized on top of the PSF support layer by IP between 2% (wt/v) MPD in water and 0.1% (wt/v) TMC in hexane. Then, the membrane was cured at 60°C to increase the crosslinking degree of the polyamide layer. FO performance was evaluated using 10 mM NaCl solution as the feed and 2 M NaCl solution as the draw, and it was found that the water flux increased from 14 L/m^{2}h for the TFC without TiO_2 nanoparticles to 42 L/m^{2}h for the TFNC with 1 wt.% TiO2 nanoparticles. However, the performance of FO TFNC membranes were compromised by an increase in reverse solute flux from 5 g/m^{2}h to 18 g/m^{2}h and a reduction in the salt rejection from 92% to 74%.

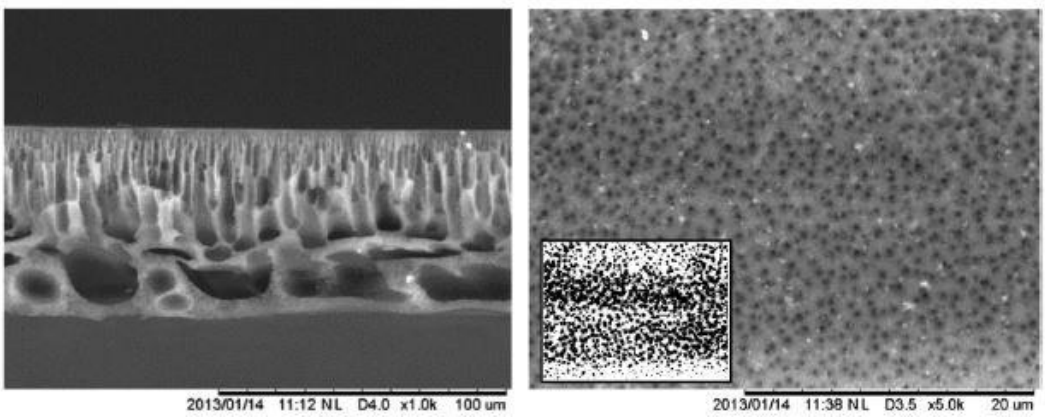

Figure 2.4: SEM of cross-section and top surface of PSF support layer with 0.5 wt.% TiO2 [52]

Recently, multi-walled carbon nanotubes (MWCNTs) were used in the fabrication of FO membranes. MWCNTS were incorporated into the support layer to enhance its mechanical strength. In addition, MWCNTs were added to the rejection polyamide layer to increase both salt rejection and FO water flux [53].

In 2013, Wang et al. [54] synthesized TFC for FO by incorporation of functionalized MWCNTs into the support layer. MWCNTs were functionalized with carboxylic groups using sulfuric and nitric acids at 60°C. The support layer was synthesized using 15 wt.% PES, 5 wt.% PVP, and the functionalized MWCNTs that were added with concentrations from 0 to 2.5 wt.% in dimethyl acetamide (DMAc) used as a solvent for the mixture. Then, a rejection layer from polyamide was synthesized on top of the support layer by IP between 3.4 wt.% aqueous MPD and 0.15 wt.% TMC in hexane solution. The effect of adding functionalized MWCNTs on the morphology and the performance of the TFC was investigated, and the results showed that MWCNTs improved

tensile strength, salt rejection and FO water flux. For example, the membrane with 2.5 wt.% MWCNTs exhibited a tensile strength that was twice that of the membrane without MWCNTs. In addition, the membranes with different amounts of MWCNTs showed improved salt rejections, higher than 90% as compared with the salt rejections for membranes without MWCNTs and for commercial membranes of 78% and 89% respectively. Additionally, MWCNTs containing membranes exhibited higher water fluxes due to production of a much porous structure and smoother rejection layer that developed over the hydrophilic support layer containing functionalized MWCNTs with carboxylic groups that had a high affinity to water.

In the same year 2013, Amini et al. [55] incorporated amine functionalized MWCNTs into the polyamide rejection layer during IP on top of the polysulfone support layer with concentrations ranging from 0.01 to 0.1 wt%. The support layer was synthesized using 16 wt% PSF, 2 wt% PVP as a pore former and 82 wt% DMF as a solvent. Then, the mixture was cast on a glass plate followed by phase inversion in water bath with 1 wt/vol% SDS and 2 wt/vol% DMF to initiate phase inversion. The rejection polyamide layer was synthesized using 1 wt% aqueous MPD and 0.1 wt% TMC in hexane. The amine functionalized MWCNTs were incorporated in the rejection polyamide layer by sonication with MPD solution for 4 hours. Then, the membrane was immersed in this solution followed by immersion in TMC hexane solution. It was found that incorporation of amine functionalized MWCNTs improved the performance of TFNC membranes for FO applications. The thin film nanocomposite membranes showed higher hydrophilicity and roughness than the membranes without amine functionalized MWCNTs, and the most permeable TFNC membrane in FO mode had a water flux of 40 L/m^2h, which is 60% higher than that of the thin film composite membrane without amine functionalized MWCNTs. In addition, TFNC with 0.05 wt% MWCNTs showed the highest NaCl rejection with 89.3%. However, further increasing of MWCNTs in the membrane resulted in a lower NaCl rejection of 73% for 0.1 wt% MWCNTs, and this was attributed to the agglomeration of MWCNTs during IP.

In 2015, Wang et al. [56] went further to modify the porous support layer of polyethersulfone (PES) using reduced graphene oxide (rGO) modified graphitic carbon nitride (g-C_3N_4) which is represented by CN/rGO. CN/rGO nanosheets were synthesized by Hummer's method followed by cyanamide polycondensation on the surface of GO. Different CN/rGO were added to the

mixture solution of PES in a mixed solvent of 1:1 ratio of NMP to DMAC. CN/rGO amount was varied from 0.2 to 1 wt.% to study their effect on the structure and performance of TFC membrane. Then, the solution mixture was sonicated by a tip sonication for 3 hours followed by continuous stirring for 24 hours to ensure a complete dispersion of CN/rGO. After that, the solution mixture was cast on a glass plate followed by immersion in a deionized water bath to initiate phase inversion. In addition, a rejection polyamide layer was developed on top of the support layer using IP between 2 wt.%. MPD, 2 wt.% triethylamine (TEA), 0.1 wt.% SDS in aqueous solution and 0.15wt % TMC in n-hexane solution. It was found that increasing the amount of CN/rGO in the support layer resulted in increasing FO water flux, with the highest FO water flux of 41.4 L/m^{2}h using deionized water in the feed solution and 2M NaCl in the draw solution was achieved using 0.5wt% CN/rGO modified membrane.

D. Factors affecting the support layer

a. Effect of solvent

In 2005, Madaeni et al. [57] studied the effect of different solvents on the morphology and performance of polysulfone membrane used in ultrafiltration applications. The solvents used in the study were N, N dimethylacetamide (DMAc), N, N-dimethyl formamide (DMF) and 1-methyl-2-pyrrolidone (NMP). The results showed that highly porous membranes were obtained in different solvents. When DMAc was used as the solvent for polysulfone, the porosity of the membrane increased. When NMP was utilized as the solvent for PSF, a membrane with a dense upper layer was developed with a low porosity sub-layer. The membrane with lowest lowest porosity was obtained using DMF as solvent in the casting solution. However, this membrane showed the desired sponge-like structure with a large number of small pores.

Similarly, in 2011, Tiraferri et al. [58] investigated the effect of solvent type on the morphology and performance of polysulfone support layer. They used 12% of PSF in different solvent systems of NMP and DMF. As the DMF amounts increased, the non-solvent would move to the polymer solution more slowly, and the resulting membrane exhibited a sponge-like structure. As NMP amounts increased, the non-solvent would move faster to the polymer solution, resulting in a larger number of finger-like macrovoids structures. The water flux obtained from PSF membrane dissolved in DMF showed an FO water flux of 17.6 L/m^{2}h while the membrane dissolved in NMP showed 13.9 L/m^{2}h FO water flux.

b. Effect of PVP (polyvinylpyrrolidone)

Polyvinylpyrrolidone (PVP) has been widely used as a casting solution during the preparation of polysulfone (PSF) membranes by phase inversion. PVP is an additive that can act as a pore former, and it can increase the viscosity of the casting solution. It has been reported that the addition of PVP can develop macrovoids in the membrane structure, resulting in increased water flux. In 2002, Myeong et al. [59] varied the amount of PVP from 0 to 20 wt.% , and then added to 15 wt.% PSF casting solution dissolved in NMP. It was found that increasing PVP resulted in a higher viscosity solution that facilitated the casting process. PVP had a great effect on enhancing and acceleration of the phase inversion process. It was found that 5 wt.% PVP was responsible for macrovoids enlargement.

In 2008, Chakrabarty et al. [60] synthesized PSF membranes from casting solutions that contained 12 wt% of PSF dissolved in NMP and DMAc by phase inversion. Different molecular weights of PVP were employed as additives for casting solutions of PSF. The different molecular weights used in the study were 24,000, 40,000 and 360,000 Da. The effect of different PVP molecular weights on the morphology and performance of the PSF membranes was investigated, and the results showed that an increase in the molecular weight of PVP resulted in an increase in the measured water content from 46% to 70%. Water content was measured by measuring the weight difference between dry and wet membranes. This increasing trend indicated the increased membrane hydrophilicity with large number of pores. This was explained by the fact that increasing the PVP molecular weight could lead to an increase in the casting solution viscosity that caused a kinetic hindrance against the phase inversion. Therefore, large number of pores could be produced, leading to an increased porosity.

E. Different factors affecting synthesis of rejection polyamide layer

To fabricate a thin film composite membrane, a rejection layer must be developed on top of a porous support layer. The most common technique used to develop the rejection layer is interfacial polymerization (IP), which includes a reaction between two monomers (diamine, acid chloride) dissolved in different solutions (aqueous and organic solutions, respectively) in order to form a thin rejection polyamide layer. Most of the researchers have used m-phenylene diamine dissolved in water and trimesoyl chloride dissolved in hexane or heptane as the reactive monomers to perform the IP reaction. The rejection polyamide layer must be uniformly

distributed over the support layer, and it should exhibit good salt rejection values while not adversely affecting the FO water flux. Many studies have reported the effect of different factors on the performance of the rejection polyamide layer [61].

a. Monomer concentration

In 2011, Wei et al. [62] investigated the effect of changing the concentrations of the reacted monomers on the performance of the rejection PA layer in FO desalination. The rejection PA layer was synthesized on top of a polysulfone (PSF) support layer by IP between aqueous MPD and TMC in hexane. They prepared two series of FO membranes. In the first series, MPD concentrations in water were varied from 0.5 to 2 wt.% while the concentration of TMC in hexane was kept fixed with a value of 0.5 wt./v%. In the second series, TMC concentrations in hexane were varied from 0.05 to 1 wt./v% while the concentration of MPD in water was kept constant with a value of 1 wt.% . The results revealed that water flux decreased from 5.7 to 1.3 L/m^2h after increasing the MPD concentration from 0.5 to 1 wt.% at a fixed concentration of TMC. In addition, salt rejection increased from 45% to 75%. On the other hand, the water flux was increased after increasing TMC concentration, and the salt rejection decreased to 51%. The results showed that a higher TMC concentration could lead to a shortage in MPD available for the IP reaction. The study concluded that higher MPD/TMC ratio resulted in higher degree of crosslinking that lead to a denser rejection PA layer with higher salt rejection and lower water flux. Similar results have been reported by Roh et al. [63].

b. Effect of additives

It has been reported that adding different additives influenced the structure of the rejection PA layer. In 2008, Ghosh et al. [64] investigated the effect of adding TEA with (CSA) acid to the aqueous solution of MPD, and they found that the membranes with TEA and CSA showed an increased water flux. However, the salt rejection remained constant.

Another approach suggested addition of surfactants like SDS to the aqueous MPD solution in order to improve the hydrophilicity of the PSF support layer to facilitate the IP reaction on the support layer [61]. In 2009, Saha and Joshi [65] studied the effect of adding SD to the aqueous solution of MPD during IP reaction. It was found that the performance of the membrane remained constant at a low concentration of SDS (0.1wt.%), and by increasing SDS

concentration from 0.1 to 0.5 wt.%, the salt rejection decreased from 48% to 10%. However, they suggested adding SDS to facilitate the transfer of amine molecules to the organic phase by decreasing the interfacial tension of the membrane. In 2011, Jing Wei et al. [66] studied the effect of adding 0.1 wt.% SDS to the aqueous phase of MPD, and it was found that water flux increased from 107 to 190 L/m^{2}h. However, the salt rejection decreased slightly from 94% to 93%.

c. Effect of thermal curing

It has been reported that thermal curing could affect the performance of the thin film composite. In 2015, Hermans et al. [67] investigated the effect of curing temperature on TFC. TFC membranes were heated at temperatures ranging from 25 °C to 110 °C. It was found that increasing the curing temperature led to a lower water flux and a higher salt rejection. Water flux declined from 10 to 3.5 L/m^{2}h when the curing temperature increased from 25 to 50 °C, and the salt rejection increased from 92 to 97%. This was explained by an increased degree of crosslinking during the IP reaction to form a rejection PA layer. However, increasing the temperature to 110 °C resulted in a strong decline in water flux to 0.02 L/m^{2}h due to collapsing of the support layer pores. Therefore, it was suggested to cure the TFC membrane with a suitable temperature that can achieve the high selectivity and optimal water flux.

2.3. Development of draw solutions for FO applications

Draw solutions play an essential role in the process of FO because the difference in osmotic pressures between the draw and the feed solutions is considered to be the driving force for the FO process. The ideal draw solution must exhibit certain characteristics to promote the efficacy of the FO process. Firstly, it must produce higher osmotic pressure than that of the feed solution which can be achieved by increasing its concentration. Secondly, it must result in low reverse solute flux. Thirdly, the diluted draw solution after the FO process must have an easy recovery with lower energy and cost. Finally, the draw solution is to preferably have a high diffusion coefficient to minimize internal concentration polarization (ICP), and this can be achieved by using low viscosity draw solutions [68][69].

Different draw solutions have been investigated over the past several years. In 1992, Yaeli [70] utilized a saturated solution of cane sugar containing sucrose and glucose as the draw solution

for FO desalination. This investigation aimed at desalination of the sea water using FO system through a semi-permeable membrane. Sea water was used as the feed solution while cane sugar solution was used as the draw solution because it has high solubility in water (6 moles/L), and it has osmotic pressure which was ten times higher than that of sea water. Thus, a high pressure difference was created through the semi permeable membrane, leading to a significant water flow from the sea water side to the sugar solution without any applied pressure. In addition, cleaning the membranes from sugars was feasible because sugar molecules can be dissolved easily by boiling water. Moreover, the diluted sugar solution was recovered by Reverse Osmosis (RO) to reject the sugar molecules and to pass pure water through a semipermeable membrane with large pore sizes in order to reduce the applied mechanical pressure. Large pore size membranes were efficient to reject the sugar molecules that had larger pore sizes. Hence, the recovery process by RO system did not require high energy and cost.

Furthermore, several studies have been conducted to investigate salts as solutes for the draw solutions. In 1997, Loeb et al. [71] examined different concentrations of $MgCl_2$ for FO applications to study their effect on the water flux of CA membranes. In this investigation, 6% $MgCl_2$ was used as the feed solution while 12% $MgCl_2$ was used as the draw solution, and the resulting water flux was 2.5 L/m^2h. Then, the water flux increased to 3.9 L/m^2h when the concentration of the draw solution increased to 18% $MgCl_2$. This increase was attributed to the higher osmotic pressure difference between the feed and the draw solutions from 90 atm to 240 atm.

In 2002, McGinnis [72] used KNO_3 and SO_2 as draw solutions for seawater desalination. KNO_3 and SO_2 were selected as draw solutions because their solubility in water is temperature dependent, and this facilitated the water recovery by thermal manipulation. In this investigation, sea water was used as the feed solution while KNO_3 saturated solution was used as the first draw solution and SO_2 saturated was used as the second draw solution. The investigation was done by a two-stage FO system through a semi-permeable membrane. Firstly, sea water was heated, and water passed to the first draw side by the effect of osmotic pressure. Secondly, the first draw solution was cooled though a heat exchanger that led to salt precipitation. Thirdly, water passed from the first draw side to the second draw side with a higher osmotic pressure, and the solution

was heated leading to a decrease in SO_2 concentration. Then, a very low concentration solution was obtained.

In 2005, McCutcheon et al. [73] utilized NH_4HCO_3 draw solution to extract water from a saline feed solution through CA membranes by FO system. NH_4HCO_3 was used as the draw solution since it had high solubility in water, and it showed a high osmotic pressure that reached 150 atm for 6 M NH_4HCO_3 solution. This osmotic pressure was higher than sea water in the feed solution (25 atm) that facilitated the water flow from the feed side to the draw side. In addition, the water flux was investigated using 0.5 M NaCl feed solution and different concentrations of NH_4HCO_3 draw solutions, and the results showed an increase in the water flux by increasing the concentration of the draw solution from 10 L/m^{2}h for 2 M NH_4HCO_3 solution to 22 L/m^{2}h for 6 M NH_4HCO_3 solution. Moreover, the recovery of pure water from the draw solution was achieved easily by heating at 60^{o}C because NH_4HCO_3 decomposed to NH_4 and CO_2 gases. These gases could be removed easily by low-temperature distillation using low energy.

In 2008, Cornelissen et al. [74] tested different draw solutions of $MgSO_4$, NaCl, $NaNO_3$ and $ZnSO_4$ under FO mode using deionized water as the feed solution. It was found that higher water fluxes were obtained from the monovalent rather than the bivalent draw solutions, and this was explained by the higher diffusivity of the monovalent salts through the porous structures. Therefore, the water fluxes of 1.5 M different draw solutions were 9.5 L/m^{2}h for NaCl, 8 L/m^{2}h for $NaNO_3$, 5 L/m^{2}h for $MgSO_4$ and 4.2 L/m^{2}h for $NaNO_3$.

On the other hand, in 2007, Adham et al. [75] used magnetic nanoparticles like magnetoferritin bound by polyethylene glycol in the draw solution for FO. The magnetic nanoparticles showed high dispersion in water using ultrasonication although the ultrasonication could affect the magnetic properties of these nanoparticles. In addition, the magnetic nanoparticles could be recovered from the purified water by a magnetic separator. However, the development of suitable magnetic nanoparticles with high osmotic pressure is still challenging, and the cost is too high.

In 2010, Achilli et al. [76] analyzed different draw solutions for FO applications. They found that $CaCl_2$, $KHCO_3$, $MgCl_2$, $MgSO_4$, KCl and $NaHCO_3$ solutions could be used as draw solutions for FO applications, and it was found that KCl resulted in the highest water flux (10.9 L/m^{2}h) among the different draw solutions.

Another approach for draw solutions was reported by Phuntsho et al. [77]. They used fertilizers as solutes for the draw solutions for FO desalination in order to be available for irrigation. In this investigation, deionized water was used as the feed solution while 2 M different fertilizers solutions were used as the draw solutions. The investigated fertilizers included KNO_3, KCl, $NaNO_3$, $NH_4H_2PO_4$, $(NH_4)_2SO_4$ and $Ca(NO_3)_2$. It was found that $CaNO_3$ showed the highest osmotic pressure of 108.5 atm. However, the highest water flux (22.87 L/m^2h) was achieved using KCl draw solution. Moreover, it was found that 1 Kg of the fertilizer could extract from 11 to 29 L water from the feed solution. Then, the diluted fertilizers solutions could be used in agricultural purposes since the fertilizers elements were required for the plants, and this process is called fertilizer drawn forward osmosis.

2.4. Research Objective

This work aims at developing a TFNC FO membrane with high FO water flux and salt rejection with the lowest possible reverse solute flux to be used in water desalination. The fabrication of an efficient TFNC FO membrane is affected by different parameters of both the support and rejection layers. Therefore, the work started by studying the effect of different factors on the support layer to achieve a highly porous support layer with high FO water flux and low reverse solute flux compared to the literature. Then, the effect of different factors affecting the synthesizing of the rejection layer on top of the support layer, were studied to develop an efficient rejection layer with high salt rejection. Finally, the effect of carboxyl-functionalized multi-walled carbon-nanotubes (F-MWCNTs) incorporation in the rejection layer, was studied by incorporating different concentrations of F-MWCNTs in the rejection layer, and then, the performance of the synthesized TFNC FO membranes was determined. This study aims to investigate the effect of F-MWCNTs on the performance of TFNC FO membranes after their incorporation in the rejection layer since few studies in the literature have reported the effect of F-MWCNTs on TFNC FO membrane performance, and their work focused on the incorporation of F-MWCNTs in the support layer rather than the rejection layer.

3. Chapter 3: Theoretical Background

This chapter presents the different techniques and instruments used in this study. These include phase inversion, interfacial polymerization (IP), Brunauer Emmett-Teller (BET), Fourier-Transform Infrared Spectrophotometer (FTIR), contact angle instrument, Atomic Force Microscopy (AFM) and Scanning Electron Microscopy (SEM). In addition, the principle of the Design-Expert statistical software is explained at the end of this chapter.

3.1. Phase inversion technique

Phase inversion is a controlled process of converting a polymer solution from a liquid phase to a solid phase. It is frequently used in membranes fabrication by removing the solvent from the polymer liquid solution to obtain a solid, porous membrane. By controlling the phase inversion process, multiple morphologies can be obtained to be used in different applications. Highly porous membranes are used in microfiltration while denser membranes are used in reverse osmosis, and complete defect-free membranes are used in gas separation. There are four main types of phase inversion technique: vapor phase precipitation, controlled evaporation precipitation, thermally induced phase separation and immersion precipitation.

Vapor phase precipitation is carried out by placing a solvent-polymer solution on a film. Then, it is placed in a vapor atmosphere with a non-solvent saturated with the same solvent. The high concentration of solvent in the vapor atmosphere prevents the solvent evaporation from the cast film into the atmosphere, and the membranes are produced by the non-solvent diffusion into the cast film. This process is used to produce porous membranes.

Controlled evaporation precipitation is carried out by dissolving the polymer in a solvent and a non-solvent mixture. Then, the solvent evaporates due to the high volatility. Therefore, the mixture with higher non-solvent and polymer contents is produced, and the polymer precipitates to produce a skinned membrane.

Thermally induced phase separation is achieved by cooling down a solvent-polymer solution, and solvent evaporation induces the membrane fabrication. This process is used to produce microfiltration membranes.

Immersion precipitation is the most widely method for membranes preparation, and it includes dissolving the polymer in a suitable solvent. Then, the polymer solution is cast on a solid support

(glass substrate) followed by an immersion in a coagulation non-solvent (water) bath to induce the phase inversion by the solvent and non-solvent exchange to produce the membrane. The membrane structure is controlled by the phase separation and the mass transfer [78].

Furthermore, the immersion precipitation phase inversion is controlled by the polymer, the solvent, the non-solvent and the additive that might be a pore forming agent. A ternary diagram shown in Figure 3.1 is used to explain the phase inversion process of a system containing polymer, solvent and non-solvent. From Figure 3.1, the triangle is divided by the binodal curve into a single phase region where all the mixture components are immiscible, and a two phase region that includes a solid (polymer rich) phase and a liquid (polymer lean) phase. The whole precipitation process is described by the path between the initial casting solution and the final membrane composition points at which the solvent is replaced by the non-solvent. The precipitation point is the point at which the polymer is initiated. While the precipitation occurs, the viscosity of the precipitated polymer highly increases to form a solid membrane at a certain point. By drawing a tie line at this point, the compositions of the polymer rich (polymer matrix) and polymer lean (pore) phases can be identified. Therefore, the final membrane morphology is strongly affected by the initial casting solution composition, the precipitation path and the binodal curve position. In polymeric systems, the system kinetics affects the precipitation path line while the system thermodynamics affects the position of binodal points [78][79].

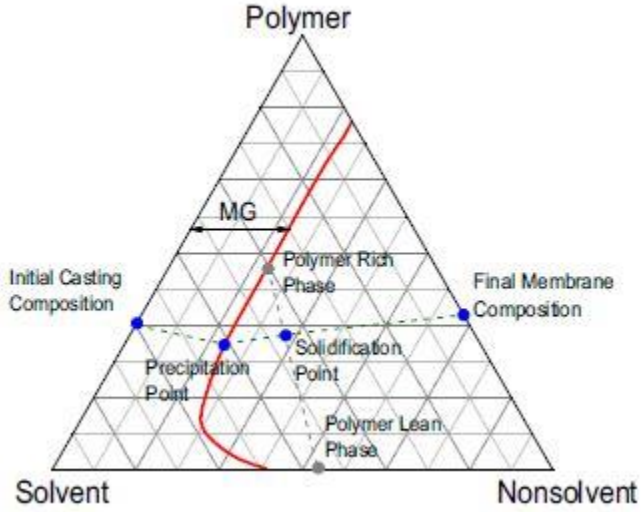

Figure 3.1: A ternary phase diagram describing the binodal curve and the precipitation pathway [79]

In membrane technology, polysulfone (PSF) is widely used as a polymer for microfiltration and ultrafiltration membranes, and it is also used as a support layer for RO and FO membranes. Support membranes require a highly porous structure to enhance the water flux, and this can be achieved by adding a hydrophilic pore forming agent like polyvinylpyrrolidone in the casting solution of PSF in dimethyl formamide (DMF) to increase the demixing rate (solvent and non-solvent exchange) leading to enhanced membrane porosity and higher water flux. Figure 3.2 describes the phase inversion process of a PSF support membrane using DMF as a solvent, deionized water as a non-solvent and PVP as a pore forming agent [59].

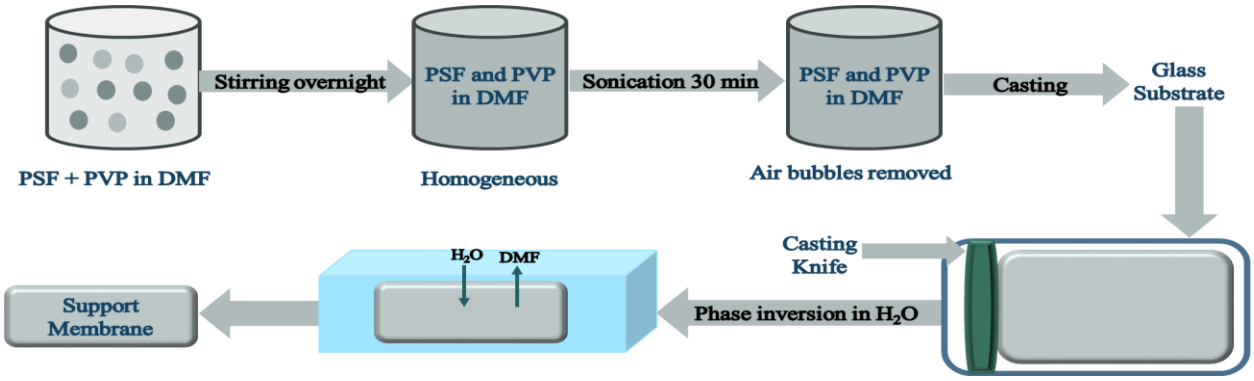

Figure 3.2: Phase inversion process description of PSF support membrane

3.2. Interfacial polymerization (IP) technique

Interfacial polymerization (IP) is an irreversible, fast reaction that has been used to prepare a thin, rejection layer for thin film composite (TFC) membranes that can be used in RO and FO applications. IP technique is based on a polycondensation reaction between two monomers: polyamines and polyacyl chlorides dissolved in two immiscible solvents. Polyamines are dissolved in water to form an aqueous solution while polyacyl chlorides are dissolved in an organic solvent to form an organic solution. Then, a thin, rejection layer is developed quickly at the interface between the two immiscible solutions. The rejection layer is usually prepared on top of a support membrane to produce a TFC membrane [80][81].

The polymer formation occurs at the interface, and higher molecular weights can be achieved at mild reaction conditions compared to bulk polymerization. The properties of the synthesized polymer depends on the reactivity and the concentration of the reacting monomers, the number of reactive groups on each of the monomers, and the stability of the solvent interface [81].

Interfacial polymerization includes the reaction of multi-functionalized monomers. One of the monomers usually has a nucleophile reactant (amine), and the other monomer has an electrophile reactant (acid chloride). Polyamide (PA) is one of the most common polymers resulting from the IP process. PA is synthesized by the reaction between MPD aqueous solution and TMC organic solution. This reaction results in the production of linear polyamide and cross-linked polyamide. However, increasing the MPD/TMC concentration ratio and thermal curing are two main approaches that have been used to promote more cross-linked units to produce an efficient PA rejection layer. Figure 3.3 shows the conventional IP process to prepare a polyamide rejection layer [81][82].

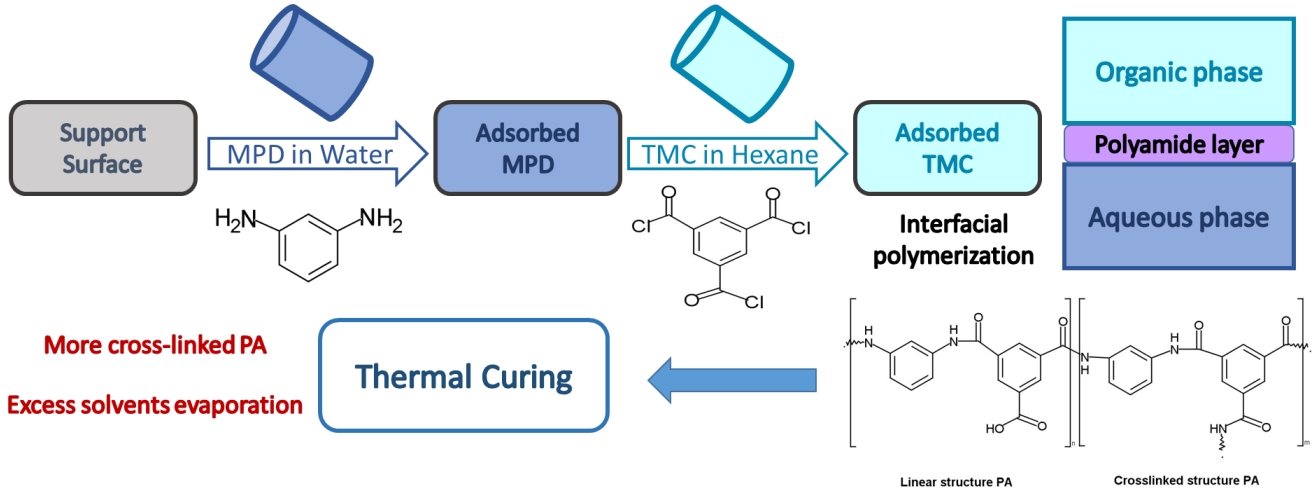

Figure 3.3: Interfacial polymerization process to produce PA rejection layer for TFC membrane

3.3. Brunauer Emmett-Teller (BET)

BET allows the determination of the surface area and the pore size distribution of porous materials. BET theory is based on the measurement of gas adsorption on the solid surface by measuring the adsorbed amount and the corresponding applied pressure. Generally, adsorption is the interaction of gas or liquid molecules on the solid surface. This interaction can be physical (physisorption) or chemical (chemisorption). In physisorption, adsorbed species can maintain their identity, and they return to the original fluid phase (gas or liquid) after the desorption while in chemisorption, adsorbed species react with the adsorbent (solid surface) losing their identity. In addition, chemisorbed molecules cannot be recovered after the desorption.

Porous materials are characterized by different pore sizes. Pore sizes can be categorized according to the pore width to three types: macropore (> 50nm), mesopore (2 to 50 nm) and micropore (< 2nm) [83].

3.3.1 BET isotherms

When gas physisorption is used for analysis of porous materials, the adsorbent should be free from any adsorbate molecules to determine the actual surface area and pore size, and this is achieved by heating the adsorbent under vacuum. Then, an inert gas, such as N_2, is introduced and adsorbs onto the adsorbent surface, reaching an equilibrium between adsorbed species and free species. Increasing the gas pressure leads to increased adsorption. The amount of adsorbed molecules with increasing the pressure, at constant temperature, are presented by an isotherm chart, where the amount of adsorbed species is plotted against the relative pressure P/Po, where Po is the saturation pressure of the adsorbed molecules on the adsorbent. There are 6 different types of isotherms as shown in Figure 3.4.

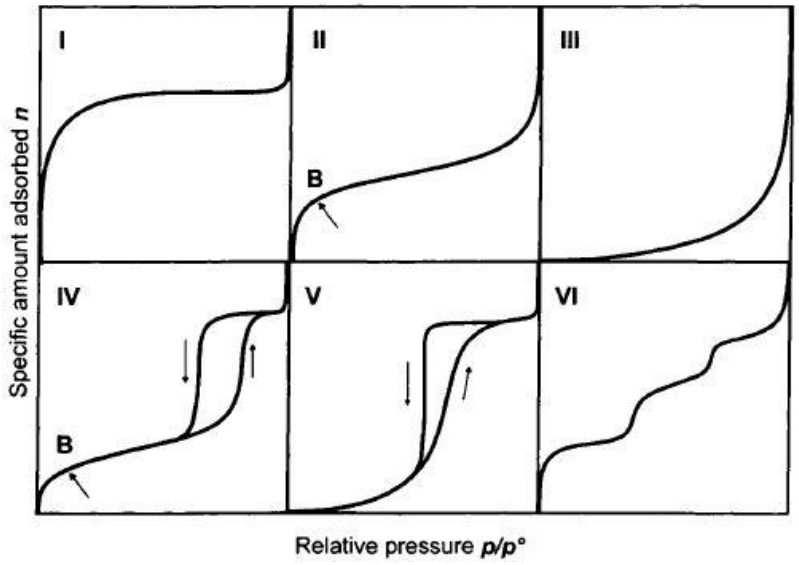

Figure 3.4: Different types of isotherm charts [83]

Type I isotherm represents the most characteristic form. The adsorbed amount rises sharply at low relative pressures. Then, a plateau is attained indicating no more adsorption. This type of isotherm occurs with microporous materials. A decrease in the micropore size leads to an increase in the adsorption energy and a decrease in the relative pressure at which the micropore filling occurs. The presence of a horizontal plateau indicates that the adsorbent surface area is very small since the micropores are narrow, filling up with monolayer adsorption at low relative pressure.

Type II isotherm represents the formation of an adsorbed layer with thickness that increases gradually with increasing relative pressure until the relative pressure approaches 1. This isotherm is characterized by the presence of a knee (B) which indicates a complete formation of a monolayer on the adsorbent, and the rest of the curve represents the formation of multilayers. This isotherm is obtained with non-porous or macroporous materials.

Type III isotherm is convex to the relative pressure axis over the whole range, and the knee is absent. This isotherm represents weak interactions between adsorbent surface and adsorbate molecules, which form multilayers rather than a monolayer. This isotherm is not a common type.

Type IV isotherm is similar to the Type II isotherm with the presence of a knee that indicates the starting point of multilayers formation. In addition, this isotherm is characterized by the presence

of a hysteresis loop which is associated with the filling and emptying of the adsorbent. Type IV isotherms are common when the porous materials have mesopores.

Type V isotherm is initially convex to the relative pressure like type III. In addition, it represents weak interactions between the adsorbent surface and the adsorbed molecules. This isotherm is different from type III due to the presence of a hysteresis loop which is associated with the filling and emptying of the adsorbent. This isotherm also occurs with the materials containing mesopores.

Type VI isotherm is a stepped isotherm that occurs rarely. It is associated with layer by layer adsorption on a highly uniform non-porous surface. This isotherm is characterized by the presence of the steps. Each step represents the formation of a monolayer. The sharpness of the steps depends on the system and the temperature [83].

3.3.2 Hysteresis loops

Hysteresis loops are associated with wide range of physisorption isotherms during capillary condensation. The different types of hysteresis loops are classified according to IUPAC system to four major types: H1, H2, H3, and H4 are shown in Figure 3.5.

Type H1 loop appears as a narrow loop with steep and parallel adsorption and desorption curves. It is usually associated with adsorbents that have a narrow distribution of uniform pores.

Type H2 loop appears as a broad loop with a long, flat plateau adsorption curve and a sharp desorption curve. It is usually associated with the adsorbents that have complex pore structures with inter-connected pores of different shape and size.

Type H3 loop does not terminate in the plateau at a high applied pressure. Therefore, the limiting desorption boundary curve cannot be attained easily. It is usually accompanied with adsorbents that contain particles aggregates or slit-shaped pores.

Type H4 loop is similar to H3 because it also does not terminate in the plateau at a high applied pressure, and the limiting boundary curve cannot be attained easily. This loop is also associated with adsorbents that have slit-shaped pores. However, the pore size distribution is mainly for micropores [83].

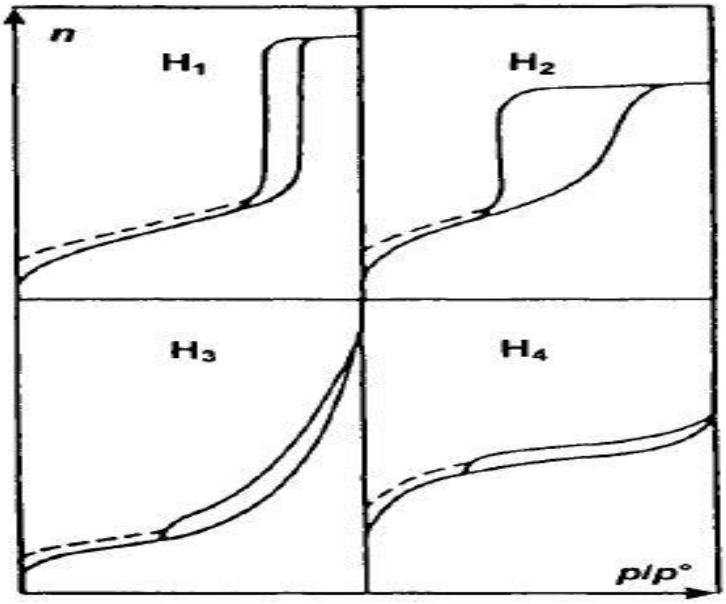

Figure 3.5: Different types of hysteresis loop [83]

3.3.3 BET theory

BET theory explains the physical adsorption of gas molecules (adsorbate) on a solid surface (adsorbent). BET theory is an extension of the Langmuir theory. Langmuir theory is based on three assumptions:

a. Adsorption is limited to only monolayer coverage on the adsorbent.

b. All sites of adsorbent are equivalent, and each site can be occupied by one atom of the adsorbate.

c. There is no interaction between the adsorbed molecules.

BET theory extends an explanation to the gas adsorption on a solid surface to form monolayer molecular adsorption or multilayer adsorption with the following assumptions:

a. Gas molecules can be physically adsorbed on a solid surface in infinite layers.

b. There is no interaction between adsorption layers.

c. BET theory can be applied to each layer.

The derived BET equation is expressed in a linear form as the following:

$$\frac{P/Po}{V(1-\frac{P}{Po})} = \frac{1}{Vm\,C} + \frac{C-1}{Vm\,C}\left(\frac{P}{Po}\right) \qquad \textit{equation 1}$$

Where V is the total volume of adsorbate at a relative pressure (P/Po), P is the equilibrium pressure, Po is the saturation pressure, Vm is the volume of the monolayer and C is a constant that depends on the isotherm type.

To construct BET plot, (P/Po)/V (1-P/Po) is plotted against P/Po. Thus, a straight line is obtained with a slope (S) = (C-1)/Vm C and intercept (I) = 1/Vm C as shown in Figure 3.6.

By solving these two equations simultaneously, two important equations are obtained to determine Vm and C.

$$Vm = \frac{1}{S+I} \qquad \textit{equation 2}$$

$$C = \frac{S}{I} + 1 \qquad \textit{equation 3}$$

However, this linear relationship is achieved only in the range of 0.05 to 0.3 P/Po [84] [85].

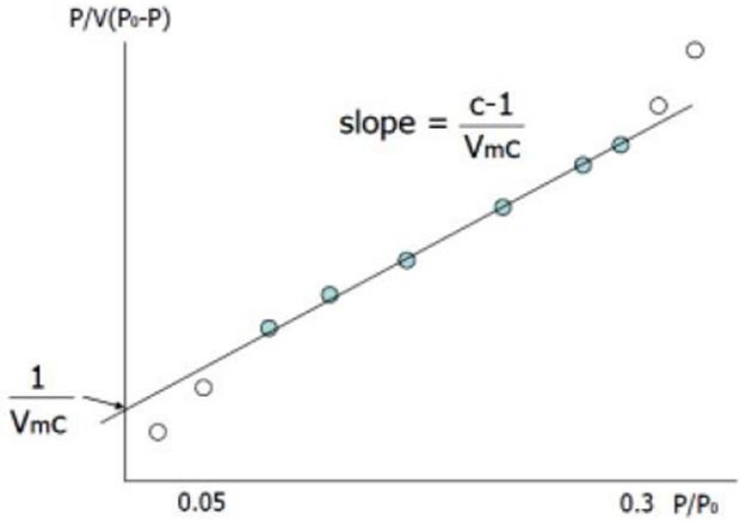

Figure 3.6: BET plot with the slope and the intercept [85]

3.3.4 Porosity by DFT model

Density functional theory (DFT) is used to determine the differential pore volumes and areas with the pore size distribution. DFT approach allows a mathematical calculation of the equilibrium density profile, ρ(r), of the adsorbate on the adsorbent. The main idea of DFT model is that the free energy of the adsorbate which is a function of ρ(r) can be expressed by a sum of hard sphere, short range impact and an attractive force, long range impact. By minimizing the free energy, the equilibrium density profile ρ(r) can be obtained. Accordingly, useful information can be obtained including pores shapes and sizes, pore size distribution, adsorption isotherm, density and relevant thermodynamic functions. Therefore, DFT model is a powerful method for investigating the simple geometry systems with pure and mixed fluids composed of spherical molecules [84][86].

3.3.5 BET instrumentation

A schematic diagram of the BET instrument is shown in Figure 3.7. Vacuum is used for the sample degassing. N_2 highly pure gas is used as the adsorbate since it interacts physically well with the solid adsorbent. He gas is used to calibrate the dead volume before and after each test. A thermostat is used to control the temperature during the test. The isotherms are generated at 77 kelvin, which is the temperature of liquid N2 [87].

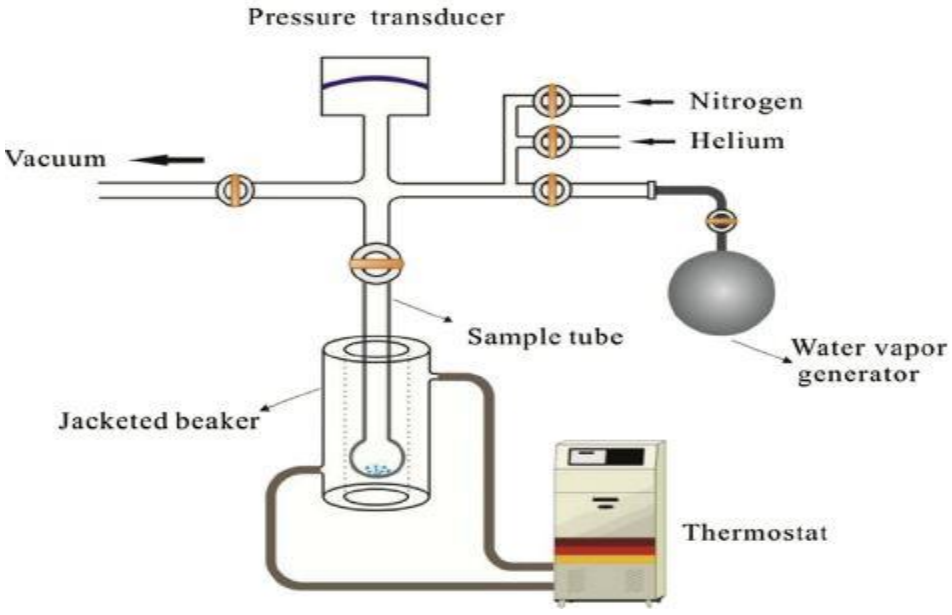

Figure 3.7: Schematic diagram of BET instrument [87]

3.4. Fourier-transform spectrophotometer (FTIR)

Infrared spectroscopy is one of the most important analytical techniques used for materials analysis. Infrared spectroscopy is based on the vibrational modes of a molecule. When IR radiation is passed through a sample, some of the infrared radiation is absorbed by the chemical bonds of the sample, causing molecular vibrations. The energies of the absorbed IR radiation depends on the specific bond strengths and atoms, and the resulting spectrum represents the molecular absorption. This spectrum is considered a molecular fingerprint of the sample. Therefore, IR spectroscopy can be used mainly for qualitative analysis of different materials, and it can be used for quantitative analysis with the advanced software using the area of different peaks in IR spectrum [88].

Infrared spectrometers have been used since the 1940s when the instrument configuration relied on dispersive prisms. These instruments separated the individual frequencies of energy emitted from the infrared source by a prism or grating. The detector measures the amount of energy at each frequency passed through the sample, and this leads to an IR spectrum which is a plot of intensity of the transmitted IR radiation versus the frequency or wave number (cm^{-1}). Recently, Fourier-transform infrared (FTIR) spectrometers are used for materials identification to overcome the limitations of the dispersive IR spectrometer, such as slow scanning time and low sensitivity.

The basic principle of FTIR is to measure all the infrared frequencies simultaneously, rather than individually. This is achieved by the use of an interferometer. The interferometer splits a beam of IR radiation into two different paths and then recombines the two beams after measuring the difference in the two paths. Then, interference between the two beams can take place. This interference results in variations in the output beam intensity that can be measured as a function of the difference in the path length. Most interferometers have a beam splitter which takes the incoming infrared beam and divides it into two optical beams. One beam strikes a stationary mirror while the second beam strikes a moving mirror. The two beams reflect from their respective mirrors and are recombined when they return back at the beam splitter. Because the path that one beam travels is a fixed length and the other is constantly changing as its mirror moves, the resulting signal from the interferometer is the result of these two interfering beams. The interference of the two beams could be constructive or destructive according to the

difference in the path length between the two beams. Then, the IR beam passes through the sample where some energy is absorbed and some is transmitted. The transmitted portion reaches the detector, which records the total intensity. The detector response yields an interferogram [88]. This signal is processed using a computer to extract the individual frequencies into a spectrum which is done by the Fourier transformation, and then the plot is reconstructed to give the typical infrared spectrum as a function of frequency (wave number). Computerized FTIR instruments work on a single beam spectrum. The major advantages of a single beam FTIR spectrophotometer are the high speed, sensitivity, mechanical stability and internal calibration [89].

3.4.1 Instrumentation

The basic components of FTIR spectrometer are presented in Figure 3.8 as the following:

IR source: IR energy is emitted from a glowing black body source. This beam passes through an aperture which controls the amount of energy directed to the sample.

Interferometer: The beam enters the interferometer to produce an interferogram signal.

Sample compartment: The beam enters the sample compartment where it is transmitted through or reflected off the surface of the sample.

Detector: The beam finally passes to the detector for final measurement. Pyroelectric device including deuterium tryglycine sulfate (DTGS) was commonly used as a detector.

Computer: The measured signal is digitized and sent to the computer where the Fourier transformation takes place to generate the final IR spectrum [88][89].

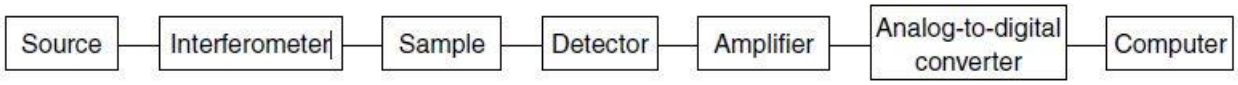

Figure 3.8: Schematic diagram of FTIR [88]

3.4.2 KBr pellet method

KBr pellet method is usually used to prepare the solid sample for FTIR analysis because KBr is IR inactive since it is ionic compound. The solid sample is ground well to avoid IR beam scattering during the analysis. Then, a larger amount of KBr is added to the ground sample, and

then pressed under high pressure and vacuum to remove the moisture. Accordingly, a transparent KBr pellet containing the sample is produced and analyzed [88].

3.5. Contact angle measurements

Wettability of solid substrates is characterized by measuring the contact angle between a liquid drop and a substrate surface. This measurement is useful for evaluating surface roughness, hydrophilicity and surface energies of the substrate. The contact angle increases by decreasing the wettability. When the substrate surface is completely wetted by a liquid, the contact angle is 0°, and this substrate is considered to be highly hydrophilic. From 0° to 90°, the substrate is hydrophilic. When the contact angle of a solid substrate exceeds 90°, this substrate is considered to be hydrophobic [90][91].

Basically, the shape of a liquid drop is determined by the surface tension that tends to keep the sphere shape of a liquid drop and the gravity that tends to deform the liquid drop. In a pure liquid, each molecule in the bulk is pulled equally in all directions by the neighboring liquid molecules. Therefore, the net force affecting the drop shape is equal to zero. However, the molecules exposed at the surface do not have neighboring molecules in all directions. Hence, liquid drops are pulled inward by the neighboring molecules, leading to an internal pressure that contracts the liquid surface area to keep the lowest surface free energy. This contraction force is called the surface tension [92].

The drop shape can be represented by Laplace equation as shown below:

$$\Delta P = \gamma \left(\frac{1}{r1} + \frac{1}{r2}\right) \qquad \textit{equation 4}$$

Where ΔP is the pressure difference at the interface, γ is the liquid interfacial tension and r1, r2 are the radii of curvature of the liquid drop.

Moreover, the contact angle is characteristic for a given solid-liquid system in a certain environment. Contact angle is measured by establishing a tangent angle of a liquid drop with a substrate surface. According to Young's equation, the contact angle θ of a liquid drop on a substrate surface is defined by the mechanical equilibrium of the drop under the effect of three interfacial tensions: solid-vapor (γ_{sv}), solid-liquid (γ_{sl}) and liquid-vapor (γ_{lv}) as represented in Figure 3.9 [93].

$$COS\ \theta = \frac{\gamma sv - \gamma sl}{\gamma lv} \qquad \textit{equation 5}$$

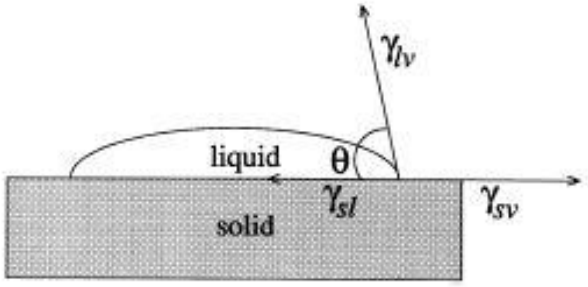

Figure 3.9: Contact angle measurement using Young's equation [92]

3.5.1 Instrumentation

Drop shape analysis (DSA) is a technique used for contact angle determination. The measurement is carried out by simply aligning the tangent of the liquid drop at the contact point with the surface on the right and left sides. This method is called a sessile drop method where the liquid droplet is settled on the solid surface, and air surrounds the liquid droplet as shown in Figure 3.10. On the other hand, a captive bubble method is used to measure the contact angle of an air bubble with the solid surface immersed in the testing liquid [92][94].

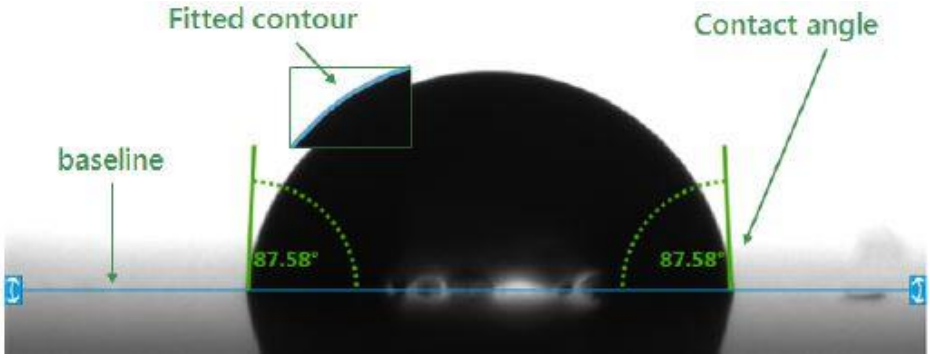

Figure 3.10: Sessile drop contact angle measurement [94]

As shown in Figure 3.11, the instrument consists of a horizontal stage to place a solid or liquid sample, a micrometer syringe to form a liquid drop, an illumination source, and a video camera with a zooming lens. The camera records the image of the drop. A motor-driven syringe can be added to control the rate of adding the liquid to form the liquid drop [94].

Figure 3.11: Drop shape analyzer description [94]

3.6. Atomic Force Microscopy (AFM)

Atomic Force Microscopy (AFM) is a scanning probe microscopy. The basic principle of AFM is the use of a solid force probe that comes into contact with the sample surface in order to get images that describe the surface topography on the nanometer scale. The main advantages of AFM are that it can be used for both conductive and non-conductive materials, it can operate in air, vacuum, or even in liquid. AFM measures the sample topography by moving a solid probe over the sample surface horizontally. The probe tip is attached to a cantilever. Then, the atomistic interactions between the probe tip and the sample surface are measured by detecting the deflections of the cantilever using a laser beam that is reflected on the backside of the cantilever toward a split photodiode. The cantilever deflections result in changes in the direction of the reflected beam, and accordingly, the photodiode can detect these changes. An AFM topography image is the result of the cantilever scanning over the sample surface. The elevated and lowered features on the sample surface affect the cantilever deflection, which is detected by the photodiode. Then, a topographic map of the sample surface can be obtained [95][96]. The main components of AFM are shown in Figure 3.12.

AFM does not depend on any light source other than the laser beam that is focused on the backside of the cantilever. There are no color properties of the sample being imaged since there is no absorption of light of any wavelength happening during the imaging. Therefore, AFM images are often depicted using a degree of coloration based on the height or depth of a feature

found on the sample surface. The bright spots usually correspond to the elevated features on the sample surface while the dark spots represent the lowered features. One of the main surface properties that AFM can measure, is the surface roughness, which represents the closely spaced irregularities on the sample surface by measuring the mean value of the surface height [97].

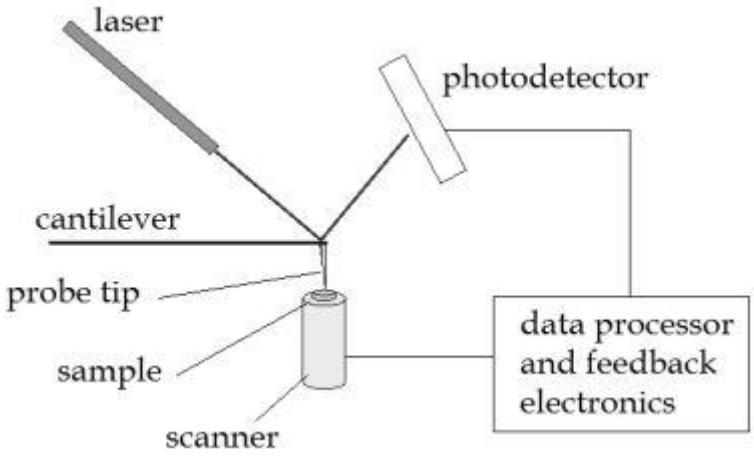

Figure 3.12: Schematic diagram of AFM [98]

3.6.1 AFM modes for surface topography

AFM can be operated in different modes to identify different surface properties of the sample. For surface topography, for which AFM was used in this study, the used modes are contact and tapping modes.

In contact mode, the probe is lowered to the surface of the sample to be imaged and it remains in contact with the sample during the whole imaging process. Contact mode imaging provides basic surface topography by using a cantilever that is made of lower spring constant material. Any changes in the height of surface features leads to a tip deflection, which is associated with a surface feature that can be thus recorded. The contact mode is used for rough samples and in friction measurements. The main advantage of the contact mode is the fast scanning time. However, the main disadvantage is that the constant contact between the probe tip and the sample surface can deform the samples [98][99].

In tapping mode, the cantilever uses a piezoelectric element mounted on the top to oscillate it near its resonance frequency with an amplitude from 20-200 nm. The probe taps on the sample surface during scanning, and it contacts the surface at the bottom of its swing. Therefore, the

probe interacts with the sample in a much reduced time. The tapping mode requires long scanning time. However, it causes less damage to the sample than contact mode and it is more accurate. Therefore, this mode is suitable for polymers and thin films, and it was used to investigate the membrane samples in this work [98][99].

3.7. Scanning electron microscopy

Scanning electron microscopy (SEM) is an essential technique to observe the morphology and composition of different micro and nano-materials with high resolution. The SEM scans the surface of a sample using an electron beam that is produced by an electron probe which focuses the beam over the surface. The electron beam of an SEM can achieve wavelengths that reach 1 nm, which leads to high resolution images [100].

3.7.1 Interaction between the electron beam and the sample

The formation of SEM images depends on the acquisition of signals produced from the interactions between the electron beam and the sample. These interactions can be divided to elastic and inelastic interactions.

Elastic interactions occur when incident electrons are scattered by the sample nucleus or by outer shell electrons. The energy required for this interaction can be neglected since the scattered electrons have similar energies to the sample nucleus or outer shell electrons. If the incident electrons are scattered by an angle of more than 90°, the scattered electrons can be called backscattered electrons (BSE). BSE are used for imaging the sample.

On the other hand, inelastic interactions take place by multiple interactions between the incident electrons and the sample atoms or electrons. The incident electrons transfer significant energy to that atom, leading to excitation of the sample electrons during the ionization of the sample atoms. Thus, secondary electrons (SE) are produced. SE electrons possess energies of less than 50 eV, and they can be used to image the sample. In addition, there are other signals produced when an electron beam hits a sample, including the emission of characteristic x-rays and Auger electrons. When an inner shell electron is displaced by collision with an incident electron, an outer shell electron may fall into the inner shell to keep proper charge balance in the orbitals, and the energy difference is released in the form of x-ray or Auger electron. The characteristic x-ray

and Auger electrons are used to provide information about the chemical composition of the sample [101]. The different electron beam-sample interactions are shown in Figure 3.13.

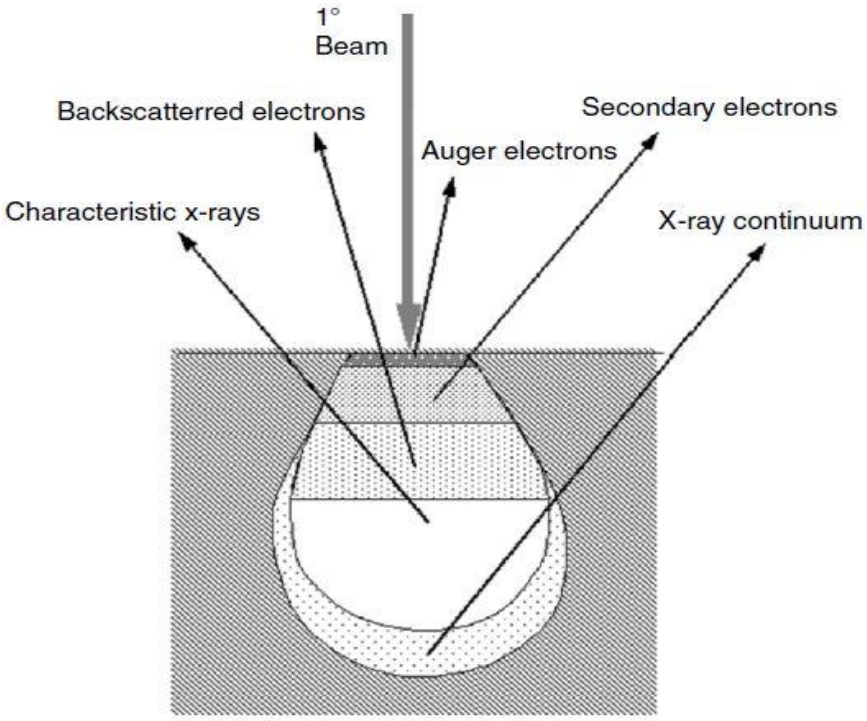

Figure 3.13: Different electron beam-sample interactions with increasing penetrating depths of the incident beam [101]

3.7.2 Instrument Components

As represented in Figure 3.14, the main components of SEM include electron gun, column with electromagnetic lenses, electron detector, sample chamber and computer to display the images. The electron gun is the source of electrons that accelerates them to an energy level from 0.1 to 30 KeV. Electromagnetic lenses and apertures are used to focus the electron beam. Then, a small focused electron spot of 1 to 100 nm wavelength can be directed to the sample to form high resolution images. The sample chamber is under high vacuum to prevent scattering of electrons by air [101].

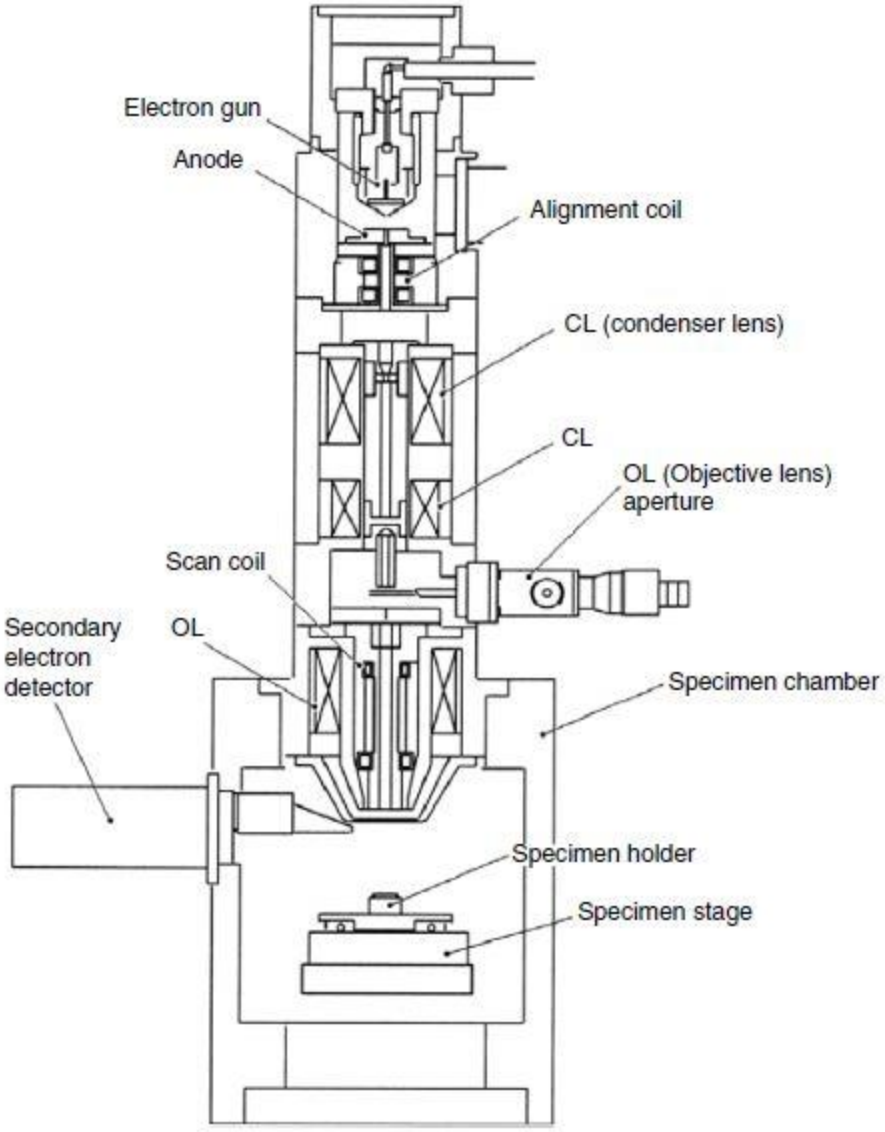

Figure 3.14: Schematic diagram of SEM [101]

The electron gun is a major component of SEM. Electron gun generates a stable electron beam with high current and variable energy. There are many types of electron gun, such as tungsten filament, lanthanum hexaboride (LaB_6) cathode and field emission gun (FEG). In addition, high vacuum is required to prevent the electrons scattering. The emission of electrons from the FEG depends on the electric field applied between the cathode and the anode. The produced electron beam exhibits higher brightness with high resolution images. However, FEG requires ultrahigh vacuum to stabilize the emission of the electrons. After emission of the electrons, a series of condenser lenses are used to focus the electron beam from the source to the column using the

applied magnetic field, and the scattered electrons are excluded by an aperture. Then, an objective lens is used to focus the beam into the sample surface with controlled lens demagnification [100][101] .

Furthermore, there are three main types of SEM according the type of the detected electron. Backscattered detector (BSD) is used to detect the backscattered electrons, secondary electron detector (SED) is used to detect the secondary electrons, and energy dispersive x-ray spectrometer (EDS) is used to detect the characteristic x-ray of different elements.

Conductive nano-materials like carbon nanotubes (CNTs) can be observed directly with SEM while non-conductive materials like polymeric membranes require coating with gold or platinum in order to avoid the accumulation of negative charges on the sample surface. Hence, high resolution images can be obtained [101][102].

3.8. Design-Expert Software

Design-Expert software (Stat-Ease, Inc.) is a commercial statistical analysis package that can be used to carry out an experimental design including a factorial design to determine the most effective parameters on the performance of a certain process or a product in terms of identified responses. Factorial design is efficient for the experiments that include the effect of more than one factor. By a factorial design, all possible combinations of the factors levels are investigated, and the change of a certain response is observed by changing the factors levels.

In addition, Design-Expert software can be used to perform analysis of variance (ANOVA) to determine the effect of the different parameters and their interactions on the performance of the process or the product. ANOVA is a test to find out if a certain factor is significant or not by calculating the variation in a certain response between different factors. One-way ANOVA is used to analyze one factor while two-way ANOVA is used to analyze two factors and so on [103].

In the current work, Design-Expert software will be used to evaluate the different factors that might affect the performance of different synthesized membranes in terms of identified responses, such as water flux, water permeability, salt rejection, and reverse solute flux. The different terms used in factorial design and ANOVA can be found in Appendix I.

4. Chapter 4: Materials and Methods

4.1. Materials

Polysulfone (molecular weight average Mn ~22,000 by MO, Sigma-Aldrich) was used as the polymer for the membrane support layer. Polyvinylpyrrolidone (PVP) powder (average molecular weight 360,000, Sigma-Aldrich) was used as a pore former. Anhydrous dimethyl formamide (DMF) (density 0.944g/ml, purity = 99.8%, Sigma-Aldrich) was used as a solvent. Deionized water (MilliPore) was used as a non-solvent.

For the polyamide rejection layer, reacting monomers encompassed m-phenylenediamine (MPD) flakes (molecular weight 108.14 g/mol, purity = 99%, Sigma-Aldrich), and 1,3,5-benzenetricarbonyltrichloride (TMC) (molecular weight 265.48 g/mol, purity = 98%, Sigma-Aldrich). Deionized water (MilliPore) was used as a solvent for MPD. Hexane (density 0.672, purity > 98.5%, Sigma-Aldrich was used as a solvent for TMC.

Elicarb MWCNTs (diameter of 10-12 nm, tens of microns in length and a density of 1.7-1.9 g/cm^3, manufactured by Thomas Swan, England) were used as nanofillers. H_2SO_4 (purity = 98%, Sigma-Aldrich) and HNO_3 (purity > 69%, Sigma-Aldrich) were used in the oxidation functionalization of MWCNTs.

4.2. Membrane preparation

4.2.1 Membrane support layer preparation

Casting solutions of different compositions were prepared by dissolving different amounts of PSF and PVP in DMF. The amounts were determined according to the required wt%, and are presented in Table 4.1. The mixture was left overnight under continuous stirring at 200 rpm until PSF and PVP were completely dissolved reaching a clear homogenous solution. The solution was then sonicated for 30 minutes and then left overnight to get rid of all air bubbles.

Membrane casting was then carried out using an Elcometer 4040 automatic film applicator with a fixed speed rate of 90 mm/sec. The casting solutions were poured into the casting equipment feed container. The solutions were then spread over a glass substrate by a moving casting knife, adjusted to a height of 175 µm. The glass substrate was then immersed in a deionized water bath at room temperature for 15 minutes. The resulting membranes were washed several times with

portions of deionized water to ensure the removal of DMF. Then, the membranes were stored in deionized water until investigation.

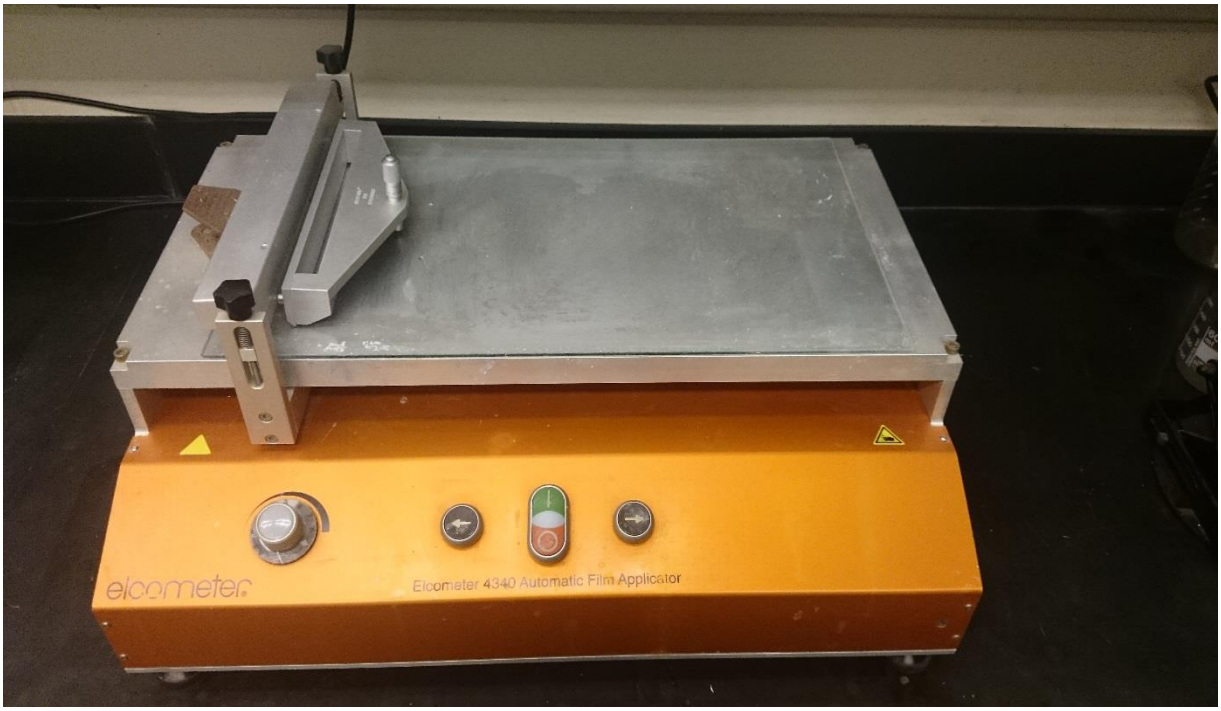

Figure 4.1: Elcometer 4040 automatic film applicator with the casting knife

Table 4.1: Casting solutions compositions

Cast solution	PSF (wt%)	PVP (wt%)	DMF (wt%)
S0	20	0	80
S1	20	1	79
S2	20	2	78
S3	20	5	75
S4	18	0	82
S5	18	1	81
S6	18	2	80
S7	18	5	77
S8	15	0	85
S9	15	1	84
S10	15	2	83
S11	15	5	80

4.2.2 Rejection layer synthesis

The PA rejection layer was prepared by interfacial polymerization (IP) on top of the support layer to produce the thin film composite (TFC) membrane. A glass mold was used for the IP step, where the support layer was placed as shown in Figure 4.2 in order to ensure exclusive reaction of the reacting monomers on the top surface of the support layer.

Different aqueous MPD solutions and organic TMC solutions were prepared by dissolving different amounts of MPD in deionized water, and different amounts of TMC in n-hexane, respectively. Each of the aqueous MPD solutions was poured on the application area of the support membrane and left for a complete diffusion through the top surface of the membrane support layer. Then, the solution was drained from the glass mold, and the membrane was dried using an air drier. An organic TMC solution was then poured on the application area incorporating the MPD. This was left for 2.5 min for the IP reaction to take place. Then, the excess solution was drained from the glass mold, and the membrane dried using an air drier. The resulting thin film composite membrane was then cured at different curing temperatures for 10 mins. Table 4.2 summarizes the preparation details for the TFC membranes.

Figure 4.2: Membrane in a glass mold for IP reaction

Table 4.2: Different thin film composites (TFCs) with different MPD/TMC concentrations, contact times and curing temperatures

TFC sample	MPD (wt/vol %)	MPD Contact time (min)	TMC (wt/vol%)	TMC Contact time (min)	Curing temperature (°C)
TFC1	1	2	0.05	1.0	25
TFC2	1	2	0.10	1.0	25
TFC3	1	2	0.15	1.0	25
TFC4	1	2	0.05	1.0	60
TFC5	1	2	0.10	1.0	60
TFC6	1	2	0.15	1.0	60
TFC7	1	5	0.05	2.5	25
TFC8	1	5	0.10	2.5	25
TFC9	1	5	0.15	2.5	25
TFC10	1	5	0.05	2.5	60
TFC11	1	5	0.10	2.5	60
TFC12	1	5	0.15	2.5	60
TFC13	2	2	0.05	1.0	25

TFC14	2	2	0.10	1.0	25
TFC15	2	2	0.15	1.0	25
TFC16	2	2	0.05	1.0	60
TFC17	2	2	0.10	1.0	60
TFC18	2	2	0.15	1.0	60
TFC19	2	5	0.05	2.5	25
TFC20	2	5	0.10	2.5	25
TFC21	2	5	0.15	2.5	25
TFC22	2	5	0.05	2.5	60
TFC23	2	5	0.10	2.5	60
TFC24	2	5	0.15	2.5	60
TFC25	3	2	0.05	1.0	25
TFC26	3	2	0.10	1.0	25
TFC27	3	2	0.15	1.0	25
TFC28	3	2	0.05	1.0	60
TFC29	3	2	0.10	1.0	60
TFC30	3	2	0.15	1.0	60
TFC31	3	5	0.05	2.5	25
TFC32	3	5	0.10	2.5	25
TFC33	3	5	0.15	2.5	25
TFC34	3	5	0.05	2.5	60
TFC35	3	5	0.10	2.5	60
TFC36	3	5	0.15	2.5	60
TFC37	4	5	0.20	2.5	80

4.2.3 Thin film nanocomposite (TFNC) synthesis

A. MWCNTs functionalization

MWCNTs were functionalized using a described method in the literature [104].

1. 2 g of Elicarb MWCNTs were added to 50 ml H_2SO_4 and 16.67 ml HNO_3 in 100 ml round bottom flask.
2. The flask was immersed in an ultrasonic bath for 10 minutes to disperse the MWCNTs.
3. The flask was then connected to a reflux with circulated water to minimize acid evaporation, and the reflux was connected to a bottle filled with concentrated NaOH solution to neutralize the excess acid vapors.
4. The flask was then heated in an oil bath for 100 minutes with increasing the temperature gradually from 90 to 133 ˚C.
5. After that, the flask was allowed to cool at room temperature.
6. MWCNTs filtration was carried out using Whatman Teflon filter membranes of 0.2 µm pore size. Teflon filter membranes were placed on a microfiltration system connected to a pump.
7. The filtered MWCNTs were washed several times by deionized water until the pH of the filtrate solution became neutral.
8. The filtered MWCNTs were then washed by acetone to ensure a complete removal of water.
9. The washed MWCNTs were placed in a desiccator under vacuum for 24 hours to ensure their complete drying.
10. Finally, the dried MWCNTs were ground on a ceramic mortar to obtain powdered particles that can be dispersed easily in water.

B. Incorporating MWCNTs into the rejection layer

Different amounts of functionalized MWCNTs (0.01, 0.05, 0.1 and 0.2 g) were dispersed in aqueous solutions of 4 g MPD in 100 ml deionized water. The dispersion was carried out by ultrasonication for 4 hours. Each solution was then stirred at 200 rpm for 30 minutes to ensure a complete dispersion of the MWCNTs, then poured over the top surface of the PSF support membrane layer within a glass mold, as shown in Figure 4.2, and left for 5 minutes. Excess solution was drained off the support membrane layer, which was then dried using an air drier.

This was followed by having the 0.2 g TMC solution in n-hexane poured on the application area incorporating the MPD with the MWCNTs. Then left for 2.5 minutes for complete IP. Then, the membrane was cured at 80 °C. This resulted in formation of PA rejection layer with incorporated MWCNTs.

4.3. Characterization

4.3.1 Viscosity measurement

Viscosity of the casting solutions were measured using a rotational viscometer (Myr,VR 3000) using L4 probe rotated with 200 rpm at room temperature.

4.3.2 Membrane porosity and surface area

Membranes porosity and surface area were determined by N_2 adsorption using Micrometrics ASAP 2020 instrument using the following procedure:

1. The membrane samples were dried in an oven at 80 °C for 30 minutes, and then cooled at room temperature.
2. The membrane samples were cut to small pieces, and then weighed.
3. The membrane samples were placed in a glass tube as a sample holder, and then mounted in ASAP 2020 instrument.
4. Degassing was carried out below 50 µm Hg at 30 °C for 30 minutes followed by heating to 80 °C for 360 minutes.
5. Adsorption process was carried out by N_2 at 77K.

4.3.3 Fourier-transform Infrared (FTIR) analysis

Infrared spectrophotometric analysis was carried out using a Thermo Scientific NICOLET 380 FTIR instrument. It was used to examine the synthesized polyamide rejection layer and the carboxylated MWCNTs. The KBr pellet method was used to prepare the examined solid samples by mixing 2 mg of the sample with 200 mg KBr (FTIR grade) and grinding the mixture vigorously using mortar and pestle. Then, the mixture was subjected to vacuum and applied pressure of 1,378 bar using a hydraulic press. Then, the resulting pellet sample was analyzed.

4.3.4 Contact angle determination

Drop Shape Analyzer (DSA 25) from Kruss, Germany, was used for water contact angle determination, and sessile drop method was used to measure the contact angle of the different

membranes in order to evaluate the membranes hydrophilicity. The measurement was repeated 3 times at different membrane sites. In addition, the right and left contact angles were measured. A micro syringe filled with deionized water was used in the measurements with a volume droplet of 5 µL.

4.3.5 Surface roughness

Dimension 3100 Atomic Force Microscope (AFM) from Digital Instruments (Veeco Metrology Group), was used to measure the surface roughness of the synthesized membranes. The samples were scanned using tapping mode with a scan size of 10 µm.

4.3.6 Membrane morphology

Membranes top, bottom surfaces and cross-sections were imaged using Leo Supra 55 (ZEISS) Field Emission Scanning Electron Microscope (FESEM). Membranes were coated with gold using a sputter coater of current (15 mA) for 2 minutes.

4.3.7 Forward Osmosis (FO) test cell

FO water flux and reverse solute flux were measured using a Sterlitech CF042 FO test cell. The measurements were carried out using the following procedure:

1. The membrane was cut to 11.2 cm x 5.6 cm, and then placed on a porous metal support fixed in the cell.
2. The membrane was oriented in FO mode with the rejection layer facing the feed solution.
3. The feed tank was filled with deionized water while the draw tank was filled with 2M NaCl. Both tanks were placed on weighing balances.
4. The feed and draw solutions were circulated at a rate of 220 ml/min in a closed loop using pumps.
5. The membrane was given 30 minutes to obtain a steady liquid flow rate.
6. The feed and draw tanks were weighed before and after the FO experiment.
7. The feed and draw solutions conductivities were measured using a conductivity meter (Jeanway).

FO water flux and reverse solute flux were measured using equations 6 and 7 respectively, and all measurements were carried out in triplicates, with the average used.

$$J = \frac{\Delta V}{A\,\Delta t} \qquad \textit{equation 6}$$

where J (L/m^{2}h) is the FO water flux, ΔV (L) is the draw solution volume change, A (m^2) is the active membrane area and Δt (h) is the time interval of the experiment.

$$Js = \frac{\Delta C\, V}{A\, \Delta t} \qquad \textit{equation 7}$$

where Js (g/m^{2}h) is the reverse solute flux, ΔC (g/L) is the feed solution concentration change, V (L) is the feed solution volume at the end of the experiment, A (m^2) is the active membrane area and Δt (h) is the time interval of the experiment.

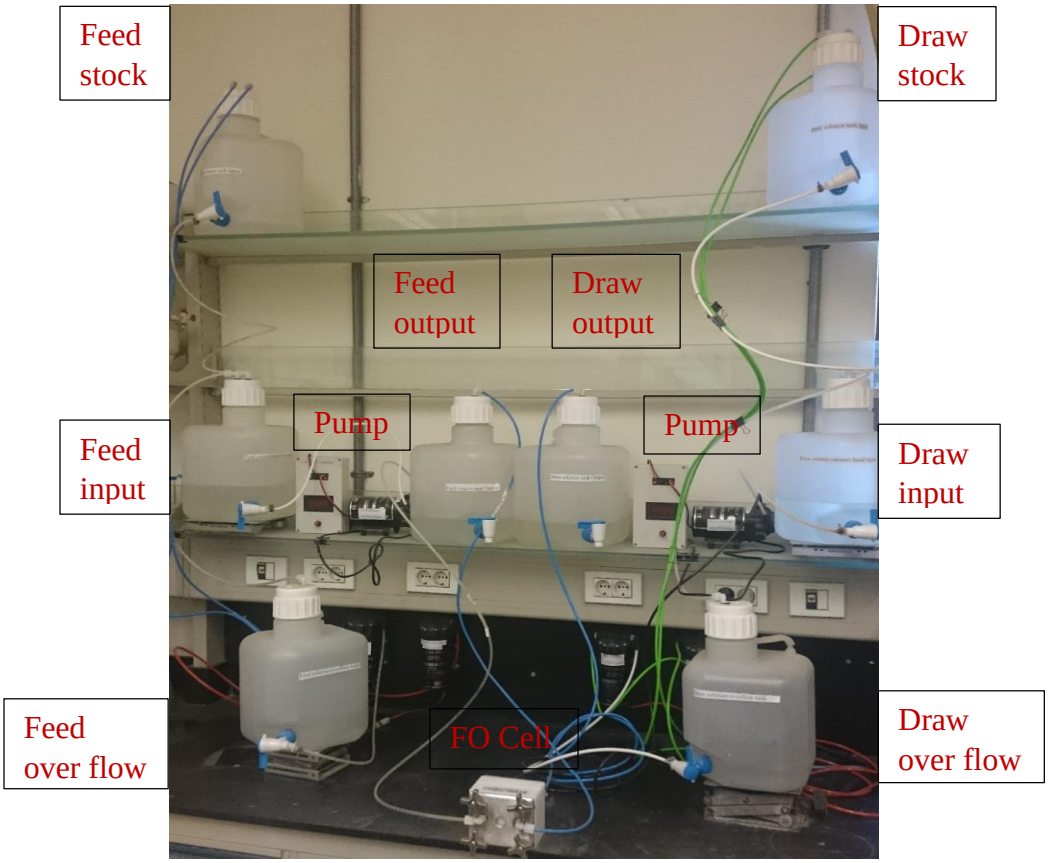

Figure 4.3: Sterlitech CF042 FO test cell setup

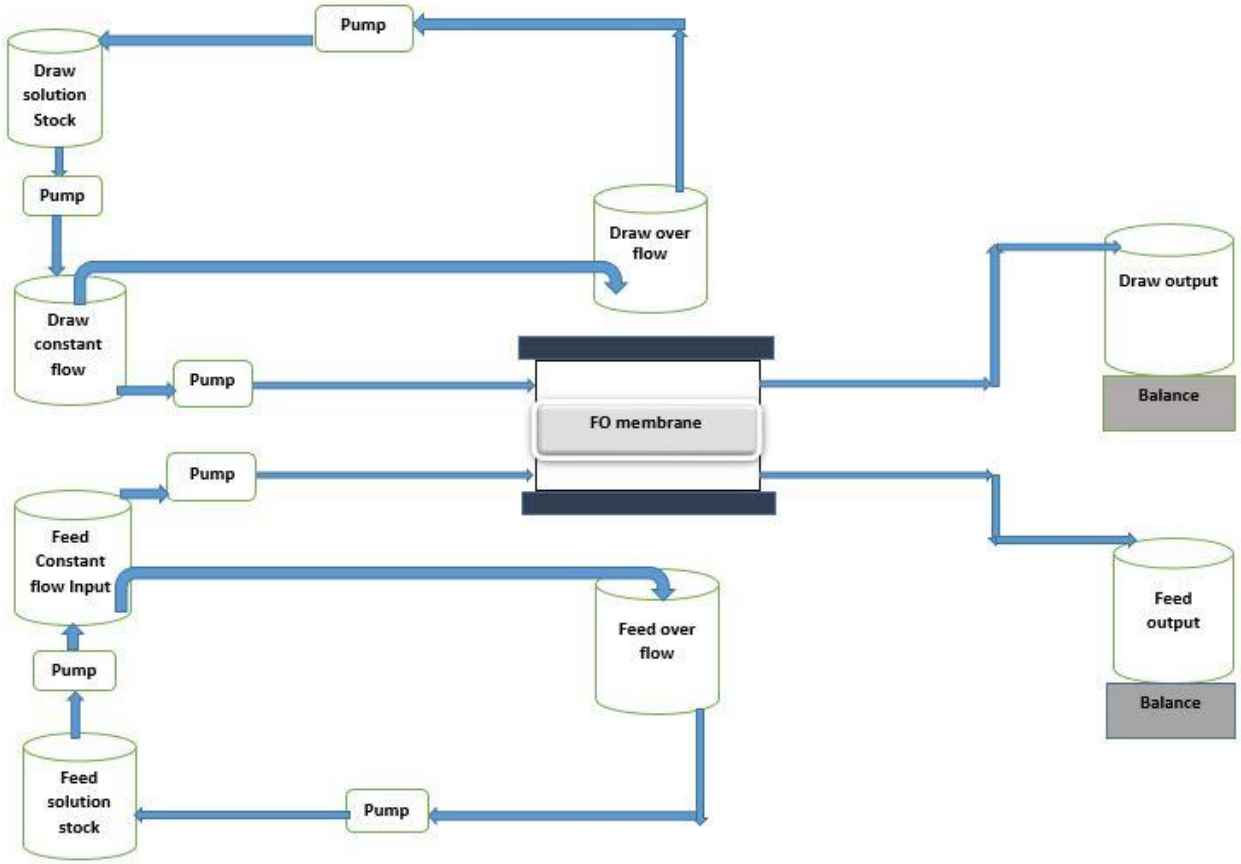

Figure 4.4: Schematic diagram of FO test cell setup

4.3.8 Dead-end test cell

Water permeability and salt rejection were measured using a Sterlitech HP4750 Stirred dead-end cell. The measurements were obtained by the following procedure:

1. The membrane was cut to 5 cm disc, and then placed on a porous metal support in the test cell.
2. The cell was filled with the feed solution of 20 mM NaCl solution.
3. A pressure of 2.5 bars was applied using compressed N_2 gas.
4. The membrane was given 10 to 15 minutes to obtain a steady liquid flow rate.
5. The permeate solution was collected in a calibrated measuring cylinder.
6. The feed and permeate conductivities were measured using a conductivity meter (Jeanway).

Water permeability was determined using equation 8 while salt rejection was determined using equation 9, and all measurements were carried out in triplicates, and then the average was taken.

$$Jw = \frac{V}{A\,\Delta t} \qquad \textit{equation 8}$$

where Jw (L/m^{2}h.bar) is the water permeability, V (L) is the permeate volume, A (m^2) is the active membrane area and Δt (h) is the time interval of the experiment.

$$R\% = 1 - \frac{Cp}{Cf} \times 100 \qquad \textit{equation 9}$$

where *R%* is the salt rejection percent, *Cp* is the permeate concentration and *Cf is* the feed concentration.

Figure 4.5: Sterlitech HP4750 Stirred dead-end cell

4.4. Statistical analysis

Statistical analysis was performed using Design-Expert software (Stat-Ease, Inc.) in order to determine the most effective parameters affecting the membrane performance. For the support layer membrane, Design of Experiments (DOE) was carried out using a full factorial design, and the results were analyzed using a two-way analysis of variance (ANOVA) to investigate the effect of different concentrations of PSF, PVP and their interaction on the support layer performance in terms of three responses FO water flux, water permeability and reverse solute flux. Three levels of PSF concentrations and four levels of PVP concentrations were used in this

statistical experiment as listed in Table 4.3. The choice of these specific levels was based on the values reported in the literature [45][50][51][52][55]. Therefore, the total number of support membrane samples was 12 membranes. Each support membrane was prepared 3 times, and the corresponding responses were measured in order to be used in the ANOVA models, and averaged. Table 4.1 shown earlier, represents the different possible combinations of PSF (wt%) and PVP (wt%) to determine their effect on the support layer performance.

Table 4.3: Support layer different factors and their levels

Factor	Units	Level 1	Level 2	Level3	Level 4
PSF concentration	wt %	15	18	20	NA
PVP Concentration	wt %	0	1	2	5

For the Thin film composite (TFC) membrane, DOE was carried out using a full factorial design, and the results were analyzed using a four-way analysis of variance (ANOVA) to investigate the effect of MPD concentration, TMC concentration, contact time, curing temperature and their possible interactions on the TFC PA rejection layer performance in terms of four responses FO water flux, water permeability, reverse solute flux and salt rejection. The different factors and their levels in this statistical experiment are listed in the Table 4.4. MPD and TMC concentrations were varied in three levels while contact time and curing temperature were varied in two levels. The choice of these specific levels was based on the values reported on the literature [51][54][55][56][62]. Therefore, the total number of TFC membrane samples was 36 membranes. Each TFC membrane was prepared 3 times, and the corresponding responses were measured in order to be used in the ANOVA models, and averaged. Table 4.2 shown earlier, represents the different possible combinations of MPD (wt/vol%), TMC (wt/vol%), contact time (min) and curing temperature ($^{\circ}$C) to determine their effect on the TFC membrane performance. The most effective parameters could be selected for further analysis and investigation. Moreover, the effect of interactions between different parameters could be analyzed using Design-Expert software.

Table 4.4: Rejection layer different factors and their levels

Factor	Units	Levels	Level 1	Level 2	Level 3
MPD concentration	wt/vol%	3	1	2	3
TMC Concentration	wt/vol%	3	0.05	0.1	0.15
Contact time	min	2	2	5	NA
Curing temperature	°C	2	25	60	NA

5. Chapter 5: Results and discussion

This chapter reports the results of the investigation on the effect of the different factors on the morphology and performance of PSF/PA TFNC membranes. The factors were varied to optimize the preparation conditions for both the support and the rejection layers of the membranes. Then, the most significant factors were identified using Design-Expert software and analysis of variance (ANOVA) for statistical analysis, as explained in Chapter 4.

5.1. TFNC support layer

In this section, the effects of PSF concentration and PVP concentration on the support layer performance will be explained.

5.1.1 Preliminary trials

To determine the PSF concentration levels to be used in designing the experiments for the support layer, some initial trials were conducted. The support layer was first synthesized using 9 wt% PSF in anhydrous DMF followed by phase inversion in deionized water. 9 wt% was chosen for being the lowest PSF concentration reported in the literature [48]. However, the obtained cast solution showed low viscosity (150 mpas), and the membrane casting did not succeed because the casting knife could not have enough time to spread the casting solution over the glass substrate even at the highest casting speed (100 mm/sec) thus resulting in an unstable membrane. Therefore, the concentration of PSF was increased to 15, 18 and 20 wt%, and those were the PSF concentration levels used in designing the subsequent experiments. The corresponding viscosities were measured. Table 5.1 shows the results of the viscosity for different PSF concentrations cast solutions.

Table 5.1: Different support membranes and viscosity

PSF wt%	DMF wt%	Viscosity mpas	Membrane stability
9%	91%	150	Unstable
15%	85%	400	Stable with small holes
18%	88%	660	Stable
20%	80%	1070	Stable with uneven thickness

5.1.2 Support layer Experimental Design

The goal of this work was to achieve a highly porous support layer with the highest possible FO water flux, water permeability and the lowest possible reverse solute flux. Therefore, PVP was added to the casting solution as a pore forming agent as reported in the literature [51][55]. Table 5.2 summarizes the average values of FO water flux, water permeability, reverse solute flux and salt rejection for the 12 different support membranes with their final thickness. Also included in Table 5.2 for the sake of completion are the values for salt rejection. As noted from the table, salt rejection of all the support membrane samples was small, varying from 2.28 to 5.29 %. Salt rejection performance does not represent a main attribute for the support layer, and has not therefore been included in the Experimental Design.

Table 5.2: Different Support membranes and their corresponding Final thickness, FO water flux, Water permeability, Reverse solute flux and Salt rejection

Support membrane	PSF wt%	PVP wt%	Final Thickness (µm)	FO water flux (L/m^2h)	Water permeability ($L/m^2h.bar$)	Reverse solute flux (g/m^2h)	Salt rejection (%)
S0	20	0	99±9	76.04±1.50	3.90±0.086	18.42±0.70	5.29±0.17
S1	20	1	101±8	77.51±2.10	3.88±0.10	17.62±1.14	4.56±0.36
S2	20	2	101±14	80.93±1.07	4.06±0.16	18.23±0.89	4.08±0.07
S3	20	5	106±6	84.67±0.43	5.38±0.42	20.13±0.84	3.60±0.22
S4	18	0	89±14	81.79±0.89	4.02±0.13	17.68±0.49	4.23±0.047
S5	18	1	90±6	86.91±0.29	5.87±0.15	18.42±0.78	3.51±0.10
S6	18	2	90±12	90.15±0.49	6.86±0.38	18.54±0.42	3.18±0.076
S7	18	5	95±13	90.92±1.60	6.80±0.39	21.25±1.14	3.33±0.065
S8	15	0	87±20	80.09±0.58	3.62±0.27	22.85±0.63	2.78±0.16
S9	15	1	88±18	85.83±0.22	5.93±0.25	23.59±1.13	2.54±0.13
S10	15	2	89±16	89.03±1.25	6.91±0.25	25.21±0.70	2.76±0.19
S11	15	5	93±20	91.84±1.20	6.96±0.34	27.90±1.29	2.28±0.15

The plots of statistical analysis can be found in Appendix II.

A. FO water flux response

According to Design-Expert software, the factorial design model for the FO water flux was successful, and the effect of PSF wt% (A), PVP wt% (B) concentrations and their interaction (AB) were significant since the p-value was less than 0.05 for the model and the factors at level

α=0.05. By dividing each individual sum of squares over the total sum of squares of the model, a contribution percent of each factor can be obtained. As shown in the ANOVA results presented in Table 5.3, PVP wt% shows the highest contribution percent (51.88%) followed by PSF wt% while the interaction between the factors (AB) shows the lowest contribution percent (2.82%) although it is significant.

Table 5.3: ANOVA results for FO water flux response

Source	Sum of squares	DF	Mean square	F-value	p-value	Contribution%
Model	944.52	11	85.86546	67.98876	2.45E-15	
A-PSF%	427.7767	2	213.8883	169.358	7.04E-15	45.29
B-PVP%	490.0991	3	163.3664	129.3544	5.97E-15	51.88
AB	26.64426	6	4.44071	3.51618	0.012224	2.82
Pure Error	30.31047	24	1.262936			
Cor Total	974.8305	35				

The high contribution % of PSF and PVP concentrations can be clearly observed in Table 5.2. For instance, decreasing PSF concentration from 20 wt% to 18 wt% led to an increase in the FO water flux from an average 76.04±1.50 L/m^{2}h for S0 to an average 90.15±0.49 L/m^{2}h and an average 90.92±1.60 L/m^{2}h for S6 and S7 respectively. In general, increasing PSF concentration leads to higher viscosity solutions as shown earlier in Table 5.1. This increase in the viscosity results in slower demixing (precipitation rate) in the non-solvent water bath resulting in denser membrane formation with smaller pores sizes [105]. Therefore, the FO water flux decreased when the PSF concentration increased, and this trend was also reported by Alberto Tiraferri et al when they varied the PSF concentration from 9 to 18 wt% [58]. Additionally, a similar trend was achieved by Sofiah Hamzah et al when they varied PSF concentration from 15 to 19 wt% [106].

On the other hand, PVP concentration had a positive effect on the FO water flux. Increasing PVP concentration from 0 to 5 wt% at a fixed PSF concentration led to increasing the FO water flux. For instance, when the PSF concentration was 20 wt%, increasing PVP concentration from 0 to 5 wt% resulted in increasing the FO water flux from an average 76.04±1.50 L/m^{2}h for S0 to an average 84.67±0.43 L/m^{2}h for S3. This increase in the FO water flux was attributed to the

hydrophilic nature of PVP that increased the demixing rate during the phase inversion process. Therefore, the casting solution solvent was displaced easily with the non-solvent water in the coagulation water bath resulting in the formation of a large number of pores with some finger-like pores. This explanation was also reported in the literature [107][59].

B. Water permeability response

Analysis of the responses confirmed that the factorial design model for the water permeability was successful, and the effect of PSF wt% (A), PVP wt% (B) concentrations and their interaction (AB) were significant since the p-value was less than 0.05 for the model and the factors at level α=0.05. As shown in the ANOVA results in Table 5.4, PVP wt% shows the highest contribution percent (53.46%) followed by PSF wt% while the interaction between the factors (AB) shows the lowest contribution percent (14.93%) although it is significant.

Table 5.4: ANOVA results for the water permeability response

Source	Sum of squares	DF	Mean square	F-value	p-value	Contribution%
Model	62.1515	11	5.650136	75.17645	7.69E-16	
A-PSF%	19.63145	2	9.815725	130.6006	1.26E-13	31.58
B-PVP%	33.23299	3	11.07766	147.391	1.36E-15	53.46
AB	9.287061	6	1.547844	20.59444	2.25E-08	14.93
Pure Error	1.8038	24	0.075158			
Cor Total	63.9553	35				

From Table 5.2, PSF and PVP concentrations have similar effects on the water permeability as the FO water flux since the two responses are directly proportional. For example, decreasing PSF concentration from 20 to 18 wt% led to an increase in the water permeability from an average 3.90±0.086 L/m^{2}h.bar for S0 to an average 6.86±0.38 L/m^{2}h.bar and an average 6.80±0.39 L/m^{2}h.bar for S6 and S7, respectively. Moreover, increasing PVP concentration from 0 to 5 wt% at fixed PSF concentration led to an increase in the water permeability. Similar explanations to the ones presented earlier for the FO water flux are applicable for water permeability.

C. Reverse solute flux response

The factorial design model for the reverse solute flux was also successful, and the effect of PSF wt% (A), PVP wt% (B) concentrations were significant since the p-value was less than 0.05 for the model and the factors at level α=0.05 while their interaction AB was not significant since the p-value was higher than 0.05. As shown in the ANOVA results in Table 5.5, PSF wt% shows the highest contribution percent (79.88%) followed by PVP wt% while the interaction between the factors (AB) shows the lowest contribution percent (2.82%), and it is not significant.

Table 5.5: ANOVA results for the reverse solute flux response

Source	Sum of squares	DF	Mean square	F-value	p-value	Contribution%
Model	376.3734	11	34.21576	43.09411	4.37E-13	
A-PSF%	298.7898	2	149.3949	188.1601	2.16E-15	79.38
B-PVP%	67.14259	3	22.38086	28.18827	4.90E-08	17.83
AB	10.44096	6	1.74016	2.191699	0.079378	2.77
Pure Error	19.05547	24	0.793978			
Cor Total	395.4289	35				

The highest contribution percent of PSF concentration effect can be clearly noticed from the results in Table 5.2. Decreasing the PSF concentration from 20 to 15 wt% resulted in an increase in the reverse solute flux from an average 18.42±0.70 g/m^{2}h for S0 to an average 27.90±1.29 g/m^{2}h for S11. However, decreasing the PSF concentration from 20 to 18 wt% did not show a significant difference, and the reverse solute flux values achieved by 20 and 18 wt% PSF support membranes were similar. In FO, when the water flux increases in a certain direction, the reverse solute flux increases in the other direction, and this explains the corresponding increase in the reverse solute flux with decreasing the PSF concentration [108][109]. Furthermore, increasing PVP concentration from 0 to 5 wt% at fixed PSF concentration resulted in an increase in the reverse solute flux due to the similar reasons of fast demixing and increased membrane porosity that increased the FO water flux in a direction and the reverse solute flux in the other direction.

5.1.3 Optimal support layer composition

From the support layer design of experiment, sample S6 (PSF 18 wt% and PVP 2 wt%) was found to be the optimal support layer since it exhibited the highest possible FO water flux and

water permeability of 90.15±0.49 L/m^2h and 6.86±0.38 L/m^2h.bar with the lowest possible reverse solute flux of 18.54±0.42 g/m^2h.

5.1.4 Support layer BET analysis

The porosity measurements of different support layers were investigated using BET analysis in order to reach a better understanding of the effect of pore size distribution on the performance of the support layer. The analysis focused on two sample series: samples S4, S5, S6, and S7 to investigate the effect of varying amounts of PVP at fixed 18 wt% PSF; and samples S2, S6, and S10 to investigate the effect of varying amounts of PSF at fixed 2 wt% PVP. In each of these series, the best performing sample, S6, is compared with others. Results for the remaining samples are included in Appendix III.

A. Effect of PVP concentration at fixed PSF concentration of 18wt%

Table 5.6 summarizes the BET surface area and the average pore width for the support membranes S4, S5, S6, and S7. Figures 5.1, 5.2 and 5.3 show the pore volume distribution while Figures 5.4 and 5.5 show the corresponding pore area distribution.

The BET surface area increased from 21.27 to 27.17 m^2/g and the corresponding average pore width increased from 7.49 to 8.11 nm with increasing the PVP wt% from 0 to 5 wt% which reflects the role of PVP in the pore formation. Increasing PVP concentration at fixed PSF concentration resulted in increasing the membrane porosity. The same trend was also reported in the literature [59].

Table 5.6: Support membranes of different PVP wt% and their BET surface area with the average pore width

Support membrane	PSF wt%	PVP wt%	BET surface area (m^2/g)	Average pore width (nm)
S4	18	0	21.27	7.49
S5	18	1	23.86	7.63
S6	18	2	24.94	7.86
S7	18	5	27.17	8.11

From the differential pore volume distribution plots of S4, S5, S6 and S7 shown in Figures 5.1, 5.2 and 5.3, the largest differential volume of pores was exhibited by S7 (5 wt% PVP) and the least was exhibited by S4 (0 wt% PVP), and this can be attributed to the effect of PVP on the pore formation.

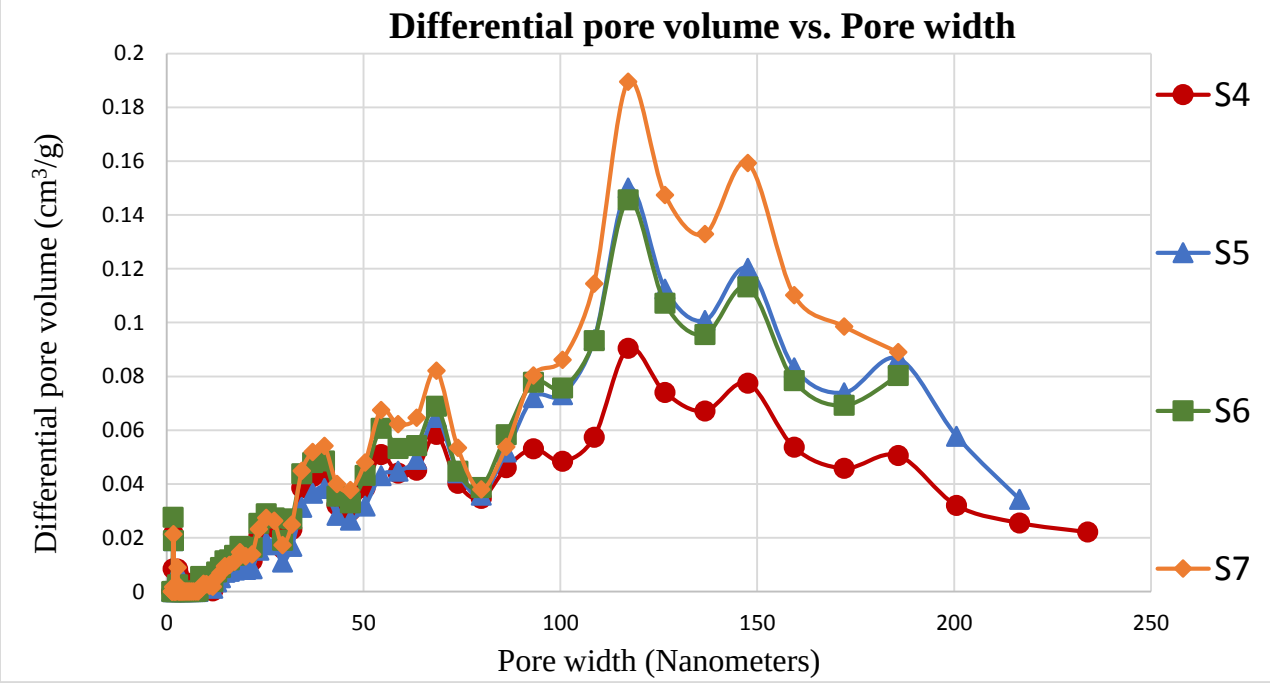

Figure 5.1: Plot of differential pore volume vs. pore width for S4, S5, S6 and S7, range 0 - 240 nm

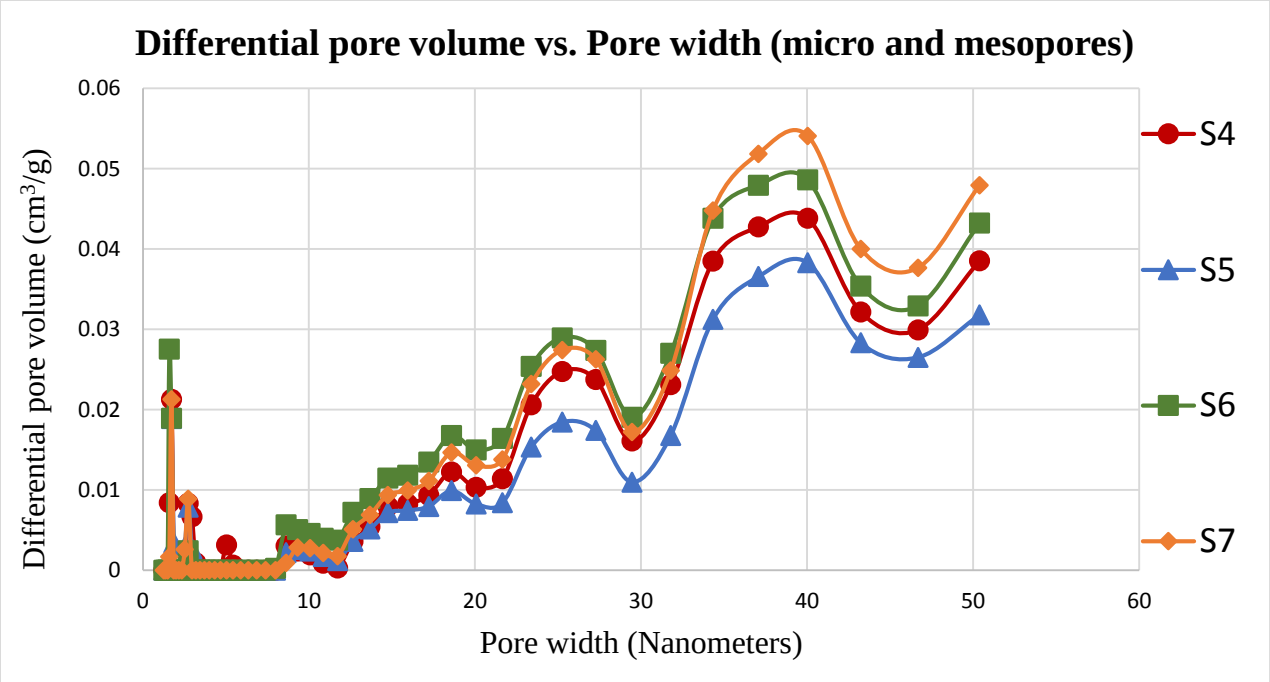

Figure 5.2: Plot of differential pore volume vs. pore width (micro and mesopores) for S4, S5, S6 and S7, range 0 -50 nm

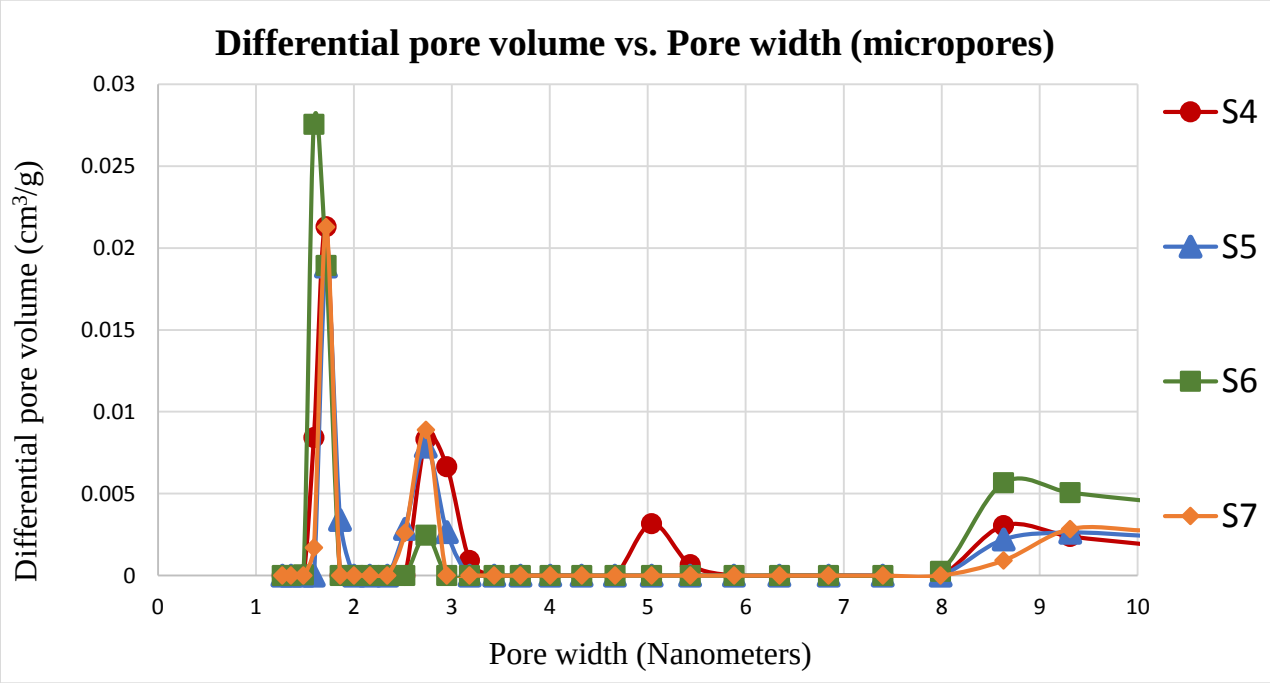

Figure 5.3: Plot of differential pore volume vs. pore width (micropores) for S4, S5, S6 and S7, range 0 – 10 nm

From the corresponding differential surface area distribution plots for S4, S5, S6 and S7 shown in Figures 5.4 and 5.5, the largest differential surface area of pores was occupied by S6 and S7. This was also attributed to the effect of PVP on pore formation. The differential surface area for pores larger than 10 nm was too small for the investigated samples.

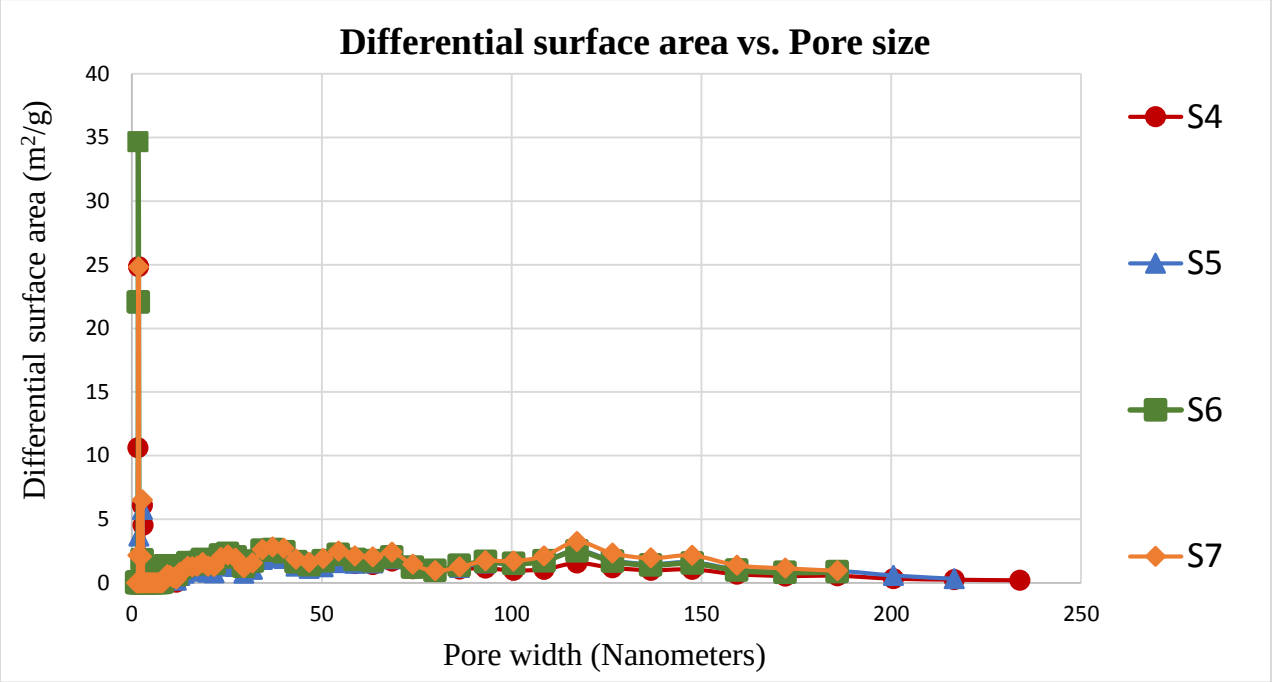

Figure 5.4: Plot of differential surface area vs. pore width for S4, S5, S6 and S7, range 0 – 240 nm

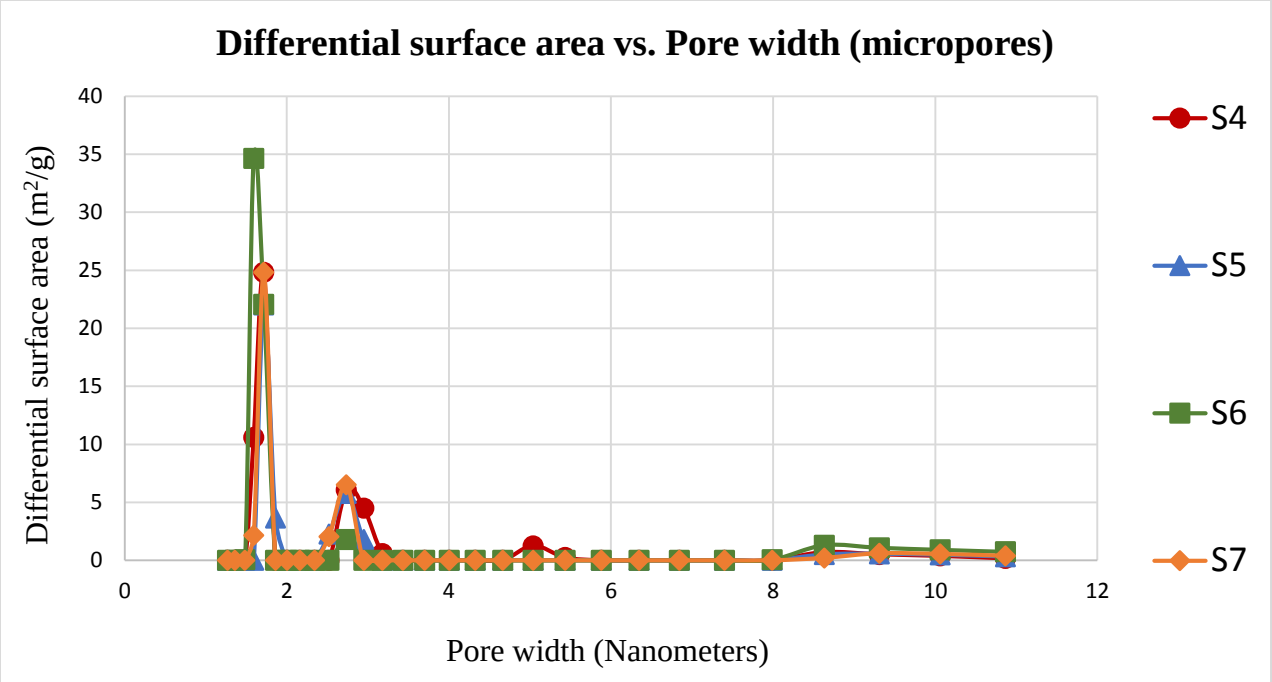

Figure 5.5: Plot of differential surface area vs. pore width (micropores) for S4, S5, S6 and S7, range 0 – 11 nm

BET results demonstrate that increasing PVP concentration increased the support membrane porosity. In addition, the large differential pore volume that corresponded to low differential surface area for pores larger than 10 nm reflected their limited number. This is contrasted by pores between 1 and 2 nm exhibiting large differential surface areas and low differential pore volumes reflecting their large numbers.

The porosity of S6 and S7 are clearly higher than the other samples throughout the different pore size ranges. The porosity distribution of S5 seems to be close to that of S6 porosity, and they are both lower than that of S7 for the pores above 50 nm. However, the porosity distribution of S5 falls clearly below S6 for the pores below 50 nm, and this corresponds to the observed lower FO water flux of S5 than S6 and S7. In addition, this is in line with the observed higher reverse solute flux of S7 for the same FO water flux as S6.

Although the porosity distribution of S4 falls clearly below all the other samples for the pores above 50 nm, it is higher than S5 below 50 nm, and this corresponds to the lowest FO water flux and reverse solute flux of S4.

B. Effect of PSF concentration at fixed PVP concentration

Table 5.7 summarizes the BET surface area and average pore width for the support membranes S2, S6, and S10. Figures 5.6, 5.7 and 5.8 show the differential pore volume distribution of the different support membranes while Figures 5.9 and 5.10 show the corresponding differential pore area distribution.

The BET surface area increased from 13.87 to 16.88 m^2/g and the corresponding average pore width virtually showed no increase when decreasing the PSF wt% from 20 to 15 wt%. S6 membrane showed the highest BET surface area of 24.94 m^2/g with average pore width of 7.86 nm, which, when compared with the values for the other two samples, clearly denote the higher number of pores of S6.

Table 5.7: Support membranes of different PSF wt% and their BET surface area with the average pore width

Support membrane	**PSF wt%**	**PVP wt%**	**BET surface area (m^2/g)**	**Average pore width (nm)**
S2	20	2	13.87	8.06
S6	18	2	24.94	7.86
S10	15	2	16.88	8.19

From the differential pore volume distribution plots of S2, S6 and S10 shown in Figures 5.6, 5.7 and 5.8, the largest pore volume is generally exhibited by S6, even though that below pore diameter of about 22 nm, this is not the case. The fact that the differential pore surface area is highest for S6, denotes that this sample includes a higher number of larger pores, relative to S2 and S10. The higher porosity of S6 as compared to S2 is obvious: a higher content of PSF in S2 leads to more limited porosity. However, with lower PSF content, S10 is exhibiting a lower BET surface area, though with larger average pore width diameters. This, coupled with the plots of differential pore volume and differential pore surface area seem to indicate that S10 includes on average larger but fewer pores relative to S6.

The above is in line with the water flux and reverse solute flux results. S2 has the lowest water flux and the lowest reverse solute flux, due to its more limited porosity. S6 and S10 have comparable water flux, with S10 having significantly larger reverse solute flux. This seems to indicate that the average pore size, rather than the number of pores, plays a lead role in this respect.

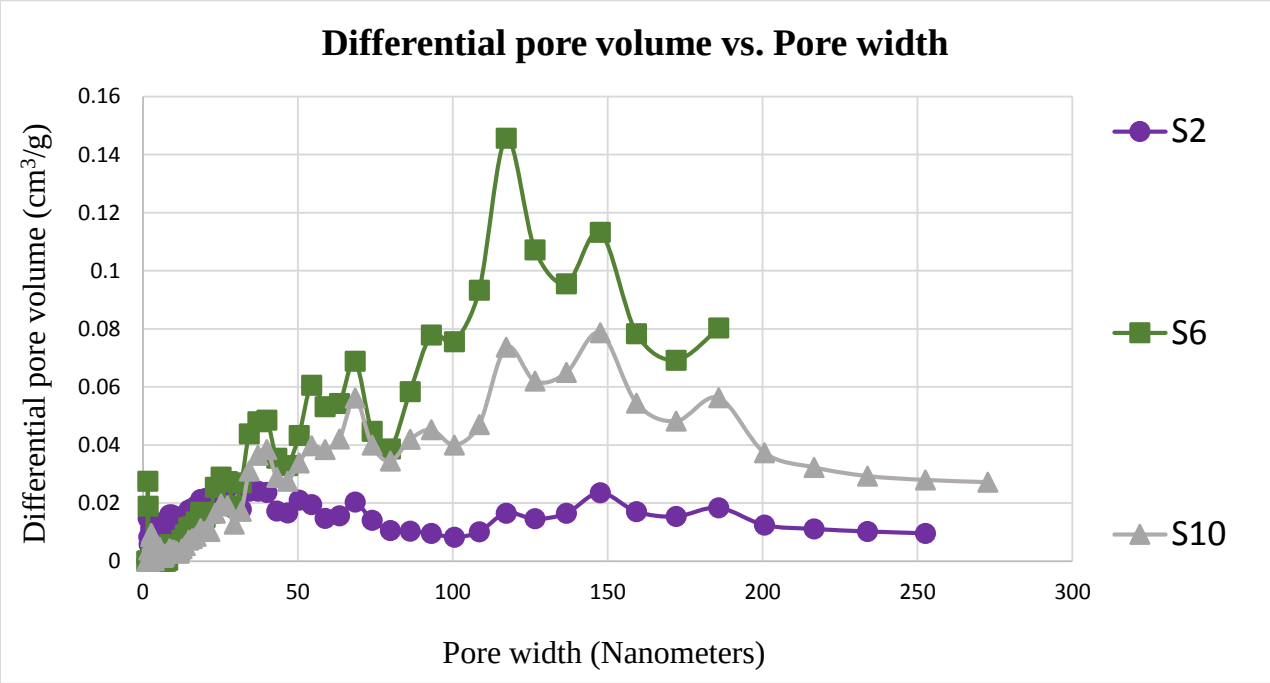

Figure 5.6: Plot of differential pore volume vs. pore width for S2, S6 and S10, range 0 – 275 nm

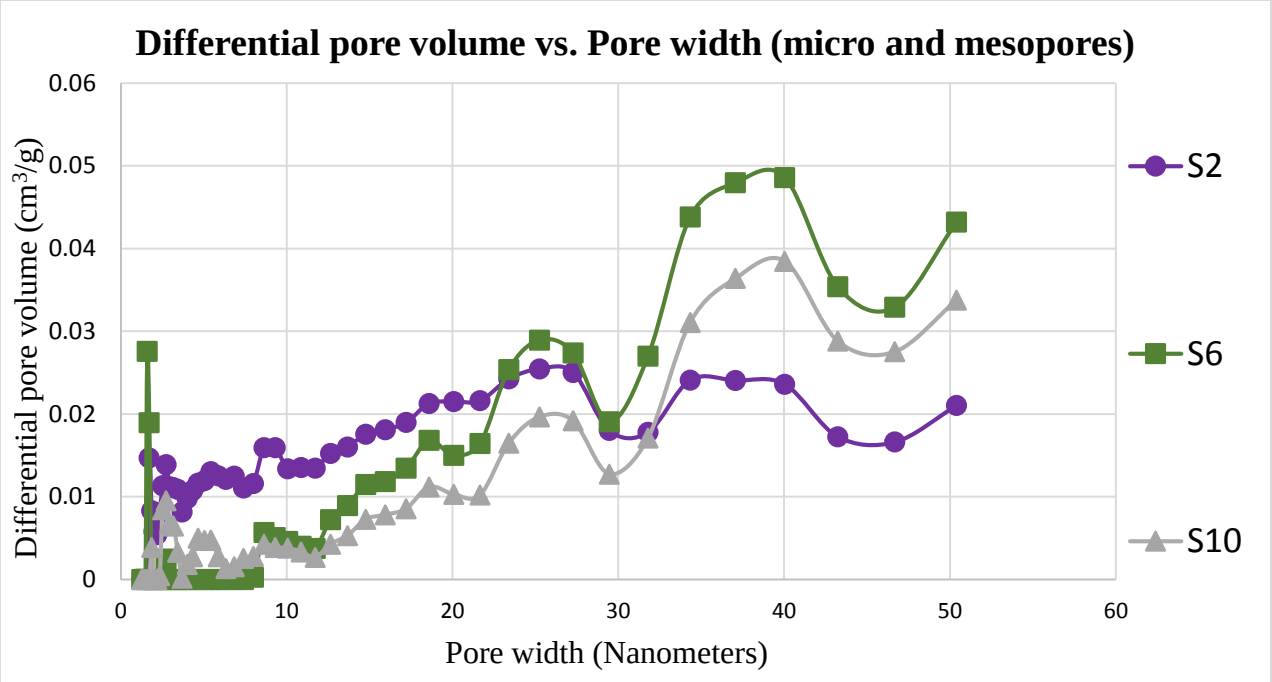

Figure 5.7: Plot of differential pore volume vs. pore width (micro and mesopores) for S2, S6 and S10, range 0 – 50 nm

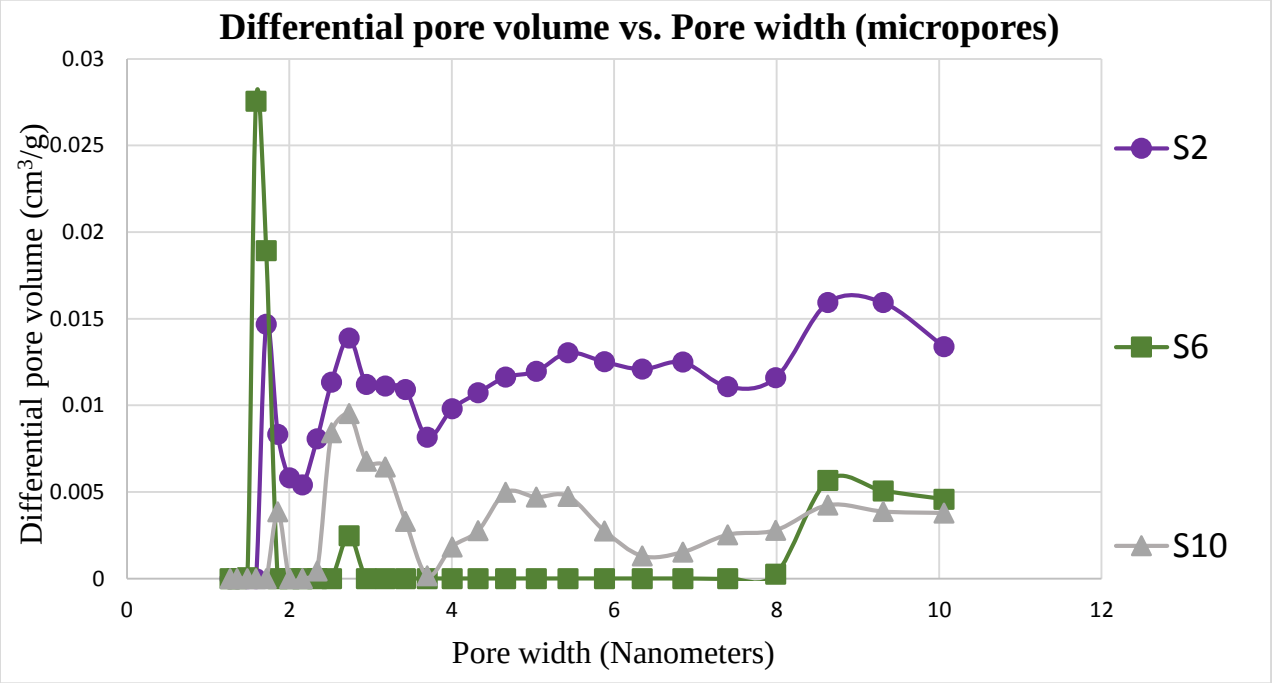

Figure 5.8: Plot of differential pore volume vs. pore width (micropores) for S2, S6 and S10, range 0 – 10 nm

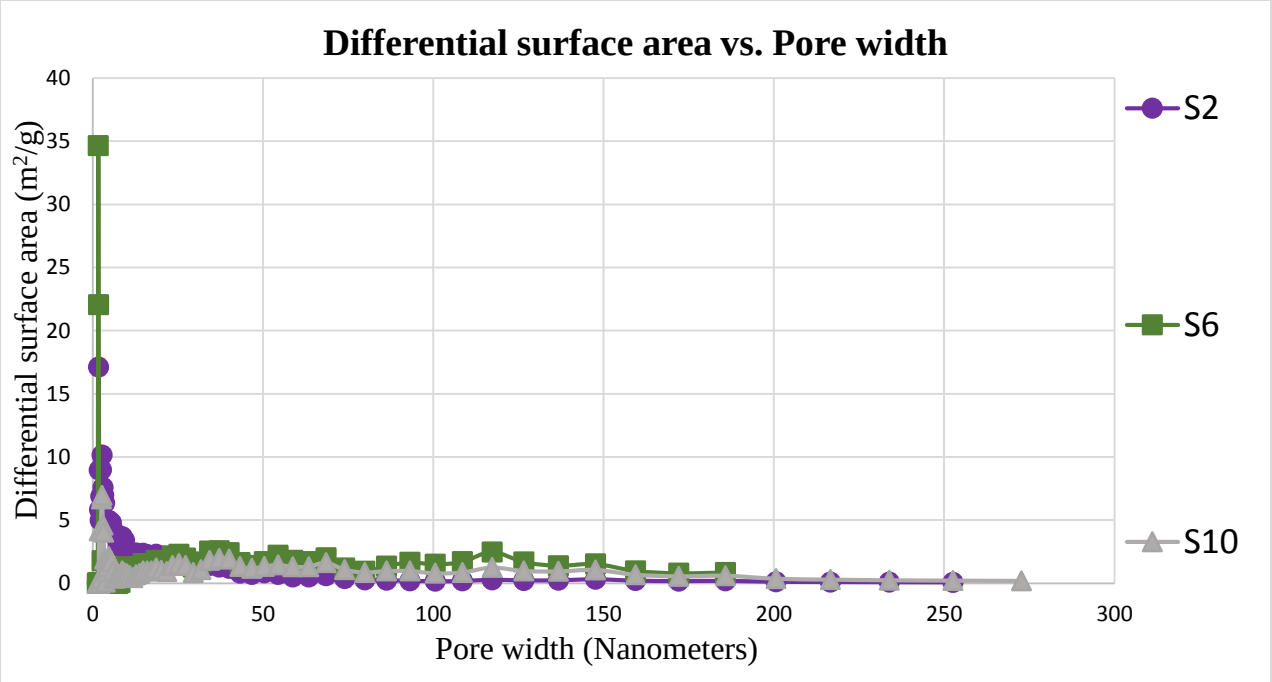

Figure 5.9: Plot of differential surface area vs. pore width for S2, S6 and S10, range 0 – 275 nm

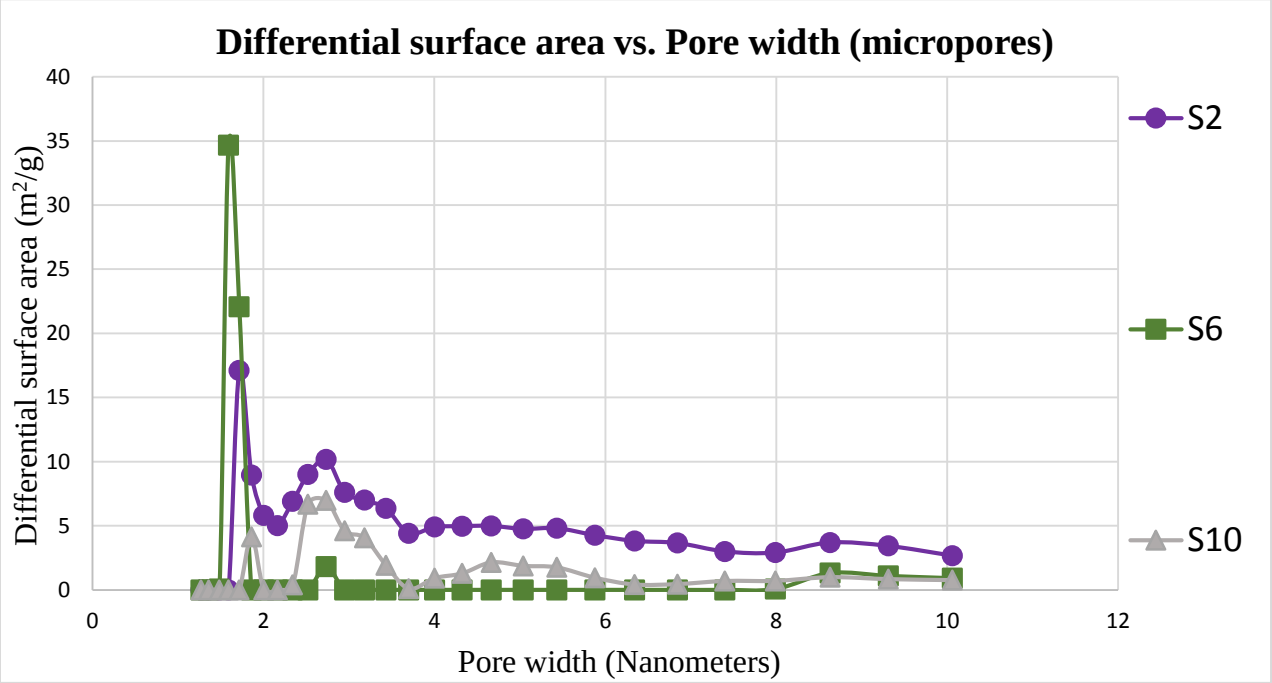

Figure 5.10: Plot of differential surface area vs. pore width (micropores) for S2, S6 and S10, range 0 – 10 nm

5.1.5 Membrane Support Morphology

SEM images were obtained for the series S4, S5, S6, and S7, in which the PVP wt% varies for a fixed amount of PSF, and the series S2, S6, and S10 for which the PSF wt% varies for a fixed PVP amount.

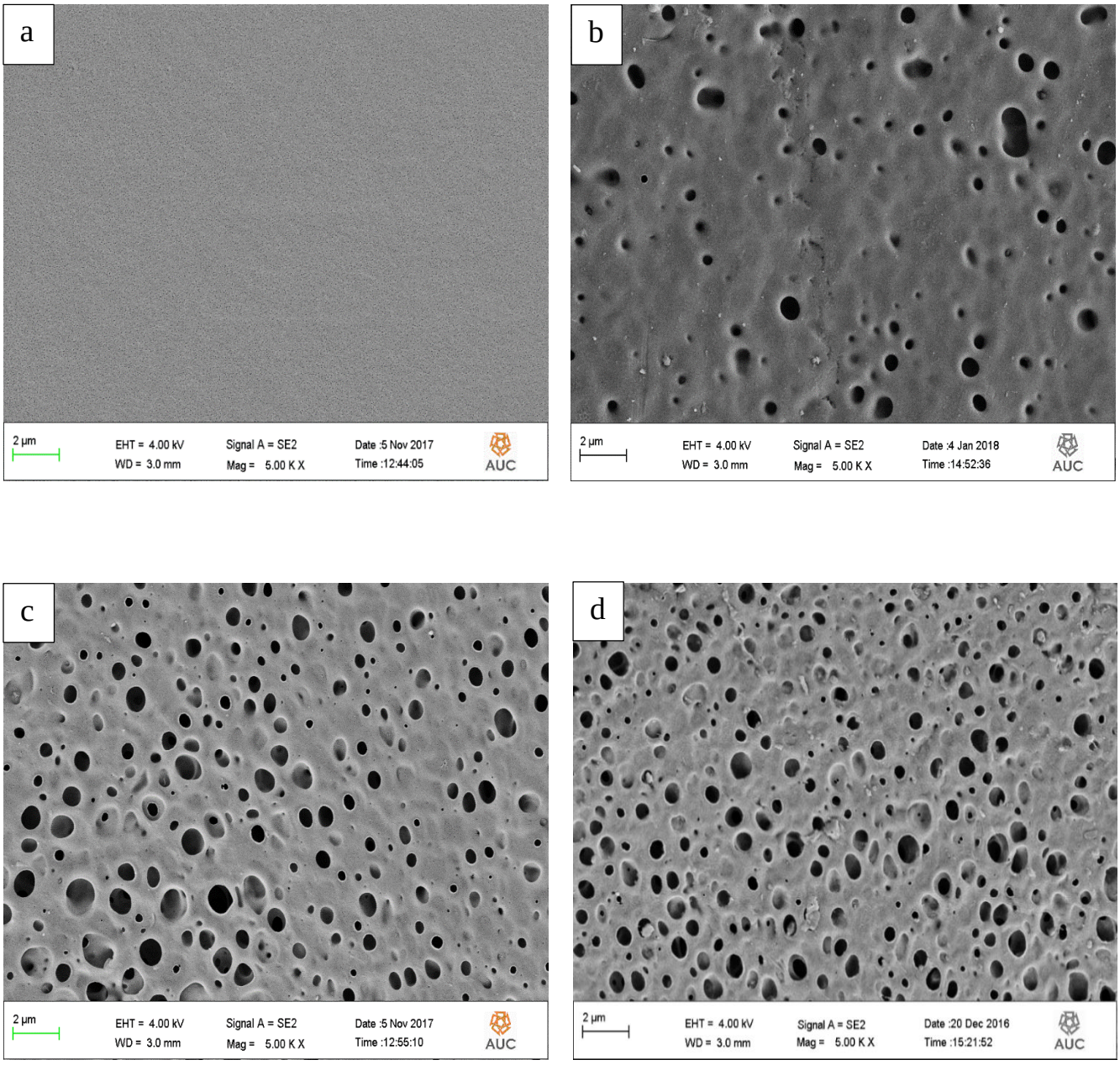

Figure 5.11: SEM top surface of (a) S4, (b) S5, (c) S6 and (d) S7 at 5.00 KX magnification

Top surface morphology is shown in Figure 5.11 for the former series, and in Figure 5.12 for the latter series.

The top surface of S6 and S7 had the highest number of pores reflecting the higher PVP contents of 2 and 5 wt% respectively. This is in line with the BET surface area results. On the other hand, S4 with 0 wt% of PVP did not show pores at the same magnification, and S5 with 1 wt% PVP showed a limited number of pores.

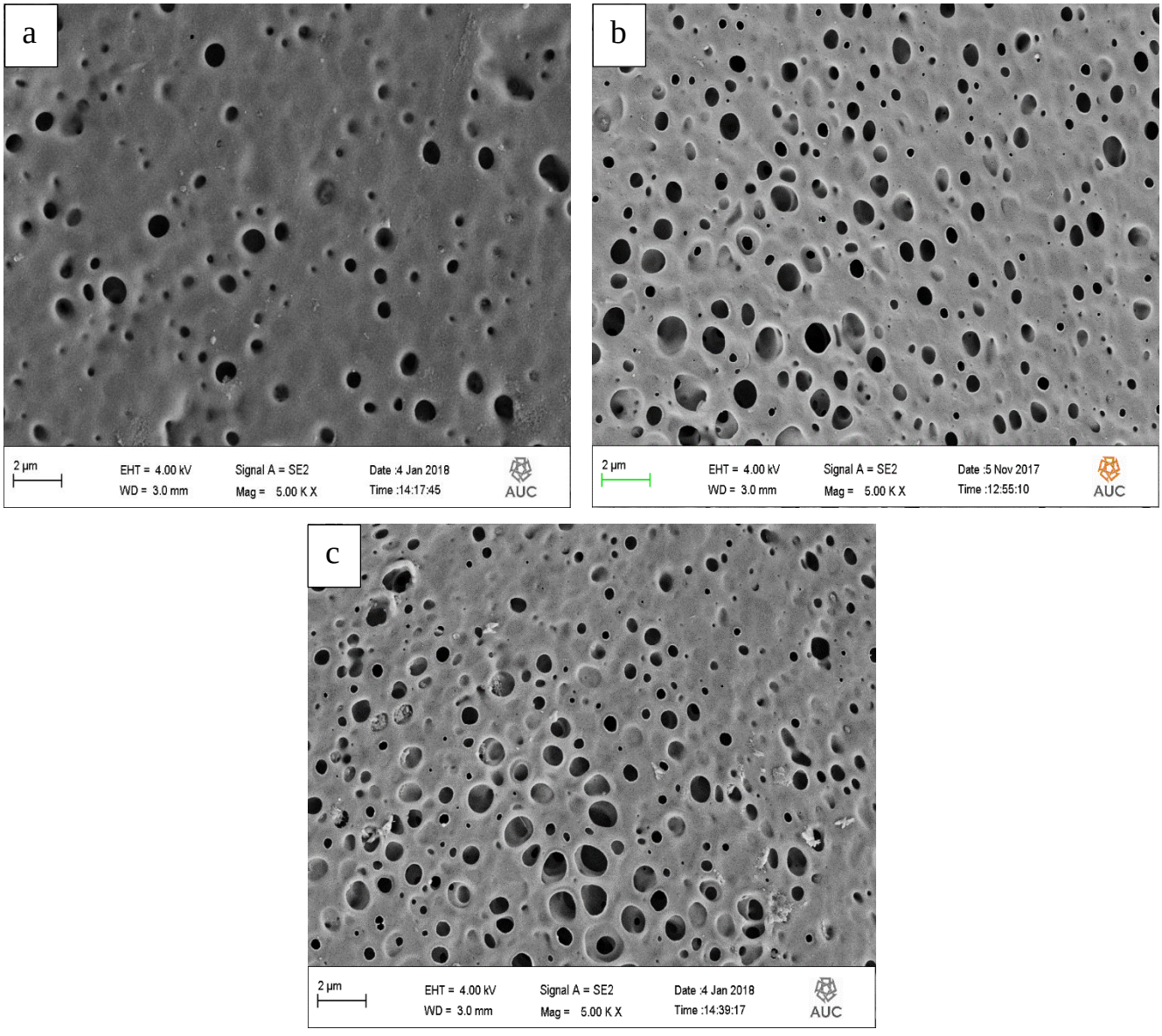

Figure 5.12: SEM top surface of (a) S2, (b) S6 and (c) S10 at 5.00 KX magnification

The top surface of S2 membrane had the lowest number of pores reflecting the pore suppressing effect of PSF, and this is in line with the BET surface area results since S2 had the lowest BET surface area.

Moreover, Figure 5.13 shows the optimal support membrane S6 cross-section images at different locations.

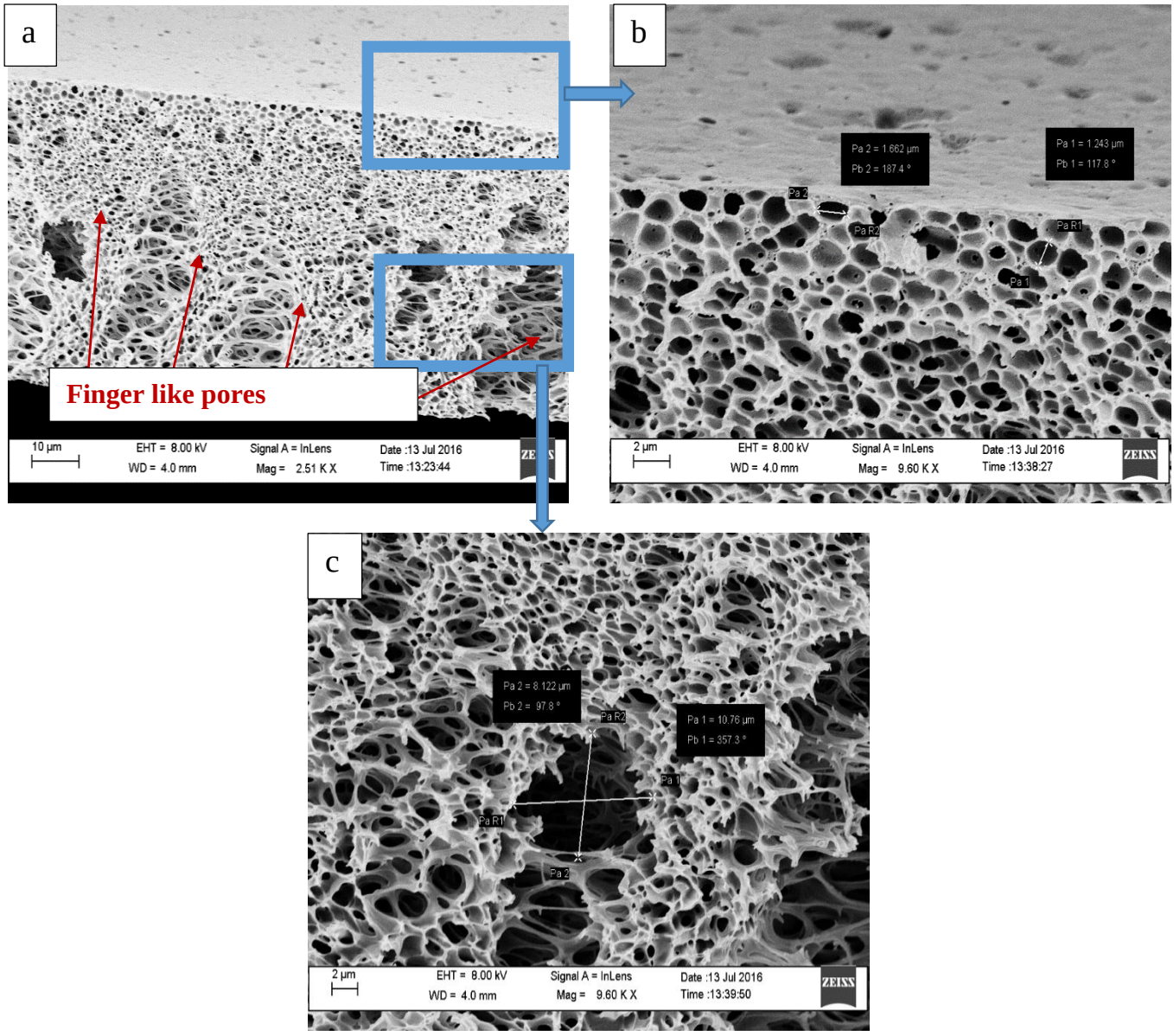

Figure 5.13: SEM cross-section of S6 (a) Overall cross-section, (b) near top and (C) near bottom

The cross-section of S6 showed a highly porous sponge-like structure with some finger like macrovoids in the lower part of the cross-section. It is believed these increased the FO water flux. The porous structure was also present in the upper part of the membrane, and this was important to allow an efficient IP reaction by diffusion of MPD aqueous solution in the top surface layer for the reaction with TMC for the formation of the rejection layer. The same explanation was observed by Ghosh and et al, 2009 [110].

5.2. Thin film composite (TFC) rejection layer

In this section, the investigation of the effects of monomers concentration (MPD and TMC), contact time and curing temperature on the TFC rejection layer are reported and discussed.

5.2.1 Rejection layer Experimental Design

The goal of this part of the work is to achieve a thin film composite (TFC) polyamide (PA) rejection layer with the highest possible salt rejection and the lowest reverse solute flux while maintaining high FO water flux and water permeability. Therefore, the effect of different factors on interfacial polymerization was investigated. Table 5.8 summarizes the average values of FO water flux, water permeability, reverse solute flux and salt rejection for the different TFC membranes. The plots for the statistical analysis can be found in Appendix II.

Table 5.8: Different thin film composites (TFCs) with different MPD/TMC concentrations, contact times and curing temperatures

Thin film composite	MPD (wt/vol %)	MPD Contact time (min)	TMC (wt/vol%)	TMC Contact time (min)	Curing temperature (°C)	FO water flux (L/m^2h)	Water permeability ($L/m^2h.bar$)	Reverse solute flux (g/m^2h)	Salt retention (%)
TFC1	1	2	0.05	1	25	85.32±0.55	4.92±0.70	12.79±0.35	27.66±0.64
TFC2	1	2	0.1	1	25	80.89±0.40	4.81±0.38	10.39±0.24	35.48±0.94
TFC3	1	2	0.15	1	25	88.49±0.22	6.24±0.29	13.80±0.18	22.50±1.13
TFC4	1	2	0.05	1	60	78.32±0.46	4.20±0.24	11.66±0.31	35.92±0.82
TFC5	1	2	0.1	1	60	73.73±0.36	3.26±0.45	10.16±0.34	44.94±0.76
TFC6	1	2	0.15	1	60	75.95±0.28	3.60±0.1	10.21±0.11	32.03±0.44
TFC7	1	5	0.05	2.5	25	83.27±0.33	5.45±0.30	11.52±0.29	29.96±0.49
TFC8	1	5	0.1	2.5	25	78.30±0.76	3.99±0.23	9.98±0.45	38.17±0.67
TFC9	1	5	0.15	2.5	25	86.11±0.18	6.18±0.20	12.30±0.31	25.10±0.73
TFC10	1	5	0.05	2.5	60	75.69±0.42	3.80±0.09	10.28±0.47	40.33±0.74
TFC11	1	5	0.1	2.5	60	70.00±0.27	3.22±0.24	8.53±0.38	48.75±0.59
TFC12	1	5	0.15	2.5	60	78.23±0.75	5.31±0.25	11.88±0.59	29.85±0.30

Thin film composite	MPD (wt/vol %)	MPD Contact time (min)	TMC (wt/vol%)	Contact time (min)	Curing temperature (°C)	FO water flux (L/m2h)	Water permeability (L/m2h.bar)	Reverse solute flux (g/m2h)	Salt retention (%)
TFC13	2	2	0.05	1	25	76.32±0.71	4.20±0.13	11.36±0.32	40.36±0.80
TFC14	2	2	0.1	1	25	72.50±0.55	3.72±0.15	8.24±0.18	55.03 ±0.46
TFC15	2	2	0.15	1	25	79.88±0.25	6.11±0.09	13.52±0.31	30.61±0.56
TFC16	2	2	0.05	1	60	72.43±0.73	3.90±0.30	12.80±0.34	46.21±0.43
TFC17	2	2	0.1	1	60	69.59±0.57	2.95±0.25	8.06±0.42	63.49±0.36
TFC18	2	2	0.15	1	60	75.06±0.63	5.77±0.40	10.24±0.40	35.51±0.61
TFC19	2	5	0.05	2.5	25	74.22±0.35	4.74±0.24	9.19±0.43	44.27±0.39
TFC20	2	5	0.1	2.5	25	70.55±0.53	4.25±0.22	7.08±0.22	58.80±0.50
TFC21	2	5	0.15	2.5	25	76.18±0.31	5.33±0.26	11.22±0.13	33.98±0.18
TFC22	2	5	0.05	2.5	60	66.57±0.53	2.54±0.21	9.84±0.41	50.53±0.28
TFC23	2	5	0.1	2.5	60	62.73±0.68	2.18±0.13	6.07±0.31	70.03±0.47
TFC24	2	5	0.15	2.5	60	69.32±0.62	3.66±0.17	9.47±0.29	38.96±0.28

Thin film composite	MPD (wt/vol %)	MPD Contact time (min)	TMC (wt/vol%)	TMC Contact time (min)	Curing temperature (°C)	FO water flux (L/m2h)	Water permeability (L/m2h.bar)	Reverse solute flux (g/m2h)	Salt retention (%)
TFC25	3	2	0.05	1	25	85.27±0.64	6.57±0.14	15.37±0.44	25.50±0.51
TFC26	3	2	0.1	1	25	70.25±0.42	5.58±0.22	12.39±0.41	45.27±0.47
TFC27	3	2	0.15	1	25	65.19±0.34	4.06±0.15	7.91±0.18	60.20±0.81
TFC28	3	2	0.05	1	60	80.13±0.26	5.66±0.21	14.56±0.32	29.41±0.68
TFC29	3	2	0.1	1	60	73.14±0.60	4.74±0.13	12.49±0.25	48.26±0.54
TFC30	3	2	0.15	1	60	55.26±0.59	1.99±0.15	6.52±0.31	72.33±0.70
TFC31	3	5	0.05	2.5	25	82.27±0.26	5.75±0.18	13.58±0.62	28.01±0.78
TFC32	3	5	0.1	2.5	25	68.04 ±0.30	4.60±0.24	10.76±0.78	47.15±0.44
TFC33	3	5	0.15	2.5	25	62.75±0.52	3.93±0.26	6.48±0.32	63.34±0.49
TFC34	3	5	0.05	2.5	60	75.41±0.65	5.10±0.19	14.11±0.42	35.50±0.60
TFC35	3	5	0.1	2.5	60	70.13±0.26	4.45±0.24	10.57±0.40	52.64±0.56
TFC36	3	5	0.15	2.5	60	50.94±0.52	1.54±0.11	5.31±0.53	76.50±0.70

A. FO water flux response

According to Design-Expert, the factorial design model for the FO water flux was successful, and the effect of MPD concentration (A), TMC concentration (B), contact time (C), curing temperature (D) and their interactions (AB, AC, AD, BC, BD, CD, ABC, ABD, ACD, BCD, ABCD) were significant since the P-value was less than 0.05 for the model and the factors at level α=0.05. By dividing each individual sum of squares over the total sum of squares of the model, a contribution percent of each factor can be obtained. As shown in ANOVA Table 5.9, the interaction between MPD, TMC concentrations (AB) showed the highest contribution percent (36.26%) followed by MPD concentration and curing temperature with 25.75% and 15.02%, respectively. Moreover, it was found that the FO water flux decreased by increasing MPD and TMC concentrations together with keeping the concentration ratio of MPD/TMC 10 or higher. On the other hand, increasing contact time had a limited effect on the average FO water flux. The effect of curing temperature was more significant since increasing the curing temperature from 25 to 60 $^{\circ}$C led to a significant decrease in the average FO water flux.

Table 5.9: ANOVA of the different factors effects on the FO water flux

Source	Sum of squares	DF	Mean square	F-value	P-value	Contribution%
Model	7105.550677	35	203.0157336	809.7895254	6.07E-81	
A-MPD concentration	1829.72118	2	914.8605898	3649.197575	4.31E-73	25.7505894
B-TMC concentration	904.714363	2	452.3571815	1804.363143	3.09E-62	12.73250173
C-Contact time	271.035075	1	271.035075	1081.105197	4.19E-45	3.81441337
D-Curing temperature	1067.287408	1	1067.287408	4257.197944	8.48E-66	15.02047423
AB	2576.745609	4	644.1864023	2569.531886	7.78E-77	36.26384114
AC	28.77843889	2	14.38921944	57.39574454	1.24E-15	0.405013492
AD	64.18323889	2	32.09161944	128.0071097	1.96E-24	0.903283107
BC	2.720266667	2	1.360133333	5.425302299	0.006387	0.038283685
BD	133.1788222	2	66.58941111	265.6119635	5.84E-34	1.874292765
CD	12.32888981	1	12.32888981	49.17749799	1.05E-09	0.173510687
ABC	16.06886111	4	4.017215278	16.02387556	1.99E-09	0.22614519
ABD	156.3413389	4	39.08533472	155.9036538	1.15E-34	2.200270549
ACD	23.38235741	2	11.6911787	46.63379475	1.02E-13	0.329071714
BCD	8.736007407	2	4.368003704	17.42310107	6.74E-07	0.12294624
ABCD	10.32882037	4	2.582205093	10.29990434	1.19E-06	0.145362701
Pure Error	18.05053333	72	0.250701852			
Cor Total	7123.60121	107				

B. Water permeability

According to Design-Expert, the factorial design model for the water permeability was successful, and the effect of MPD concentration (A), TMC concentration (B), contact time (C), curing temperature (D) and their interactions (AB, AC, BD, CD, ABC, ABD, ACD, BCD, ABCD) were significant since the P-value was less than 0.05 for the model and the factors at level α=0.05. However, AD and BC interactions were not significant since P-value was higher than 0.05. As shown in ANOVA Table 5.10, the interaction between MPD, TMC concentrations (AB) showed the highest the contribution percent (48.12%) followed by curing temperature and TMC concentration with 25.72% and 6.46%, respectively. Similar to the FO water flux results, it was found that water permeability decreased by increasing MPD and TMC concentrations while keeping their concentration ratio (MPD/TMC) 10 or higher. On the other hand, increasing contact time had a limited effect on the water permeability.

Table 5.10: ANOVA of the different factors effects on the water permeability

Source	Sum of squares	DF	Mean square	F-value	P-value	Contribution%
Model	164.3586546	35	4.695961561	69.87267835	3.10E-43	
A-MPD concentration	4.499424074	2	2.249712037	33.47416786	5.26E-11	2.737564434
B-TMC concentration	10.62313519	2	5.311567593	79.03247272	6.88E-19	6.463386555
C-Contact time	3.262156481	1	3.262156481	48.53864488	1.27E-09	1.984779255
D-Curing temperature	42.27504537	1	42.27504537	629.0236002	2.58E-37	25.72121649
AB	79.10502037	4	19.77625509	294.2570746	8.52E-44	48.1295132
AC	3.486701852	2	1.743350926	25.93986278	3.28E-09	2.121398389
AD	0.187568519	2	0.093784259	1.395445277	0.254341	0.114121474
BC	0.037824074	2	0.018912037	0.281398104	0.755554	0.023013132
BD	2.264590741	2	1.13229537	16.84777637	9.95E-07	1.3778348
CD	0.431934259	1	0.431934259	6.426884713	0.013413	0.262799827
ABC	5.539775926	4	1.384943981	20.60701394	2.37E-11	3.370541051
ABD	3.824987037	4	0.956246759	14.22829411	1.32E-08	2.327219729
ACD	5.46657963	2	2.733289815	40.66947261	1.52E-12	3.326006557
BCD	1.234812963	2	0.617406481	9.18658382	0.000279	0.75129172
ABCD	2.119098148	4	0.529774537	7.882680756	2.51E-05	1.289313394
Pure Error	4.838933333	72	0.067207407			
Cor Total	169.197588	107				

C. Reverse solute flux

According to Design-Expert, the factorial design model for the reverse solute flux was successful, and the effect of MPD concentration (A), TMC concentration (B), contact time (C), curing temperature (D) and their interactions (AB, AC, AD, BC, BD, CD, ABC, ABD, BCD, ABCD) were significant since the P-value was less than 0.05 for the model and the factors at level α=0.05. However, ACD interaction was not significant since P-value was higher than 0.05. As shown in ANOVA Table 5.11, the interaction between MPD, TMC concentrations (AB) showed the highest the contribution percent (53.68%) followed by TMC concentration and contact time with 22.91% and 7.28%, respectively. It was found that the reverse solute flux decreased with increasing MPD and TMC concentrations with keeping their concentration ratio (MPD/TMC) 10 or higher. In addition, increasing contact time and curing temperature led to a decrease in the reverse solute flux. However, the decrease was not high.

Table 5.11: ANOVA of the different factors effects on the reverse solute flux

Source	Sum of squares	DF	Mean square	F-value	P-value	Contribution%
Model	675.3488	35	19.29568	131.4461073	8.24E-53	
A-MPD concentration	37.46246667	2	18.73123333	127.6009815	2.14E-24	5.547128634
B-TMC concentration	154.7537167	2	77.37685833	527.106939	1.01E-43	22.91463562
C-Contact time	49.2075	1	49.2075	335.2115252	8.38E-29	7.286234906
D-Curing temperature	19.00083333	1	19.00083333	129.4375516	9.54E-18	2.81348443
AB	362.5557833	4	90.63894583	617.4509837	6.84E-55	53.68422707
AC	5.867088889	2	2.933544444	19.98390301	1.25E-07	0.868749436
AD	3.585066667	2	1.792533333	12.21110263	2.71E-05	0.530846678
BC	2.682705556	2	1.341352778	9.137568674	0.000290	0.397232594
BD	16.87200556	2	8.436002778	57.46777134	1.21E-15	2.498265423
CD	0.756681481	1	0.756681481	5.154668567	0.026177	0.112043063
ABC	3.364372222	4	0.841093056	5.729697425	0.000463	0.498168091
ABD	7.141561111	4	1.785390278	12.16244268	1.32E-07	1.057462619
ACD	0.494940741	2	0.24747037	1.685818631	0.192523	0.073286684
BCD	6.717224074	2	3.358612037	22.87955014	2.03E-08	0.994630341
ABCD	4.886853704	4	1.221713426	8.32256101	1.42E-05	0.723604411
Pure Error	10.56926667	72	0.14679537			
Cor Total	685.9180667	107				

D. Salt rejection

According to Design-Expert, the factorial design model for the salt rejection was successful, and the effect of MPD concentration (A), TMC concentration (B), contact time (C), curing temperature (D) and their interactions (AB, AC, AD, BC, BD, CD, ABC, ABD, ACD, BCD, ABCD) were significant since the P-value was less than 0.05 for the model and the factors at level α=0.05. As shown in ANOVA Table 5.12, the interaction between MPD, TMC concentrations (AB) showed the highest the contribution percent (50.52%) followed by MPD concentration, TMC concentration and curing temperature with 21.40%, 17.75% and 7.58%, respectively. Moreover, it was found that salt rejection increased by increasing MPD and TMC concentrations together with keeping the concentration ratio of MPD/TMC 10 or higher. On the other hand, increasing contact time had a limited effect on the increase of the average salt rejection.

Table 5.12: ANOVA of the different factors effects on the salt rejection

Source	Sum of squares	DF	Mean square	F-value	P-value	Contribution%
Model	21433.91203	35	612.3974864	1611.014915	1.14E-91	
A-MPD concentration	4587.317039	2	2293.658519	6033.855735	6.80E-81	21.4021455
B-TMC concentration	3804.827289	2	1902.413644	5004.620078	5.46E-78	17.75143653
C-Contact time	310.5240454	1	310.5240454	816.8858947	4.96E-41	1.448751143
D-Curing temperature	1625.487223	1	1625.487223	4276.118402	7.25E-66	7.583716968
AB	10829.30662	4	2707.326656	7122.079563	1.06E-92	50.52417221
AC	18.08855741	2	9.044278704	23.79250113	1.17E-08	0.084392235
AD	17.00269074	2	8.50134537	22.36422339	2.79E-08	0.07932612
BC	12.62136296	2	6.310681481	16.60131241	1.18E-06	0.058885018
BD	7.534762963	2	3.767381481	9.910732641	0.000157	0.035153466
CD	6.655334259	1	6.655334259	17.5079797	7.97E-05	0.031050488
ABC	12.82075926	4	3.205189815	8.431792606	1.23E-05	0.059815302
ABD	165.5145148	4	41.3786287	108.8534644	9.43E-30	0.772208613
ACD	9.456446296	2	4.728223148	12.43838876	2.29E-05	0.044119087
BCD	16.56534074	2	8.28267037	21.78896191	3.99E-08	0.077285662
ABCD	10.19003704	4	2.547509259	6.701652937	0.000121	0.047541657
Pure Error	27.36946667	72	0.380131481			
Cor Total	21461.28149	107				

5.2.2 TFC Design of Experiment summary and discussion

It was concluded from the TFC Design of Experiment that higher salt rejection with lower FO water flux, water permeability and reverse solute flux were obtained by primarily increasing MPD with TMC concentrations, and curing temperature. Most importantly, TFC36 achieved the highest salt rejection with 76.50±0.70%, and the lowest reverse solute flux with 5.31±0.53 g/m^{2}h. Although the sample exhibited the lowest FO water flux with 50.94±0.52 L/m^{2}h, the flux is higher than what is reported in the literature [51][2][45]. On the other hand, the achieved salt rejection was lower than the values in the literature.

It was found that MPD concentration should be higher than TMC concentration to obtain an efficient rejection layer of high salt rejection. At 1 wt% MPD, the MPD/TMC concentration ratio of 10 leads to the highest salt rejection values. At 2 or 3% MPD, a ratio of 20 leads to the highest salt rejection. This is in accordance with values reported in the literature [45][50][51][52][55].

Higher MPD concentration is needed because the IP reaction occurs at the interface between the aqueous MPD and organic TMC solutions. This polymerization reaction depends on the diffusion of MPD, rather than TMC to this interface because MPD has a good solubility in organic solvents while TMC has a negligible solubility in water. Therefore, increasing MPD/TMC concentration ratio allows the diffusion of more amine groups (available in the MPD) for the IP reaction with the acyl chloride groups of TMC. Figure 5.14 presents the polymerization reaction between MPD and TMC. It is clear that excess amine groups are needed to diffuse to the aqueous/organic solutions interface in order to react with the acetyl groups[111][112][113]. This leads in an increased degree of polymerization and cross-linked units, and hence increased salt rejection [47][63][62][82].

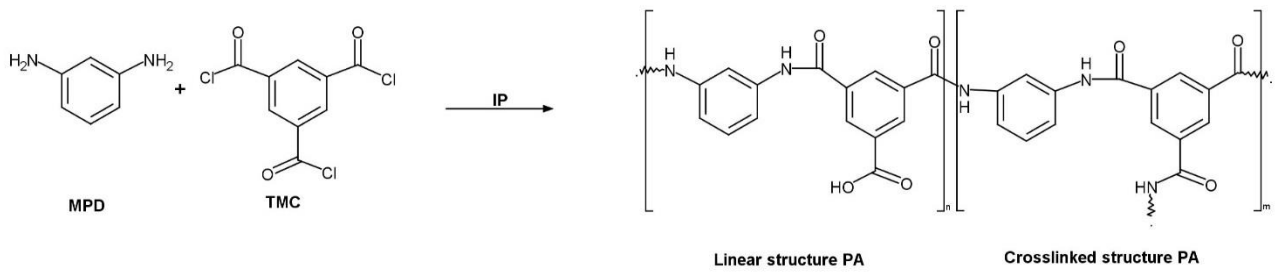

Figure 5.14: Chemical structures of MPD, TMC and PA with the IP reaction

In addition, the curing temperature had a significant effect on the rejection layer performance because salt rejection increased at higher curing temperature of 60 °C while the corresponding FO water flux and reverse solute flux decreased. This could be attributed to the promotion of more cross-linked PA units. Higher temperature facilitates the migration of MPD molecules toward TMC molecules in the reaction zone, thus enhancing the rate of the polymerization reaction. Similar trend and explanation were also reported in the literature [64][114][115][116].

5.2.3 TFC Model Validation

In order to validate the effect of higher curing temperature and monomers concentrations on the TFC performance, the curing temperature was further raised to 80°C and the monomers concentrations were raised to 4 wt/vol% MPD and 0.2 wt/vol% TMC while the contact time was kept at the level of 5 minutes. The resulting TFC37 membrane exhibited the highest salt rejection of 88.30±0.11% and the lowest reverse solute flux of 3.51±0.23 g/m^{2}h with FO water flux of 43.7±0.51 L/m^{2}h. These values compare favorably with values reported in the literature, where reported FO water flux ranged from 15 to 30 L/m^{2}h, reverse solute flux ranged from 4 to 8 g/m^{2}h and salt rejection ranged from 70 to 90 % [55][52][45]. Figures 5.15 and 5.16 show the morphology of TFC37, and the formation of the rejection layer on top of the support layer (S6).

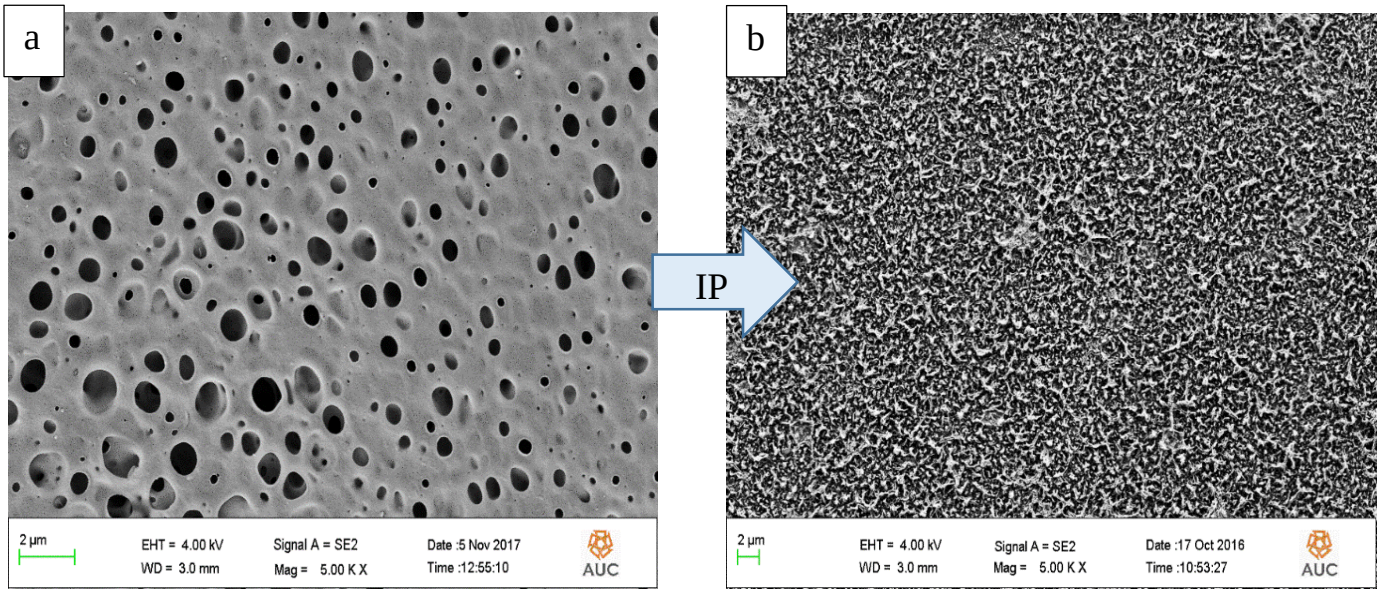

Figure 5.15: SEM top surface at 5.00 KX magnification factor of (a) S6 support membrane and (b) TFC37 rejection layer

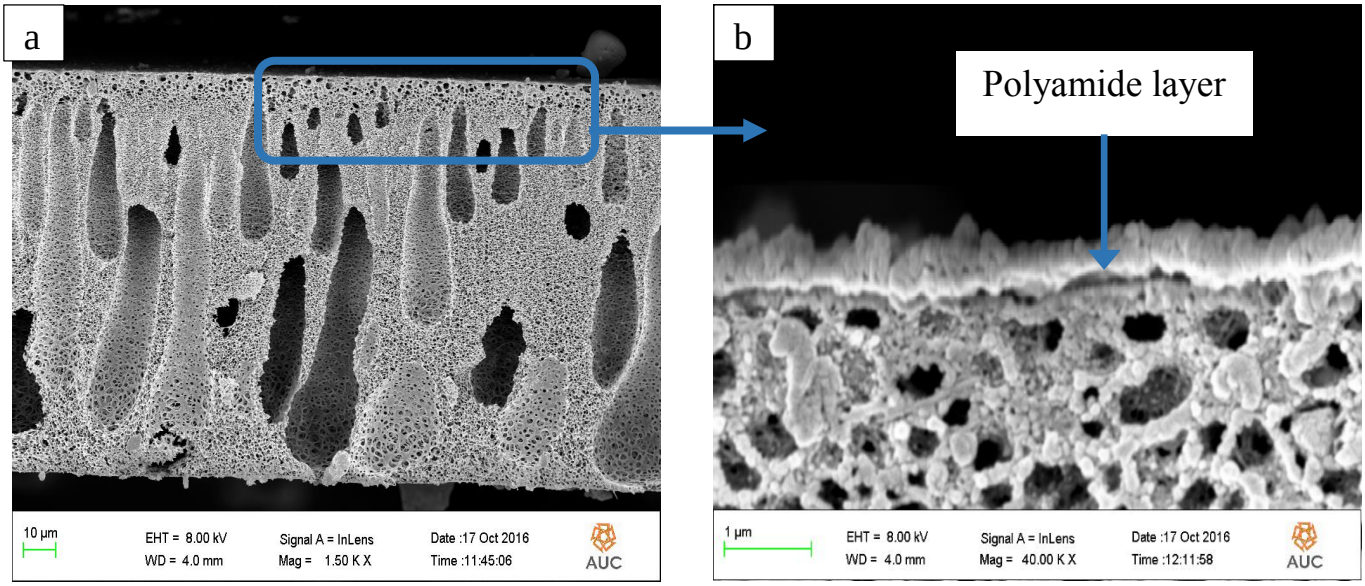

Figure 5.16: SEM cross-section of TFC37 rejection layer for (a) Total cross-section at 150 KX and (b) Near top cross-section at 40.00 KX

5.2.4 FTIR spectra of TFC membrane and support membrane

FTIR spectroscopy measurements were carried out to validate the formation of PA rejection layer. Figure 5.17 presents the FTIR spectra of the support membrane and the TFC membrane. The spectra reflect the difference in chemical structures of the two layers. For the support membrane, the FTIR spectrum exhibits a broad peak at 3447 cm^{-1} representing the O-H hydrogen bonding stretching, and the weak peak at 2967 cm^{-1} representing the aromatic C-H bond stretching, while 1634 cm^{-1} represented the aromatic C-H bending vibration [117]. These peaks were also present in the TFC membrane. However, the support membrane was characterized by S=O stretching vibrations at 1250, 1149 cm^{-1}. On the other hand, TFC membrane showed additional N-H stretching vibrations at 3378 cm^{-1} and 3066 cm^{-1}, which were also present in the pure PA FTIR spectrum shown in Figure 5.18. In addition, C=O of amide bond was represented by the strong peak at 1585 cm^{-1} while N-H bending vibration was present at 1503 cm^{-1}, C-N stretching vibration was present at 1294 cm^{-1} [118]. Similar peaks were also present in the pure PA spectrum that confirmed the successful formation of PA rejection layer.

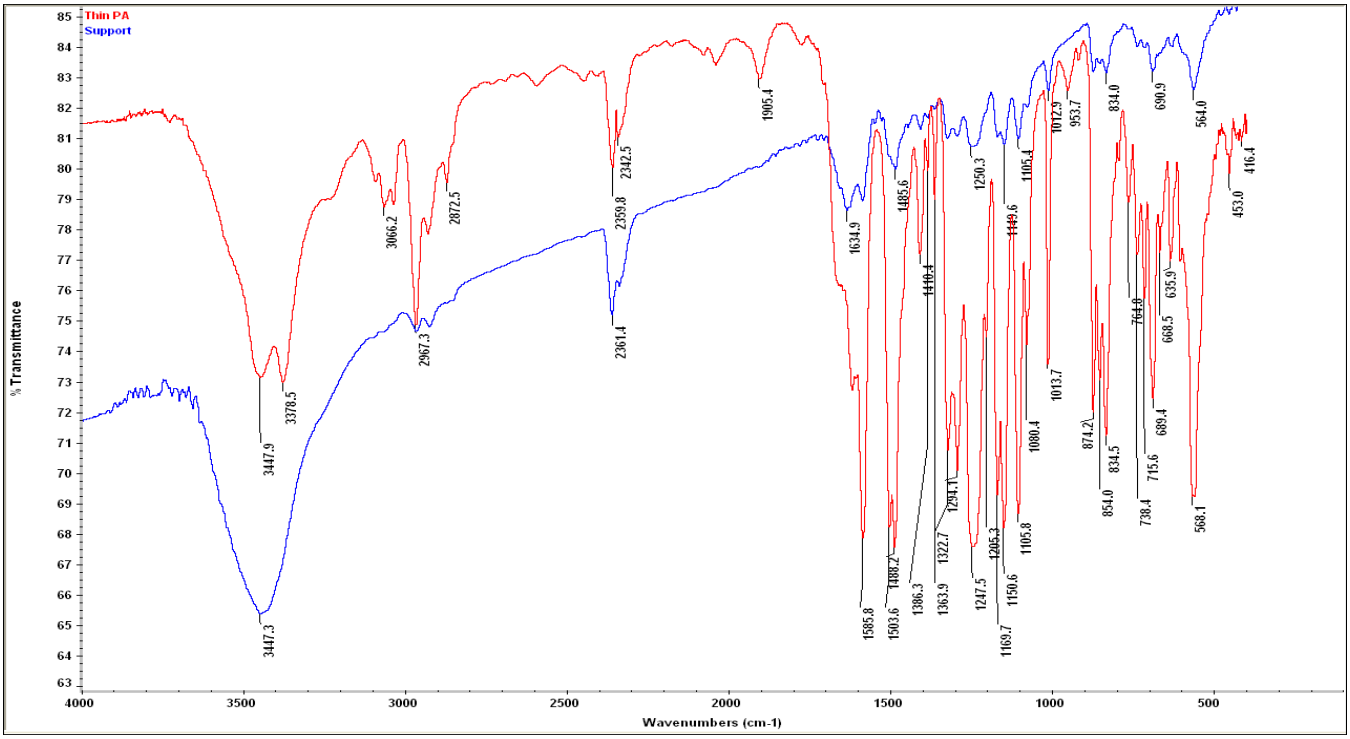

Figure 5.17: Combined FTIR spectrums of thin PA membrane (red) vs. support membrane (blue)

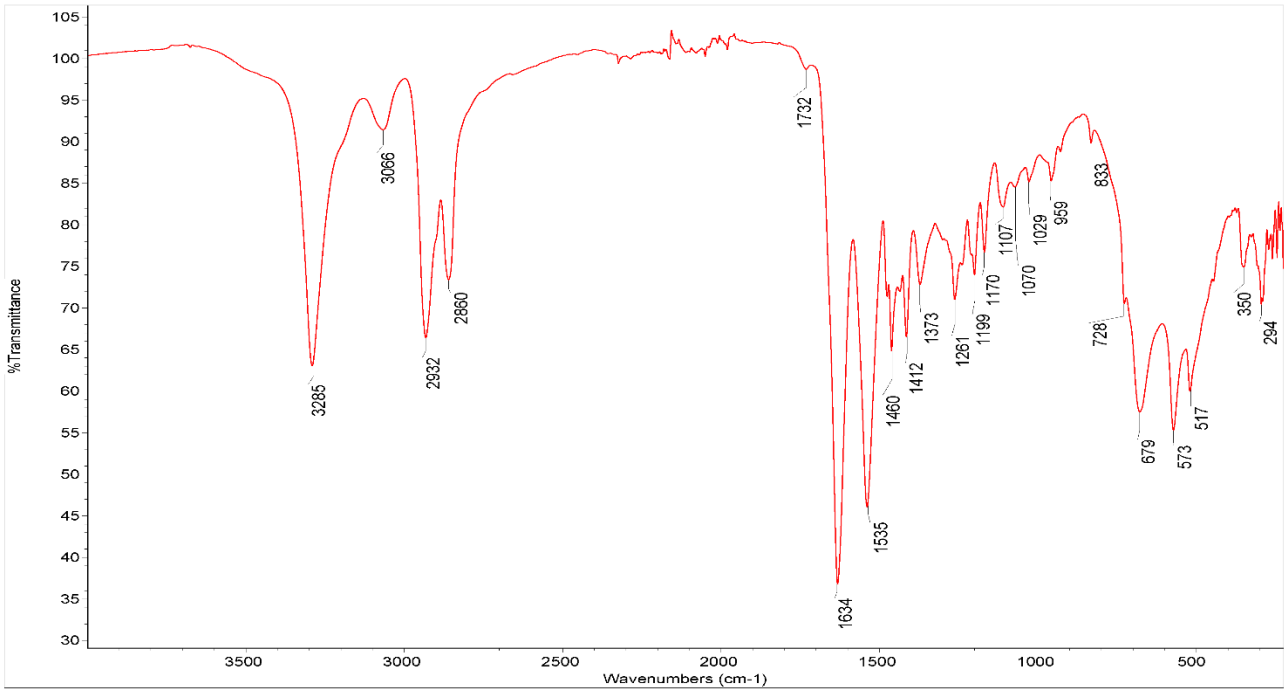

Figure 5.18: FTIR spectrum of pure Polyamide [119]

5.3. TFNC membranes

This section presents and discusses the TFNC membrane incorporating functionalized MWCNTs. The results of the performance and morphology of TFNC membranes are presented and discussed, together with the effect of functionalized MWCNTs on the membrane hydrophilicity and surface roughness. FTIR evidence of the successful functionalization of the MWCNTs is included in Appendix IV.

5.3.1 TFNC performance

The performance of various TFNC membranes was determined after incorporation of different F-MWCNTs amounts within the polyamide rejection layer of the thin film composite membrane TFC37. A summary Table 5.13 shows the FO water flux, water permeability, reverse solute flux and salt rejection of TFC, TFNC 0.01%, TFNC 0.05%, TFNC 0.1% and TFNC 0.2% with their different F-MWCNTs concentrations.

Table 5.13: FO water flux, water permeability, reverse solute flux and salt rejection of TFC and TFNC membranes using S6 sample for the support layer and the preparation conditions for the TFC37 for the rejection layer

Membrane	F-MWCNT (wt/vol %)	FO water flux (L/m^2h)	Water permeability ($L/m^2h.bar$)	Reverse solute flux (g/m^2h)	Salt rejection (%)
TFC37	0	43.70±0.51	0.67±0.08	3.51±0.23	88.30±0.11
TFNC 0.01%	0.01	50.23±0.93	2.54±0.59	2.76±0.21	90.05±0.25
TFNC 0.05%	0.05	55.92±2.45	3.75±0.69	3.74±0.51	89.01±0.36
TFNC 0.1%	0.1	64.63±2.51	5.77±0.59	6.15±0.34	73.64±3.55
TFNC 0.2%	0.2	73.15±2.66	6.04±0.56	8.21±0.65	63.88±1.76

Figure 5.19 shows the effect of increasing F-MWCNTs on FO water flux, reverse solute flux and salt rejection. It was found that increasing the concentration of F-MWCNTs in the aqueous solution of MPD resulted in a high increase in both FO water flux. FO water flux increased from 43.7±0.51 L/m^{2}h for TFC37 to 73.15±2.66 L/m^{2}h for TFNC 0.2%. On the other hand, the reverse solute flux slightly decreased to 2.76±0.21 g/m^{2}h for TFNC 0.01%, and then it increased consistently with further addition of F-MWCNTs to reach 8.21±0.65 g/m^{2}h for TFNC 0.2% while salt rejection slightly increased to 90.05±0.25% and 89.01±0.36% for TFNC 0.01% and TFNC 0.05%, respectively, and then it decreased with further addition of F-MWCNTs to reach 63.88±1.76% for TFNC 0.2%.

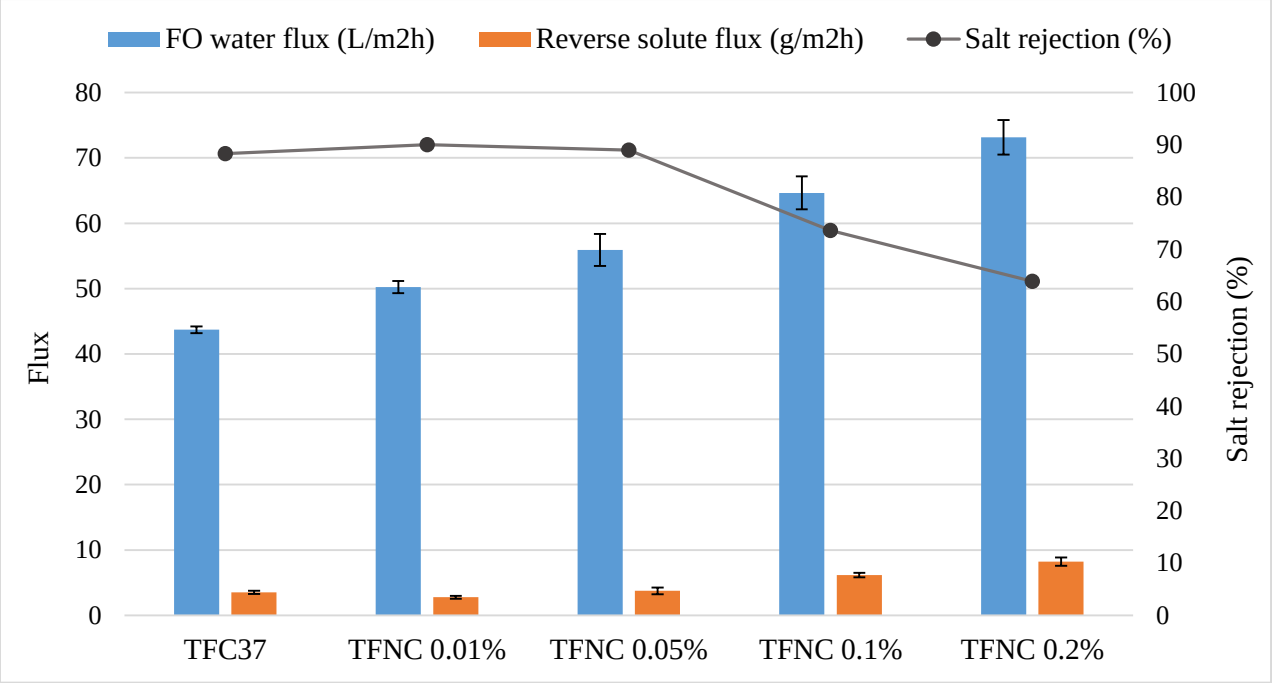

Figure 5.19: Combined chart of FO water flux, Reverse solute flux and Salt rejection of different TFNC membranes and TFC37 membrane

5.3.2 Contact angle measurements

The contact angle is a good indicator to determine the membrane hydrophilicity, which could be responsible for the changes of the FO water flux values. Contact angle measurements were carried out to the support (S6), TFC37, TFNC 0.01%, TFNC 0.05%, TFNC 0.1% and TFNC 0.2% membranes. Figure 5.20 shows water contact angle measurements images for the different

membranes while Figure 5.21 shows the correlation between the contact angle and FO water with increasing the concentration of F-MWCNTs.

It was found that increasing F-MWCNTs concentration decreased the contact angle consistently from 62.15±0.43° for TFC37 to 41.85±0.17° for TFNC 0.2%, reflecting the increase in membrane hydrophilicity. Furthermore, FO water flux was increased due to the increased hydrophilicity that increased the attraction between the membrane surface and the water molecules that allowed easy flow of water molecules through the membrane surface [51][52][120].

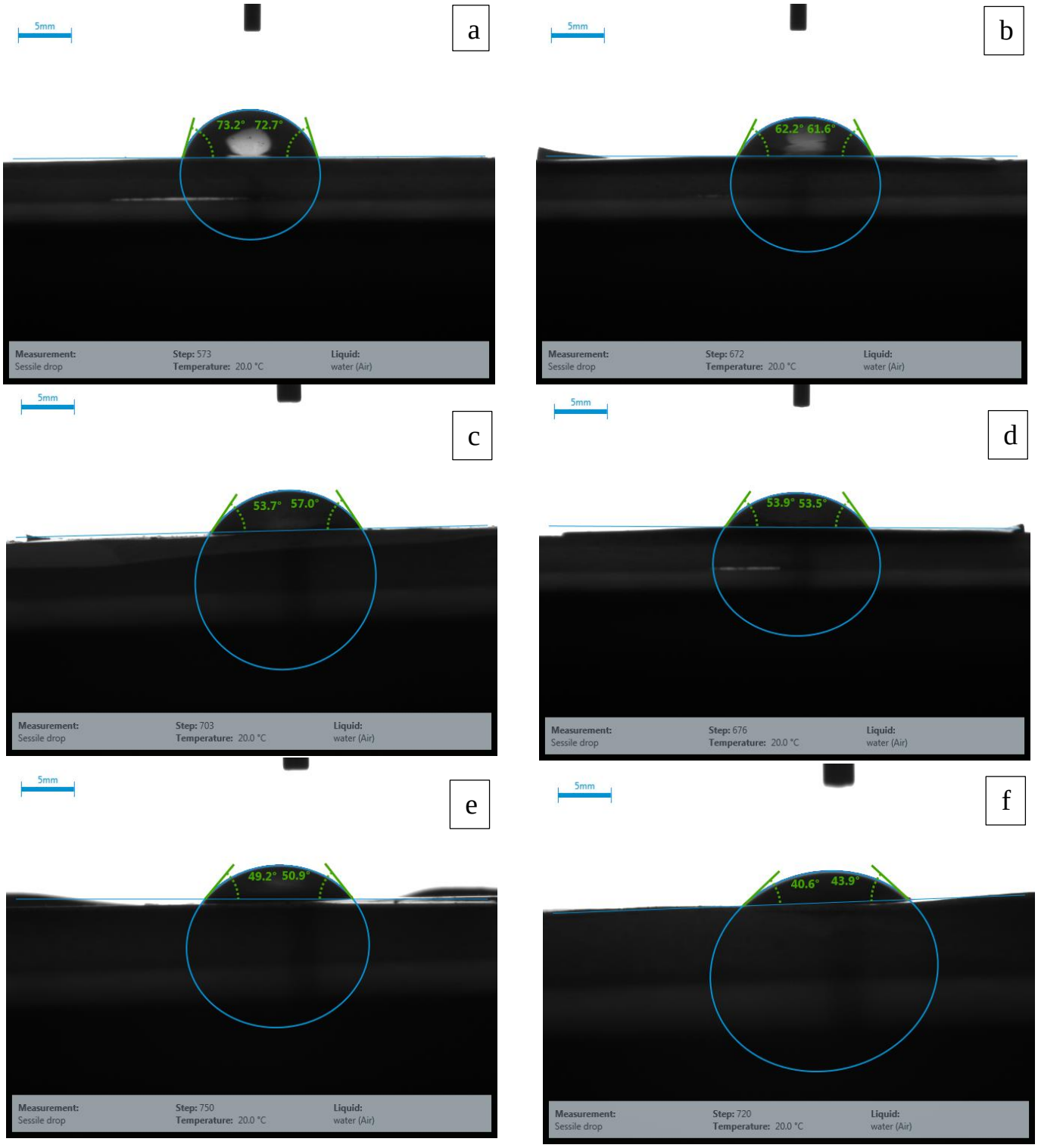

Figure 5.20: Water contact angle of (a) Support (S6), (b) TFC37, (c) TFNC 0.01%, (d) TFNC 0.05%, (e) TFNC 0.1% and (f) TFNC 0.2%

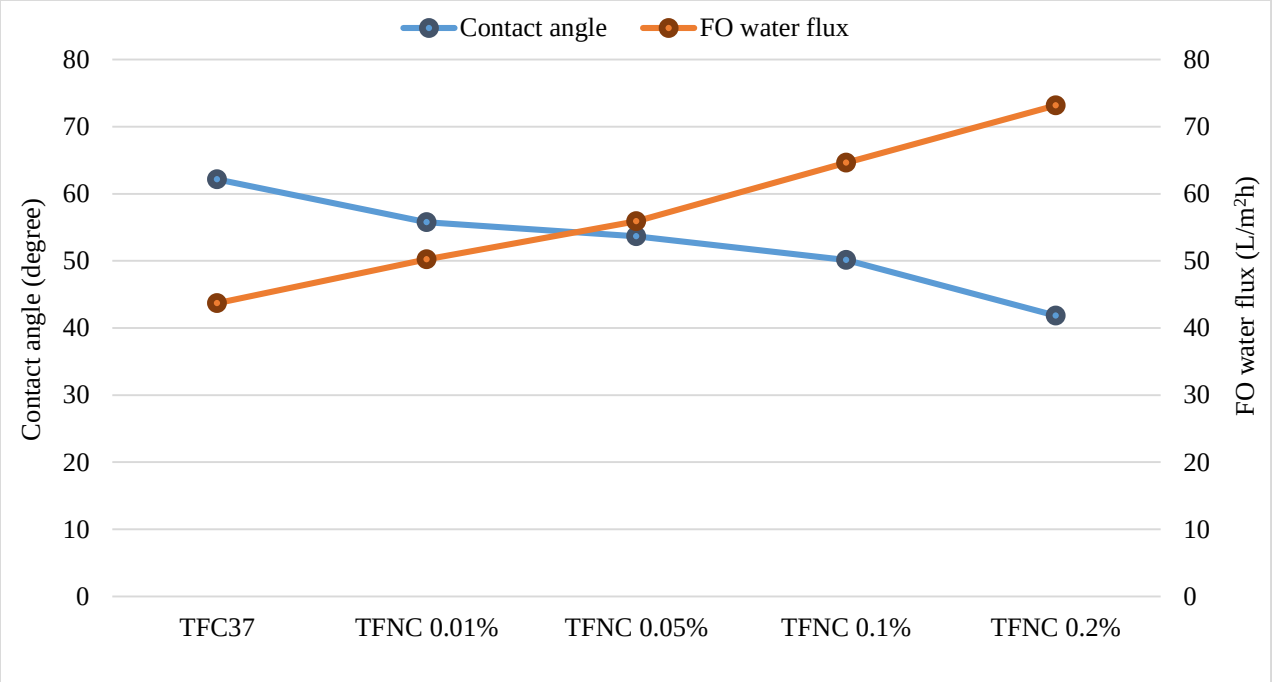

Figure 5.21: Contact angle and FO water flux correlation for TFC37, TFNC 0.01%, TFNC 0.05%, TFNC 0.1% and TFNC 0.2%

5.3.3 AFM (surface roughness)

AFM was used to investigate the effect of F-MWCNTs on the mean surface roughness (Ra) of the surfaces of the synthesized membranes. Table 5.14 presents the surface roughness (Ra) values for the different membranes. Figure 5.22 shows AFM 2D and 3D images of these membranes.

Table 5.14: Surface roughness Ra for the support, TFC and TFNC membranes

Membrane	F-MWCNTs (wt/vol%)	Surface roughness (Ra) (nm)
Support (S6)	0.00	7.47
TFC37	0.00	32.67
TFNC 0.01%	0.01	41.87
TFNC 0.05%	0.05	43.94
TFNC 0.1%	0.10	50.91
TFNC 0.2%	0.20	67.30

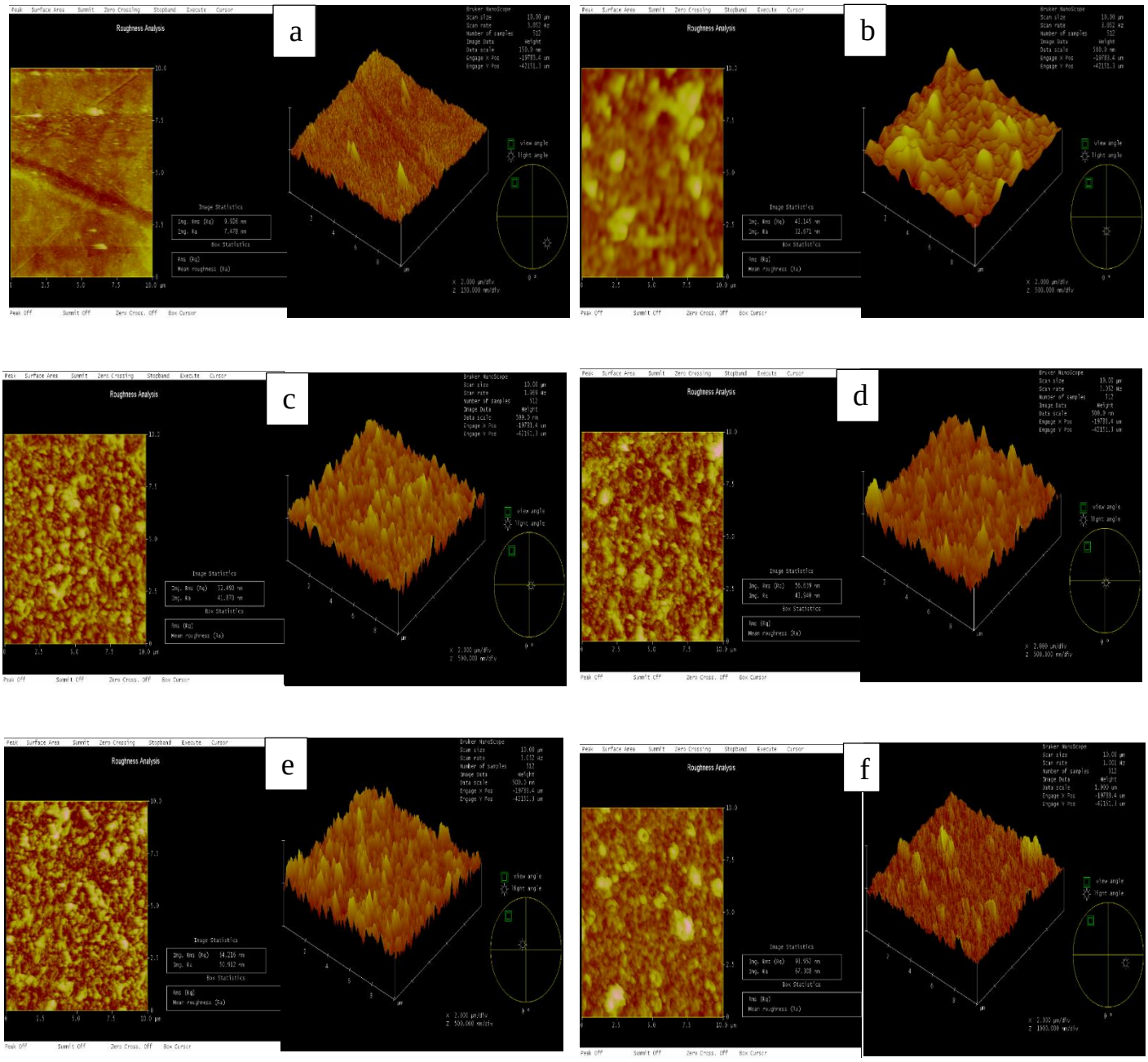

Figure 5.22: AFM images of (a) Support (S6), (b) TFC37, (c) TFNC 0.01%, (d) TFNC 0.05%, (e) TFNC 0.1% and (f) TFNC 0.2% where 2D images on left and 3D images on right

Most importantly, the surface roughness (Ra) increased gradually with increasing the F-MWCNTs concentration in the rejection layer reaching 67.3 nm for TFNC 0.2%. The support membrane Ra value was only 7.47 nm while the TFC37 Ra value was 32.67 nm. In addition, TFNC 0.01% and TFNC 0.05 had Ra values of 41.87 and 43.94 nm respectively.

These results confirm the ridge-valley structure of PA which increased with the incorporation of F-MWCNTs. This was associated with a noticeable increase in the FO water flux, probably due to formation of additional nano-channels within the PA rejection layer [55]. Further increasing F-MWCNTs concentration above 0.05 wt/vol% resulted in a decrease in the salt rejection. This might be attributed to agglomeration of F-MWCNTs at high concentration that might interrupt the IP reaction by slowing down the diffusion of amine groups of MPD toward the acetyl groups of TMC, resulting in a lower cross-linked units of PA. Similar results were reported by Maryam Amini and et al, 2013 using amine functionalized MWCNTs in the rejection layer [55], Ning Ma and et al, 2013 using zeolite in the support layer [51], Emadzadeh and et al, 2014 using TiO_2 in the support layer [52]. However, the FO water flux achieved by our study was higher. A correlation between surface roughness and FO water flux for the synthesized membranes is shown in Figure 5.23.

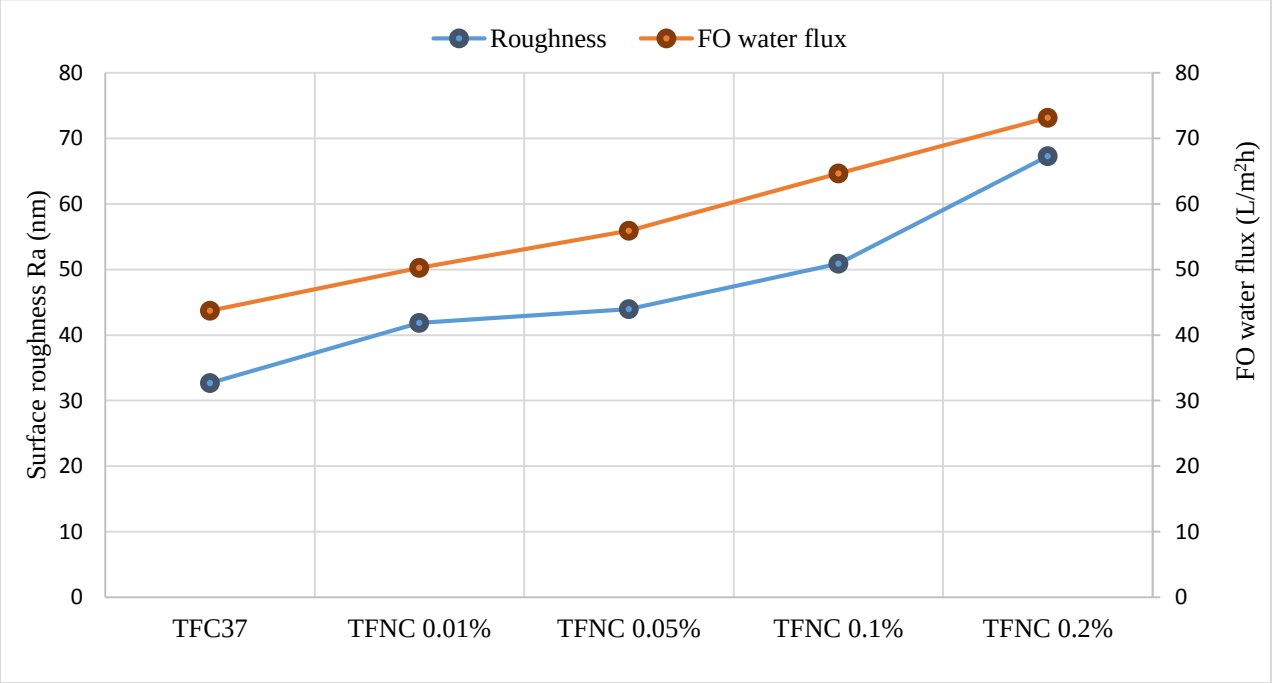

Figure 5.23: Surface roughness and FO water flux correlation for TFC37, TFNC 0.01%, TFNC 0.05%, TFNC 0.1% and TFNC 0.2%

5.3.4 BET analysis of TFNC membranes

In this series, the effect of F-MWCNTs on the porosity of the TFNC membranes was investigated. Table 5.15 summarizes the BET surface area and average pore width for the different TFNC membranes and TFC37 membrane. Figures 5.24 and 5.25 show the differential pore volume distribution vs. pore width of the different TFNC membranes while Figures 5.26 and 5.27 show the corresponding pore area distribution. From Table 5.15, the BET surface area generally increased with increasing F-MWCNT content. This is in agreement with the increase of the surface roughness of the samples. The variation of average pore width is less pronounced.

Table 5.15: TFC37 and TFNC membranes with their BET surface area and the average pore width

Membrane	F-MWCNT wt/vol%	BET surface area (m^2/g)	Average pore width (nm)
TFC37	0	18.07	8.43
TFNC 0.01%	0.01	20.62	7.58
TFNC 0.05%	0.05	21.88	8.01
TFNC 0.1%	0.1	20.10	8.45
TFNC 0.2%	0.2	21.69	8.41

The differential pore volume distribution plots of Figures 5.24 and 5.25, when considered together with the differential pore surface area plots of Figures 5.26 and 5.27, indicate that pores larger than 10 nm, exhibiting large differential volumes but small differential surface area, are limited in number. On the other hand, pores lower than 2 nm, exhibiting small differential volumes but large differential surface area, are significant in number.

The TFC37 blank sample exhibited the largest differential pore volumes for pores > 130 nm. However Figure 5.26 shows comparable differential pore surface areas for TFC37, TFNC 0.1% and TFNC 0.2%, denoting larger number of pores for samples TFNC 0.1% and TFNC 0.2%. For pores between 8 nm and 130 nm, sample TFNC 0.2% exhibited the largest differential pore volume with a corresponding largest differential surface area denoting a large number of these

pores. Sample TFNC 0.1% followed. These pore structures for TFNC 0.1% and TFNC 0.2% might be responsible for the higher values of FO water flux and reverse solute flux.

Comparing the three samples TFC37, TFNC 0.01% and TFNC 0.05%, which exhibited comparable salt rejection values, but increasing FO water flux, and reverse solute flux, it can be noted that their pore distribution patterns do not seem to indicate this trend in FO water flux and reverse solute flux. For pores > 8 nm, differential pore volumes and differential pore surface areas indicate that sample TFC37 has the largest number of pores. This is also the case for pores < 8 nm in spite of the well-developed pore structures for sample TFNC 0.01% at pore width values of 3 nm and 5 nm. This would be expected to lead to lower FO water flux and reverse solute flux. However, the opposite is found. This seems to indicate that the different values of FO water flux and reverse solute flux are not primarily dependent on pore structures for these samples. The incorporation of F-MWCNTs in the TFC layer seems to facilitate water transport.

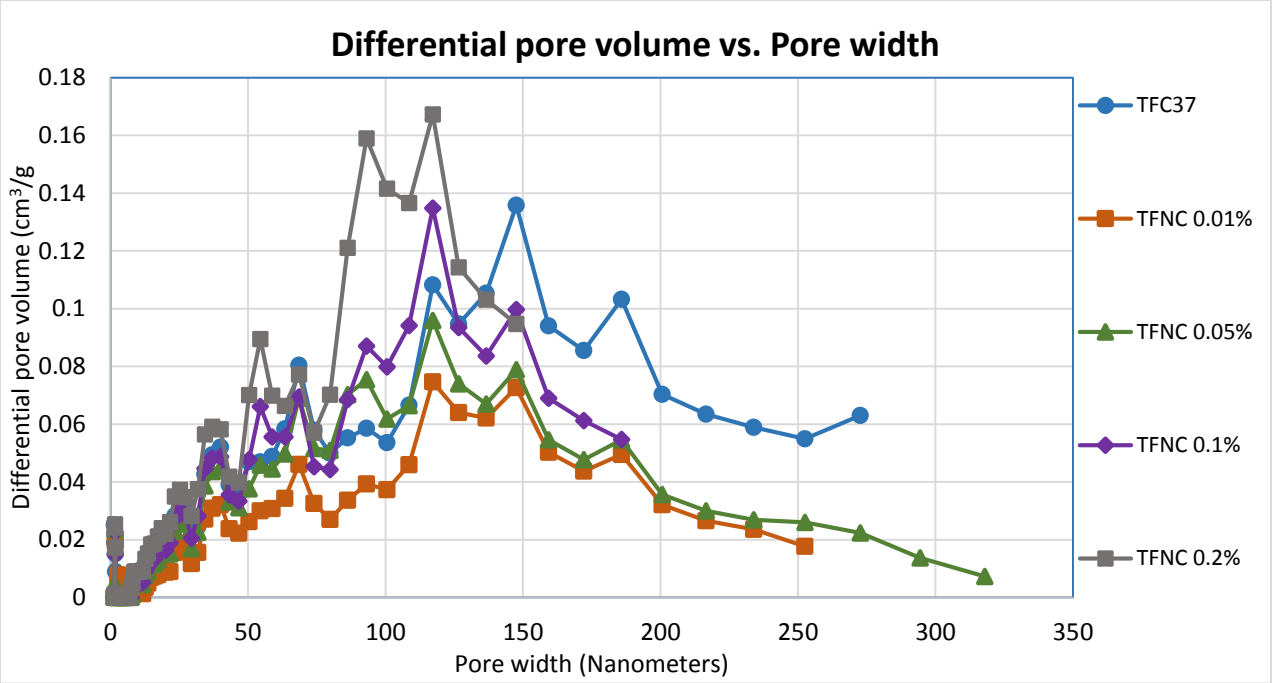

Figure 5.24: Plot of differential pore volume vs. pore width for TFC37 and TFNC membranes, range 0 – 325 nm

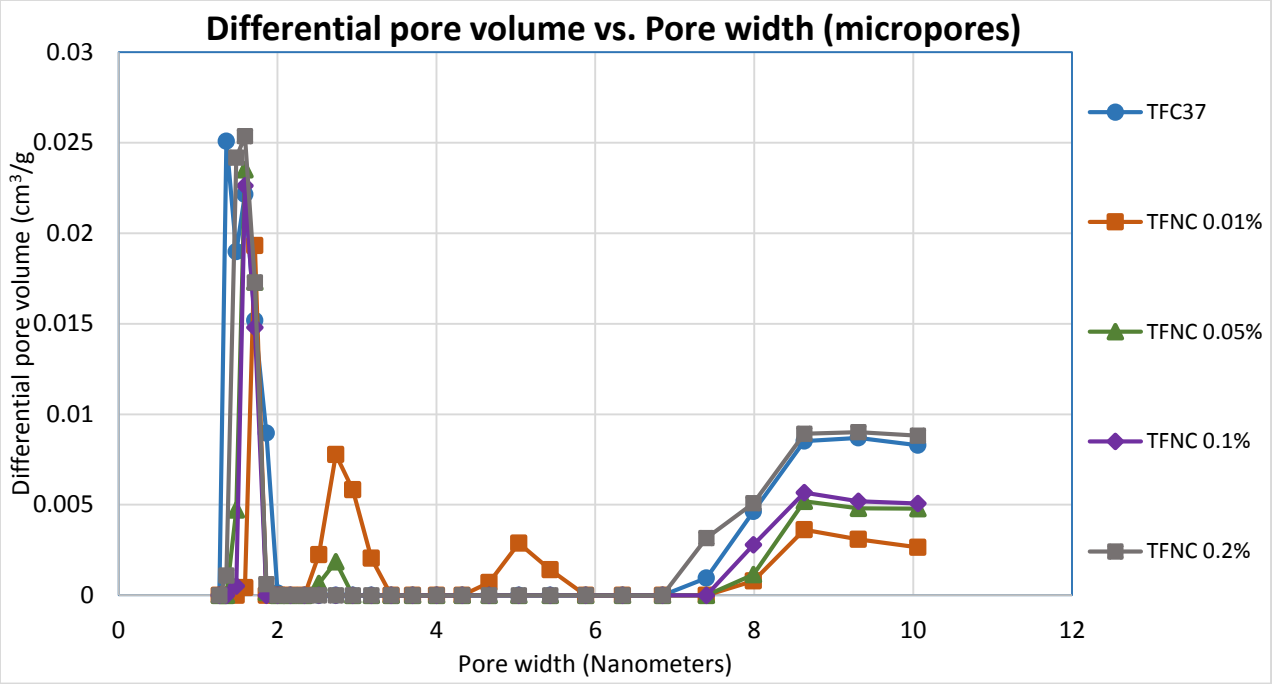

Figure 5.25: Plot of differential pore volume vs. pore width for TFC37and TFNC membranes, range 0 – 10 nm

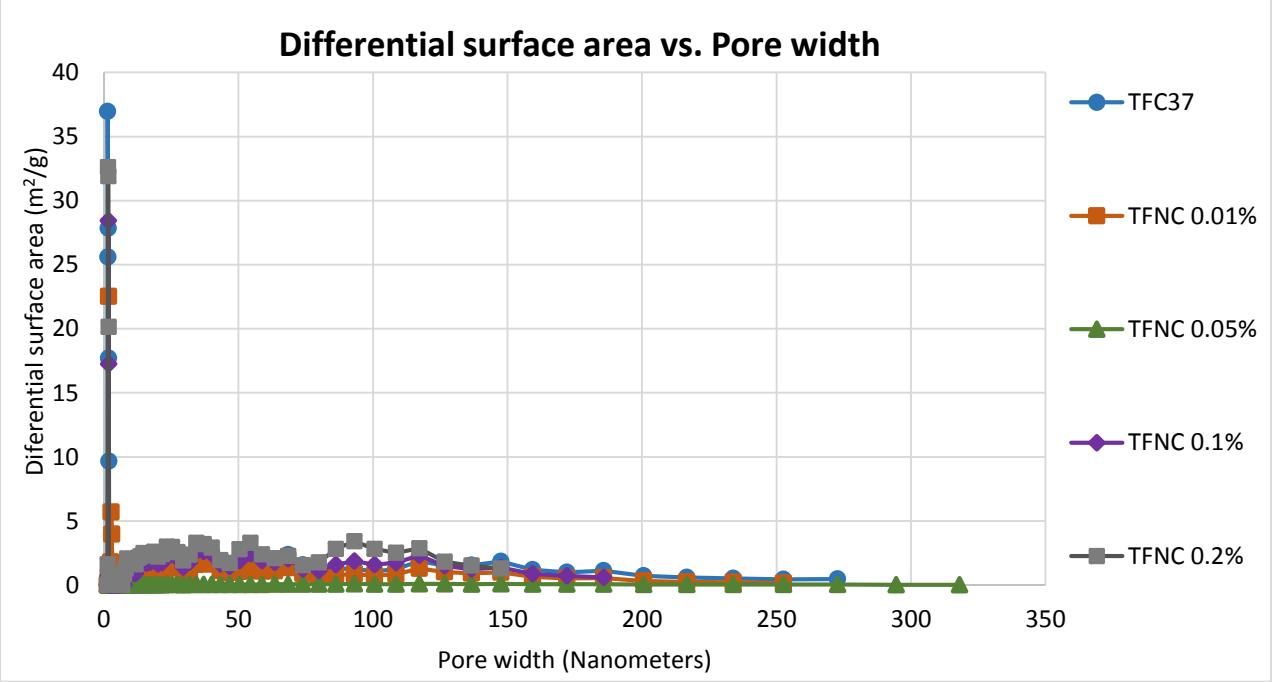

Figure 5.26: Plot of differential surface area vs. pore width for TFC37 and TFNC membranes, range 0 – 325 nm

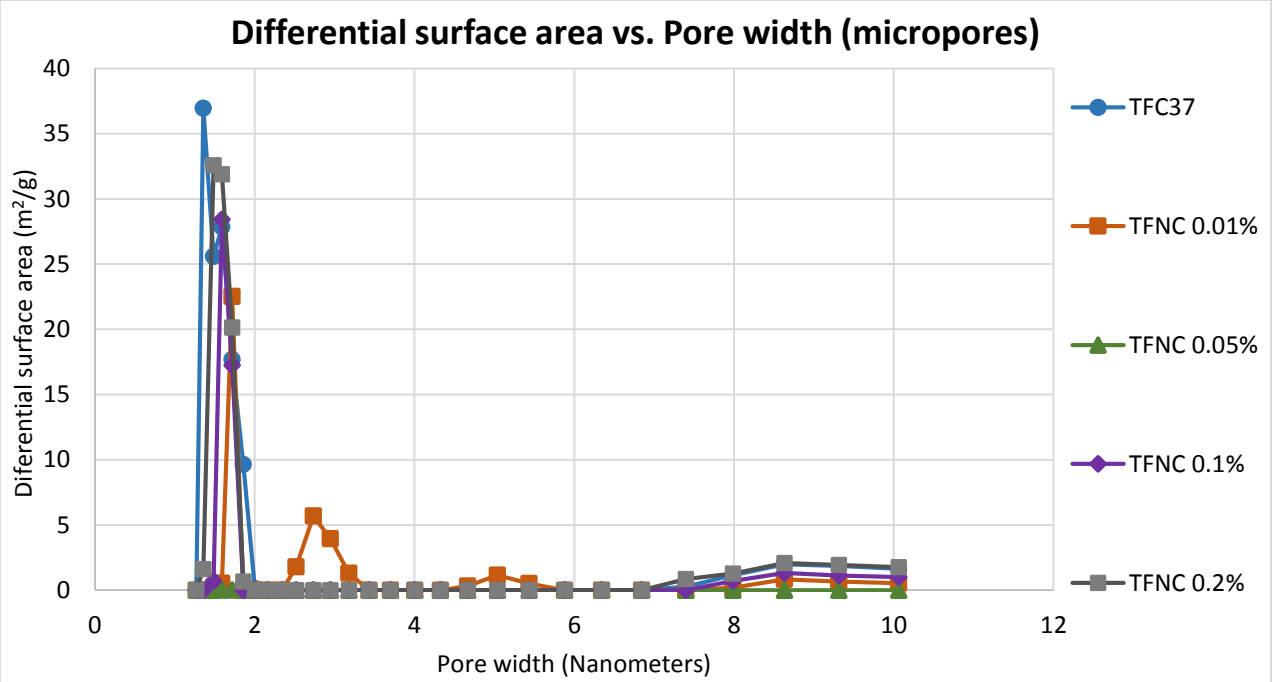

Figure 5.27: Plot of differential surface area vs. pore width for TFC37 and TFNC membranes, range 0 – 10 nm

It is important to note that the direct contribution of the incorporated F-MWCNTs in the TFC layer to the BET results is expected to be limited because of the significantly small amounts of the F-MWCNTs in the composite membrane samples, the F-MWCNTs being only present in the thin TFC layer which represents a very limited fraction of the overall composition of membranes being analyzed. However, the differences observed in the BET results between different samples could be due to the effect of the incorporated F-MWCNTs on the development of the porosity of the TFC membranes during IP.

5.3.5 TFNC morphology

SEM top surface images of TFNC membranes are included in Figure 5.28 with low and high magnifications. The presence of the F-MWCNTs within the PA rejection layer can be observed, especially for the case of TFNC 0.01% membrane. At higher concentration of F-MWCNTs (above 0.05 wt/vol %), the indication of the presence of F-MWCNTs was less pronounced, probably due to agglomeration of some F-MWCNTs that are presented by red circles in Figure 5.28. In order to observe the nano-channels in the TFNC 0.01% membrane, the surface was magnified to 147.23 KX in Figure 5.29. The nano-channels are indicated by red arrows and their

corresponding surface width ranged from 8.01 to 8.38 nm. In addition, the cross-section images of the top performing TFNC 0.01% were shown in Figure 5.30.

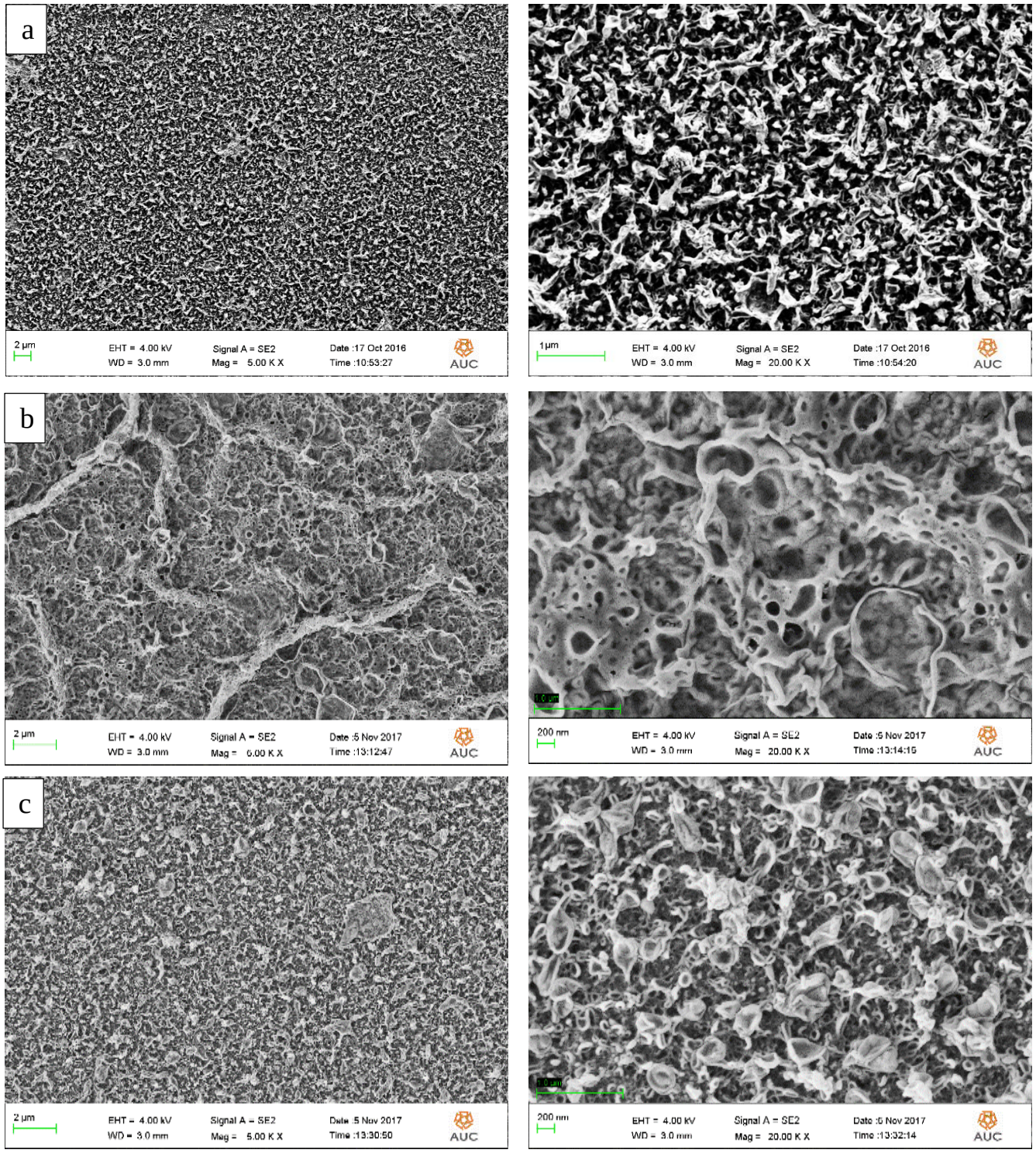

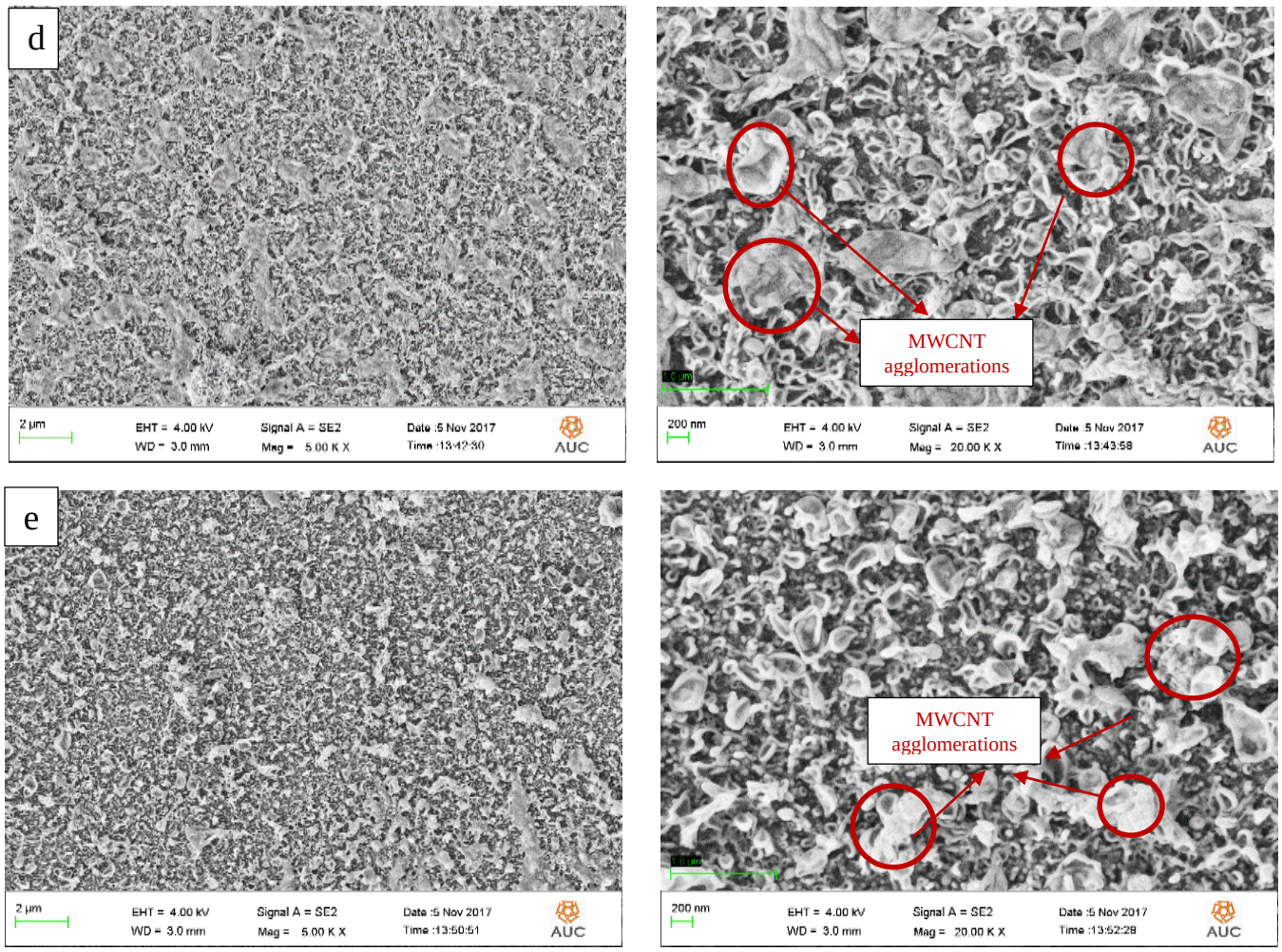

Figure 5.28: SEM top surface of (a) TFC37, (b) TFNC 0.01%, (c) TFNC 0.05%, (d) TFNC 0.1% and (e) TFNC 0.2% at 5.00 KX magnification on left and 20.00 KX magnification on right

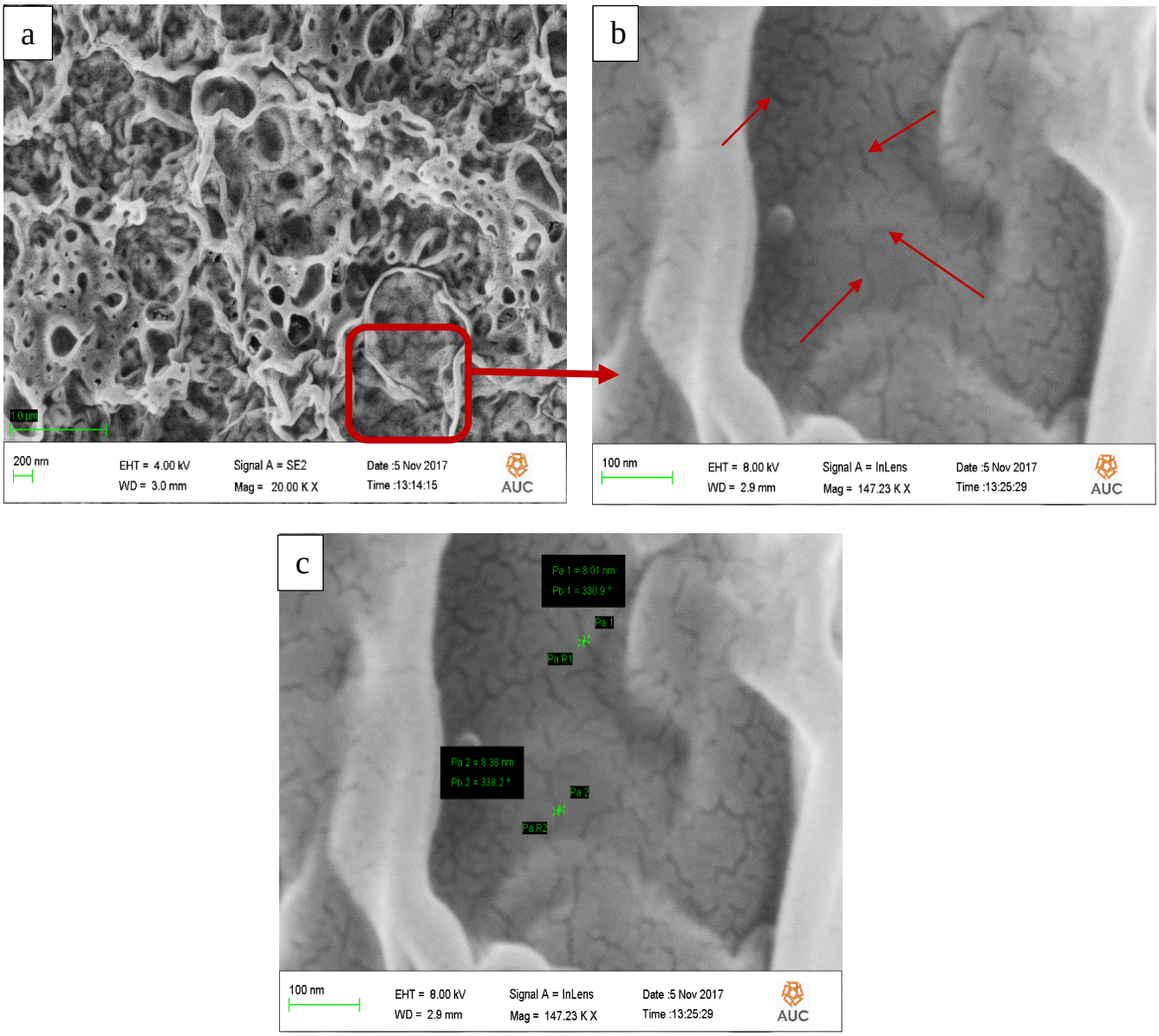

Figure 5.29: SEM top surface of TFNC 0.01% (a) at 20.00 KX, (b) at 147.23 KX and (c) at 147.23 KX with nano-channels surface width

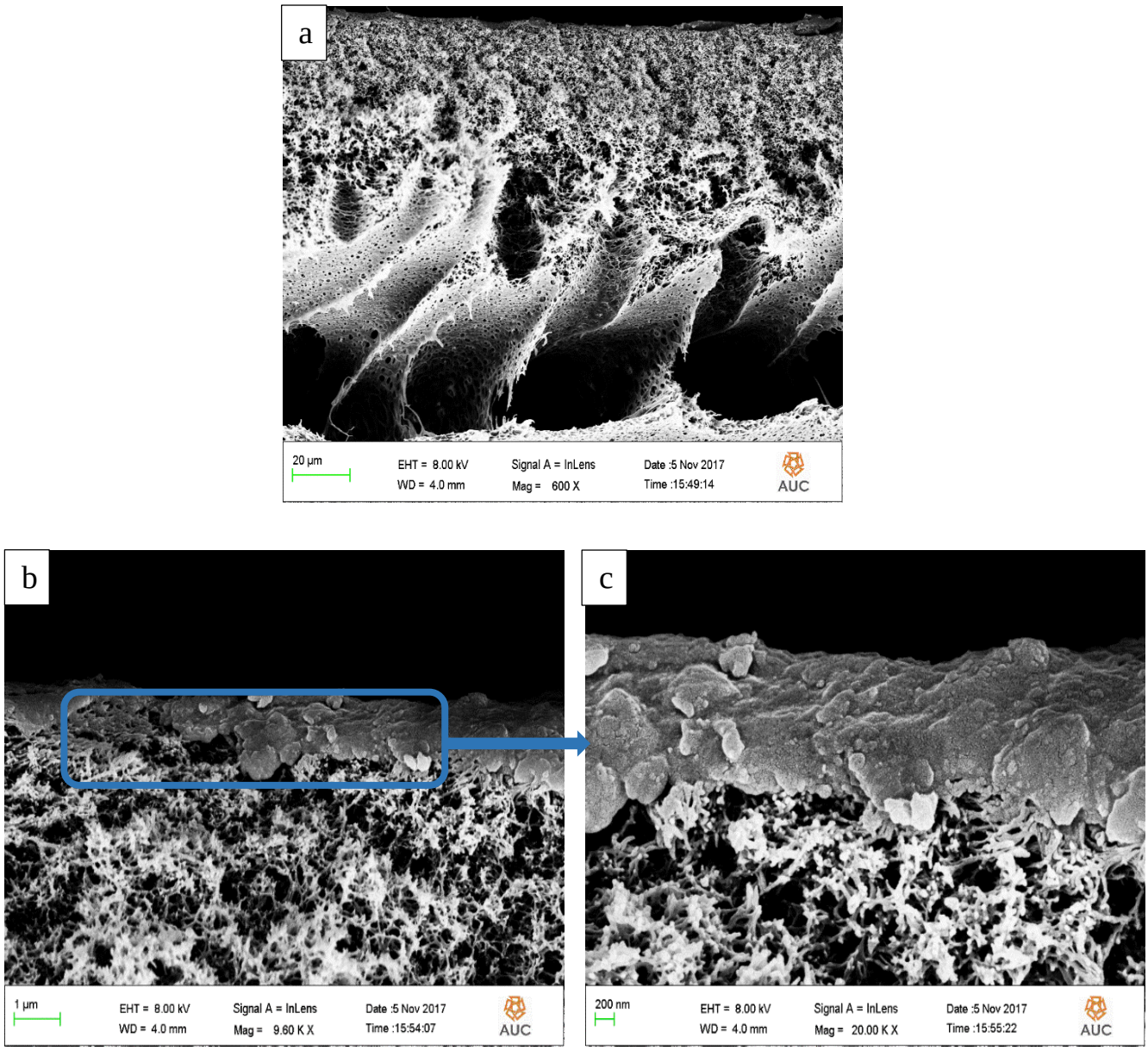

Figure 5.30: Cross-section SEM images of TFNC 0.01% (a) total cross-section at 600 X, (b) near top cross-section at 9.60 KX and (c) near top cross-section at 20.00 KX

5.3.6 TFNC membranes summary

The F-MWCNTs were incorporated in the best performing TFC in order to investigate their effect on the membrane performance and structure. It was found that FO water flux and water permeability were sharply increased with increasing the concentration of F-MWCNTs in the rejection PA layer. The highest FO water flux was attained by TFNC 0.2% with 73.15±2.66 L/m^2h. This increase is believed to be due to the increased hydrophilicity that facilitates the passage of water molecules through the membranes. The increased hydrophilicity was demonstrated by the lower water contact angle values after incorporation of F-MWCNTS due to the strong attraction between water molecules and the hydrophilic surface of the membrane.

In addition, the increase of surface roughness with increasing the concentration of F-MWCNTs supported the improved hydrophilicity of the TFNC membranes since higher surface roughness led to larger surface area due to the presence of higher number of different surface features (peaks and valleys), and this might be the reason for the improved FO water flux [55][121].

BET results indicate that the correlation between pore structures and FO water flux and reverse solute flux for TFNC membranes is complex. The results indicate that samples TFNC 0.2% and TFNC 0.1%, having a large number of pores between 8 nm and 130 nm, exhibit the largest and second largest values for FO water flux and reverse solute flux respectively. This is understandably correlated with the smallest values for salt rejection. On the other hand, the BET results indicate that samples TFNC 0.01% and TFNC 0.05% have more limited porosities, not only relative to samples TFNC 0.2% and TFNC 0.1%, but also relative to the blank sample TFC37. The lower FO water flux and reverse solute flux of the former samples relative to the latter are understandable. However, their higher FO water flux and reverse solute flux relative to the blank TFC37 seems to indicate that these values are not primarily dependent on pore structures for these samples. The incorporation of F-MWCNTs in the TFC layer seems to facilitate water transport.

Another reason for enhancing the FO water flux and water permeability could be due to the observed nano-channels on the membrane top surface. Furthermore, the internal nano-channels in the core of the nano-tubes and the external nano-channels in the interface between the PA layer and the F-MWCNTs can interact to create additional channels that also enhanced the FO water flux [55][121].

The decline in salt rejection with increasing F-MWCNTs concentration above 0.05 wt/vol% could be attributed to the accumulation of the F-MWCNTs during the interfacial polymerization process that decreased the polymerization efficiency by blocking the active sites in the reaction zone and slowing down the diffusion of MPD amine groups toward the acyl groups of TMC that resulted in defected PA rejection layer with lower salt rejection that dropped to 63.88±1.76% for TFNC 0.2% [55].

Furthermore, the reverse solute flux decreased with the incorporation of 0.01 wt/vol % F-MWCNTs. it then increased with further increasing of F-MWCNTs. The lowest reverse solute flux was also attained by TFNC 0.01% with 2.76±0.21 g/m^2h, and this was expected because of the more limited porosity of this sample.

Therefore, it can be concluded that an efficient TFNC FO membrane can be synthesized with extremely high FO water flux compared to the literature, satisfactory salt rejection and very low reverse solute flux using F-MWCNTs from 0.01 to 0.05 wt/vol % in the top surface of the rejection PA layer.

Table 5.16 shows a comparison between the best performing TFNC 0.01% membrane and the membranes mentioned in the literature using FO mode.

Table 5.16: Comparison between the best performing TFNC 0.01% membrane and the membranes in the literature using FO mode

Membrane type	**Nano-filler incorporation**	**Loading amount for best performance**	**FO water flux (L/m^2h)**	**NaCl Salt rejection (%)**	**Reverse solute flux (g/m^2h)**	**Reference**
TFNC	Carboxyl MWCNTs	0.01 wt/vol % in the rejection layer	50.23±0.93	90.05±0.25	2.76±0.21	This work
TFNC	Carboxyl MWCNTs	2 wt% in the support layer	12	90	2.2±0.9	[54]
TFNC	Amine MWCNTs	0.05 wt/vol % in the rejection layer	30	89.30	2.86±0.40	[55]
TFNC	Amine MWCNTs	0.01 wt/vol % in the rejection layer	40	88	3.62±0.8	[55]
TFNC	TiO2	0.5 wt% in the support layer	29.70	92.70	7.30	[52]
TFNC	Zeolite	0.4 wt/vol% in the rejection layer	15	90.50	9.17	[50]
TFNC	Zeolite	0.5 wt% in the support layer	39	90	28	[51]
TFC PSF/PA	NA	NA	12	93.40	4.90	[66]
CTA flat sheet	NA	NA	9	81.90	5.30	[66]

6. Conclusion

Thin film Nano-composite membranes (TFNC) were synthesized by the incorporation of carboxyl Functionalized Multi-walled Carbon Nanotubes (F-MWCNTs) in a polyamide (PA) rejection layer on top of a polysulfone (PSF)/ polyvinylpyrrolidone (PVP) support layer in order to be used in Forward Osmosis (FO) water desalination.

The support layer was optimized by varying the concentration of both PSF and PVP in the casting solution, and the effects of PSF and PVP were determined by carrying out statistical analysis to the different support membranes by measuring FO water flux, water permeability and reverse solute flux. In addition the porosity of the support membranes were determined by BET analysis.

From the support layer analysis, the following conclusions can be drawn.

1. PVP has a positive effect on the membrane porosity
2. PSF has a suppressing effect on the membrane porosity
3. The support layer of 18 wt% PSF and 2 wt% PVP is considered an optimal support layer for FO TFNC membrane due to its high FO water flux with the minimum reverse solute flux.

Moreover, The rejection layer was optimized by varying the monomers concentrations (MPD, TMC), contact time and curing temperature, and the effects of the latter factors were determined by carrying statistical analysis to the different thin film composite membranes by measuring FO water flux, water permeability, reverse solute flux and salt rejection.

From the rejection layer analysis, the following conclusions can be considered

1. Simultaneous increase of monomers concentration (MPD, TMC) enhances the membrane salt rejection and decreases the FO water flux.
2. Increasing both contact time and curing temperature leads to highly cross-linked rejection layer that improves the membrane salt rejection at the expense of FO water flux.
3. The reverse solute flux can be minimized with increasing monomers concentration, contact time and curing temperature.

Furthermore, the incorporation of carboxyl F-MWCNTs in the rejection layer is effective in improving the FO water flux. F-MWCNTs seem to facilitate the possible creation of additional

nano-channels for water molecules that leads to an increase in FO water flux. In addition, introducing F-MWCNTs in the rejection layer enhances the membrane hydrophilicity by decreasing the water contact angle of the membrane and increasing the surface roughness, all with positive effects on improving FO water flux. On the other hand, the membranes salt rejection are not negatively impacted with the introduction of small amounts of F-MWCNTS. Higher concentrations of F-MWCNTs (> 0.05 wt/vol) do however lead to an observed decrease in salt rejection because of the possible agglomeration of F-MWCNTs that might interrupt interfacial polymerization, thus reducing polymer crosslinking in the rejection layer, with the result of a significant increase in porosity, which in turn negatively impacts salt rejection.

7. Future work

Finally, several experiments could be carried out in the future to enrich our knowledge about forward osmosis thin film nano-composite membranes:

- Studying the effect of different pore forming agents on the support membrane porosity.
- Studying the effect of different draw solutions on the forward osmosis membrane performance.
- Investigating higher levels of monomers concentrations and curing temperatures.
- Investigating the effect of different nano-fillers on the membrane performance.
- Comparing between the effect of nano-fillers on the support layer and the rejection layer.
- Investigating the effect of nano-fillers on membrane fouling.

8. References

[1] V. I. Grover, "Water : Global Common and Global Problems," Science Publishers, 2006, pp. 16–235.

[2] J. M. C. Puguan, H. S. Kim, K. J. Lee, and H. Kim, "Low internal concentration polarization in forward osmosis membranes with hydrophilic crosslinked PVA nanofibers as porous support layer," *Desalination*, vol. 336, no. 1, pp. 24–31, 2014.

[3] J. Kucera, "Desalination : Water from Water," 1st ed., John Wiley & Sons Incorporated, 2014, pp. 35–166.

[4] A. E. D. Abdin and T. Gaafar, "Rational water use in Egypt.pdf," *Technol. Perspect. Ration. use water Resour. mediterrnanean Reg.*, vol. 27, pp. 11–27, 2009.

[5] R. Osman, E. Ferrari, and S. McDonald, "Water Scarcity and Irrigation Efficiency in Egypt," *Water Econ. Policy*, vol. 2, no. 4, p. 1650009, 2016.

[6] W. A. Gad, "Water Scarcity in Egypt : Causes and Consequences," vol. 8, pp. 40–47, 2017.

[7] A. Alkaisi, R. Mossad, and A. Sharifian-Barforoush, "A Review of the Water Desalination Systems Integrated with Renewable Energy," *Energy Procedia*, vol. 110, no. December 2016, pp. 268–274, 2017.

[8] A. Subramani and J. G. Jacangelo, "Emerging desalination technologies for water treatment: A critical review," *Water Res.*, vol. 75, pp. 164–187, 2015.

[9] A. D. Khawaji, I. K. Kutubkhanah, and J. M. Wie, "Advances in seawater desalination technologies," *Desalination*, vol. 221, no. 1–3, pp. 47–69, 2008.

[10] H. T. El-Dessouky and H.M. Ettouney, "Multi-Stage Flash Desalination," in *Fundamentals of salt water desalination*, 1st ed., Amsterdam: Elsevier B.V., 2002, pp. 271–406.

[11] M. Al-Sahali and H. Ettouney, "Developments in thermal desalination processes: Design, energy, and costing aspects," *Desalination*, vol. 214, no. 1–3, pp. 227–240, 2007.

[12] R. Bahar, M. N. A. Hawlader, and L. S. Woei, "Performance evaluation of a mechanical

vapor compression desalination system," *Desalination*, vol. 166, pp. 123–127, 2004.

[13] N. H. Aly and A. K. El-Fiqi, "Mechanical vapor compression desalination systems - A case study," *Desalination*, vol. 158, no. 1–3, pp. 143–150, 2003.

[14] H. Strathmann, "Assessment of Electrodialysis Water Desalination Process Costs," *Proc. Int. Conf. Desalin. Costing, Lemassol, Cyprus, December 6-8, 2004*, pp. 32–54, 2004.

[15] M. Sadrzadeh and T. Mohammadi, "Sea water desalination using electrodialysis," *Desalination*, vol. 221, no. 1–3, pp. 440–447, 2008.

[16] H. J. Lee, F. Sarfert, H. Strathmann, and S. H. Moon, "Designing of an electrodialysis desalination plant," *Desalination*, vol. 142, no. 3, pp. 267–286, 2002.

[17] K. P. Lee, T. C. Arnot, and D. Mattia, "A review of reverse osmosis membrane materials for desalination-Development to date and future potential," *J. Memb. Sci.*, vol. 370, no. 1–2, pp. 1–22, 2011.

[18] C. Fritzmann, J. Löwenberg, T. Wintgens, and T. Melin, "State-of-the-art of reverse osmosis desalination," *Desalination*, vol. 216, no. 1–3, pp. 1–76, 2007.

[19] S. Jiang, Y. Li, and B. P. Ladewig, "A review of reverse osmosis membrane fouling and control strategies," *Sci. Total Environ.*, vol. 595, pp. 567–583, 2017.

[20] G. Kang and Y. Cao, "Development of antifouling reverse osmosis membranes for water treatment: A review," *Water Res.*, vol. 46, no. 3, pp. 584–600, 2012.

[21] T. S. Chung, L. Luo, C. F. Wan, Y. Cui, and G. Amy, "What is next for forward osmosis (FO) and pressure retarded osmosis (PRO)," *Sep. Purif. Technol.*, vol. 156, pp. 856–860, 2015.

[22] T. Y. Cath, A. E. Childress, and M. Elimelech, "Forward osmosis: Principles, applications, and recent developments," *J. Memb. Sci.*, vol. 281, no. 1–2, pp. 70–87, 2006.

[23] M. Qasim, N. A. Darwish, S. Sarp, and N. Hilal, "Water desalination by forward (direct) osmosis phenomenon: A comprehensive review," *Desalination*, vol. 374, pp. 47–69, 2015.

[24] S. E. Kwan, E. Bar-Zeev, and M. Elimelech, "Biofouling in forward osmosis and reverse osmosis: Measurements and mechanisms," *J. Memb. Sci.*, vol. 493, pp. 703–708, 2015.

[25] N. Akther, A. Sodiq, A. Giwa, S. Daer, H. A. Arafat, and S. W. Hasan, “Recent advancements in forward osmosis desalination: A review,” *Chem. Eng. J.*, vol. 281, pp. 502–522, 2015.

[26] N. Widjojo, T. S. Chung, M. Weber, C. Maletzko, and V. Warzelhan, “A sulfonated polyphenylenesulfone (sPPSU) as the supporting substrate in thin film composite (TFC) membranes with enhanced performance for forward osmosis (FO),” *Chem. Eng. J.*, vol. 220, pp. 15–23, 2013.

[27] SOLVAY, “Processing Guide for Polymer Membranes,” Bruxelles, Belgium, 2015, Retrieved 5 May, 2017 from https://www.solvay.com/en/markets-and-products/markets/specialty-polymers-for-membranes.html.

[28] S. Loeb and S. Srinivasa, “Sea Water Demineralization by Means of an Osmotic Membrane,” in *Saline Water Conversion*, 2nd ed., Washington: American Chemical Society, 1962, pp. 117–132.

[29] G. W. Batchelder, “Process for the demineralization of water,” *US. Pat.* p. 3171799, 1965.

[30] B.S. Frank, “Desalination of sea water,” *US. Pat.*3670897, 1972.

[31] S. M. B. and D. K. A. F. Votta, “Concentration of industrial waste by direct osmosis: completion report,” M.S. thesis, Rhode Island University, Providence, Rhode Island, 1974.

[32] D. K. Anderson, “Concentration of Dilute Industrial Wastes by Direct Osmosis,” M.S. thesis, Rhode Island University, Providence, Rhode Island, 1977.

[33] R.E.Kravath and J. A. Davis, “Desalination of sea water by direct osmosis,” *Desalination*, vol. 16, no. 2, pp. 151–155, 1975.

[34] Goosens and V. Haute, “The use of direct osmosis tests as complementary experiments to determine the water and salt permeabilities of reinforced cellulose acetate membranesitle,” *Desalination*, vol. 26, no. 3, pp. 299–308, 1978.

[35] J.-J. Qin, W. C. L. Lay, and K. A. Kekre, “Recent developments and future challenges of forward osmosis for desalination: a review,” *Desalin. Water Treat.*, vol. 39, no. 1–3, pp.

123–136, 2012.

[36] K. Y. Wang, T. S. Chung, and J. J. Qin, “Polybenzimidazole (PBI) nanofiltration hollow fiber membranes applied in forward osmosis process,” *J. Memb. Sci.*, vol. 300, no. 1–2, pp. 6–12, 2007.

[37] Q. Yang, K. Y. Wang, and T. S. Chung, “Dual-layer hollow fibers with enhanced flux as novel forward osmosis membranes for water production,” *Environ. Sci. Technol.*, vol. 43, no. 8, pp. 2800–2805, 2009.

[38] S. Zhang, K. Y. Wang, T. S. Chung, Y. C. Jean, and H. Chen, “Molecular design of the cellulose ester-based forward osmosis membranes for desalination,” *Chem. Eng. Sci.*, vol. 66, no. 9, pp. 2008–2018, 2011.

[39] M. Sairam, E. Sereewatthanawut, K. Li, A. Bismarck, and A. G. Livingston, “Method for the preparation of cellulose acetate flat sheet composite membranes for forward osmosis-Desalination using MgSO4 draw solution,” *Desalination*, vol. 273, no. 2–3, pp. 299–307, 2011.

[40] R. C. Ong, T. S. Chung, B. J. Helmer, and J. S. De Wit, “Characteristics of water and salt transport, free volume and their relationship with the functional groups of novel cellulose esters,” *Polym. (United Kingdom)*, vol. 54, no. 17, pp. 4560–4569, 2013.

[41] N. Y. Yip, A. Tiraferri, W. A. Phillip, J. D. Schiffman, and M. Elimelech, “High Performance Thin-Film Composite Forward Osmosis Membrane,” *Environ. Sci. Technol.*, vol. 44, no. 10, pp. 3812–3818, 2010.

[42] N. Widjojo, T. S. Chung, M. Weber, C. Maletzko, and V. Warzelhan, “The role of sulphonated polymer and macrovoid-free structure in the support layer for thin-film composite (TFC) forward osmosis (FO) membranes,” *J. Memb. Sci.*, vol. 383, no. 1–2, pp. 214–223, 2011.

[43] M. Park, J. J. Lee, S. Lee, and J. H. Kim, “Determination of a constant membrane structure parameter in forward osmosis processes,” *J. Memb. Sci.*, vol. 375, no. 1–2, pp. 241–248, 2011.

[44] G. Han, T. S. Chung, M. Toriida, and S. Tamai, “Thin-film composite forward osmosis

membranes with novel hydrophilic supports for desalination," *J. Memb. Sci.*, vol. 423–424, pp. 543–555, 2012.

[45] Y. Sun, L. Xue, Y. Zhang, X. Zhao, Y. Huang, and X. Du, "High flux polyamide thin film composite forward osmosis membranes prepared from porous substrates made of polysulfone and polyethersulfone blends," *Desalination*, vol. 336, no. 1, pp. 72–79, 2014.

[46] R. C. Ong, T. S. Chung, J. S. de Wit, and B. J. Helmer, "Novel cellulose ester substrates for high performance flat-sheet thin-film composite (TFC) forward osmosis (FO) membranes," *J. Memb. Sci.*, vol. 473, pp. 63–71, 2014.

[47] M. Tian, C. Qiu, Y. Liao, S. Chou, and R. Wang, "Preparation of polyamide thin film composite forward osmosis membranes using electrospun polyvinylidene fluoride (PVDF) nanofibers as substrates," *Sep. Purif. Technol.*, vol. 118, pp. 727–736, 2013.

[48] A. Tiraferri, Y. Kang, E. P. Giannelis, and M. Elimelech, "Highly Hydrophilic Thin-Film Composite Forward Osmosis Membranes Functionalized with Surface-Tailored Nanoparticles Highly Hydrophilic Thin-Film Composite Forward Osmosis Membranes Functionalized with Surface- Tailored Nanoparticles ACS Applied Materials," *ACS Appl. Mater. Interfaces*, vol. 4, pp. 5044–5053, 2012.

[49] N. Niksefat, M. Jahanshahi, and A. Rahimpour, "The effect of SiO2 nanoparticles on morphology and performance of thin film composite membranes for forward osmosis application," *Desalination*, vol. 343, pp. 140–146, 2014.

[50] N. Ma, J. Wei, R. Liao, and C. Y. Tang, "Zeolite-polyamide thin film nanocomposite membranes: Towards enhanced performance for forward osmosis," *J. Memb. Sci.*, vol. 405–406, pp. 149–157, 2012.

[51] N. Ma, J. Wei, S. Qi, Y. Zhao, Y. Gao, and C. Y. Tang, "Nanocomposite substrates for controlling internal concentration polarization in forward osmosis membranes," *J. Memb. Sci.*, vol. 441, pp. 54–62, 2013.

[52] D. Emadzadeh, W. J. Lau, T. Matsuura, M. Rahbari-Sisakht, and A. F. Ismail, "A novel thin film composite forward osmosis membrane prepared from PSf-TiO2 nanocomposite substrate for water desalination," *Chem. Eng. J.*, vol. 237, pp. 70–80, 2014.

[53] Y. X. Jia, H. L. Li, M. Wang, L. Y. Wu, and Y. D. Hu, “Carbon nanotube: Possible candidate for forward osmosis,” *Sep. Purif. Technol.*, vol. 75, no. 1, pp. 55–60, 2010.

[54] Y. Wang, R. Ou, Q. Ge, H. Wang, and T. Xu, “Preparation of polyethersulfone/carbon nanotube substrate for high-performance forward osmosis membrane,” *Desalination*, vol. 330, pp. 70–78, 2013.

[55] M. Amini, M. Jahanshahi, and A. Rahimpour, “Synthesis of novel thin film nanocomposite (TFN) forward osmosis membranes using functionalized multi-walled carbon nanotubes,” *J. Memb. Sci.*, vol. 435, pp. 233–241, 2013.

[56] Y. Wang, R. Ou, H. Wang, and T. Xu, “Graphene oxide modified graphitic carbon nitride as a modifier for thin film composite forward osmosis membrane,” *J. Memb. Sci.*, vol. 475, pp. 281–289, 2015.

[57] S. S. Madaeni and A. Rahimpour, “Preparation of polyethersulfone ultrafiltration membranes for milk concentration and effects of additives on their morphology and performance.,” *Chinese J. Polym. Sci.*, vol. 23, no. 5, pp. 539–548, 2005.

[58] A. Tiraferri, N. Y. Yip, W. A. Phillip, J. D. Schiffman, and M. Elimelech, “Relating performance of thin-film composite forward osmosis membranes to support layer formation and structure,” *J. Memb. Sci.*, vol. 367, no. 1–2, pp. 340–352, 2011.

[59] M. J. Han and S. T. Nam, “Thermodynamic and rheological variation in polysulfone solution by PVP and its effect in the preparation of phase inversion membrane,” *J. Memb. Sci.*, vol. 202, no. 1–2, pp. 55–61, 2002.

[60] B. Chakrabarty, A. K. Ghoshal, and M. K. Purkait, “Preparation, characterization and performance studies of polysulfone membranes using PVP as an additive,” *J. Memb. Sci.*, vol. 315, no. 1–2, pp. 36–47, 2008.

[61] W. J. Lau, A. F. Ismail, N. Misdan, and M. A. Kassim, “A recent progress in thin film composite membrane: A review,” *Desalination*, vol. 287, pp. 190–199, 2012.

[62] J. Wei, X. Liu, C. Qiu, R. Wang, and C. Y. Tang, “Influence of monomer concentrations on the performance of polyamide-based thin film composite forward osmosis membranes,” *J. Memb. Sci.*, vol. 381, no. 1–2, pp. 110–117, 2011.

[63] I. J. Roh, A. R. Greenberg, and V. P. Khare, “Synthesis and characterization of interfacially polymerized polyamide thin films,” *Desalination*, vol. 191, no. 1–3, pp. 279–290, 2006.

[64] A. K. Ghosh, B. H. Jeong, X. Huang, and E. M. V Hoek, “Impacts of reaction and curing conditions on polyamide composite reverse osmosis membrane properties,” *J. Memb. Sci.*, vol. 311, no. 1–2, pp. 34–45, 2008.

[65] N. K. Saha and S. V. Joshi, “Performance evaluation of thin film composite polyamide nanofiltration membrane with variation in monomer type,” *J. Memb. Sci.*, vol. 342, no. 1–2, pp. 60–69, 2009.

[66] J. Wei, C. Qiu, C. Y. Tang, R. Wang, and A. G. Fane, “Synthesis and characterization of flat-sheet thin film composite forward osmosis membranes,” *J. Memb. Sci.*, vol. 372, no. 1–2, pp. 292–302, 2011.

[67] S. Hermans, R. Bernstein, A. Volodin, and I. F. J. Vankelecom, “Study of synthesis parameters and active layer morphology of interfacially polymerized polyamide-polysulfone membranes,” *React. Funct. Polym.*, vol. 86, pp. 199–208, 2015.

[68] S. Zhao, L. Zou, C. Y. Tang, and D. Mulcahy, “Recent developments in forward osmosis: Opportunities and challenges,” *J. Memb. Sci.*, vol. 396, pp. 1–21, 2012.

[69] Y. Cai and X. M. Hu, “A critical review on draw solutes development for forward osmosis,” *Desalination*, vol. 391, pp. 16–29, 2016.

[70] J. Yaeli, “Method and Apparatus for Processing Liquid Solutions of Suspensions Particularly Useful in the Desalination of Saline Water,” 5098575, 1992.

[71] S. Loeb, L. Titelman, E. Korngold, and J. Freiman, “Effect of porous support fabric on osmosis through a Loeb-Sourirajan type asymmetric membrane,” *J. Memb. Sci.*, vol. 129, no. 2, pp. 243–249, 1997.

[72] R. L. McGinnis, “Osmoic Desalination Process,” *US. Pat.* 6391205 B1, 2002.

[73] J. R. McCutcheon, R. L. McGinnis, and M. Elimelech, “A novel ammonia-carbon dioxide forward (direct) osmosis desalination process,” *Desalination*, vol. 174, no. 1, pp. 1–11,

2005.

[74] E. R. Cornelissen *et al.*, “Membrane fouling and process performance of forward osmosis membranes on activated sludge,” *J. Memb. Sci.*, vol. 319, no. 1–2, pp. 158–168, 2008.

[75] S. Adham, J. Oppenheimer, L. Li, and M. Kumar, “Dewatering Reverse Osmosis Concentrate from Water Reuse Applications Using Forward Osmosis,” The Water Reuse Foundation Alexandria, VA, Alexandria, 2006.

[76] A. Achilli, T. Y. Cath, and A. E. Childress, “Selection of inorganic-based draw solutions for forward osmosis applications,” *J. Memb. Sci.*, vol. 364, no. 1–2, pp. 233–241, 2010.

[77] S. Phuntsho, H. K. Shon, S. Hong, S. Lee, and S. Vigneswaran, “A novel low energy fertilizer driven forward osmosis desalination for direct fertigation: Evaluating the performance of fertilizer draw solutions,” *J. Memb. Sci.*, vol. 375, no. 1–2, pp. 172–181, 2011.

[78] R. E. Kesting, “Phase inversion membranes,” *ACS Symp. Ser. ACS Symp. Ser. Vol 269*, vol. 269, no. 1967, pp. 131–164, 1985.

[79] M. Sadrzadeh and S. Bhattacharjee, “Rational design of phase inversion membranes by tailoring thermodynamics and kinetics of casting solution using polymer additives,” *J. Memb. Sci.*, vol. 441, pp. 31–44, 2013.

[80] Y. Song, P. Sun, L. L. Henry, and B. Sun, “Mechanisms of structure and performance controlled thin film composite membrane formation via interfacial polymerization process,” *J. Memb. Sci.*, vol. 251, no. 1–2, pp. 67–79, 2005.

[81] B. H. Jeong *et al.*, “Interfacial polymerization of thin film nanocomposites: A new concept for reverse osmosis membranes,” *J. Memb. Sci.*, vol. 294, no. 1–2, pp. 1–7, 2007.

[82] M. J. T. Raaijmakers and N. E. Benes, “Current trends in interfacial polymerization chemistry,” *Prog. Polym. Sci.*, vol. 63, pp. 86–142, 2016.

[83] F. Rouquerol, J. Rouquerol, K. S. W. Sing, P. Llewellyn, and G. Maurin, *Adsorption by powders and porous solids*, 1st ed. London: Academic press, 1999.

[84] A. Dabrowski, “Adsorption - From theory to practice,” *Adv. Colloid Interface Sci.*, vol.

93, no. 1–3, pp. 135–224, 2001.

[85] M. Strickland, “Physical Adsorption Theory,” Norcross, GA U.S.A., 2018, Retrieved 5 February, 2018 from https://www.scribd.com/document/257183293/GasAbsorption-micromeritics-pdf.

[86] J. Landers, G. Y. Gor, and A. V. Neimark, “Density functional theory methods for characterization of porous materials,” *Colloids Surfaces A Physicochem. Eng. Asp.*, vol. 437, pp. 3–32, 2013.

[87] X. Zheng, T. S. Ge, Y. Jiang, and R. Z. Wang, “Experimental study on silica gel-LiCl composite desiccants for desiccant coated heat exchanger,” *Int. J. Refrig.*, vol. 51, no. March, pp. 24–32, 2015.

[88] B. H. Stuart, *Infrared Spectroscopy: Fundamentals and Applications*, 1st ed., vol. 8. Washington: John Wiley & Sons, Ltd, 2004.

[89] H. J. Michael, *Modern Spectroscopy*, 4th ed. John Wiley, 2004.

[90] T. S. Meiron, A. Marmur, and I. S. Saguy, “Contact angle measurement on rough surfaces,” *J. Colloid Interface Sci.*, vol. 274, no. 2, pp. 637–644, 2004.

[91] A. Krishnan, Y.-H. Liu, P. Cha, R. Woodward, D. Allara, and E. A. Vogler, “An evaluation of methods for contact angle measurement,” *J. Colloids Surf. B*, vol. 43, no. 2, pp. 95–98, 2005.

[92] G. Bracco and B. Holst, “Contact Angle andWetting Properties,” in *Surface science techniques*, vol. 51, no. 1, Springer, 2013, pp. 1–34.

[93] D. Y. Kwok and A. W. Neumann, “Contact angle measurement and contact angle interpretation,” *J. Adv. Colloid Interface Sci*, vol. 81, no. 3, pp. 167–249, 1999.

[94] “Drop Shape Analyzer – DSA25’ Installation and Operation Manual,KRUSS GmbH,” Hamburg, 2014, Retrieved 6 April, 2017 from https://www.kruss-scientific.com/fileadmin/user_upload/website/brochures/kruss-bro-dsa25-en.pdf.

[95] R. García and R. Perez, “Dynamic atomic force microscopy methods,” *J. Surf. Sci. Rep*, vol. 47, no. 6–8, pp. 197–301, 2002.

[96] P. L. T. M. Frederix, P. D. Bosshart, and A. Engel, “Atomic force microscopy of biological membranes,” *Biophys. J.*, vol. 96, no. 2, pp. 329–338, 2009.

[97] F. Eghiaian, F. Rico, A. Colom, I. Casuso, and S. Scheuring, “High-speed atomic force microscopy: Imaging and force spectroscopy,” *FEBS Lett.*, vol. 588, no. 19, pp. 3631–3638, 2014.

[98] R. R. L. De Oliveira, D. a. C. Albuquerque, T. G. S. Cruz, and F. M. Y. and F. L. Leite, “Measurement of the Nanoscale Roughness by Atomic Force Microscopy: Basic Principles and Applications,” in *Atomic Force Microscopy - Imaging, Measuring and Manipulating Surfaces at the Atomic Scale*, V. Bellitto, Ed. InTech, 2012, pp. 147–174.

[99] G. Haugstad, *Atomic Force Microscopy: Understanding Basic Modes and Advanced Applications*, First. John Wiley & Sons, Incorporated, 2017.

[100] M. Suga, S. Asahina, Y. Sakuda, H. Kazumori, and H. Nishiyama, “Recent progress in scanning electron microscopy for the characterization of fine structural details of nano materials,” *Prog. Solid State Chem.*, vol. 42, no. 1–2, pp. 1–21, 2014.

[101] W. Zhou, R. P. Apkarian, and Z. L. Wang, “Fundamentals of Scanning Electron Microscopy,” in *Scanning Microscopy for Nanotechnology*, 1st ed., W. Zhou and Z. L. Wang, Eds. New York: Springer, 2007, pp. 1–40.

[102] JOEL Serving Advanced Technology, “Scanning Electron Microscope A To Z Basic Knowledge for Using The SEM,” Tokyo, 2006, Retrieved 25 June, 2017 from https://www.jeol.co.jp/en/applications/pdf/sm/sem_atoz_all.pdf.

[103] D. Montgomery C., “*Design and Analysis of Experiments.*” pp. 60–126, 2007.

[104] C. Gao, C. D. Vo, Y. Z. Jin, W. Li, and S. P. Armes, “Multihydroxy polymer-functionalized carbon nanotubes: Synthesis, derivatization, and metal loading,” *Macromolecules*, vol. 38, no. 21, pp. 8634–8648, 2005.

[105] A. Idris, Z. Man, A. Maulud, and M. Khan, “Effects of Phase Separation Behavior on Morphology and Performance of Polycarbonate Membranes,” *Membranes (Basel).*, vol. 7, no. 2, p. 21, 2017.

[106] S. Hamzah, N. Ali, M. M. Ariffin, A. Ali, and A. W. Mohammad, “High performance of polysulfone ultrafiltration membrane: Effect of polymer concentration,” *ARPN J. Eng. Appl. Sci.*, vol. 9, no. 12, pp. 2543–2550, 2014.

[107] A. V. Bildyukevich, T. V. Plisko, A. S. Liubimova, V. V. Volkov, and V. V. Ususky, “Hydrophilization of polysulfone hollow fiber membranes via addition of polyvinylpyrrolidone to the bore fluid,” *J. Memb. Sci.*, vol. 524, no. November 2016, pp. 537–549, 2017.

[108] X. Li, T. He, P. Dou, and S. Zhao, *Forward Osmosis and Forward Osmosis Membranes BT - Comprehensive Membrane Science and Engineering*, 2nd ed. Oxford: Elsevier, 2017.

[109] N. N. Bui, J. T. Arena, and J. R. McCutcheon, “Proper accounting of mass transfer resistances in forward osmosis: Improving the accuracy of model predictions of structural parameter,” *J. Memb. Sci.*, vol. 492, pp. 289–302, 2015.

[110] A. K. Ghosh and E. M. V Hoek, “Impacts of support membrane structure and chemistry on polyamide-polysulfone interfacial composite membranes,” *J. Memb. Sci.*, vol. 336, no. 1–2, pp. 140–148, 2009.

[111] Y. Jin and Z. Su, “Effects of polymerization conditions on hydrophilic groups in aromatic polyamide thin films,” *J. Memb. Sci.*, vol. 330, no. 1–2, pp. 175–179, 2009.

[112] J. Lee, A. Hill, and S. Kentish, “Formation of a thick aromatic polyamide membrane by interfacial polymerisation,” *Sep. Purif. Technol.*, vol. 104, pp. 276–283, 2013.

[113] C. Guo, L. Zhou, and J. Lv, “Effects of expandable graphite and modified ammonium polyphosphate on the flame-retardant and mechanical properties of wood flour-polypropylene composites,” *Polym. Polym. Compos.*, vol. 21, no. 7, pp. 449–456, 2013.

[114] S. Yu, M. Liu, X. Liu, and C. Gao, “Performance enhancement in interfacially synthesized thin-film composite polyamide-urethane reverse osmosis membrane for seawater desalination,” *J. Memb. Sci.*, vol. 342, no. 1–2, pp. 313–320, 2009.

[115] A. Soroush, J. Barzin, M. Barikani, and M. Fathizadeh, “Interfacially polymerized polyamide thin film composite membranes: Preparation, characterization and performance evaluation,” *Desalination*, vol. 287, pp. 310–316, 2012.

[116] M. Zargar, B. Jin, and S. Dai, “An integrated statistic and systematic approach to study correlation of synthesis condition and desalination performance of thin film composite membranes,” *Desalination*, vol. 394, pp. 138–147, 2016.

[117] R. Silverstein and F. Webster, *Spectrometric identification of organic compounds*, 7th ed. Hoboken, NJ: John Wiley & Sons, c2005., 2005.

[118] D. L. Pavia, *Introduction to Spectroscopy*, 4th ed. Washington: Brooks/Cole, Cengage Learning, 2009.

[119] S. Vahur, A. Teearu, P. Peets, L. Joosu, and I. Leito, “ATR-FT-IR spectral collection of conservation materials in the extended region of 4000-80 cm–1,” *Anal. Bioanal. Chem.*, vol. 408, no. 13, pp. 3373–3379, 2016.

[120] S. Xia, L. Yao, Y. Zhao, N. Li, and Y. Zheng, “Preparation of graphene oxide modified polyamide thin film composite membranes with improved hydrophilicity for natural organic matter removal,” *Chem. Eng. J.*, vol. 280, pp. 720–727, 2015.

[121] T. H. Lee, M. Y. Lee, H. D. Lee, J. S. Roh, H. W. Kim, and H. B. Park, “Highly porous carbon nanotube/polysulfone nanocomposite supports for high-flux polyamide reverse osmosis membranes,” *J. Memb. Sci.*, vol. 539, no. June, pp. 441–450, 2017.

Appendix I

Terms used in the factorial design and ANOVA

Total sum of squares (TSS or SST) is a quantity that appears as part of a standard way of presenting results of certain analysis. It is defined as the sum, over all observations, of the square differences of each observation from the overall mean.

Degree of freedom (DF) is the number of values that are free to vary in the final calculation of a statistical analysis. The number of independent ways by which a dynamic system can move without violating any restriction enforced on it. If the sample size is n so the degree of freedom is n-1.

F-value is a statistical term that can be calculated by dividing the variance of the group means over the mean within the group. If the F-value is too high and higher than the F-statistic, the null hypothesis can be rejected and the alternative hypothesis can be considered with the observed data.

P-value is a statistical term that helps in determination the significance of the results. It is a number between 0 and 1. By selecting a significance level of α=0.05, a P-value lower than 0.05 means that the results are significant, and the null hypothesis can be rejected that supports the observed results.

Appendix II

Model graphs of the experimental design

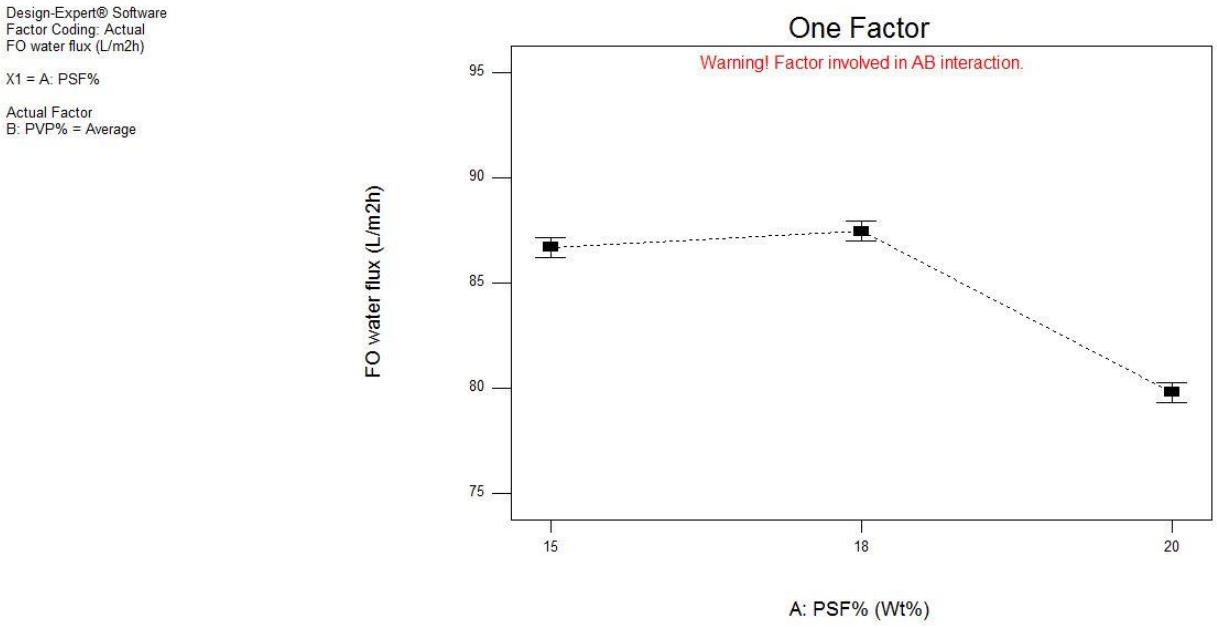

Model graph of PSF wt% versus FO water flux

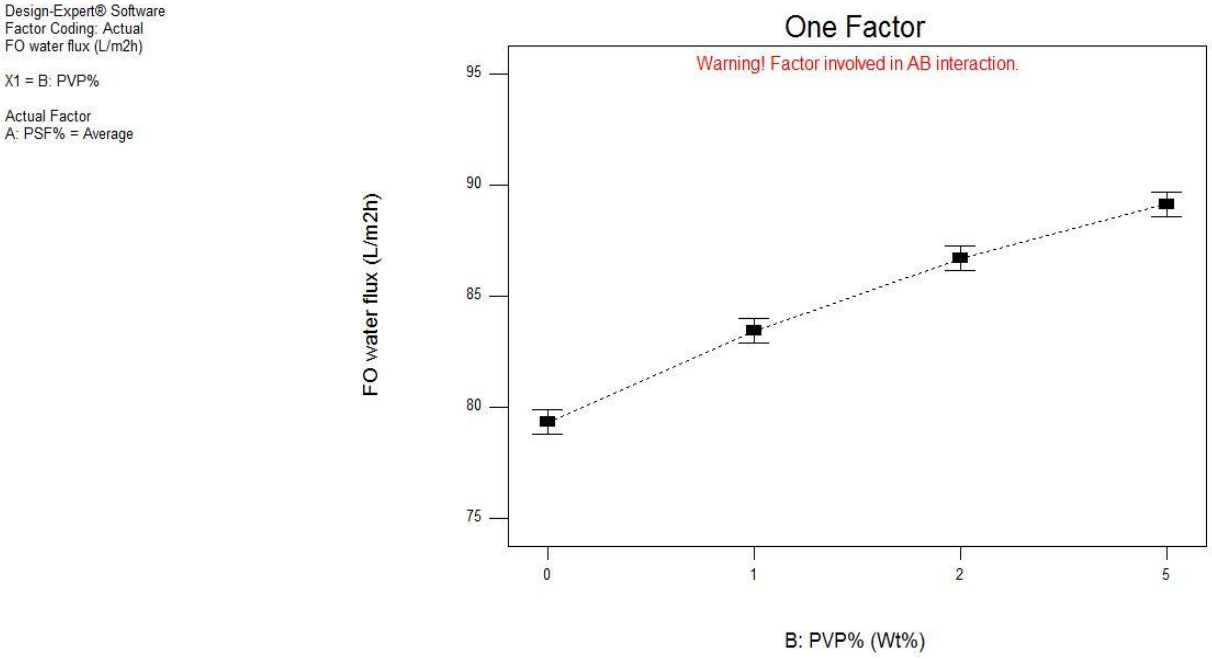

Model graph of PVP wt% versus FO water flux

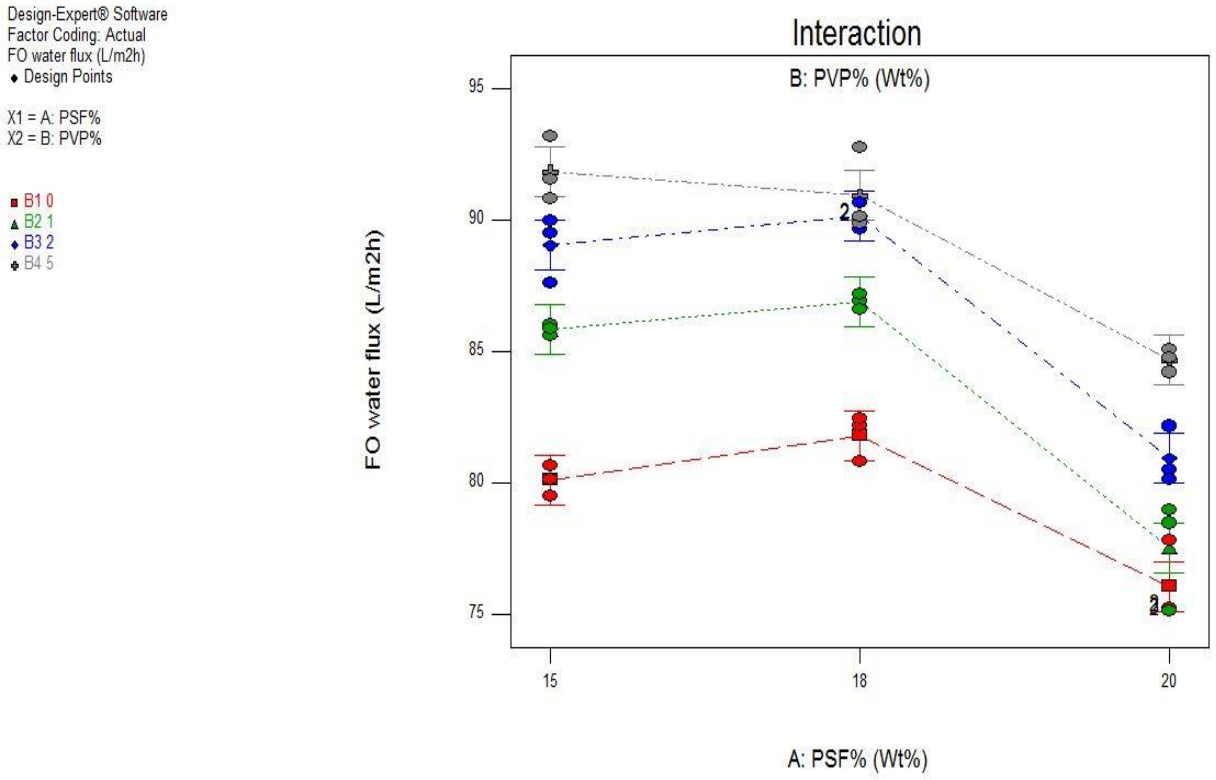

Model graph of interaction between PSF wt% and PVP wt% versus FO water flux

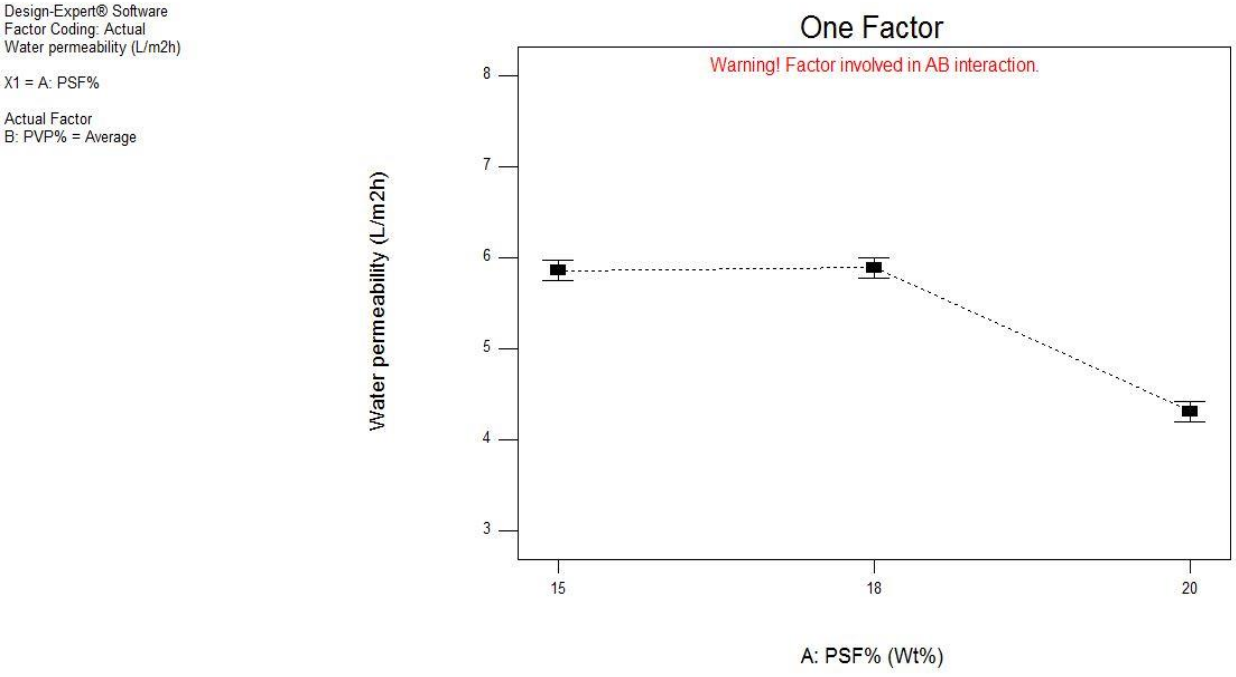

Model graph of PSF wt% versus water permeability

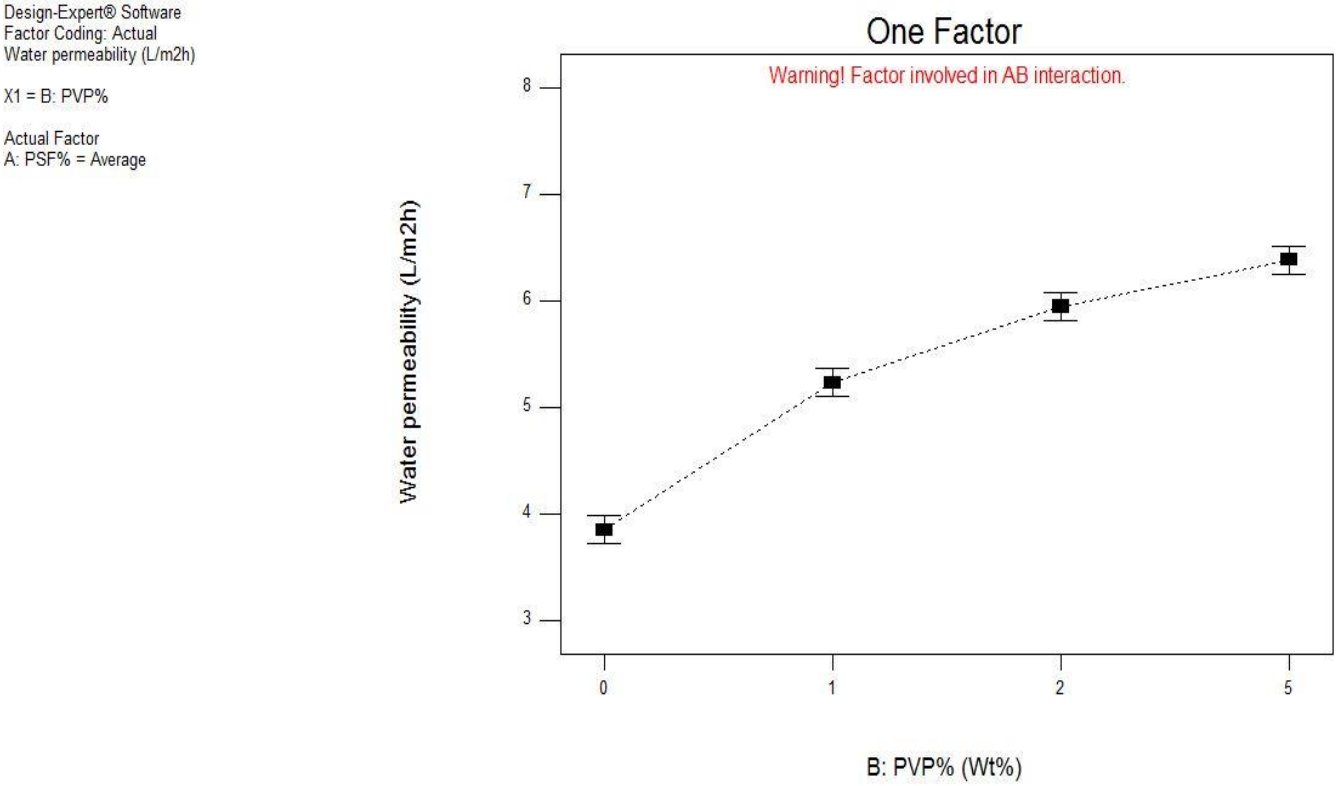

Model graph of PVP wt% versus water permeability

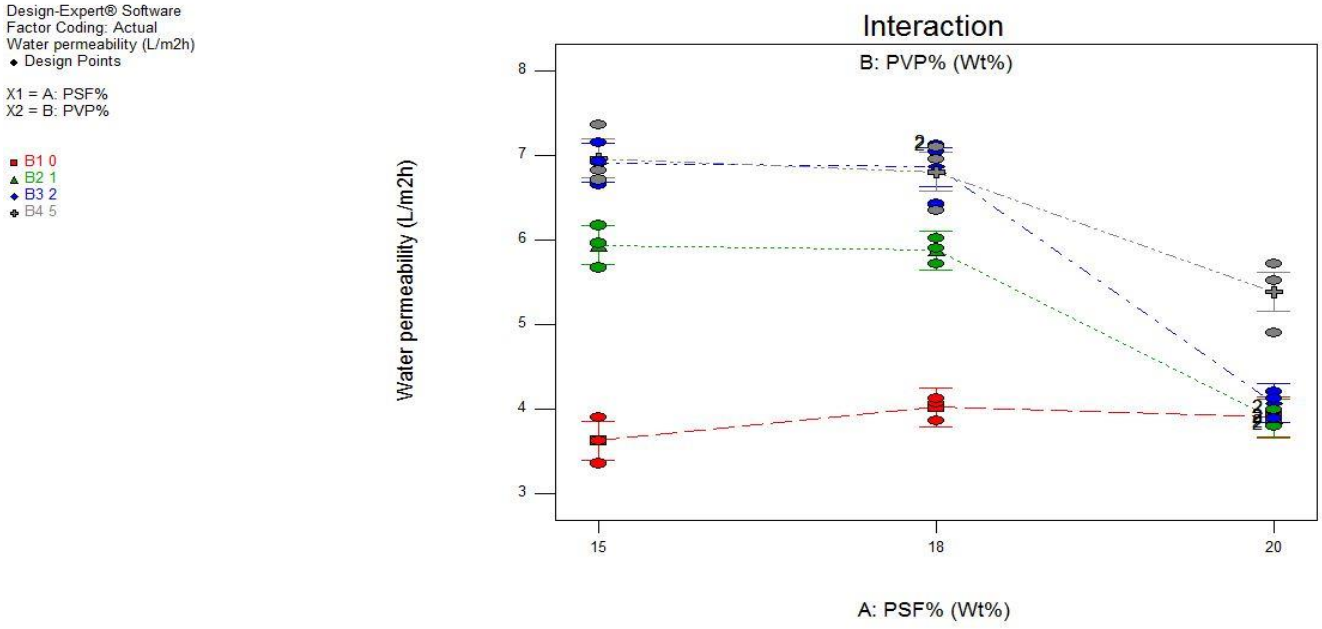

Model graph of interaction between PSF wt% and PVP wt% versus water permeability

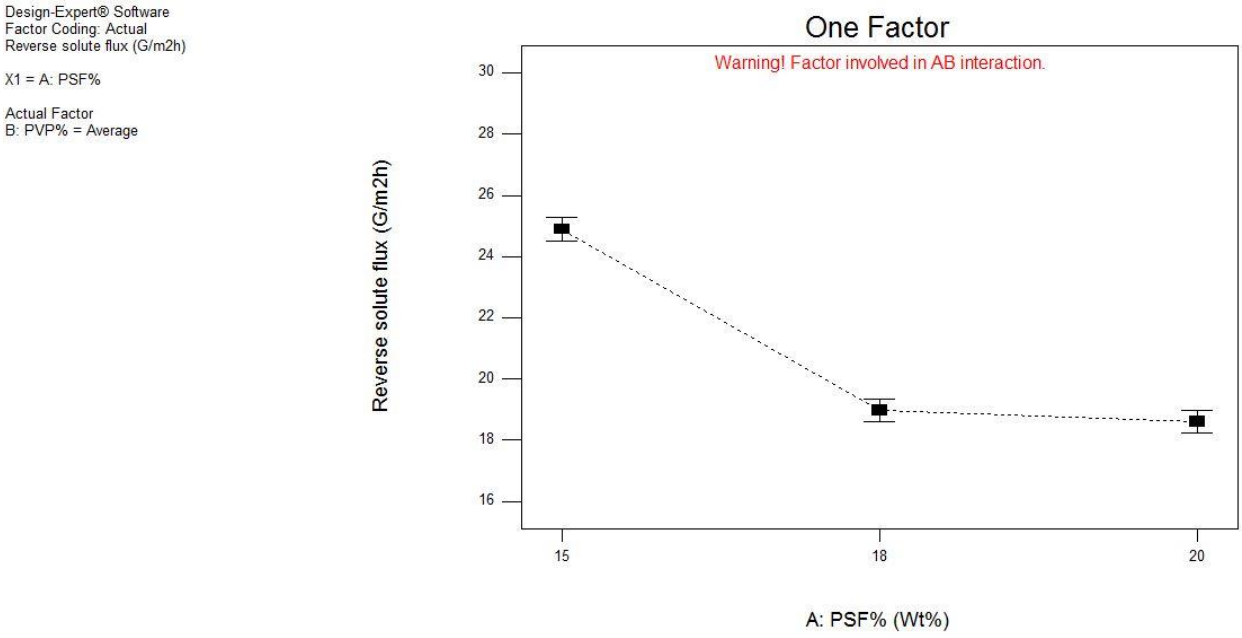

Model graph of PSF wt% versus reverse solute flux

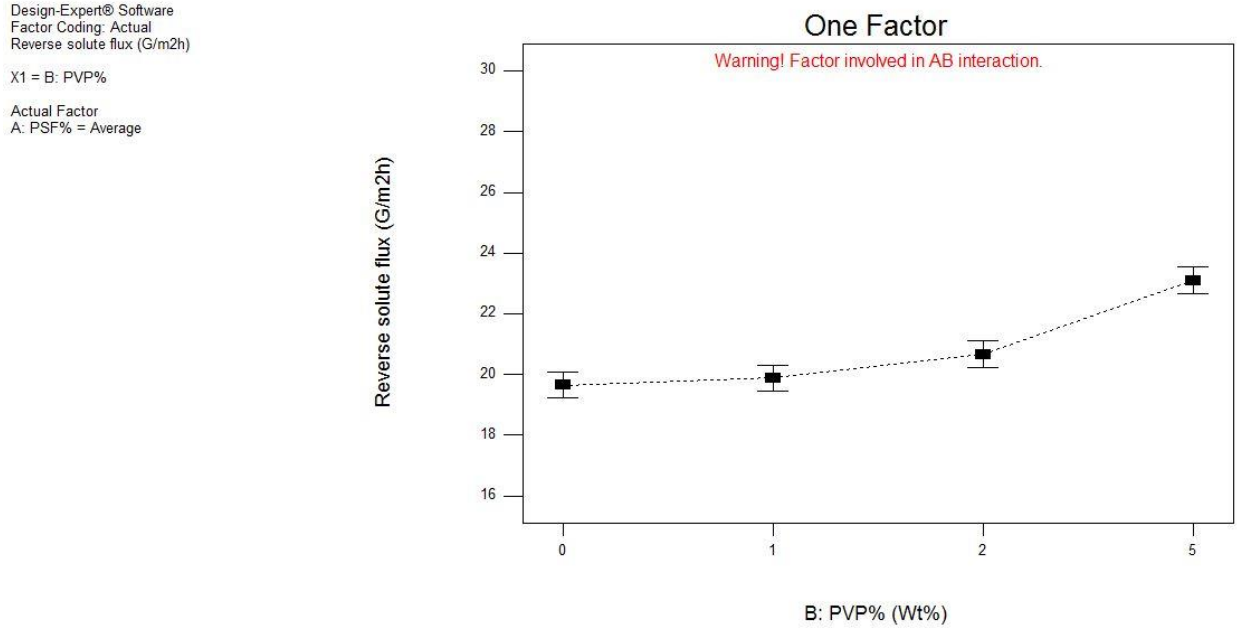

Model graph of PVP wt% versus reverse solute flux

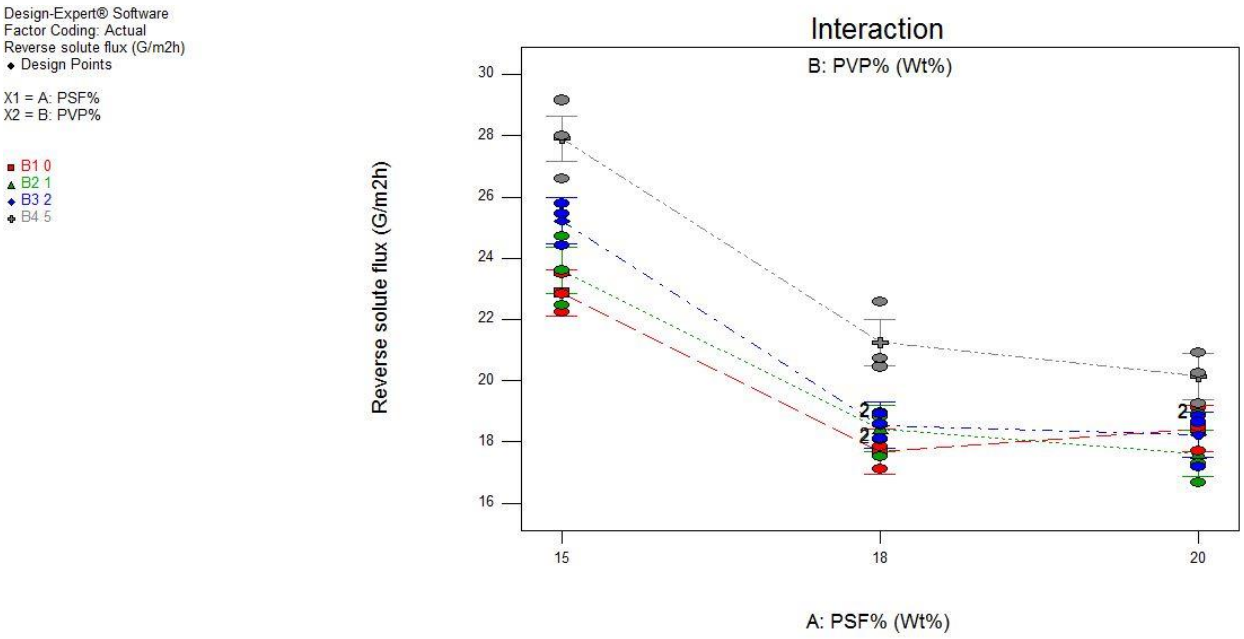

Model graph of interaction between PSF wt% and PVP wt% versus reverse solute flux

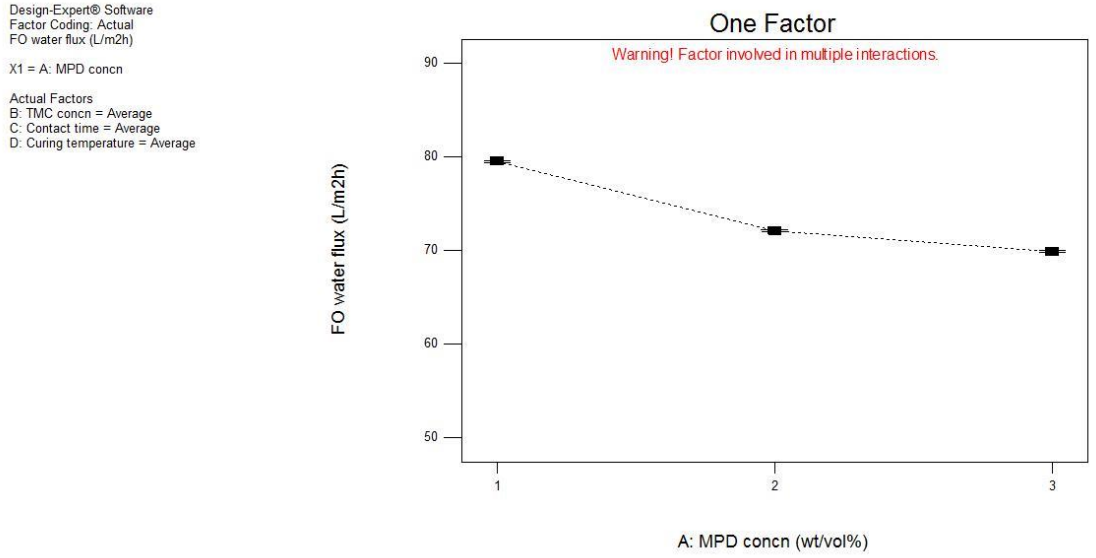

Model graph of MPD concentration vs. FO water flux

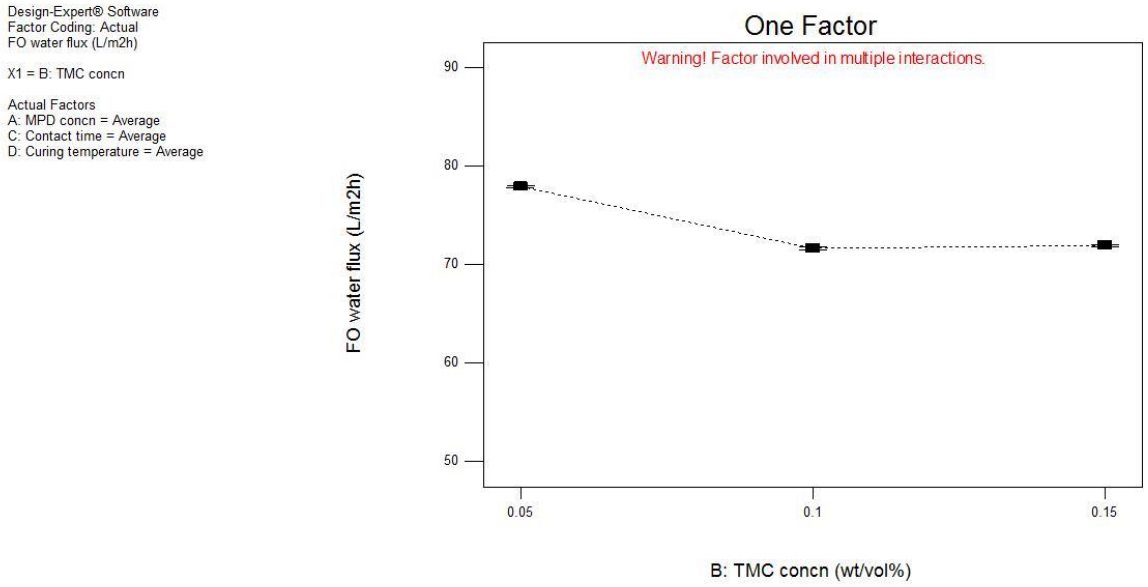

Model graph of TMC concentration vs. FO water flux

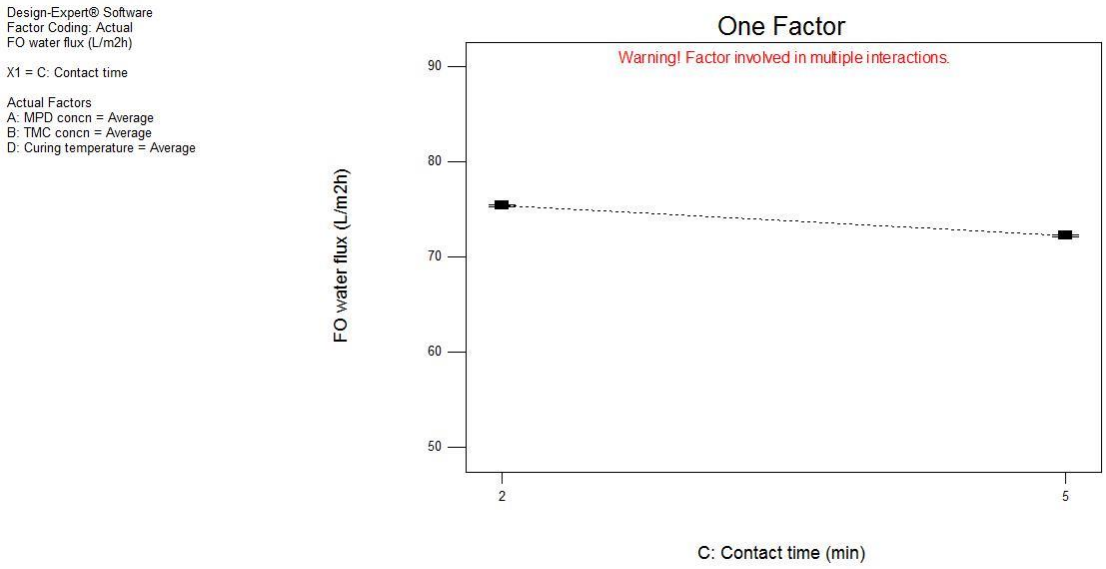

Model graph of contact time vs. FO water flux

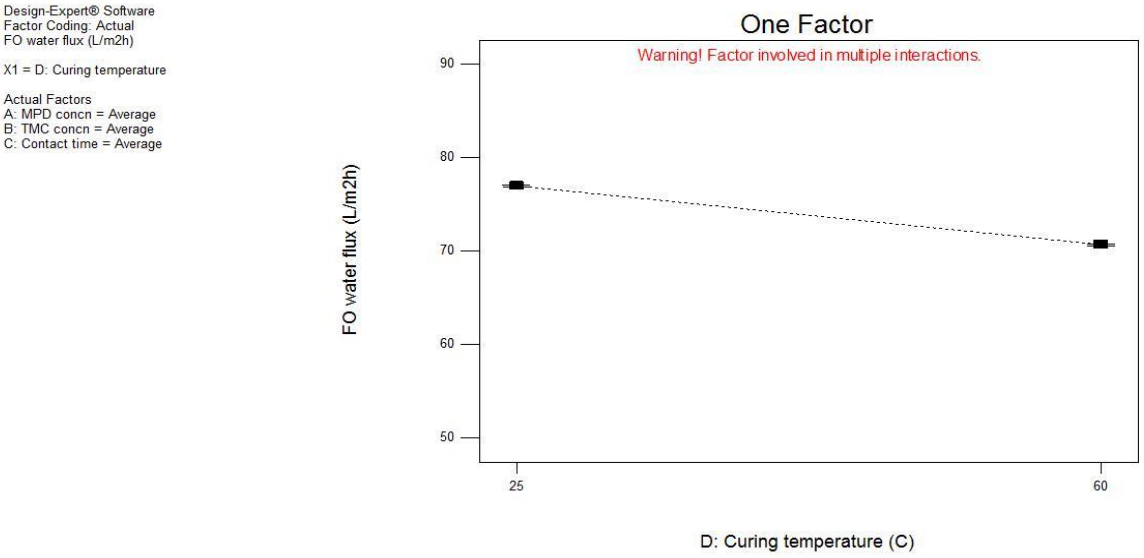

Model graph of curing temperature vs. FO water flux

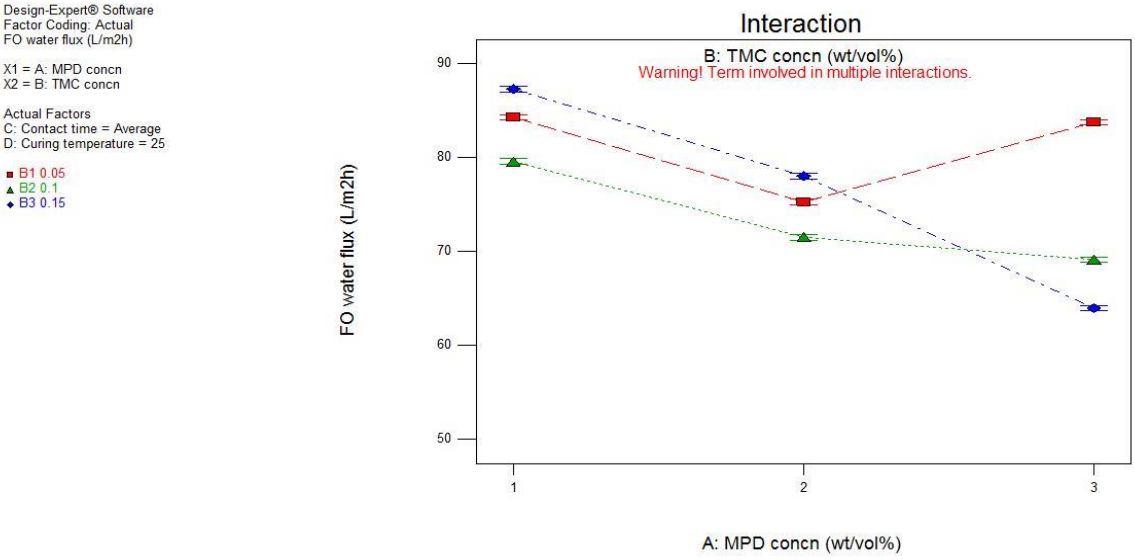

Interaction model graph between MPD, TMC concentrations and FO water flux at 25°C curing temperature

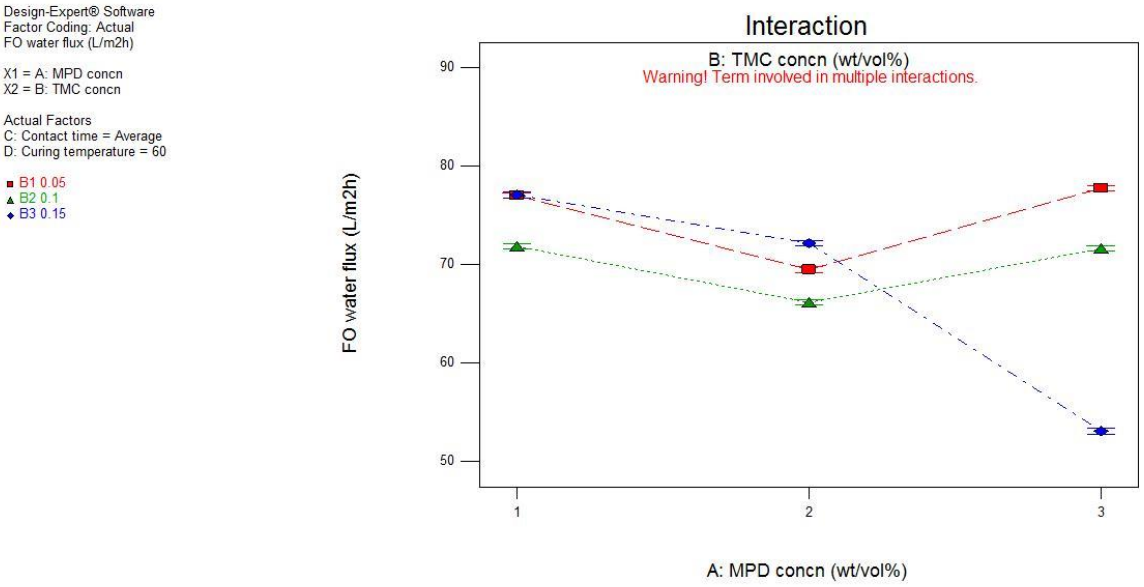

Interaction model graph between MPD, TMC concentrations and FO water flux at 60°C curing temperature

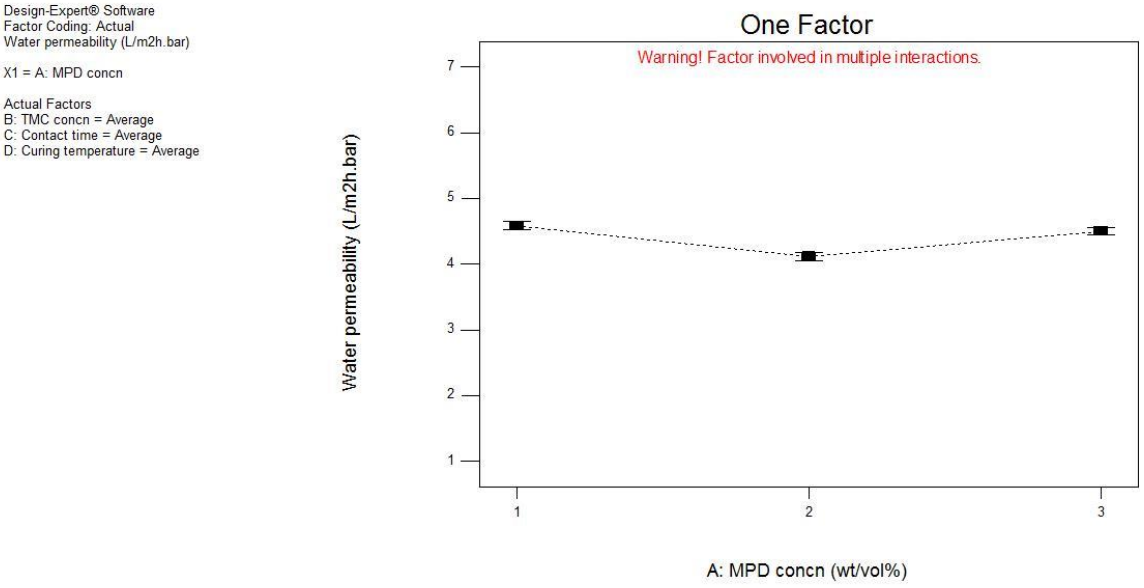

Model graph of MPD concentration vs. water permeability

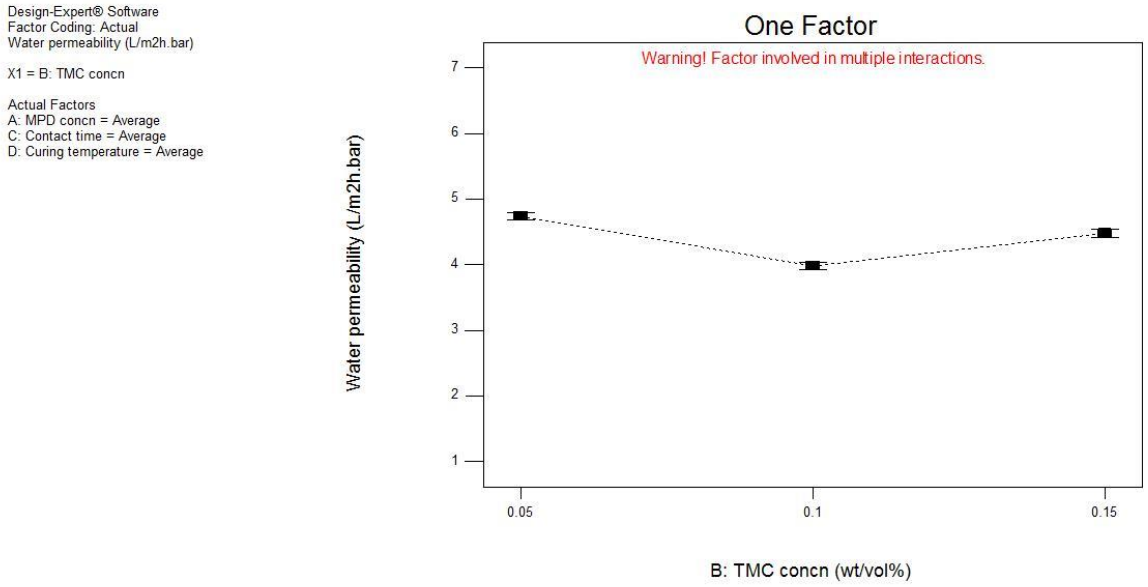

Model graph of TMC concentration vs. water permeability

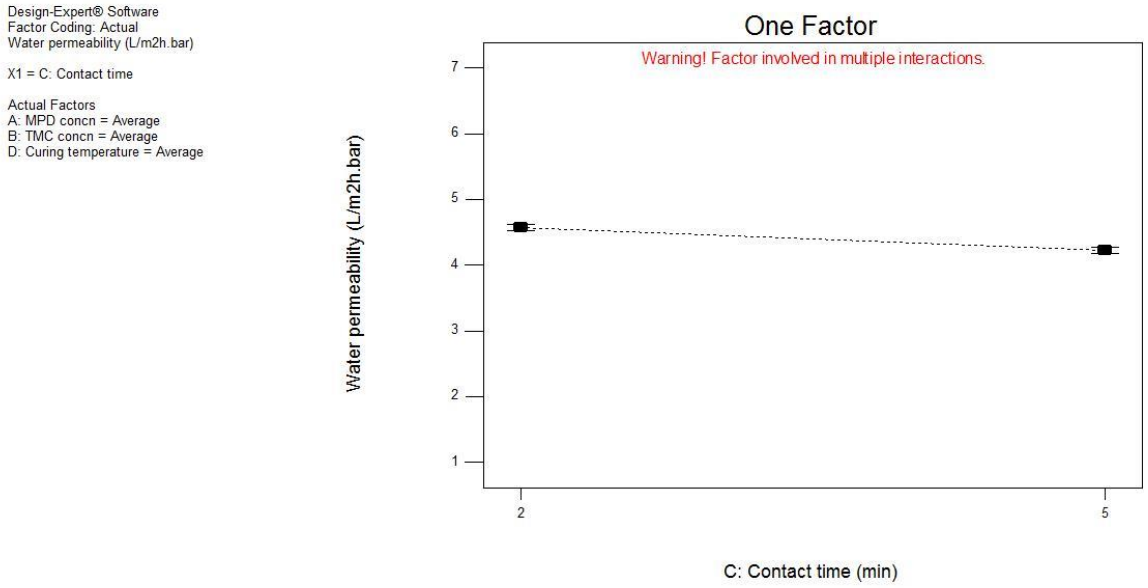

Model graph of contact time vs. water permeability

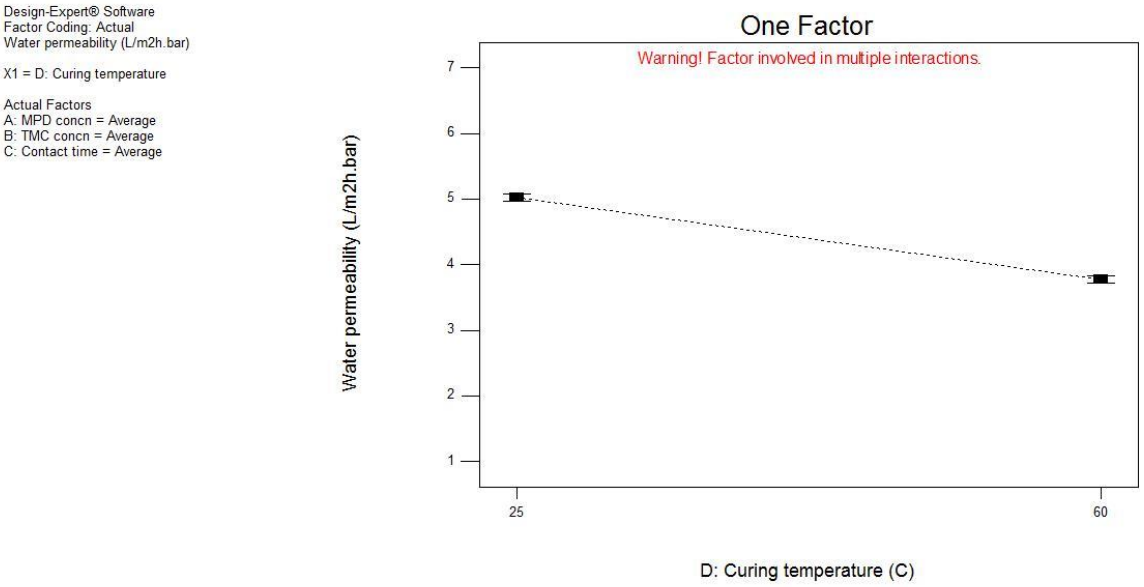

Model graph of curing temperature vs. water permeability

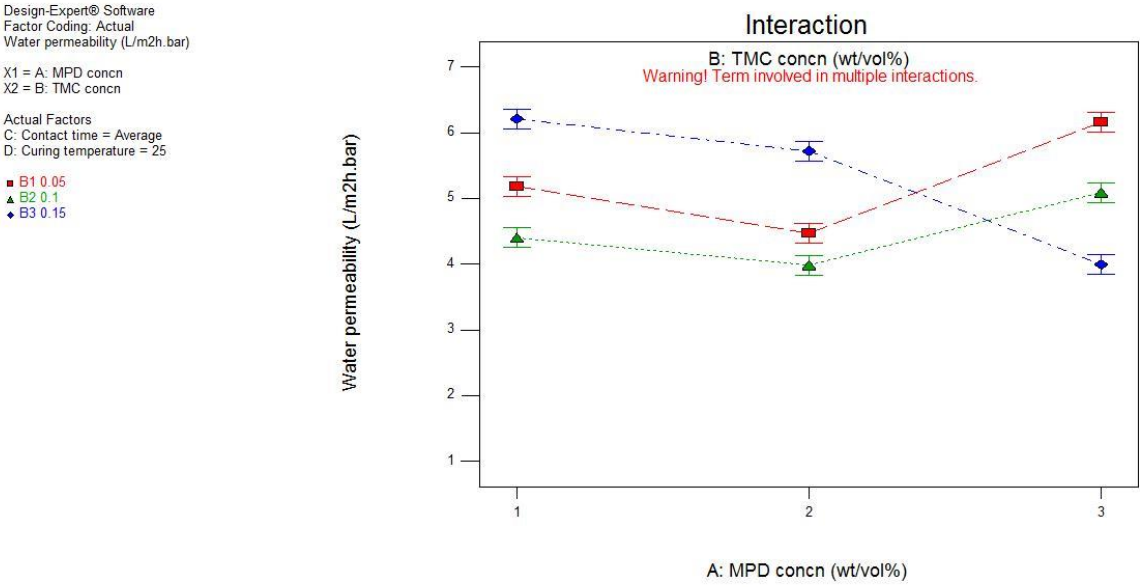

Interaction model graph between MPD, TMC concentrations and water permeability at 25°C curing temperature

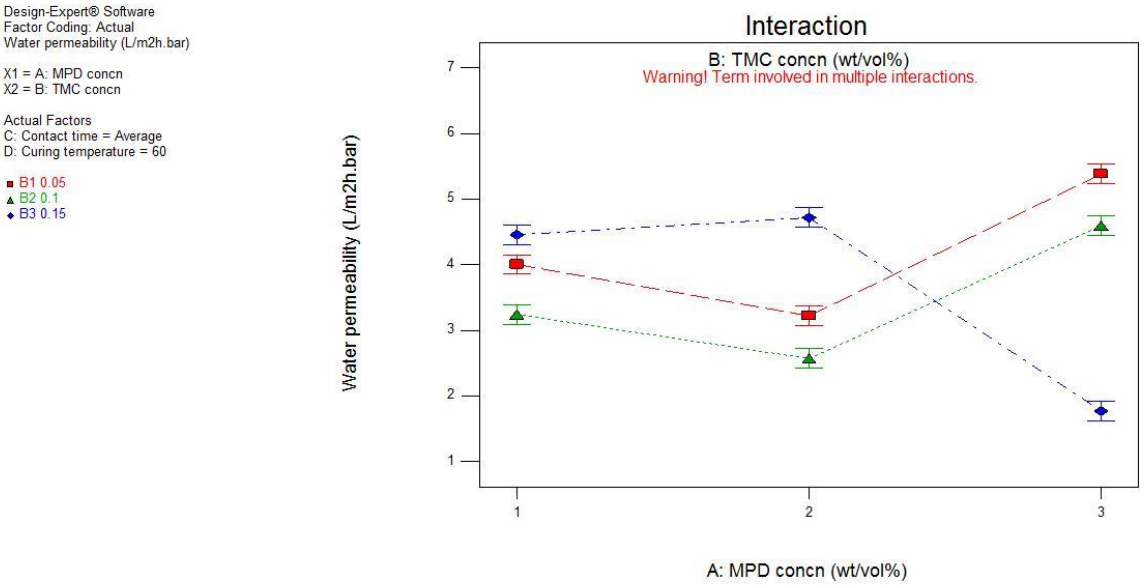

Interaction model graph between MPD, TMC concentrations and water permeability at 60°C curing temperature

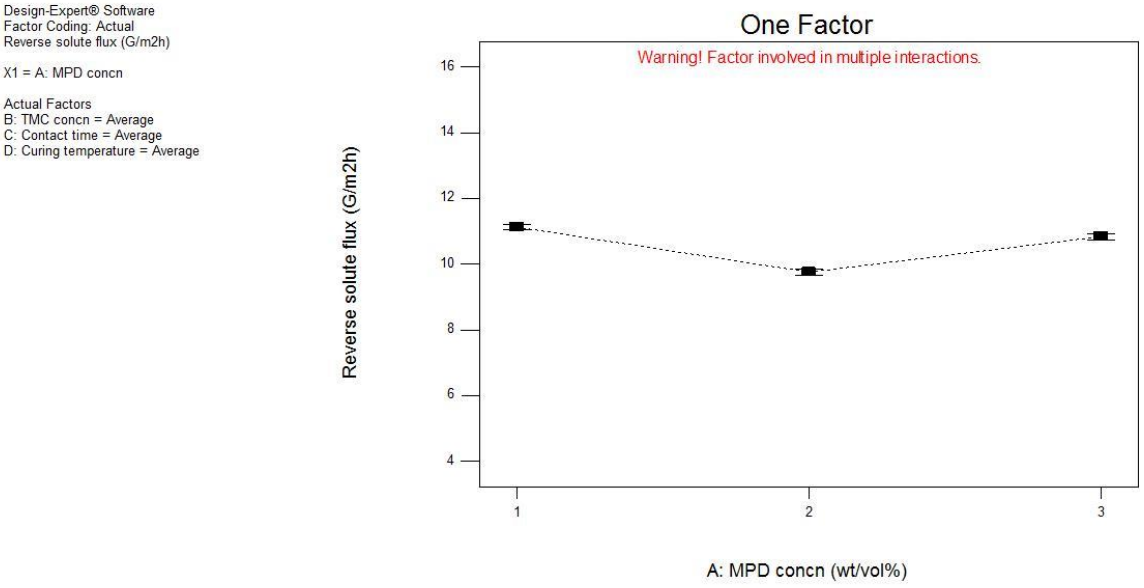

Model graph of MPD concentration vs. reverse solute flux

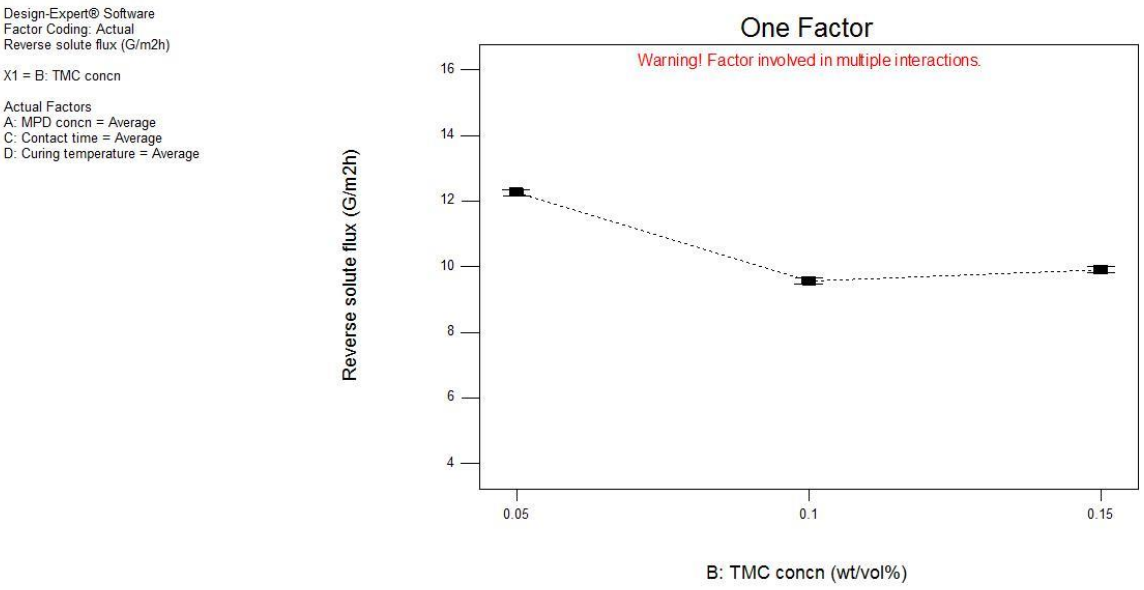

Model graph of TMC concentration vs. reverse solute flux

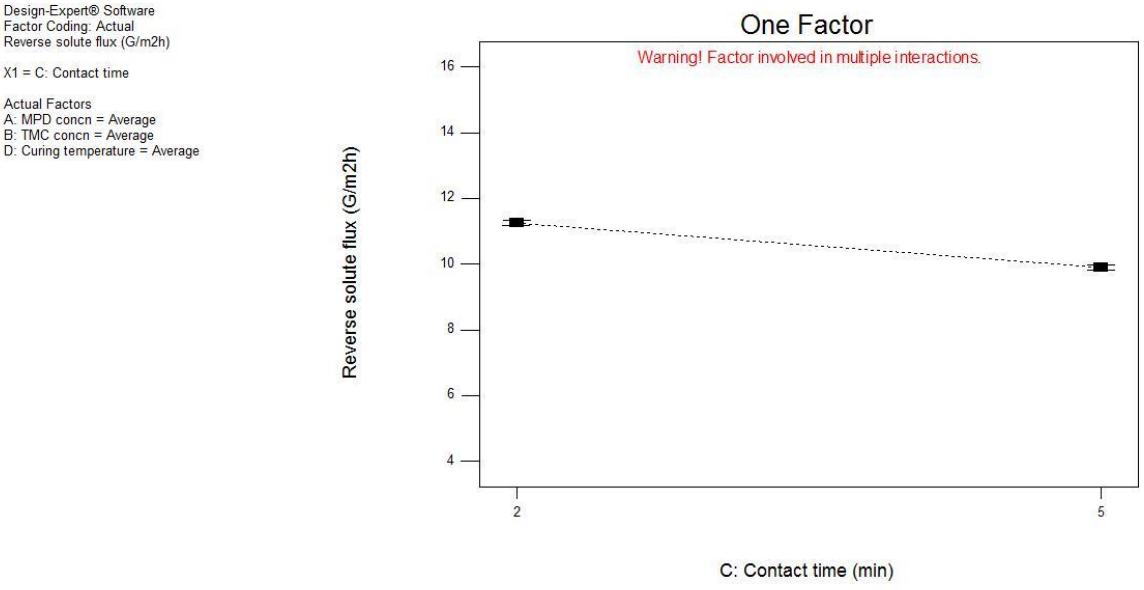

Model graph of contact time vs. reverse solute flux

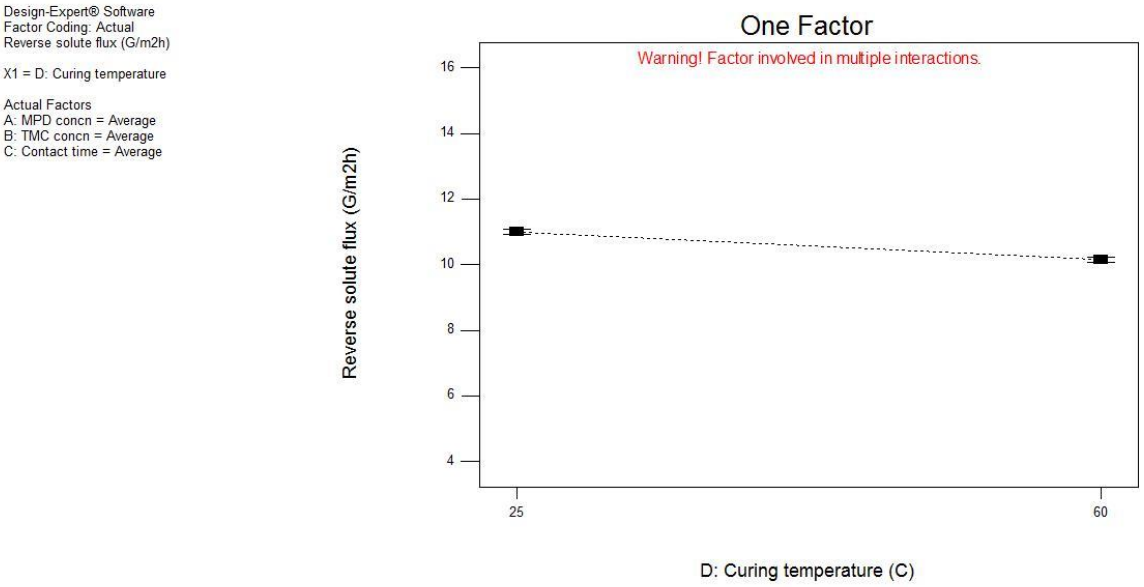

Model graph of curing temperature vs. reverse solute flux

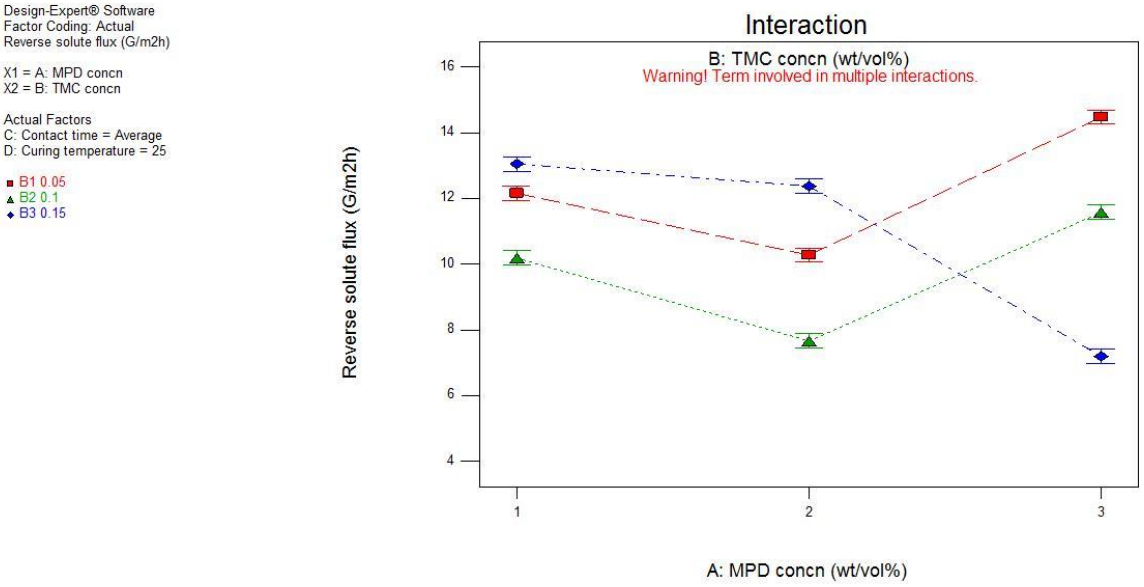

Interaction model graph between MPD, TMC concentrations and reverse solute flux at 25°C curing temperature

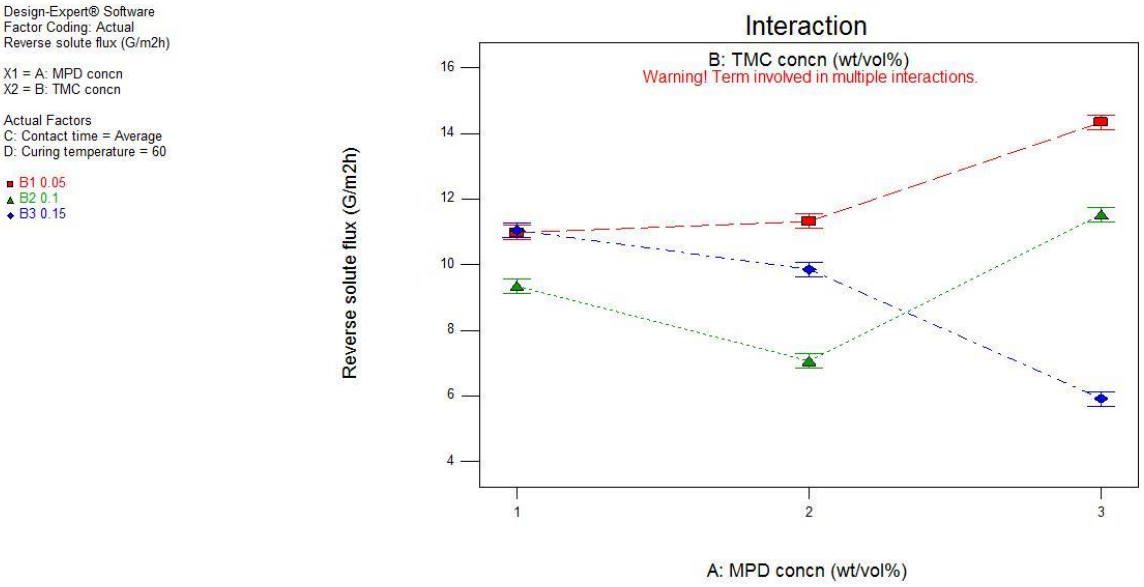

Interaction model graph between MPD, TMC concentrations and reverse solute flux at 60°C curing temperature

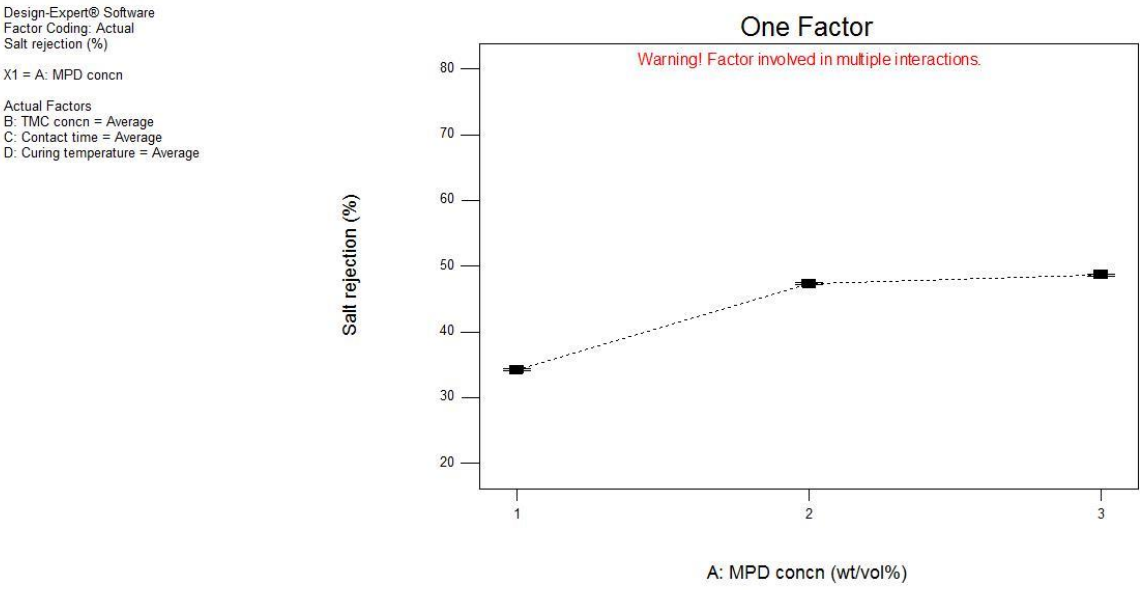

Model graph of MPD concentration vs. salt rejection

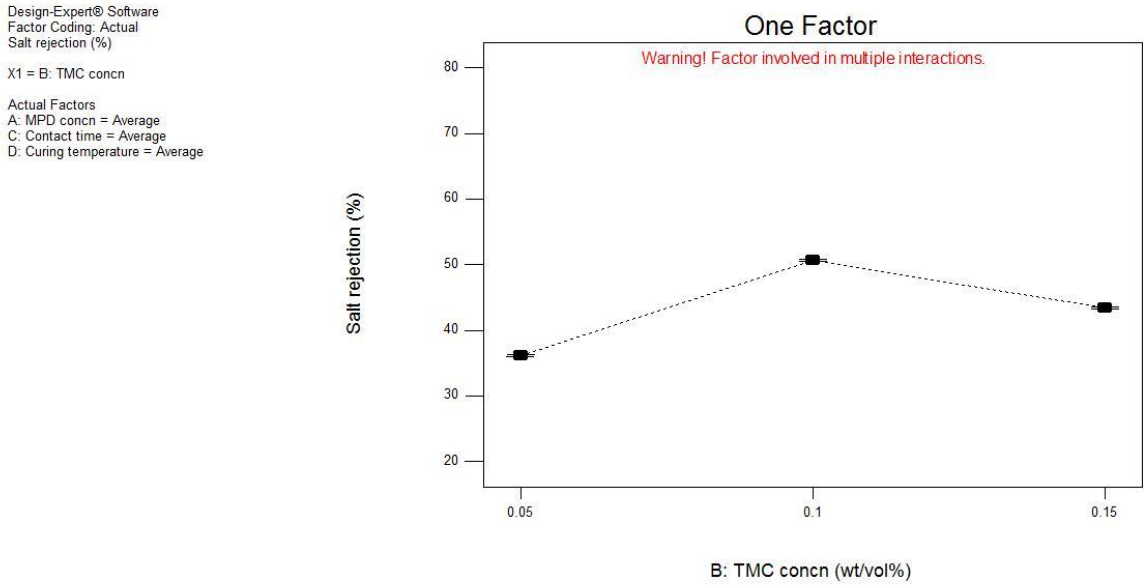

Model graph of TMC concentration vs. salt rejection

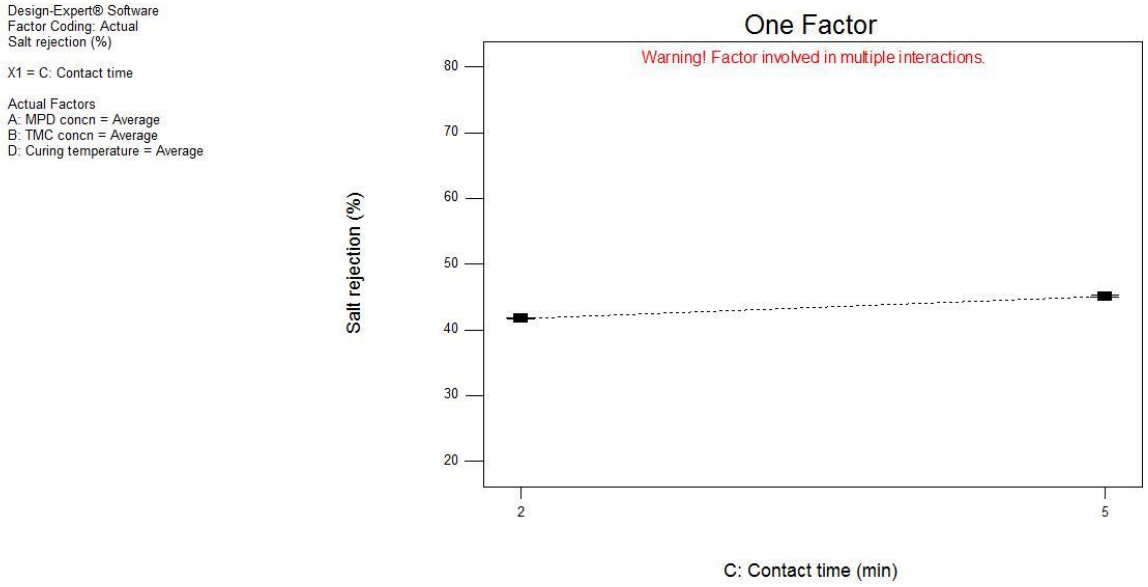

Model graph of contact time vs. salt rejection

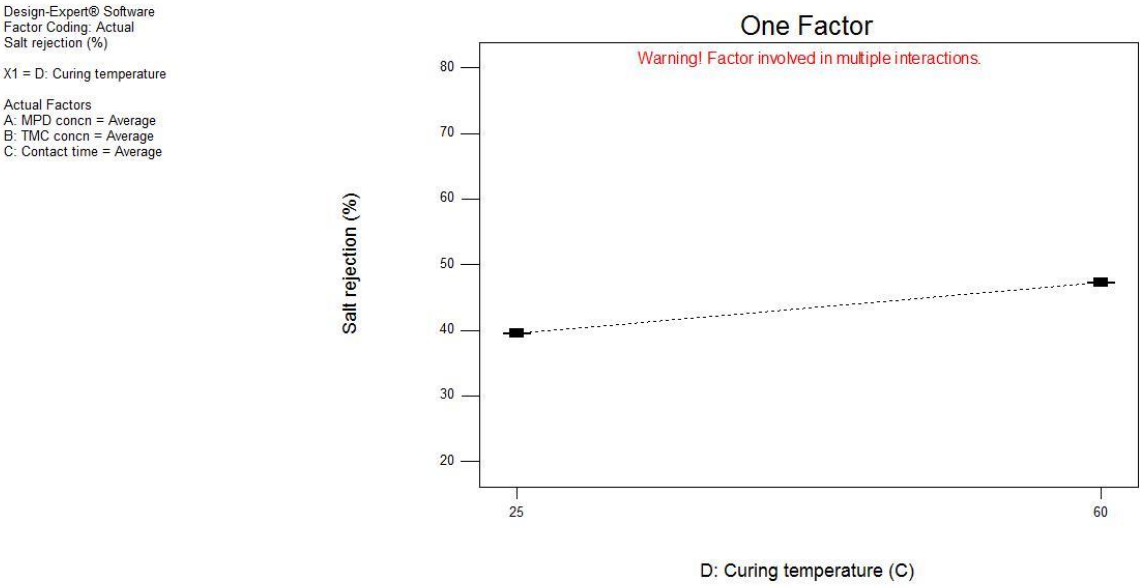

Model graph of curing temperature vs. salt rejection

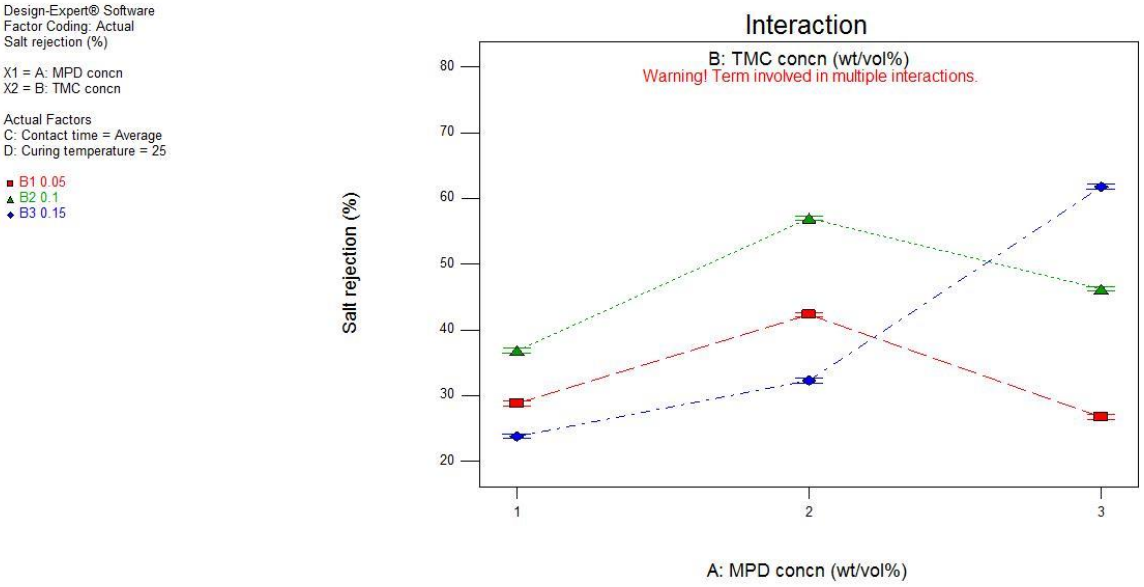

Interaction model graph between MPD, TMC concentrations and salt rejection at 25°C curing temperature

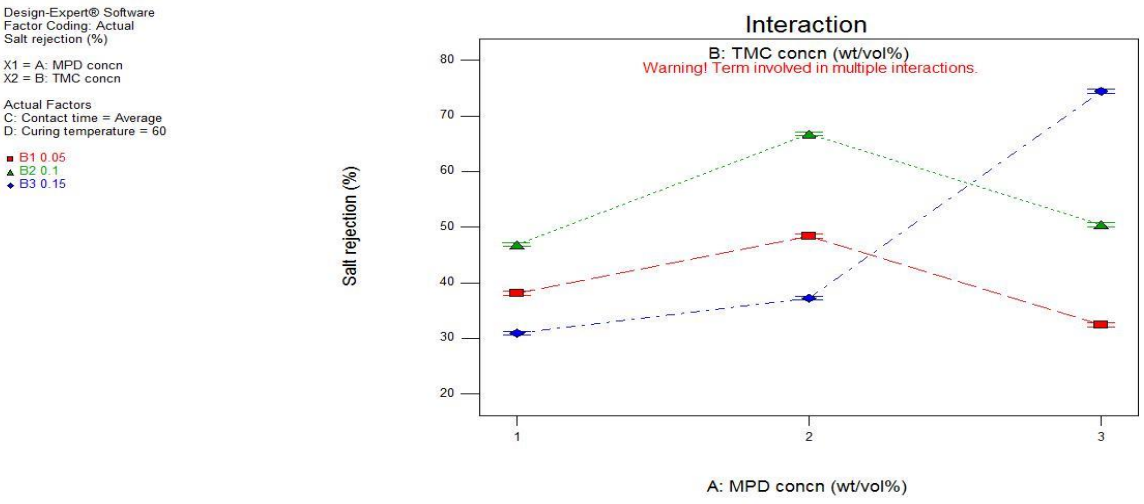

Interaction model graph between MPD, TMC concentrations and salt rejection at 60°C curing temperature

Appendix III

BET differential graphs for the different support membranes

1. Effect of PVP at fixed 15% PSF

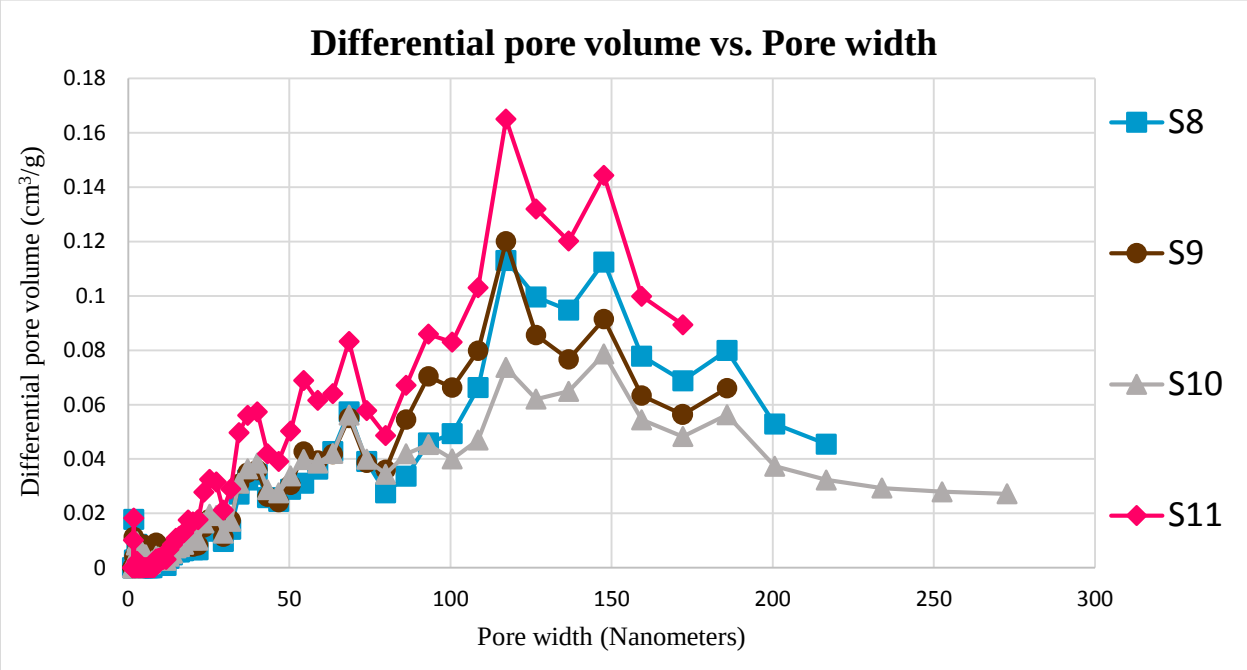

Plot of differential pore volume vs. pore width for S8, S9, S10 and S11

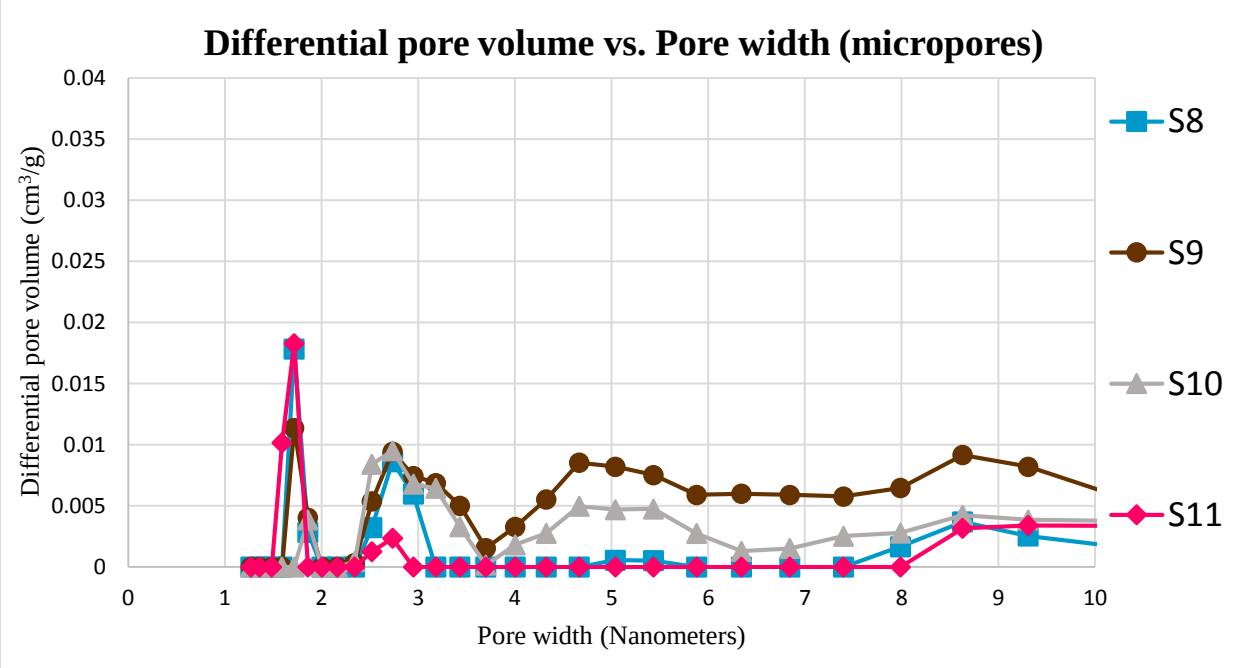

Plot of differential pore volume vs. pore width (micropores) for S8, S9, S10 and S11

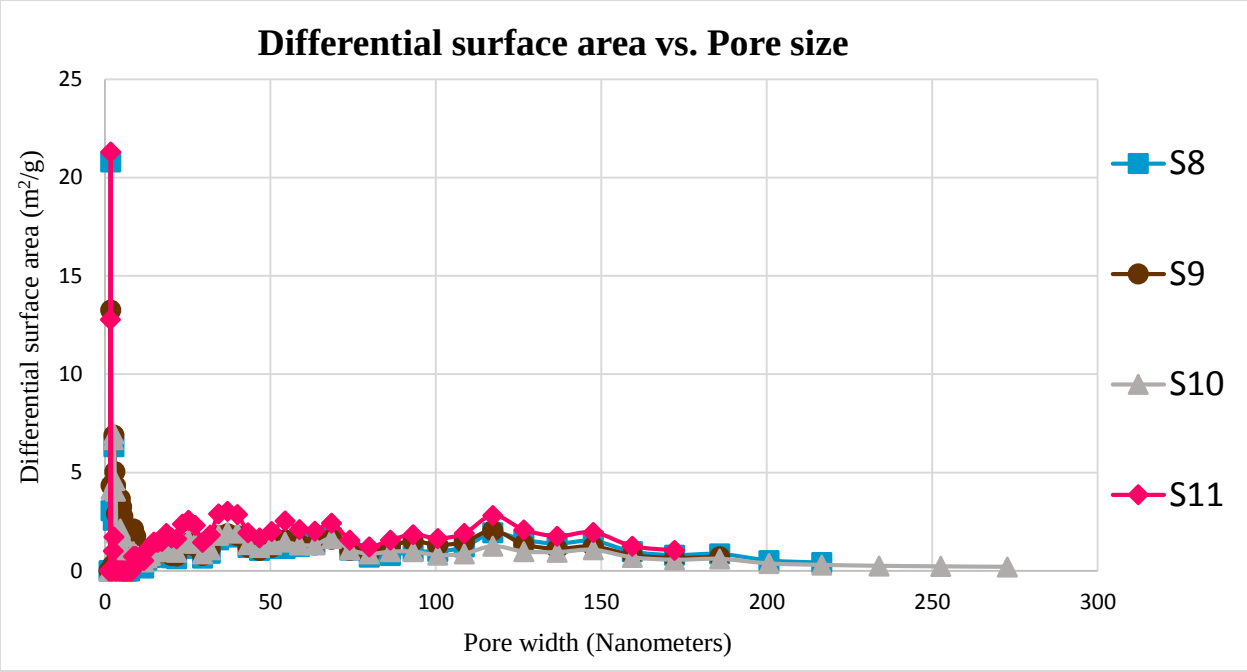

Plot of differential surface area vs. pore width for S8, S9, S10 and S11

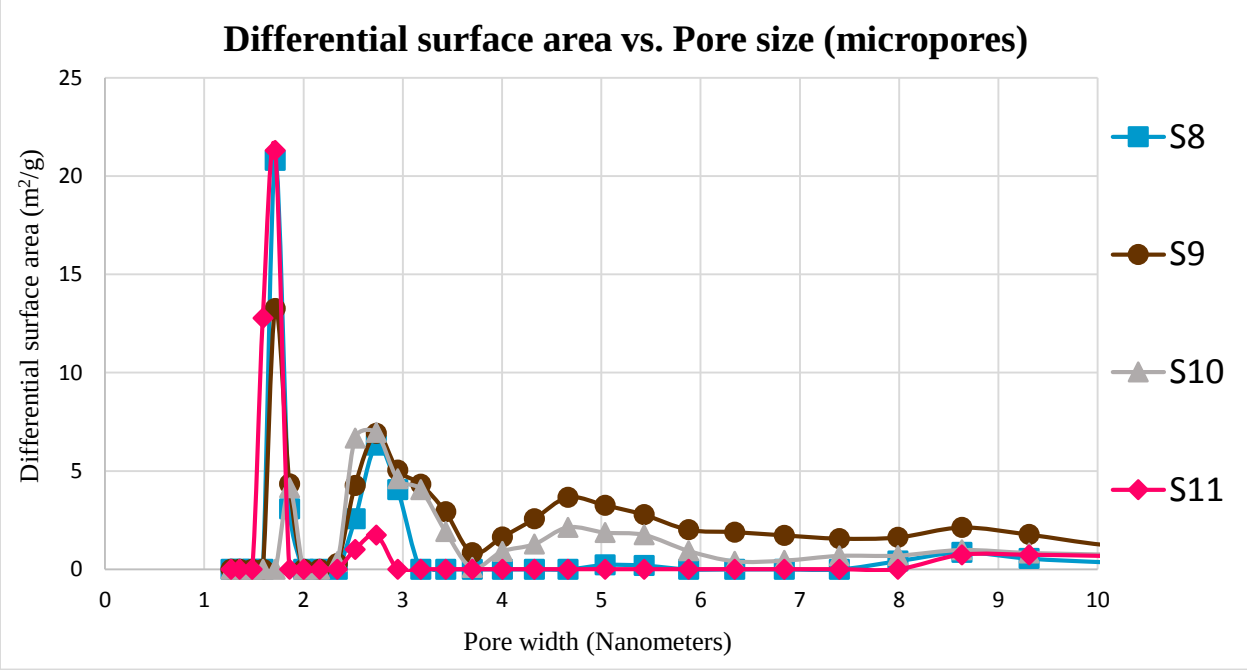

Plot of differential surface area vs. pore width (micropores) for S8, S9, S10 and S11

2. Effect of PVP at fixed 20% PSF

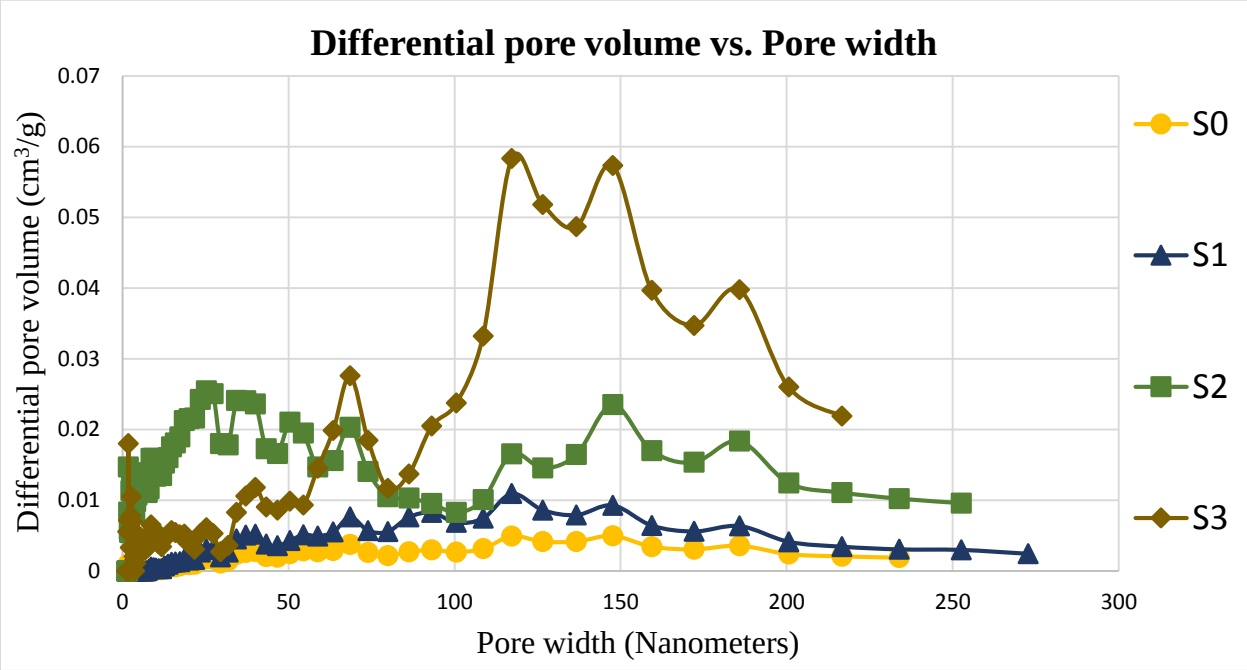

Plot of differential pore volume vs. pore width for S0, S1, S2 and S3

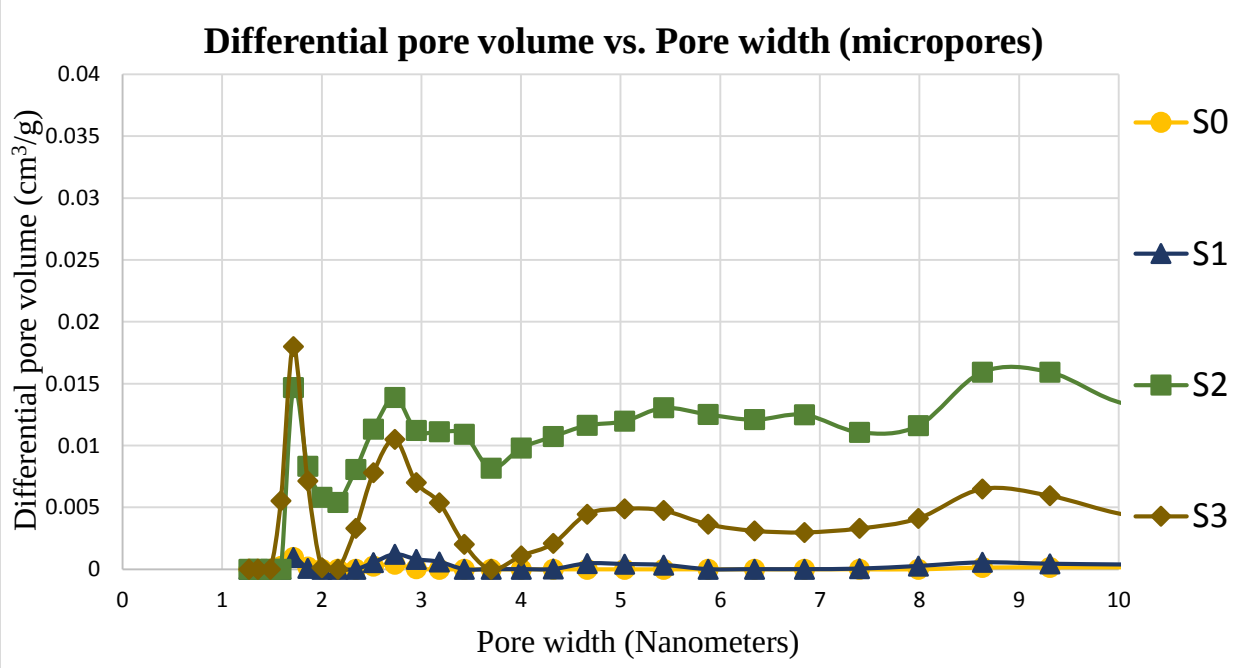

Plot of differential pore volume vs. pore width (micropores) for S0, S1, S2 and S3

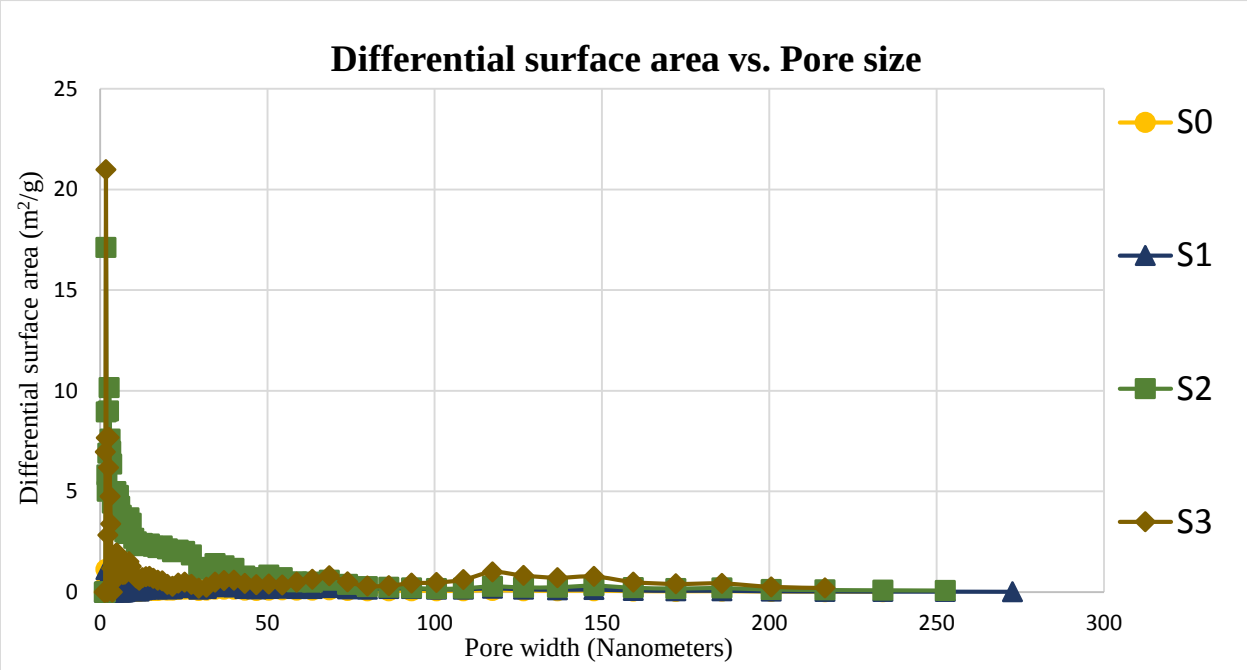

Plot of differential surface area vs. pore width for S0, S1, S2 and S3

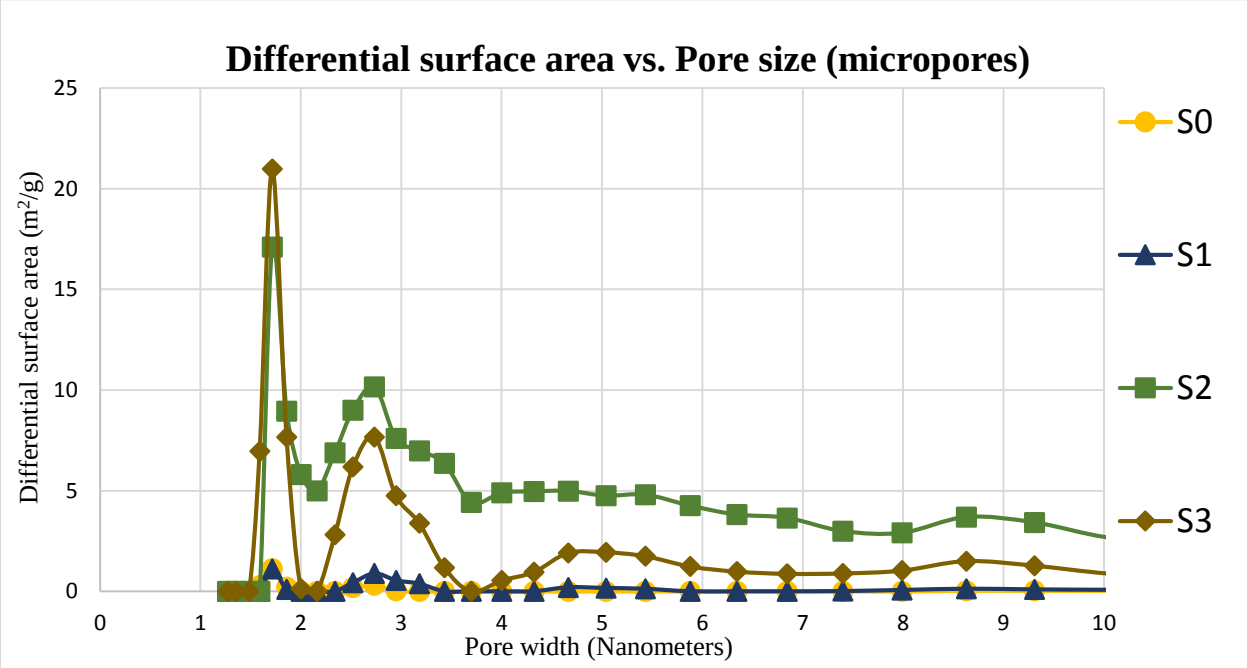

Plot of differential surface area vs. pore width (micropores) for S0, S1, S2 and S3

3. Effect of PSF at fixed 0% PVP

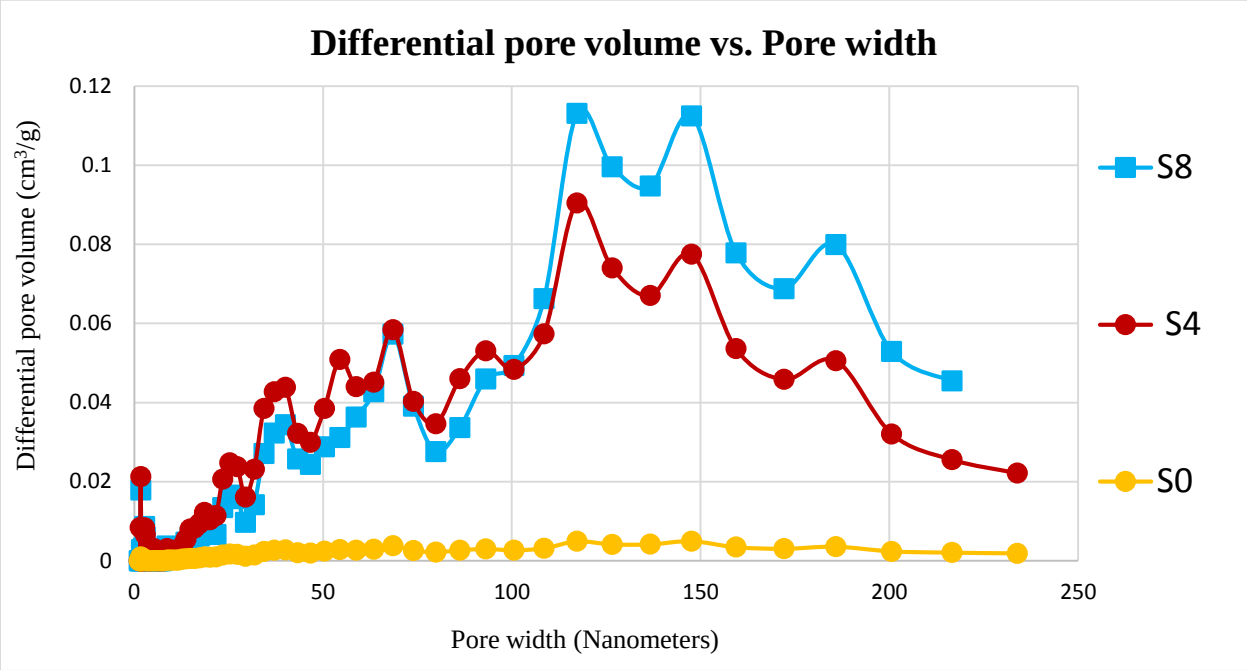

Plot of differential pore volume vs. pore width for S8, S4, and S0

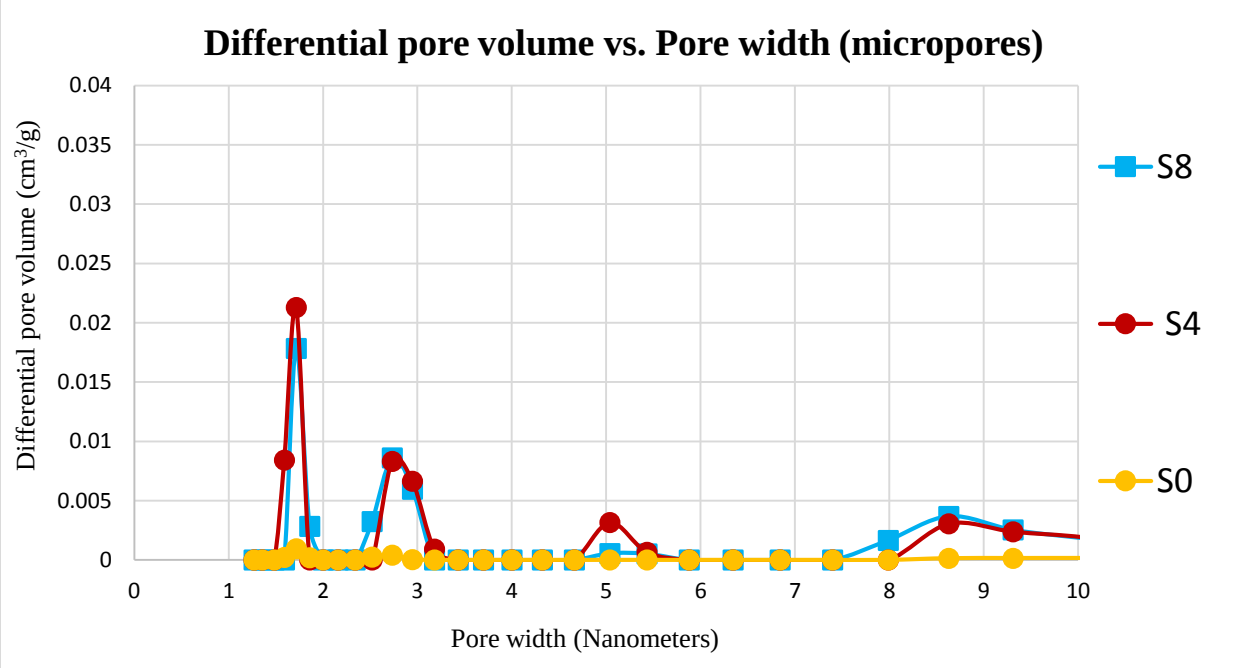

Plot of differential pore volume vs. pore width (micropores) for S8, S4, and S0

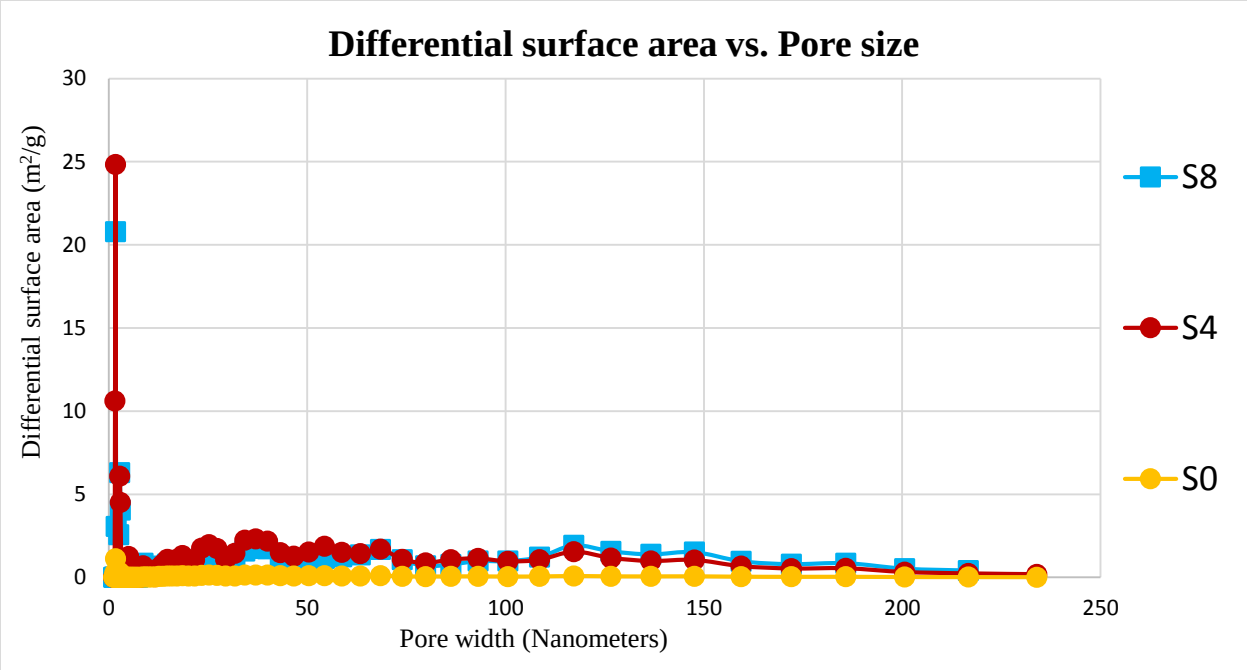

Plot of differential surface area vs. pore width for S8, S4, and S0

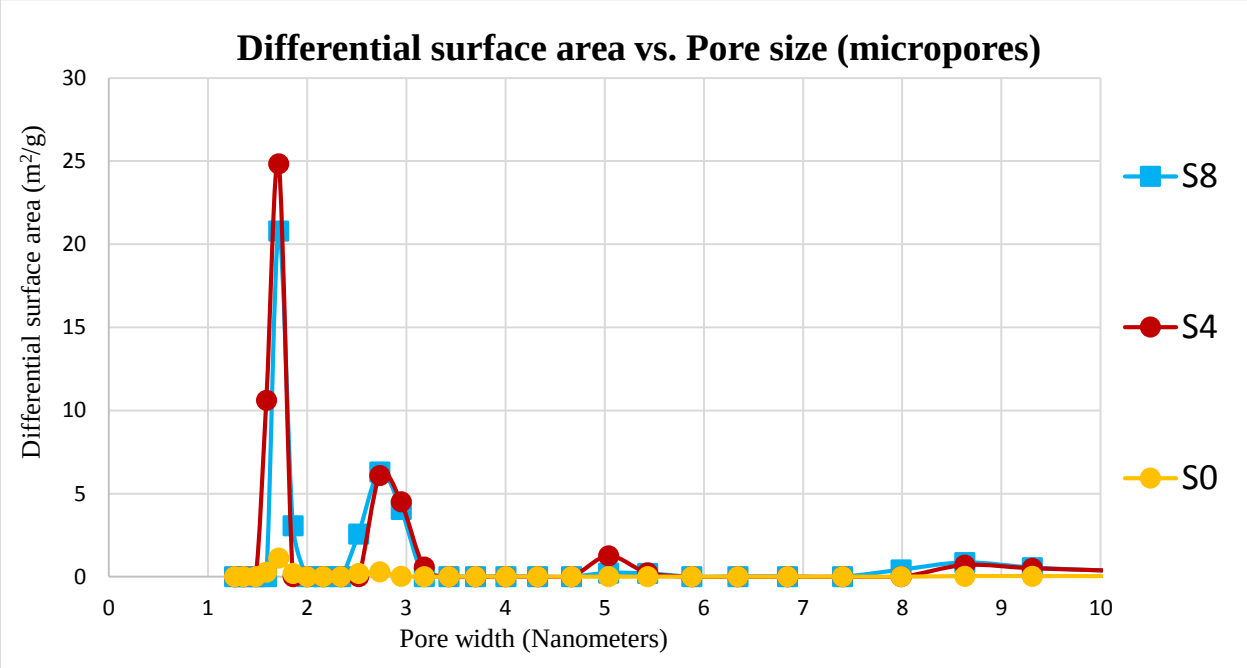

Plot of differential surface area vs. pore width (micropores) for S8, S4, and S0

4. Effect of PSF at fixed 1% PVP

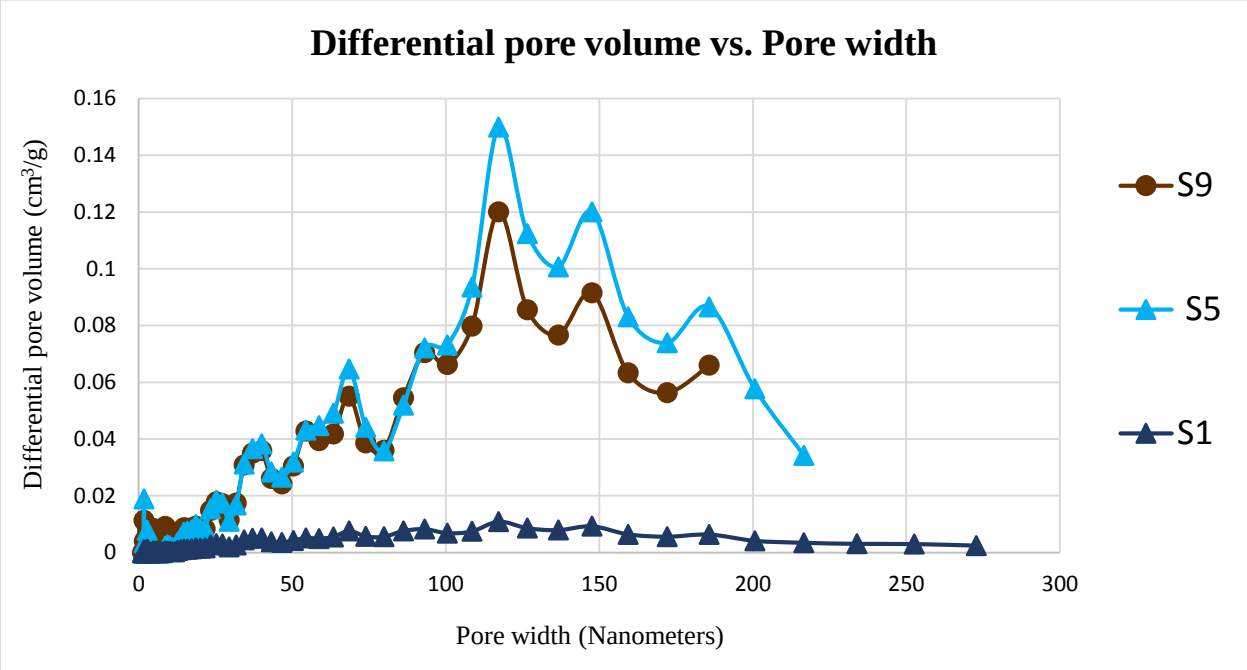

Plot of differential pore volume vs. pore width for S9, S5, and S1

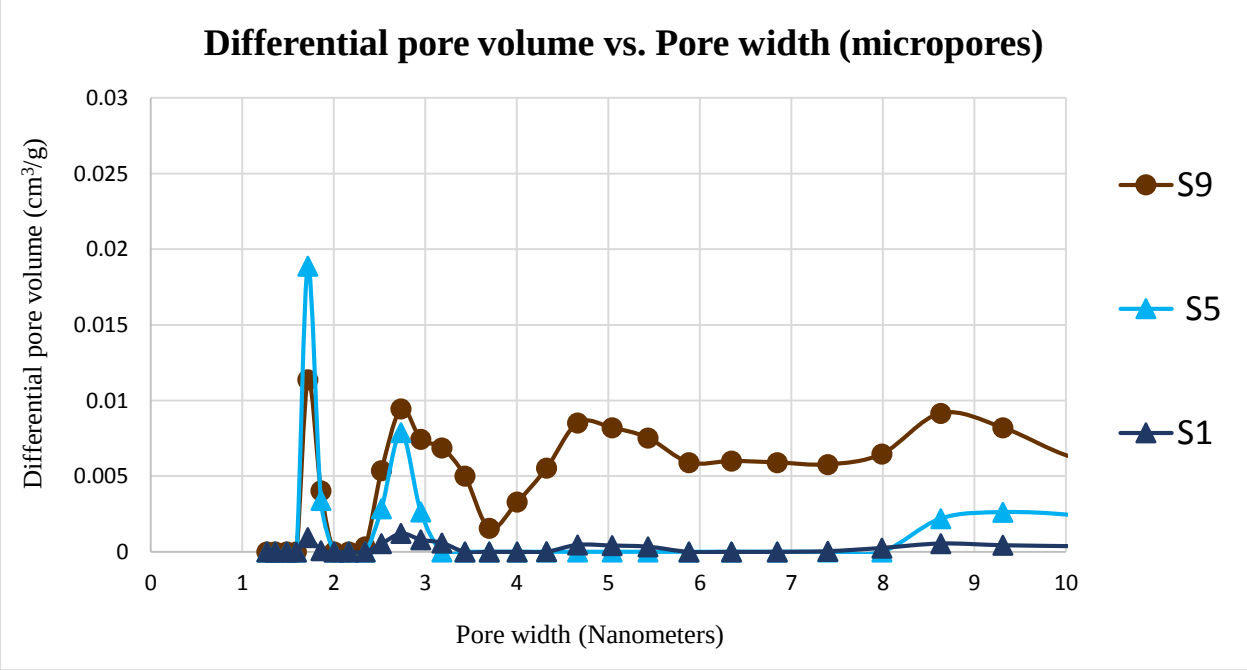

Plot of differential pore volume vs. pore width (micropores) for S9, S5, and S1

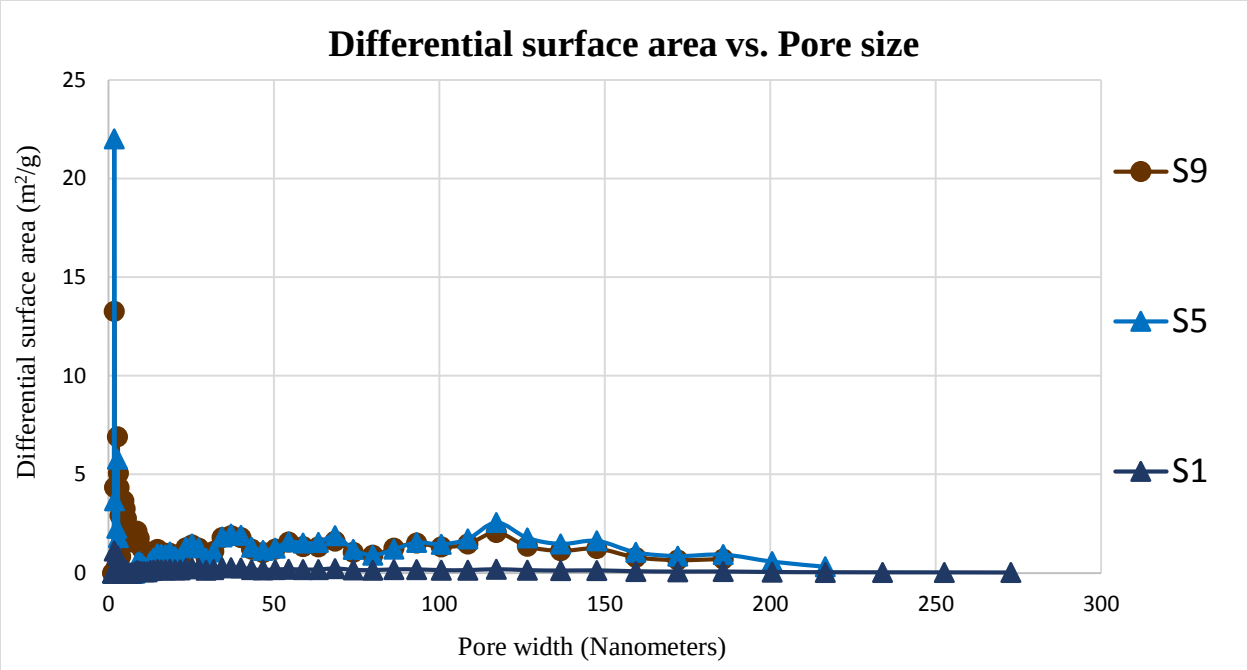

Plot of differential surface area vs. pore width for S9, S5, and S1

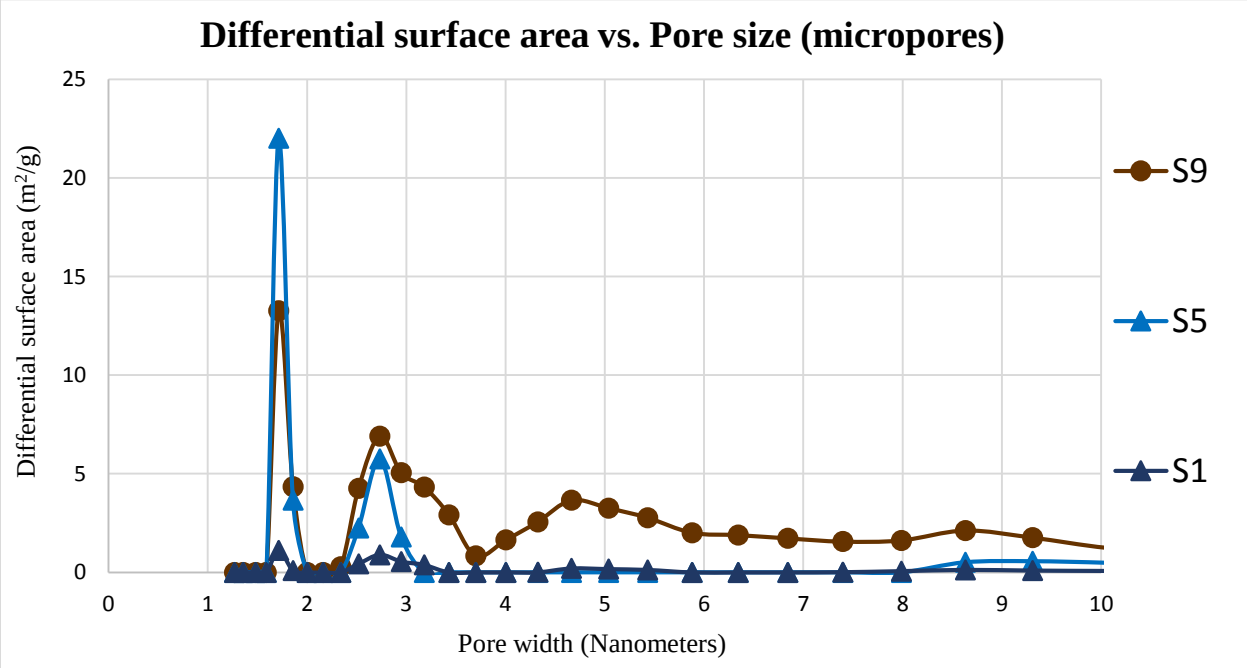

Plot of differential surface area vs. pore width (micropores) for S9, S5, and S1

5. Effect of PSF at fixed 5% PVP

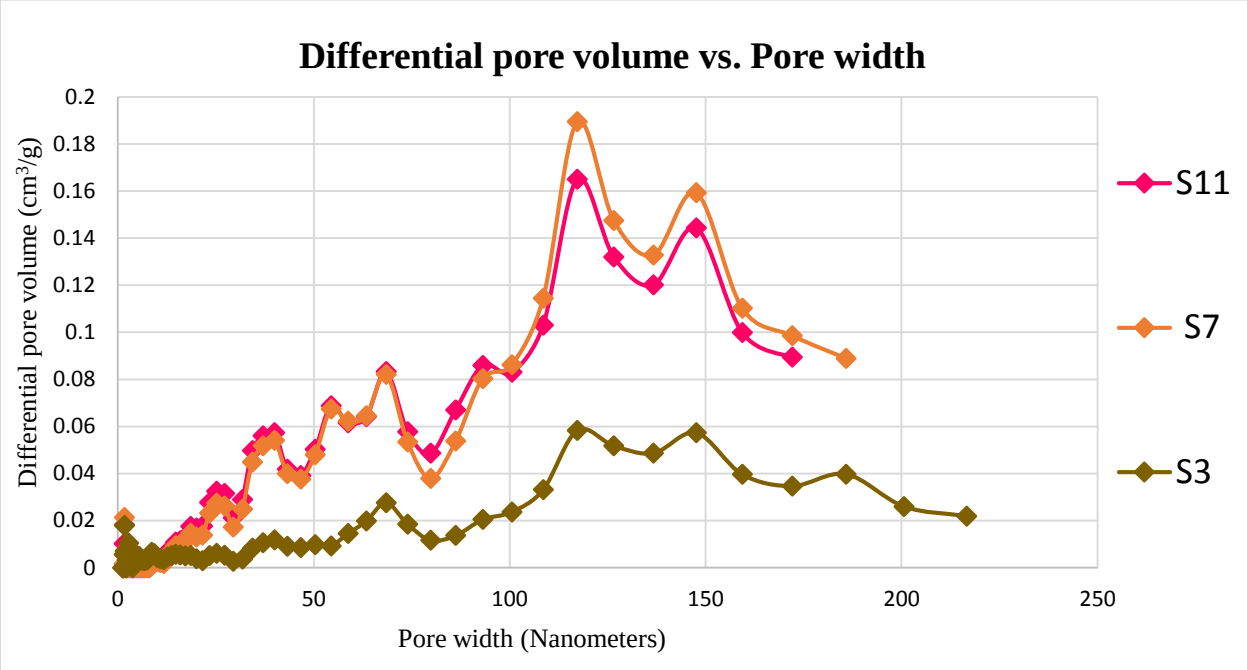

Plot of differential pore volume vs. pore width for S11, S7, and S3

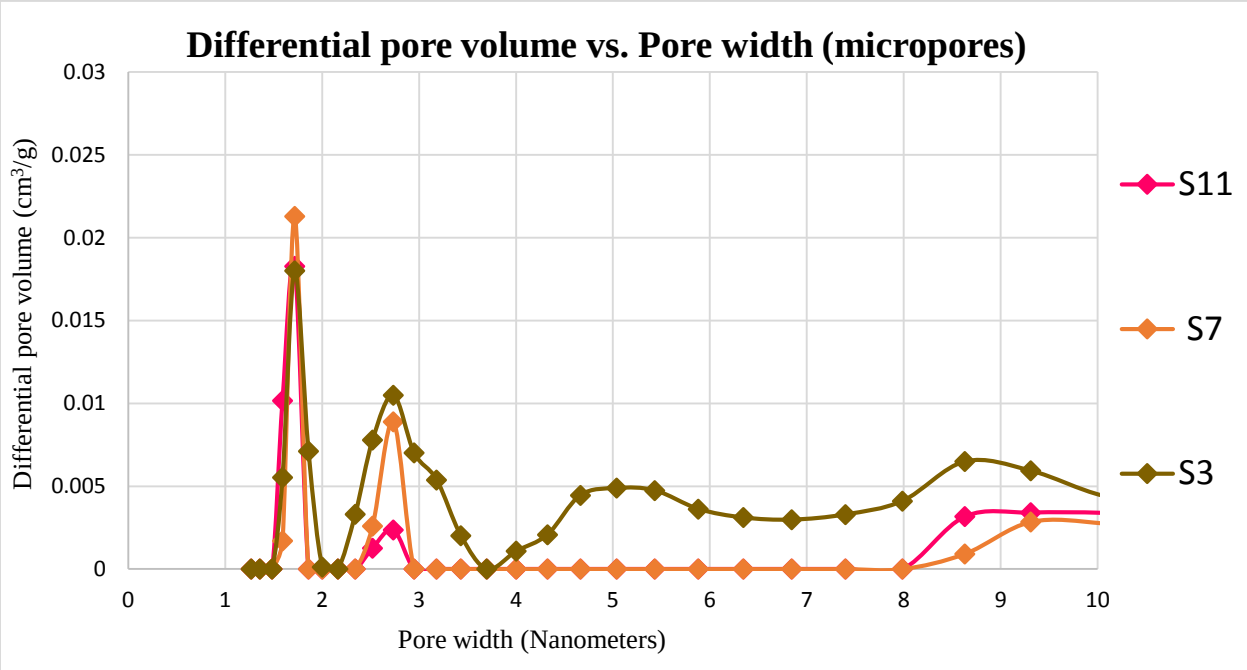

Plot of differential pore volume vs. pore width (micropores) for S11, S7, and S3

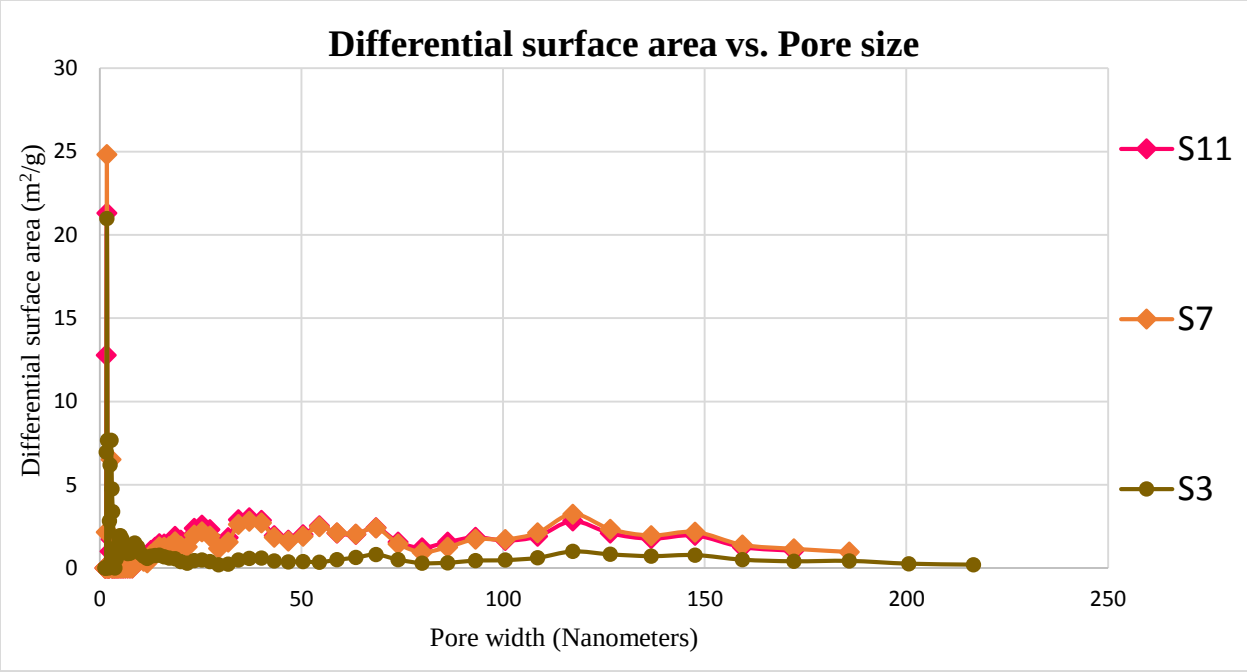

Plot of differential surface vs. pore width for S11, S7, and S3

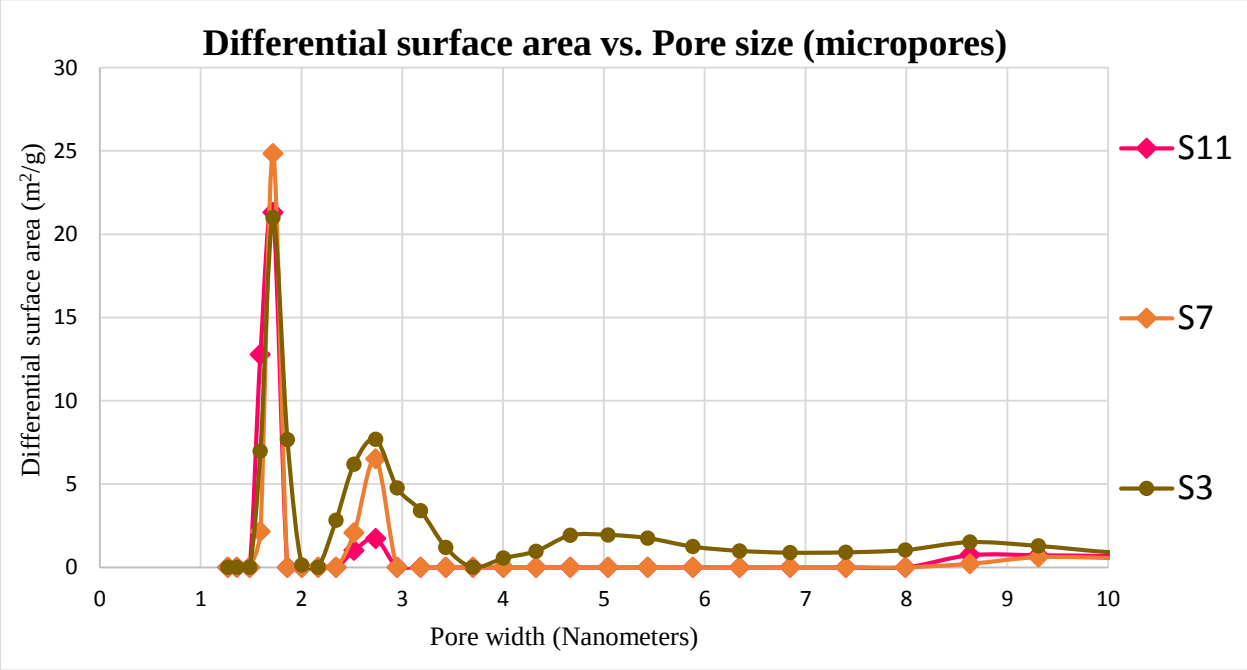

Plot of differential surface vs. pore width (micropores) for S11, S7, and S3

Appendix IV

Functionalization of MWCNTs

MWCNTs were functionalized in order to enhance their dispersion in the aqueous solution of MPD. Functionalization was carried out by oxidation purification in acidic medium. FTIR was used to verify the outcomes of the functionalization process. Figure 5.29 shows the combined FTIR spectra of the functionalized MWCNTs vs. non-functionalized MWCNTs. The former showed a strong peak at 3454 cm^{-1} for O-H stretching, which was formed after the oxidation of carbon to carboxylic group, and a medium peak at 1627 cm-1 for the C=O bond. These bands demonstrate the successful functionalization of the MWCNTs.

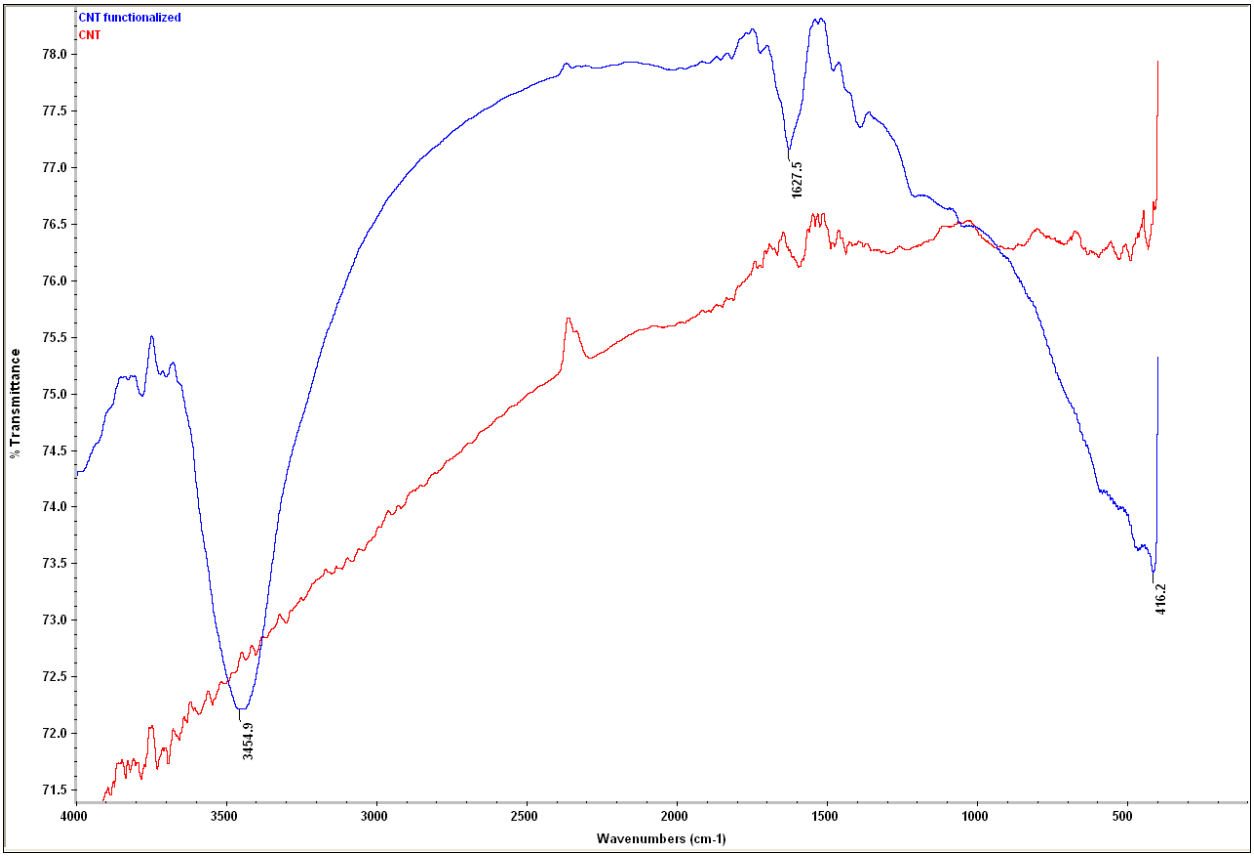

Combined IR spectrums of functionalized (blue) and non-functionalized (red) MWCNTs